Designing novel amorphous catalysts for the propane dehydrogenation reaction

Takudzwa Bere

Thesis submitted in accordance with the requirements for degree of Doctor of Philosophy

School of Chemistry

Cardiff University

Primary Supervisor: Professor Graham J. Hutchings

Secondary Supervisor: Professor Stuart H. Taylor

2022

ACKNOWLEDGEMENTS

Having completed this PhD there are several people who I would like to express my sincere gratitude to, because without them this would not have been possible. Firstly, I would like to thank my supervisors Prof Graham Hutchings and Prof Stuart Taylor for their continued guidance and support throughout the project. To Dr James Carter, thank you for your patience, guidance without reservation, our many productive discussions and your many constructive suggestions. Thanks also to Prof Chris Kiely and Dr Thomas Davies for their fruitful discussions, suggestions, and contributions to TEM presented in this thesis. I would also like to acknowledge my fellow PhD students, Jack Pitchers and Daniel Hewes, who as project teammates made the experience more enjoyable and selflessly helped with TEM and XPS analysis presented in this thesis. To Drs David Morgan and Colan Hughes for their contribution to the XPS work presented in this thesis, and NMR development, respectively. Drs Michal Perdjon, Greg Shaw and Steven Morris for their continual technical assistance and advice.

Of course, I am incredibly grateful to TotalEnergies for funding this research; my involvement in the 'Total consortium' has been a privilege for which I am incredibly thankful. In addition to financial support, I would also like to acknowledge the significant guidance, effort, scientific input and discussion towards this project from the TotalEnergies supervisory team; namely Drs. Bart Vandegehuchte and Moritz Schreiber. To the extended consortium teams, thank you for your collaborations which helped strengthen the research outcomes. Prof Laura Prati, Drs. Alberto Villa, Stefano Cattaneo, Sofia Capelli and Simone Cardaci from the University of Milan are thanked for their help with the flame spray pyrolysis materials presented in this thesis. I am also grateful to Prof Robert Raja from the University of Southampton and his group namely Drs. Matthew Potter and Marina Carravetta, Joshua LeBrocq, Alice Oakley, Mark Light and Evangeline McShane for our many project discussions and NMR method development presented in this thesis.

Finally, I am extremely grateful for the belief, support and love passed from my family and friends. Thank you all for providing me with the motivation to succeed each day.

ABSTRACT

Global demand for propene, a major platform chemical with a myriad of uses in the manufacturing and chemical industry, is anticipated to continue to grow annually. The expected growth in propene demand cannot be met by existing processes, therefore direct or on-purpose processes are being developed to fill the so-called '*propene gap'*. Many of the technologies employed for the commercial dehydrogenation of propane operate using various Pt-based catalysts. This work addresses the rationale catalyst design of the support material and the supported metal catalyst with the aim of unlocking new catalyst design strategies.

Hence, the investigations into catalyst design based on amorphous/disordered materials with an anticipated higher density of active sites for acid-catalysed catalytic reactions, are of great importance. This work addresses the systematic design of a new supercritical antisolvent-mediated (SAS) route to amorphous silica-alumina materials exploring the effect of solvent composition, process temperature, process pressure, calcination conditions, and choice of metal precursors. A route to a series of optimized and systematically varied amorphous silica-alumina was realised and the experimental approach was backed up by detailed advanced characterization. The synthesis strategy has not been previously reported in literature and preliminary investigations revealed bulk (microstructural) and local (nanoscale) structural similarities to analogous state-of-the-art, flame-spray pyrolysis (FSP) synthesized materials.

Subsequent work focussed on finding and applying a reproducible method to deposit platinum nanoparticles with small particle size and size distribution onto the support. Catalytic evaluation was carried out on two acid-catalysed reactions, the propane dehydrogenation reaction and catalytic dehydration of methanol-to-DME (MTD). A combination of XRD, TGA, NH_3-TPD, Pyridine-DRIFTS, (heteronuclear 1D MAS and 2D ^{27}Al MQMAS) Solid-state NMR, XPS, SEM/EDX, FTIR/ATR, HRTEM, and SAED helped establish structure-performance relations. Through careful catalyst design, Pt/SAS-4 and Pt/FSP-4

catalysts with moderate surface acidity displayed the highest catalyst activity, productivity, and stability. The results found the catalyst performance to be comparable to and/or superior to analogous Pt-based catalysts supported on crystalline supports and reported in literature. Similar activity correlations were realised in the methanol-to-dimethyl ether reactions, and the key active component of the catalyst was surface acidity namely the nature, concentration, density, and balance of acid sites.

A combination of several factors including aluminium speciation, morphology and surface acidity of the support explained the variations in catalytic activity. In the supported metal catalyst morphology and surface acidity played an active role in the redox properties of the support and its interaction with supported metal particles. The high propene yield, propene productivity and stability of Pt supported on supercritical antisolvent precipitation and flame spray pyrolysis synthesized SiO_2-Al_2O_3 was attributed to a high proportion of coexistent Al^{IV}- and Al^{V}-based Brønsted acid sites within the support. The former was responsible for propane activation and the latter for anchoring and stabilising deposited nanoparticles; a key observation over a 16-hour non-oxidative propane dehydrogenation reaction. Therefore, the presence of a high proportion of Al^{V} polyhedral, increased elemental homogeneity and high density of homotopic acid sites was used to rationalise a lot of the fundamental findings and relationships observed during this work.

From the combined experimental, characterization and catalytic study, moderate aluminium content (Si/Al) and thus surface acidity was pertinent to enhanced catalyst activity, selectivity and stability in acid-catalysed reactions. The implications of this work in improving the understanding of novel, robust catalyst design and subsequent catalytic applications in the field of acid-catalyzed reactions has been explored.

LIST OF ABBREVIATIONS

ATR	Attenuated Total Reflection
a.u.	Arbitrary units
BAS	Brønsted acid site
BE	Binding Energy
BET	Brunner, Emmett and Teller
BJH	Barrett, Joyner and Halenda
CEDI	Charge Enhanced Dry Impregnation
CVI	Chemical Vapour Impregnation
1D	One dimensional
2D	Two dimensional
DRIFTS	Diffuse Reflectance Infrared Fourier Transform Spectroscopy
DSC	Differential Scanning Calorimetry
EDX	Energy Dispersive X-ray Analysis
FID	Flame Ionization Detector
FSP	Flame Spray Pyrolysis
FTIR	Fourier Transform Infrared Spectroscopy
GC	Gas Chromatography
HC	Hydrocarbons
HRTEM	High Resolution Transmission Electron Microscopy
H-ZSM5	Protonic (H^+) Form Zeolite ZSM-5
ICP-OES	Inductively Coupled Plasma Optical Emission Spectroscopy
IWI	Incipient Wetness Impregnation
LAS	Lewis acid site
MAS-NMR	Magic Angle Spin Nuclear Magnetic Resonance
MQMAS	Multiple-Quantum Magic Angle Spinning
MTD	Methanol-to-Dimethyl ether
NH_3-TPD	Ammonia Temperature Programmed Desorption
PDH	Propane Dehydrogenation

SEM	Scanning Electron Microscopy
TGA	Thermogravimetric Analysis
TPD	Temperature-Programmed Desorption
wt. %	Weight percent
WHSV	Weight Hourly Space Velocity
XPS	X-ray Photoelectron Spectroscopy
XRD	X-ray Diffraction

Table of Contents

1 Introduction

1.1 Catalysis

Catalysis is an integral technology for chemical and materials manufacturing underpinning equipment and products used in daily life in a variety of applications. It is estimated that catalysis contributes to greater than 35 % of global GDP and 90 % of chemical processes currently use catalysis at some point in the production chain.[1] Catalysis makes valuable contributions in areas as diverse as energy (petrochemicals), healthcare (pharmaceuticals), transport (catalytic converters), environment (water, air-quality and purification), food production (fertilizers) and new-materials (renewable and bio-based materials and fuels).

Historically, the concept of catalysis was pioneered by Swedish scientist, J.J. Berzelius in 1836 in an effort to rationalise experimental observations on the effect of trace noble metals, platinum and palladium, on the rates of reaction.[2] The word catalysis originates from two Greek words, *kata*- meaning down and *lyein* meaning loosen.

By definition, catalysis is the acceleration of a chemical reaction by a substance that is not consumed itself. Therefore, a catalyst is a material which changes the rate of attainment of chemical equilibrium without itself being changed or consumed in the process. The International Union of Pure and Applied Chemistry (IUPAC) definition states a catalyst is a substance that increases the rate of a reaction without modifying the overall Gibbs energy change in the reaction.[3] Reaction feasibility is determined by chemical thermodynamics, if so the extend of the reaction is defined by an equilibrium limitation. The potential energy profile of a catalysed and uncatalysed reaction is illustrated in Fig 1.1. As such, a catalyst is a small amount of substance that stimulates an increase in the rate of chemical reaction(s), usually by facilitating an alternative reaction pathway with lower activation energy.

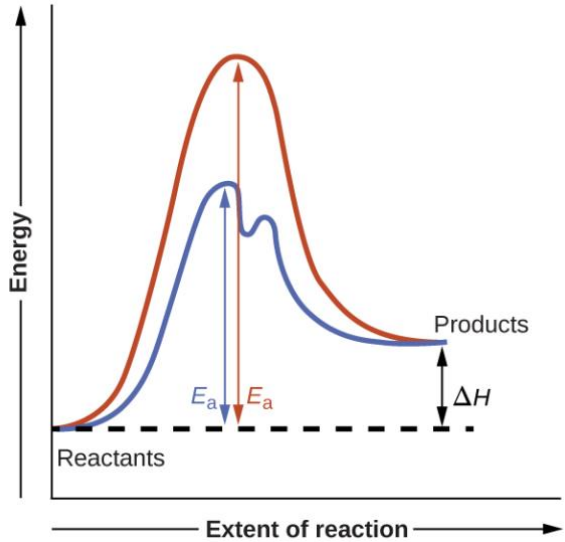

Figure 1.1: Reaction coordinate diagrams for an endothermic reaction in the absence (red) and presence (blue) of a catalyst. The catalysed pathway involves a two-step mechanism (note the presence of two transition states) and an intermediate species (represented by the valley between the two transitions states).[4]

1.2 Thermodynamic and kinetic considerations

The catalysed reaction mechanism for a reaction does not necessarily need to involve a different number of steps than the uncatalysed mechanism. However, it must provide a reaction path whose rate determining step is faster, a direct consequence of the lower activation energy. Chemical thermodynamics and kinetics have to be considered for any given reaction. The Gibbs free energy, enthalpy and entropy depend only on the initial finial states of the systems not the path taken to proceed from one to the other. Thus, they are known as state functions and are defined below:

$$\Delta G = \Delta H - T\Delta S$$

$$\Delta G = -RTln(K)$$

Where ΔG is the Gibbs free energy, ΔH is the enthalpy, ΔS is the entropy, T is the temperature, R is the Gas constant (8.314 J K^{-1} mol^{-1}) and K is the equilibrium constant. The free energy value represents the process spontaneity. When $\Delta G < 0$, $\Delta G > 0$, and $\Delta G = 0$

the reaction is spontaneous, non-spontaneous and at equilibrium, respectively. The spontaneity of the system is determined by the signs of the enthalpy and entropy changes also depending upon the temperature of the system. Equilibrium is established when the system's free energy is minimized. If a system consists of reactants and products in nonequilibrium amounts, the reaction will proceed spontaneously in the direction necessary to establish equilibrium.

Consideration of the kinetics are essential in forming a full understanding of catalyst function. Reactions deemed possible thermodynamically can be catalysed, increasing the rate of reaction. However, the laws of thermodynamics state that a catalyst is unable to initiate a reaction already deemed thermodynamically impossible. Rather, the catalyst changes the reaction kinetics allowing for the equilibrium to be reached at an increased rate by providing an alternative chemical pathway with a lower activation energy.

The kinetics are expressed through the Arrhenius Equation:

$$k = Ae^{-\frac{E_A}{RT}}$$

Where k is the kinetic rate constant. A is the pre-exponential factor, a constant dependent on the statistical probability of the reactants interacting in the proper orientation; k and T are the Boltzmann constants and temperature, respectively.

The exponential term, $e^{-\frac{E_A}{RT}}$, describes the effect of activation energy on reaction rate and the frequency factor, A, reveals how well the reaction conditions favour properly oriented collisions between reactant molecules. An increased probability of effectively oriented collisions results in larger values for A and faster reaction rates. Additionally, a higher temperature represents a correspondingly greater fraction of molecules possessing sufficient energy (RT) to overcome the activation barrier (E_A). This yields a greater value for the rate constant and a correspondingly faster reaction rate. In a catalysed system decreasing the activation energy, E_A, results in an increased rate constant, k, and subsequent increased reaction rate relative to the uncatalyzed pathway.

1.3 Catalyst performance and deactivation

The activity, selectivity and stability are important quantifiable characteristics used to assess the effectiveness and applicability of a catalyst. Catalytic activity refers to the degree at which a reaction is promoted by the catalyst. Alternatively, activity is the rate the chemical equilibrium is reached. Chemisorption is the main factor governing the activity of catalysts. The bond formed during adsorption between the catalytic surface and the reactants must not be too strong or too weak. A catalysed reaction, with a highly active catalyst, will proceed at a greater rate evident in increased conversion of the starting reactant. In contrast, a catalyst with low or negligible activity will proceed at a decreased rate evident in a decrease in conversion of the starting reactant.

Catalyst selectivity refers to the ratio of products obtained from given reactants. This is dependent on the choice of catalyst. A selective catalyst produces high fractions of desirable products and low fractions undesirable. An unselective catalyst produces high fractions of undesirable products and low fractions of desirable fractions

Catalyst stability refers to the durability of the catalyst. Catalysts in real working conditions are very complex systems. Over time catalyst gradually deactivate due to numerous factors including mechanical, chemical and thermal processes. This deactivation is the loss over time of catalytic activity and/or selectivity. The mechanisms of deactivation differ and can be grouped into six intrinsic mechanisms of catalyst decay.[5] Poisoning, vapour compound formation and/or leaching accompanied by transport from the catalyst surface or particle and vapour–solid and/or solid–solid reactions are chemical in nature. Mechanical catalyst deactivation mechanisms are fouling and attrition/crushing, illustrated in Table 1.1.

Table 1.1: Mechanisms of catalyst deactivation.[5]

Mechanism	Type	Brief definition/description
Poisoning	Chemical	Strong chemisorption of species on catalytic sites

		which block sites for catalytic reaction
Fouling	Mechanical	Physical deposition of species from fluid phase onto the catalytic surface and in catalyst pores
Thermal degradation and sintering	Thermal Thermal/chemical	Thermally induced loss of catalytic surface area, support area, and active phase-support reactions
Vapour formation	Chemical	Reaction of gas with catalyst phase to produce volatile compound
Vapour-solid and solid-solid reactions	Chemical	Reaction of vapour, support, or promoter with catalytic phase to produce inactive species
Attrition/crushing	Mechanical	Loss of catalytic material due to abrasion; loss of internal surface area due to mechanical-induced crushing of the catalyst particle

1.4 Catalyst classes and mechanisms

With the exception of enzymes which are biological catalysts, catalysts can be divided into two types, homogeneous or heterogeneous, depending on the reaction phase that they occupy. A homogeneous catalyst is present in the same phase as the reactants (typically liquid or gas). The catalyst interacts with a reactant to form an intermediate substance, which then decomposes or reacts with another reactant in one or more steps regenerating the original catalyst and forming the product.

Heterogeneous catalysts occupy a different phase to the reaction phase. Generally, heterogeneous catalysts are solid compounds that are added to liquid or gas reaction mixtures. Because of this, such catalysts present an active surface upon which a reaction can occur. This allows gas and liquid phase reactions catalysed by heterogeneous catalysts to occur on the surface of the catalyst rather than within the gas or liquid phase.

The heterogeneous catalysts can be separated from a reaction mixture in a straightforward manner, such as by filtration and centrifugation enabling an ease of recovery for catalysts, which is an important consideration for industrial manufacturing processes.

However, heterogeneous catalysts rely on the available surface area of the catalyst. A large surface-to-volume ratio increases yield. Saturation of the surface of the catalyst with reactant molecules can be detrimental. The reaction, further adsorption of reactants, cannot proceed until products are desorbed from the surface, liberating active sites for a new reactant molecule to adsorb. It is for this reason that the adsorption step in a heterogeneously catalysed reaction is oftentimes the rate-limiting step.

Heterogeneous catalysis typically involves the following processes:

- Diffusion of reactant(s) from the reaction mixture to the catalyst surface
- Adsorption of the reactant(s) onto the active site on the surface of the catalyst
- Activation of the adsorbed reactant(s)
- Reaction of the adsorbed reactant(s)
- Desorption of product(s) from the surface of the catalyst

When discussing heterogeneous catalysed reactions, three mechanisms are encountered, as shown in Fig 1.2.

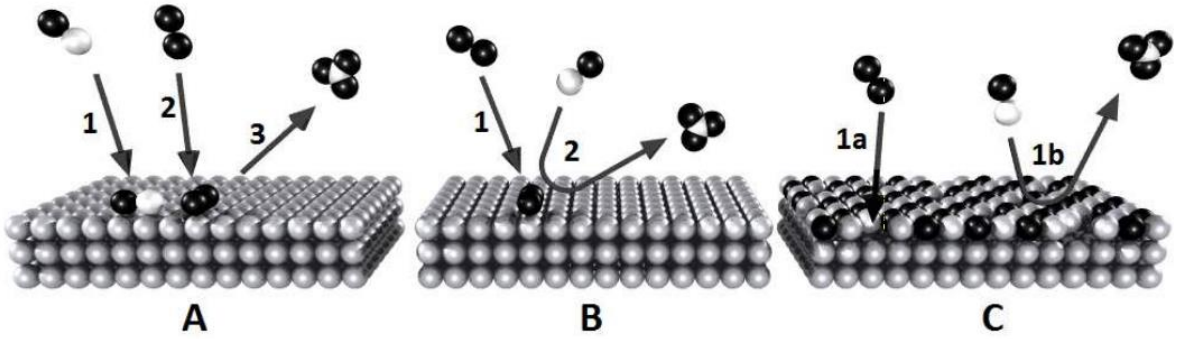

Figure 1.2: Reaction mechanism schematic for (A) Langmuir-Hinshelwood mechanism, (B) Eley-Rideal mechanism, (C) Mars-Van Krevelen mechanism. Reproduced from ref. 6 with permission from Openstax.

The Langmuir-Hinshelwood mechanism requires both reactants are adsorbed onto the catalyst surface before the reactions is initiated, reaction 1 and 2 Fig 1.2 A. The adsorbed molecules interact as a result of surface diffusion. This is followed by the desorption of the reaction product from the surface, reaction 3 Fig 1.2 A. In the Eley-Rideal mechanism, only one of the reactants adsorbs onto the surface and the second reactant molecule interacts with the adsorbed species directly from the gas phase, reaction 1-2 Fig 1.2 B. Lastly, in specific cases, the active phase of the catalyst is formed under reactions conditions due to exposure to one of the reactants. With the CO oxidation reaction as an example, a noble metal catalyst can form an oxide surface under oxygen rich conditions, which could be consumed by the reactant (CO) to form the product (CO_2) and an oxygen vacancy (O_v). Subsequently, the active surface is restored by filling the oxygen vacancy by O2(g). This mechanism is referred to as the Mars van Krevelen (MvK) mechanism.

1.5 Green Chemistry

The principle of Green Chemistry is the design of chemical products and processes that reduce or eliminate the use or generation of hazardous substances. Horvath and Anastas reported the importance of catalysis in the future development of chemical processes.[7] The authors outlined 12 principles proposing ways to minimise waste, reduce energy

consumption among other targets. The proposed guidelines are applicable to the full life cycle of a chemical product from design, manufacture, use and ultimately disposal. The 12 principles by which Green Chemistry is based on are as follows:

1. **Prevention**: It is better to prevent waste than to treat or clean up waste after it has been created.

2. **Atom Economy**: Synthetic methods should be designed to maximise the incorporation of all materials used in the process into the final product.

3. **Less Hazardous Chemical Synthesis**: Wherever practicable, synthetic methods should be designed to use and generate substances that possess little or no toxicity to people or the environment.

4. **Designing Safer Chemicals**: Chemical products should be designed to affect their desired function while minimising toxicity.

5. **Safer Solvents and Auxiliaries**: The use of auxiliary substances (e.g. solvents, separation agents, etc.) should be made unnecessary whenever possible and innocuous when used.

6. **Design for Energy Efficiency**: Energy requirements of chemical process should be recognized for their environmental and economic impacts and should be minimized. If possible, synthetic methods should be conducted at ambient temperature and pressure.

7. **Use of Renewable Feedstocks**: A raw material or feedstock should be renewable rather than depleting whenever technically and economically practicable.

8. **Reduce Derivatives**: Unnecessary derivatization (use of blocking groups, protection/de-protection, and temporary modification of physical/chemical processes) should be minimised or avoided if possible, because such steps require additional reagents and can generate waste.

9. **Catalysis**: Catalytic reagents (as selective as possible) are superior to stoichiometric reagents.

10. **Design for Degradation**: Chemical products should be designed so that at the end of their function they break down into innocuous degradation products and do not persist in the environment.

11. **Real-time Analysis for Pollution Prevention**: Analytical methodologies need to be further developed to allow for real-time, in-process monitoring and control prior to the formation of hazardous substances.

12. **Inherently Safer Chemistry for Accident Prevention**: Substances and the form of a substance used in a chemical process should be chosen to minimise the potential for chemical accidents, including releases, explosions, and fires.

Since the proposition of the principles of green chemistry three key areas have been identified: asymmetric hydrogenation reactions, hydrogen peroxide (H_2O_2) as a green solvent and the use of supercritical CO_2 as a solvent.[8] Notably, avoiding or minimizing the use of harmful solvents catalyst synthesis such as chlorinated hydrocarbons is encouraged. The use of supercritical fluids, such as supercritical CO_2, has great potential in synthetic reactions having beneficial effects due to exhibiting physical properties intermediate between both liquid and gas phases.

1.6 Literature review of amorphous silica-alumina

This thesis specifically focusses on amorphous silica alumina (ASA) materials as components in bifunctional Pt-based catalysts. The understanding of amorphous materials is not very well established and a combination of high-resolution characterization to elucidate the physical and chemical properties; and experimental observations will be undertaken. As such, a review of current synthesis methods and characterization on this class of materials is paramount to allow for a better understanding of this field of research. The focus will predominantly be on the effect of synthesis strategies and their effect on various synthetic parameters, structural descriptors such as strength, nature and type of acid sites, aluminium speciation, specific surface area and elemental homogeneity. This understanding will allow for an accurate mapping of synthesis-structure-activity relationships, identifying areas of improvement and optimization.

1.6.1 Establishing synthesis-structure-activity relationships: a review of synthesis methods

Crystalline and amorphous silica-alumina are a class of mixed metal oxides employed as potential solid acid catalysts for heavy oils hydroprocessing,[9–14] methanol to hydrocarbons,[15] Diels-Alder reactions,[16,17] dehydration of 2-propanol,[18,19] cracking of cumene,[20,21] and tetrahydrofuran polymerization.[22,23] Crystalline synthetic silica-aluminas, known as zeolites, are characterized by high-surface area, acidity, ion-exchange capacity, and shape-selective character. Amorphous silica-alumina (ASA) are heterogeneous compounds that contain a silica alumina mixed phase as well as aluminium clusters and pure silica zones displaying interesting surface chemistry which makes them of particular interest in heterogeneous catalysis.[24–26] Amorphous materials are typically disordered covering a continuous range of compositions as they are not constrained by a crystalline structure, making it possible to selectively tune their macroscopic properties.[27] The bulk and surface heterogeneity depends on the synthesis method and the Si/Al ratio. In some cases studies have shown that their catalytic performance is demonstrably better than that of their crystalline counterparts.[28–30]

This is, in part, due to their mechanical and hydrothermal stability compared to silica and alumina alone.[31,32] However, as solid acids, their catalytic behaviour is usually associated with their acid properties which arise from the functionalisation of silica by alumina resulting in aluminium atoms which are tetra- (Al^{IV}), penta- (Al^{V}) or hexacoordinated (Al^{VI}). Accurate control of the acidic properties of ASAs is affected by a lack of understanding of the origin of Brønsted acidity as well as the inhomogeneous topological composition resulting from typical synthesis methods.

A common understanding is that Brønsted acid sites (BAS) consist of tetra-coordinated aluminium sites with bridging hydroxyl (OH) groups in zeolites, as initially proposed by Thomas[33] and Tamele[34] in the late 1940s. Meanwhile, the presence of hexacoordinated aluminium species is associated with Lewis acid sites (LAS) and aluminium clusters.[35–37] However, ASAs are inherently complex owing to their amorphous character and disordered surface distribution of silicon and aluminium atoms; both of which are depend on the synthesis method.

Variations in the synthesis method and other experimental conditions can influence the level of intimacy between components of the amorphous aluminosilicates. Consequently, a composite surface consisting of well-defined alumina and silica domains and their interfacial sites is achievable with extensive development of a number of synthesis strategies.[38,39] The literature to date reports that ASAs are typically prepared by hydrothermal processing,[40] grafting,[41,42] co-precipitation,[43,44] deposition precipitation,[39,45] and sol-gel[46–48] of metal alkoxides onto surface hydroxyl groups. The different synthetic approaches yield ASA with systematic differences in porosity, morphology, composition, Al speciation and elemental distribution which directly influence acidity.

1.6.1.2 Sol-gel

The connectivity between the chemical and physical properties of ASAs with respect to the synthesis strategies was evaluated in detail by Keller *et al*.[49] In the study, a range of ASAs prepared by selecting appropriate alumina or silica supports and doping with either Si or Al

metal precursors through a pH change (deposition-precipitation) or hydrolysis (grafting). This resulted in a set of ASAs with compositional core-shell structures. Compositionally more homogeneous ASAs are typically obtained by the coagulation of appropriate silica and alumina precursors either by a pH alteration (coprecipitation) or hydrolysis (sol-gel).

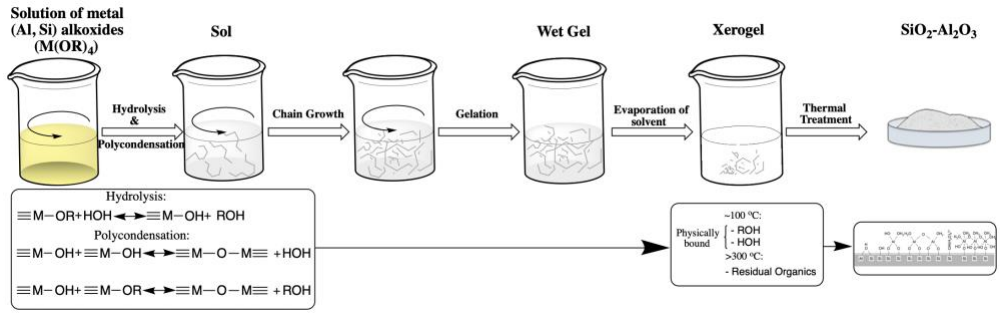

Figure 1.3: Schematic representation of the sol-gel process for ASA.

Mizukami *et al*. reported Al-O-Si bond formation occurred more effectively in sol-gel synthesized ASAs in comparison to conventional methods, such as kneading.[50] As a result, the sol-gel process has attracted much attention in the preparation of complex inorganic materials such as mixed metal oxides.[48] This is due to its ability to control homogeneity of constituent elements on the atomic scale through a low temperature synthesis, with full control of the final product microstructure. Certain parameters can be controlled including concentration and type of precursor, nature of solvent, pH of the solution, type and concentration of additives, pre- and post-thermal treatment and aging time. The sol-gel method applied to the synthesis of ASAs can be summarised, as follows:

a. Preparation of a solution of Si and Al alkoxide precursors.
b. Hydrolysis and partial condensation of alkoxides to generate a “sol”.
c. Polycondensation of hydrolyzed precursors to produce the gel.
d. Drying process whereby the gel forms a dense xerogel *via* the collapse of the porous network caused by the evaporation of the solvent. Supercritical drying results in the formation of an aerogel.
e. Calcination to obtain mechanically stable materials.

The hydrolysis reaction is thought to proceed *via* a nucleophilic substitution mechanism, which results in the replacement of an alkoxy group with a hydroxyl (Figure 1.3, reaction 1). The polycondensation reaction proceeds in parallel to the hydrolysis reaction. This is through the partially hydrolysed alkoxide molecules reacting either with another hydroxyl bearing species by removing water (Figure 1.3, reaction 2) or with an alkoxy group producing an alcohol molecule (Figure 1.3, reaction 3). The gel and material properties at all subsequent steps can be altered by systematic variations in factors affecting the hydrolysis and condensation reactions. The drying step is essential for producing monophasic mixed oxides. The thermal treatment results in the decomposition of alkoxy and other anionic residues followed by cross-condensation between Al and Si moieties.[3451] Additionally, calcination results in two competing processes, the diffusion of aluminium into the silica network and sintering of aluminium into alumina domains. However, the different rates of hydrolysis of the precursors can cause gelation to take place at different times, through homo-condensation rather than hetero-condensation, which leads to phase segregation phenomena.[39] This limitation has implications on the homogeneity and surface acidity.

1.6.1.3 Flame Spray Pyrolysis (FSP)

Further developments into the preparative strategies for mixed metal oxides have been aimed to tackle this issue. The flame spray pyrolysis (FSP) method has emerged as the most effective synthesis strategy offering the production of novel, thermally stable, scalable metastable or amorphous phases of mixed metal oxides.[52–55] Compared to wet-chemical routes with various post-treatment steps, such as filtration, washing, drying and calcination, gas-phase processes allow the preparation of the desired material without any further post-processing.

The synthesis solution is a combustible liquid composed of metal precursors dispersed in an organic solvent system and introduced either ultrasonically or by gas convection through a nozzle.[56] In the case of ASA, Baiker *et al*.[53] report metal alkoxides and a mixture

of acetic acid and methanol as appropriate metal precursors and solvent system, respectively.

Experimentally, the fine spray is introduced and then ignited, evaporating in the spray flame. The thermal decomposition of a precursor is a classical process used to induce high supersaturations in a fluid phase which leads to the nucleation of nanoparticles. The precursor is atomized and carried by a gas into a high temperature zone, the solvent evaporates from the droplets and the porous dried particles obtained sinter to form dense particles. These particles coagulate, and agglomerate. The amorphous precipitate is the result of the very short residence time (a few milliseconds) which does not allow enough time for crystallization while also promoting the homogeneous composition and formation of Al-O-Si bonds.

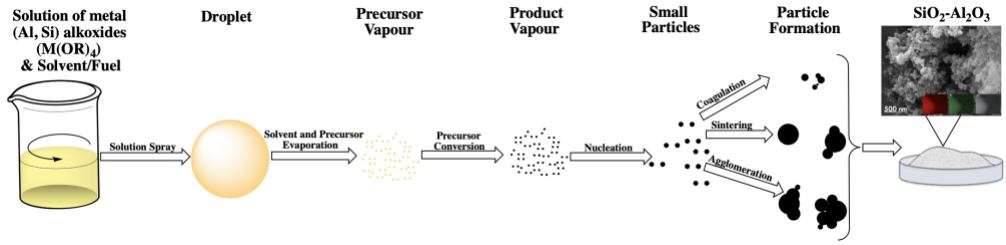

Figure 1.4: Schematic representation of the Flame Spray Pyrolysis (FSP) methodology for the synthesis of ASA.

The resultant material has a high degree of homogeneity and compositionally, mixed on the nano- and atomic-scale in a single step with intrinsic features of active catalysts such as high thermal stability, high surface area, tuneable acidity.[57–59]

1.7 Acidity characterization

It is clear that the relationship between the synthesis method, structure and resulting activity, referred to as the "synthesis-structure-activity" relationship is key to understanding ASAs. The surface and bulk structure of zeolites and origin of their acidity

has been studied extensively.[35,60–63] The high concentration of Brønsted acid sites lies in the bridging hydroxyls which are located in the walls of the zeolitic cavities, constituting the strong acid sites of protonic zeolites, shown schematically as the Si-(OH)-Al^{IV} model (Fig 1.5 C).[64] This is a result of protonation of charge defects which arise from the substitution of Si^{4+} by Al^{3+} in the silica-based crystalline framework. Many studies acknowledge that ASAs are characterized by a lower density of acid sites in comparison to their crystalline counterparts.[39,65–67] The formation of a mixed phase leads to the creation of acidic hydroxyl groups of various strength. The literature to date which has specifically studied the surface structure of amorphous silica alumina is significantly limited, with an adequate surface model still under debate. This is because ASAs are inherently complex owing to their amorphous structure thus making the correlation between structure and activity challenging to establish.

Despite advances in synthesis and post-synthetic modification of solid acids, ASAs typically possess non-uniformity of acid site strengths and chemical composition on an atomic scale as shown by NMR spectroscopy and density function theory (DFT) calculations.[38,68] This is in part due to the high degree of heterogeneity of surface acid sites which also feature other acidic surface sites specific to these materials, which are referred to as pseudo-bridging silanols (PBSs).[19,69] Consequently, characterization by most spectroscopic techniques is a challenge. However, a number of spectroscopic techniques such as Infrared (IR) spectroscopy of probe molecules, such as carbon monoxide (CO) and pyridine, as well as solid state nuclear magnetic resonance (SS NMR) spectroscopy have been employed to expand the understanding on the heterogeneous nature of amorphous aluminosilicates.[45,53,70] Such methods have been instrumental in studying structural features such as bonding and coordination around metal ions.

The presence of bridging hydroxyl groups in ASAs was previously tentatively proposed and associated with samples with trace amounts of water which is often difficult to exclude even with dehydration due to the hygroscopicity of ASAs.[71,72] Similarly, Trombetta *et al*. reported the formation of bridging hydroxyl groups that exhibit strong Brønsted acidity in

the presence of a base.[73] This was a result of a geometric effect induced by a basic molecule interacting with a silanol group in the vicinity of an Al vacancy.

On the basis of IR spectroscopy with pyridine and CO adsorption and SS NMR studies by Crépeau *et al*.[74] and Hensen *et al*.[39] the nature, strength and density of the acid sites present in sol-gel synthesized ASAs were differentiated. Conceptually, hydroxyl groups of ASA are able to protonate pyridine allowing for Lewis and Brønsted acid sites to be distinguished while CO adsorption allows for the accurate determination of the acid strength of the OH groups. Magic angle spinning (MAS) SS NMR spectroscopy assesses, qualitatively, the local environment of nuclei of interest and allows the quantification of different sites in disordered solids.[75,76] Based on initial interpretation of spectral data the acid sites are dependent on aluminium content, due to the presence of tetra-, penta-, and hexacoordinate Al^{3+} sites.[77] Structural models of ASAs suggest that Brønsted acidity originates nearby silanols on ASA surfaces.[12,78]

Historically, hydrocracking experiments by Haag *et al*.[79] suggested the low acidity of ASA was a result of a very low concentration sites of similar acidity as the bridging hydroxyl groups in zeolites such as ZSM-5. Various studies report that the assumption is that ASA contains a low concentration of sites with similar strength to Brønsted acid sites in zeolites.[80,81] However, the Brønsted acid sites in sol-gel ASAs are a result of a number of hydroxyl groups, illustrated in Fig 1.5.

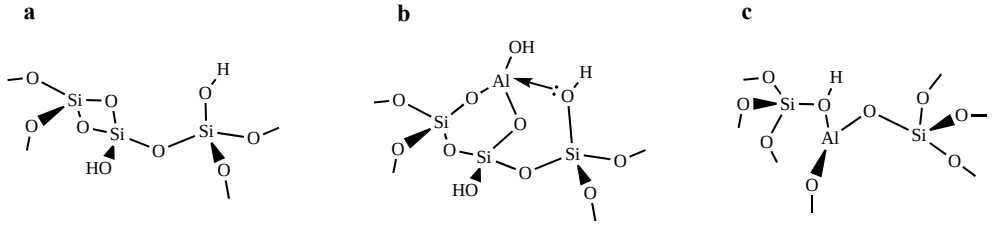

Figure 1.5: Schematic of the three types of Brønsted acid sites in ASAs (a) Non-acidic silanol and aluminol groups; (b) Silanol groups interacting with strong isolated Lewis acid sites (Al^{3+}) surface sites; and (c) Bridging, strong Brønsted acid sites in the silica network.

The zeolite like Si-(OH)-Al site is postulated to exhibit the strongest Brønsted acid sites, with the paired silanol and lewis acid Al^{3+} surface sites exhibiting Brønsted acid strength between that of the bridging-type hydroxyls and silanols. Structural and textural differences between ASAs and zeolites have implications on the localization of the Al atoms.[82] In zeolites, all Si and Al atoms in the zeolite framework are located at the surface and the small, ordered pores which effectively acts as curved surfaces favouring the formation of bridged SiOH-Al^{IV} groups. In contrast, Si and Al atoms in ASAs can be located either on the surface a consequence of the more open, planar structure. Therefore, structures proposed in Fig 1.5 cannot exist in zeolites as this requires considerable framework flexibility which should be much more available in amorphous aluminosilicates relative to their crystalline counterparts. Additionally, the Al concentration is a key determinant for the amount of Al atoms in close vicinity to neighbouring silanols. This explains the presence of silanol groups with various Brønsted acid sites strength in ASA.

Two types of Lewis acid sites are also evident. The stronger form, a result of undercoordinated Al^{3+} sites grafted to the silica surface, the concentration of which depends weakly on the aluminium concentration. The weaker form associated with segregated alumina domains and penta-coordinated Al^{3+} (Al^{V}) species. The rationalisation was made as a result of experimental observations whereby its abundance strongly increased with Al content suggesting that it is due to Lewis acid sites principal of the aluminium domains. In sol-gel ASAs, the Al^{V} species are considered as interfacial species between alumina and silica or alumina and the mixed ASA phase.

In contrast to conventional ASAs, the preparation of flame derived ASA results in better incorporation of Al atoms throughout the silica matrix. Consequently, the formation of the segregated alumina phase is minimized during the synthesis thus maximising the dispersion of Al atoms thus generating Al^{IV} in the framework for optimal acidity. Recent work revealed Brønsted acid sites can be formed based on Al^{V} species thus enhancing the Brønsted acidity of ASAs.[52,53] The high process temperatures (up to 2,000 K), and fast cooling rates facilitate the formation and dispersion of a high population of metastable Al^{V} species generating Al^{V}-

rich ASAs. Therefore, Al^{V} species are proposed to be highly dispersed in the silica matrix *via* Si-O-Al^{V} on the surface and their formation is independent of the alumina phase.[83]

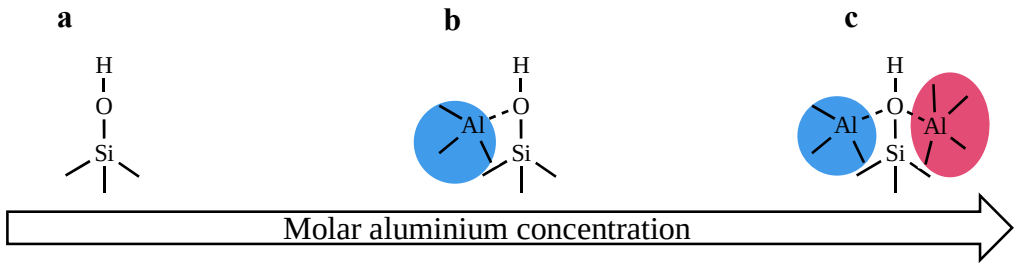

Figure 1.6: Specific surface structure and Al-O-Si bonds of (a) 0 wt% SiO2; (b) 10 wt% SiO2; and (c) 70 wt% SiO2 in FSP synthesized ASAs. Adapted from "Increasing the Brønsted Acidity of Flame-Derived Silica/Alumina up to Zeolitic Strength".[53]

The Si/Al ratio also determines the nature and strength of the different acid sites. Aluminium localised near silanol groups result in an electronic effect whereby a transfer of electron density from OH groups occurs generating strong acid sites.[69] With no aluminium present (Si/Al value of infinity), weak acid sites are present as the silanol groups have no neighbouring aluminium centres. As the aluminium concentration is increased (high to moderate Si/Al value), the tetrahedrally coordinated aluminium in the vicinity of silanol groups results in moderate Brønsted acidity. As the aluminium concentration is further increased (moderate to low Si/Al value), the population of Al^{V} increases and if Al^{V} species are in close proximity to silanol groups, they can enhance the acidity from the generated "pseudo-bridging silanol" (PBS).[84] This enhances their Brønsted acidity to strengths that are similar to or greater than those encountered in zeolites. Quantitative SS NMR spectroscopy of revealed that the concentration of Brønsted acid sites increases with increasing aluminium content, up to 70 at.%.[53,59] Therefore, with FSP derived ASAs the molar ratio of strong and weak sites can be adjusted for desired reactions by varying the aluminium content.

1.8 Acid Catalyzed Reactions

1.8.1 Propane Dehydrogenation

The catalytic dehydrogenation of propane is an important reaction used to produce propene. Propene is an important basic chemical building block for plastics and resins, with global demand on the rise and expected to reach 130 million tonnes by 2023.[85] Commercial uses include the manufacture of mechanical components, containers, fibres, film acrylonitrile fibers, ABS polymer propylene oxide propylene glycol, antifreeze, polyurethane, oxo-alcohol coatings, plasticizer cumene carbonates, phenolic resin acrylic acid coatings, adhesives, and superabsorbent polymers.[86–90] A "propene gap" exists as current technologies namely naphtha steam cracking and fluid catalytic cracking (FCC) will not be able to fulfil this increased global demand. Several on purpose methods are being employed with the direct dehydrogenation of propane (DDH) to propene emerging as a viable option. However, in the absence of an oxidant, such as oxygen or carbon dioxide, the DDH reaction is highly endothermic, equilibrium limited and must be run at very high temperatures to produce significant yields of propene. Consequently, the process requires a high energy consumption and catalyst deactivation is common due to the operating conditions. Currently, the dehydrogenation of lower alkanes is typically carried out using platinum- and chromia-based catalysts.[86,87,91]

1.8.2 Commercial Processes: Pt-based Catalysts

Currently, several industrial commercial processes utilise Pt-based catalysts illustrated in Table 1.2. The Oleflex process from UOP employs alkali metal-promoted Pt-Sn/Al_2O_3 catalysts in a reaction system composed of 3 to 4 moving bed reactors.[92,93] In this process, the catalyst is continuously regenerated in a separate regeneration circuit. The typical catalyst in the Oleflex process consists of spherical pellets of γ-alumina (surface area ca. 100 $m^2\ g^{-1}$) containing Pt (< 1 wt %) and promoted with Sn and alkali metals. The reactor is composed of three or four adiabatic radial flow reactors connected in series with gas flow preheaters operating at pressures between 1 and 3 bar and a temperature range of 525 ^oC to 705 ^oC.

The Steam Active Reforming (STAR) process from Phillips Petroleum, developed by Uhde employs a Sn promoted Pt catalyst, 0.2 to 0.6 wt.%, supported on a zinc-aluminate support, with a calcium/magnesium aluminate binder.[87,94] The reactor system is composed of two fixed bed reactors connected in series with the top of the reactor, where the majority of the dehydrogenation activity occurs, externally heated by an oven. The operating pressures and temperatures are between 6 bar and 9 bar, and 500 ^{o}C to 600 ^{o}C, respectively. Also, due to its non-acidic nature, the support does not promote undesired side reactions, such as cracking, isomerization or coke formation and contains Sn as a promoter to reduce coke formation and increases selectivity. In summary, thermocatalytic alkane dehydrogenation has been commercialized, but suffers from limited conversions and rapid deactivation a consequence of coke deposits.

Additionally, through further patent review other novel catalysts and processes for propane dehydrogenation have been discovered. Most notably, the Dow FCdh and K-PRO processes. Both processes are characterized by short cycle times, and enhanced performance. The Dow FCDh technology utilises a bimetallic Pt-Ga/ Al_2O_3 catalyst operating on a fluidised reactor system coupled with a fluidised regeneration reactor, which enables continuous operation/regeneration.[95] Moreover, compared to the Oleflex process, the Dow FCdh process has a more facile regeneration cycle which involves high temperature oxidative treatment to remove retained carbon species. This circumvents safety and environmental issues encountered in the Oleflex process's complicated regeneration protocol involving Cl_2, O_2 and then H_2. The catalyst can also be fully recoverable after the regeneration step.

Kellogg, Brown and Root (KBR), LLC developed and recently commercialised the K-PRO process with the first contract being awarded in January 2020.[96–98] This process is the latest to be commercialised with an agreed licence with JS Energy Ltd and comprises of KBR's FCC orthoflow reactor.[99] The reactor setup, an up-flowing vertical reactor riser, draws conceptual similarities to the the Dow FCDh process in that the reactor is a fluidised bed, but the regeneration section features a heat exchanger and distributed distillation for improved process efficiency.[96] The significance of this process is that the catalyst does not

contain precious metals or chromium, although the active component(s) remain proprietary information.

Table 1. 2: Industrial propane dehydrogenation technologies for Pt-based catalysts.[86,95]

Technology Name	**Oleflex**	**Uhde STAR Process**	**PDH**	**FLOTU/Tsinghua**	**Dow FCdh**	**K-PRO**
Licensor/developer	UOP LLC	Krupp-Uhde	Linde-BASF-Statoil (Sintef)	Tsinghua University	Dow	KBR LLC
Reactor Type	Adiabatic moving bed with regeneration unit	Adiabatic	Isothermal fixed bed	Bimodal fluidized bed	Fluidised circulating reactor and regenerator	Orthoflow FCC continuous + continuous catalyst regeneration
Operation	Continuous	Cyclic	Cyclic	Continuous	Continuous	Continuous
Catalyst	Alkaline promoted Pt-Sn/Al_2O_3	Pt-Sn/$ZnAl_2O_3$ /$CaAl_2O_3$	Pt/Mg(Al)O; Pt-Sn/ZrO_2	Pt-Sn/SAPO-34	Pt-Ga/ Al_2O_3	Proprietary – precious metal and Cr free
Catalyst Life	1-3 years	Unknown	Unknown	Unknown	Unknown	Unknown
Heat Input	Interstage heating	Catalyst tubes placed in furnace	Reactor heating	From secondary catalyst	Unknown	Unknown
Temperature (°C)	550-620	550-590	~590	570-610	Unknown	Unknown
Pressure (bar)	2-3	5-6	~1	0.5-1.5	1.3-1.7	1.5
Cycle Time	5-10 days	8 hours	9 hours	-	<2 min	<1 min
Conversion (%)	30-40	~40	~30	45-63	43-53	45
Selectivity (%)	84 (at 40% conversion)	~89	~90	89-91	92-96	87-90

Development Stage	Commercial	Commercial	Pilot Plant	Pilot Plant	Commercial	Commercial
Ref	92,93	94	86	86	95,100	98

1.8.3 Chemistry of dehydrogenation

Non-oxidative dehydrogenation of propane is an endothermic and equilibrium-limited reaction whereby propane is converted into propene and hydrogen.
For this reaction, it is thermodynamically favourable to operate at low pressures and high temperatures.[101,102]

Platinum is a primary component in many bifunctional dehydrogenation catalysts due to its high activity for activating C-H bonds, coupled with low activity for the breaking of C-C bonds.

$$C_3H_8 \rightleftharpoons C_3H_6 + H_2 \qquad \Delta H_{298\,K} = 124.9\ kJ\ mol^{-1} \qquad (\mathbf{1.1})$$

$$C_3H_8 + H_2 \rightleftharpoons C_2H_6 + CH_4 \qquad \Delta H_{298\,K} = -63.4\ kJ\ mol^{-1} \qquad (\mathbf{1.2})$$

$$C_3H_8 \rightleftharpoons C_2H_4 + CH_4 \qquad \Delta H_{298\,K} = 79.4\ kJ\ mol^{-1} \qquad (\mathbf{1.3})$$

$$C_3H_8 + 2H_2 \rightleftharpoons 3CH_4 \qquad (\mathbf{1.4})$$

However alkanes, otherwise referred to by an old-fashioned term ‘paraffins’, are relatively chemically inert.[103] The molecules have no empty orbitals of low energy or filled orbitals of high energy. This is a consequence of localised and strong C-C and C-H bonds which do not readily participate in a chemical reaction. A geometric effect also exists: Although H-H and C-H bonds have very similar bond strength, hydrogen is more reactive than methane[104] This is due to the omnidirectional character of the H(1s) orbital in a hydrogen molecule allowing attack in any direction.[105] On the contrary, the directed $CH_3(sp^3)$ with only one bonding direction renders activation of the C-H bond in methane more difficult.

The exact mechanism for the dehydrogenation reaction is still a matter under debate. In describing catalytic dehydrogenation reactions the most common mechanism is the Horiuti-Polanyi mechanism, proposed in 1934.[106] The mechanism proceeds as follows:

a. Dissociative adsorption of the alkane
b. C-H cleavage of a second hydrogen atom
c. Formation of a hydrogen molecule
d. Desorption of both hydrogen and the corresponding olefin

The dissociative adsorption of the alkane and the C-H cleavage steps have been suggested as rate-limiting.[107] Dehydrogenation virtually occurs on all Pt sites (reaction 1.1) which catalyses the cleavage of the C-H bonds. Due to the dehydrogenation conditions, illustrated in Table 1.2, side reactions frequently compete with the dehydrogenation reaction reducing catalyst activity and selectivity. At the high process temperatures, side reactions such as hydrogenolysis (reaction 1.2), cracking (reactions 1.3 and 1.4), aromatization and isomerization are thermodynamically and kinetically favoured.[90,108,109] Additionally, the high temperatures employed cause Pt species to sinter. The dehydrogenation reaction is catalysed by virtually all Pt sites as it is structure insensitive.[110] Small Pt clusters with Pt (211) dominating on the surface have a lower dehydrogenation energy barrier and thus higher activity. Atomic steps and kinks are responsible for decomposition *via* dehydrogenation and C-C bond cleavage, which can take place at these sites with near zero activation energy. However, the side reactions are structure sensitive and preferentially proceed on larger ensembles of Pt with Pt (111) dominating and the second C-H bond activation being the rate limiting step with increased activation energy. As a consequence of this geometric effect, sintered, larger Pt ensembles are more susceptible to hydrogenolysis, cracking and isomerization reactions.[110] Previous studies have reported the influence of Pt particle size on the catalyst activity as well as its crucial role in determining selectivity and catalyst stability.[111,112] This catalytic performance is ascribed to different Pt surface site heterogeneity. Smaller particles on the surface are predominantly terminated by steps, edges, etc., where Pt atoms are coordinatively-unsaturated. Conversely, in larger Pt particles the surface is mainly terminated by terraces and planes where Pt atoms are more coordinatively-saturated. The coordinatively-unsaturated

surface Pt sites, which are highly active, especially for C-C bond rupture in monometallic Pt catalysts, cause complete cracking of hydrocarbons which leads to coke deposits and thus catalyst deactivation.[111,113,114]

1.8.4 Overview of Non-oxidative Dehydrogenation: Support and Promotor Effects

Historically, a plethora of Pt-based catalysts supported on alumina (Al_2O_3) have been reported for the industrial dehydrogenation process.[86,87] The development of new catalysts with simultaneously enhanced activity, selectivity and stability is the ultimate goal of researchers. Alumina is characterized by a high number and density of strong acid sites, which can be detrimental to PDH performance leading to undesired side reactions. Brønsted and Lewis acid sites on the support surface promote cracking (reactions 3-4) meanwhile isomerization proceeds *via* Brønsted acid sites, whereby surface acid sites induce a faster dehydrogenation for propene than propane leading to deep dehydrogenation. The C-H bonds in olefins are more reactive than C-C bonds, thus catalysts that favour C-H over C-C bond cleavage are required to increase selectivity. Limited support acidity is needed to avoid undesirable side reactions, such as catalytic cracking, coke formation and alkane isomerization.[87] However, in order to reach a high dispersion of Pt on the support, Lewis acid sites and amphoteric OH groups are required.[115] In this section, recent advances in the use of numerous supports and catalysis synthesis methods for Pt-based catalysts and the underlying structure-activity correlations.

Recent studies have reported the importance of Al speciation in improving catalyst performance and stability. The effect of surface Al^V sites on a Pt-Sn/γ-Al_2O_3 nanosheet catalyst was studied; after 24 hour reaction time a 4.1% decrease in conversion with 45% propene yield was observed (Table 1.3, entry 2).[116] Comparatively, the conventional the PtSn/Al_2O_3 catalyst rapidly deactivated, retaining 65% of the initial activity. The Pt-Sn γ-Al_2O_3 nanosheet catalyst offered enhanced activity, due to the sheet catalyst's high proportion of Al^V sites and their ability to uniformly disperse and stabilise Pt-Sn clusters.

Jang *et al*. explored calcination process parameters, namely temperatures of 600 °C and 750 °C, to modulate the surface properties of Pt-Sn/γ-Al_2O_3 catalysts.[117] They found that varying the calcination temperature to 600 °C resulted in a 41.2% propene yield over a 20 hour reaction (Table 1.3, entries 13 and 14). The increased sinter resistance was ascribed to stabilization from the larger fraction of Al^V, strong Lewis acid sites, which enhanced the metal-support interactions and suppressed coke deposition.

Yu and co-workers investigated the influence of sol-gel (Sg), hydrothermally synthesized (Hd) and commercially (C) obtained Al_2O_3 in tuning the coordination structure of Al^{3+} species in Pt/Ga/Al_2O_3 catalysts.[118] Remarkably, catalytic tests carried out at 580 °C revealed initial propene yields of 63.5% and 57.5% for Pt/Ga/Hd- Al_2O_3, and Pt/Ga/Sg-Al_2O_3, respectively (Table 1.3, entries 3-5). The proportion of Al^V sites, which decreased in the order: Sg-Al_2O_3 > Hd-Al_2O_3> C-Al_2O_3, contributed to the impressive catalytic performance. An optimal number of Al^V sites is required as an excess of these sites had a negative impact on the activity of the Pt/Ga/Sg- Al_2O_3 catalyst which contained the largest number of Al^V sites.

Other researchers investigated the modification of the Al_2O_3 support with other metal oxides, such as CeO_2[119] and TiO_2[120]. The most active catalyst, Pt/TiO_2-Al_2O_3 catalyst (with a TiO_2 loading of 10 wt.%) displayed high activity, selectivity, and stability with an initial propene formation rate of 79.2 $mol_{C3H6}\ kg^{-1}_{Pt}\ h^{-1}$ (Table 1.3, entries 15-17). This was due to electron transfer and acid site modulation effects resulting in changes to the adsorptive properties of Pt. Equally, rational design of Pt_3Ga/Al_2O_3 and Pt_3Ga/CeO_2-Al_2O_3 catalysts yielded initial propene production rates of 82.9 $mol_{C3H6}\ kg^{-1}_{Pt}\ h^{-1}$ and 86.9 $mol_{C3H6}\ kg^{-1}_{Pt}\ h^{-1}$, respectively (Table 1, entries 23 and 24).

Similarly, Chen *et al*.[121] reported a PtIn/$LaAlO_3$/γ-Al_2O_3 catalyst with an initial propene yield of 45% (Table 1.3, entry 7). Also, the potential industrial applications are promising as the reaction reached steady state conditions after 5 hours offering propene yields of 25% during prolonged catalytic testing. The excellent performance was ascribed to synergistic

effects between Pt and In species as well as the altered surface acidity and enhanced coking-resistance.

Alternative supports such as calcined hydrotalcite (Mg(Al)O) belonging to the layered double hydroxide (LDH) family, and their counterparts have garnered increased interest. Pt/Mg(Al)O modified with In was prepared using the co-precipitation method by Tolek and co-workers achieving 24.2% initial propane conversion and 98.2% selectivity.[122] The Pt/Mg(In)(Al)O catalyst's attained performance was attributed to a high fraction of metallic state In (In^0) together with Pt dispersion and average Pt particle sizes of 43.9% and 0.91 nm, respectively.

Shen *et al.* reported work on Pt/Mg(In)(Al)O catalysts, wherein excellent results were obtained by manipulated calcination temperature and Mg/Al ratio.[123] For instance, a calcination temperature of 600 °C and Mg/Al ratio of 4 delivered catalysts with initial propene production rates of 44.7 $mol_{C3H6}\ kg^{-1}_{Pt}\ h^{-1}$ and 29.5 $mol_{C3H6}\ kg^{-1}_{Pt}\ h^{-1}$, respectively. These Pt/Mg(Al)O catalysts were characterised by the lowest fraction of strong acid sites and highest specific surface areas.

Improved results were obtained on zinc modified PtSn/Mg(Al)O catalysts. For instance, the PtSn/Mg(Zn)AlO catalyst displayed an initial propene production rate of 136 $mol_{C3H6}\ kg^{-1}_{Pt}\ h^{-1}$ (Table 1.3, entry 18).[124] Doping the support with an optimal amount of Zn resulted in smaller, and more uniformly dispersed metal particles distributed on the Mg(Al)O support.

Zeolites have been studied as potential supports for Pt-based catalysts due to their high surface areas, well-defined pores and tuneable surface acidities.[125,126] Wannapakdee *et al.* explored silicate-1 (Si-MFI-NS) and Al_2O_3 based monometallic catalysts for lower temperature (550 °C) reactions.[127] Long term (10 hour) activity differed between Pt/Si-MFI-NS and Pt/Al_2O_3 evident in >99% and 60% propene selectivity, respectively. The modified hierarchical structure, high specific surface area and presence of weak acid sites on Pt/Si-MFI-NS proved beneficial.

Another study elucidated the positive effect of ultrasmall bimetallic PtZn nanoclusters encapsulated in silicate-1, with an initial specific activity of 84.3 $mol_{C3H6}\,kg^{-1}{}_{Pt}\,h^{-1}$, and exceptional cyclic stability during four PDH cycles at 600 °C.[128] Xu *et al.* evaluated a series of PtSn/Si-Beta catalysts, with different Pt/Sn ratios, with catalytic tests at 570 °C reporting high initial propane conversions, ca. 50%, irrespective of Pt/Sn ratio.[129] The $PtSn_{2.00}$/Si-Beta demonstrated an initial propene yields of 47.5%, decreasing by 3.4% in a 48-hour reaction period in contrast to the unmodified Pt/Si-Beta catalyst which displayed a 47% reduction in the propene yield under identical reaction conditions. Through extensive characterisation the enhanced performance and stability was attributed to ultra-small, uniformly dispersed particles, ranging from 1.0 to 1.4 nm. This favoured the structure sensitive, size dependent dehydrogenation pathway. It was found that embedding Sn in the zeolite framework was an effective geometric diluter for Pt ensembles resulting in smaller, isolated Pt atoms which are beneficial in increasing the propylene selectivity.

Other metal oxides are also applied as supports for Pt-based catalysts. Wu and co-workers demonstrated work on controlled intermetallic formation of a Pt_3Mn/SiO_2 catalyst with an initial specific activity of 41.3 $mol_{C3H6}\,kg^{-1}{}_{Pt}\,h^{-1}$ (Table 1.3, entry 9).[130] Operando characterization attributed this to Pt_3Mn's intermetallic subsurface which significantly improved the C-H bond activation, lowering the heats of hydrocarbon and hydrogen adsorption of the surface sites. Continuous testing for a week revealed the long-term stability, and size distributions of spent catalysts similar to those of the fresh catalysts. Interestingly, Deng *et al.* reported a highly selective Pt/SiO_2 and $PtSn/SiO_2$ catalysts prepared under oxidative, reductive and inert atmospheres.[1] The $PtSn/SiO_2$ prepared in inert and reductive atmosphere displayed initial propene yields of 17.8% and 25.7%, respectively. This was attributed to the reductive treatment and presence of Sn inducing electron and surface modifications of Pt nanoparticles following direct reduction in H_2 atmosphere in excess of 500 °C.[133]

Pt-based catalysts supported on a Boron (B) modified ZrO_2 with a pH modification, PtSn/B-ZrO_2-x (x = pH 9, 10, 11), were compared.[134] The most active and stable, PtSn/B-ZrO_2-10,

catalyst achieved a specific activity of 13.0 $mol_{C3H6}\,kg^{-1}{}_{Pt}\,h^{-1}$, attributed to B-$ZrO_2$-10's moderate surface acidity (Table 1.3, entry 10). Impressive dehydrogenation results have been disclosed by Wang *et al.* who disclosed hexagonal boron nitride (h-BN) nanosheets as the support for Pt/Cu (0.01 wt% Pt and 1.0 wt% Cu loadings) clusters.[1] This afforded propene formation rates of 12.3 $mol_{C3H6}\,kg^{-1}{}_{Pt}\,h^{-1}$ and 19.6 $mol_{C3H6}\,kg^{-1}{}_{Pt}\,h^{-1}$ at 520 °C and 600 °C, respectively (Table 1.3, entries 20 and 21). Under identical conditions this catalyst showed enhanced specific activity, and stability than analogous catalysts supported on $MgAl_2O_4$, H-ZSM5, SBA-15, SiC and Al_2O_3. The h-BN-sheets provided abundant stacking fault edges terminating with the B–O defects characterised by unpaired electrons, which strongly interact with metal active species; helping to strengthen the interaction between the metal and support.[136,137]

Similar to support modifications, numerous researchers have investigated the role of promoting elements in enhancing catalyst performance and stability. Rimaz *et al.*[138] explored modification of Pt/Al_2O_3 catalysts with different Ge loadings, followed by reduction at different temperatures. An initial propene yield of 53.8% was achieved on a PtGe/Al_2O_3 catalyst constituting of 0.5 wt.% Pt and 1.5 wt.% Ge reduced at 600 °C. The catalytic ability was credited to alloy formation coupled with positive implications on geometric and electronic properties of Pt ascribed to the reduction temperature and the degree of Ge reduction. Similarly, isolated single atom Pt atoms in a Cu matrix (10 wt.% Cu and 0.1 wt.% Pt) supported on Al_2O_3 simultaneously enhanced catalyst activity, selectivity and stability over a 120 hour period.[139] In producing a single-atom alloys, structure sensitive, undesired side reactions were suppressed. Thus, isolated Pt atoms dispersed on Cu nanoparticles were identified as active centres with high propene selectivity; dramatically enhancing the desorption of surface bound propene, prohibiting its further dehydrogenation.

In summary, key structure-activity relationships were related to aspects of particle size, bimetallic formulation and metal support interactions. Control of these variables influenced the catalytic properties, the mechanism: either Horiuti-Polanyi for monometallic Pt catalyst or heterolytic dissociation for bimetallic formulations, such as Ga

promoted catalysts. This directly influences the nature of adsorbed intermediates effectively modulating specific activity and selectivity.

To quantitatively evaluate the platinum utilization efficiency in the dehydrogenation of propane, we normalized the catalytic activity of propylene formation per gram of catalyst i.e., moles of propylene formed per kilogram of catalyst per hour; the results are listed in Table 1.3.

Table 1.3: Summary for catalytic performances of propane dehydrogenation over the typical platinum catalysts reported in literature.

Entry	Catalyst	Feed Composition	Reaction Temp [° C]	WHSV [h^{-1}]	X [%]	S [%]	Specific activity [$mol_{C3H6}\ kg^{-1}_{Pt}\ h^{-1}$]	Ref
1	PtZN@S-1	C_3H_8/N_2= 1:1.73	600	6.5	31	99.8	84.3	[128]
2	$PtSn/Al_2O_{3sheet}$	$C_3H_8/H_2/N_2$= 1:1.25:4	590	9.4	48.7	98.3	31.4	[116]
3	Pt/ C-Al_2O_3	C_3H_8/N_2= 1:9	580	-	36.7	96	17.5	[118]
4	Pt/ Sg-Al_2O_3	C_3H_8/N_2= 1:9	580	-	59	98	28.6	[118]
5	Pt/ Hd-Al_2O_3	C_3H_8/N_2= 1:9	580	-	65.5	97	31.5	[118]
6	Pt/In/Mg(Al)O	$C_3H_8/H_2/Ar$= 8:7:35	620	3.3	69	98	44.7	[123]
7	PtIn/$LaAlO_3$/ γ-Al_2O_3	$C_3H_8/H_2/N_2$= 8:7:35	600	3.0	47	96	25.6	[121]
8	PtIn/Mg(Al)O-4	$C_3H_8/H_2/Ar$= 8:7:35	620	3.3	47	95	29.5	[140]
9	Pt_3Mn/SiO_2	C_3H_8/N_2= 1.25:98.75	550	-	6.8	98	41.3	[130]
10	PtSn/B-ZrO_2-10	$C_3H_8/H_2/N_2$= 1:1:8	550	3	36	97	13.0	[134]

11	Pt/Mg(In)(Al)O	C_3H_8=100	550	-	24.2	98.2	7.8	[122]
12	$Pt/Al_2O_{3\text{-}600}$	$C_3H_8/H_2/He$= 1:1.25:4	590	5.2	48.5	36.9	23.3	[117]
13	$Pt/Al_2O_{3\text{-}750}$	$C_3H_8/H_2/He$= 1:1.25:4	590	5.2	48.3	37.1	23.2	[117]
14	$PtGa/SiO_2$	C_3H_8/Ar= 1:4	550	98	31.9	99.6	7871.2	[141]
15	Pt/TiO_2-Al_2O_3-0	$C_3H_8/H_2/N_2$= 1:1:1.85	600	10	50.5	59	64.0	[120]
16	Pt/TiO_2-Al_2O_3-10	$C_3H_8/H_2/N_2$= 1:1:1.85	600	10	47.3	78	79.2	[120]
17	Pt/TiO_2-Al_2O_3-20	$C_3H_8/H_2/N_2$= 1:1:1.85	600	10	45.5	88	86.0	[120]
18	PtSn/Mg(3Zn)AlO	C_3H_8/N_2= 1:4	600	18.9	55.2	99.4	136.0	[124]
19	Pt/Si-MFI-NS	C_3H_8/N_2= 1:4	550	2.8	35	95	29.7	[127]
20	Pt/Cu/*h*-BN	$C_3H_8/H_2/N_2$= 1:1:3.9	520	4	14.7	99.8	12.3	[135]
21	Pt/Cu/*h*-BN	$C_3H_8/H_2/N_2$= 1:1:3.9	600	4	24	97.3	19.6	[135]

22	Pt_3Ga/Al_2O_3	$C_3H_8/H_2/N_2$= 1:1:1.85	600	10	39.4	98	82.9	[119]
23	Pt_3Ga/CeO_2 - Al_2O_3	$C_3H_8/H_2/N_2$= 1:1:1.85	600	10	41.1	98.5	86.9	[119]

Note: WHSV, space velocity, grams of propane per gram of catalyst per hour; X(C_3H_8), initial propane conversion; S(C_3H_6), initial propene selectivity; Specific activity, moles of propylene formed per kilogram of catalyst per hour. C= Commercial, Sg= Sol-gel synthesized, Hd= Hydrothermal synthesized.

1.8.5 Methanol to DME

In recent years, alternative eco-friendly fuels have attracted attention due to environmental, economic and sustainability measures. Such fuels include synthetic natural gas (syngas), alcohols, ethers, esters, hydrogen, biofuels and Fischer-Tropsch fuels. Dimethyl ether (DME) is a non-toxic, colourless, non-corrosive, non-carcinogenic liquified gas, which is considered a promising eco-friendly fuel and a potentially fundamental chemical feedstock of the future. Industrial research efforts demonstrated the possible large-scale manufacture of DME from methanol with a simple dehydration technology[142] through which DME is produced from syngas ($CO/H_2/CO_2$). The syngas-to-DME process developed by Topsoe is an indirect, two-step process using a hybrid catalyst comprising a methanol synthesis and a methanol dehydration component. The catalyst consists of two types of active sites: one for the synthesis of methanol by hydrogenation of CO/CO_2 over a copper based catalyst[143–145] and another for dehydration of methanol to DME over an acidic catalyst[146,147].

$$CO + 2H_2 \rightleftharpoons CH_3OH \quad \Delta H_{298\,K} = -90.47\ kJ\ mol^{-1};\ \Delta G_{298\,K} = -25.17\ kJ\ mol^{-1} \quad (\mathbf{1.5})$$

$$CO_2 + 3H_2 \rightleftharpoons CH_3OH + H_2O \quad \Delta H_{298\,K} = -49.43\ kJ\ mol^{-1}; \Delta G_{298\,K} = 3.46\ kJ\ mol^{-1} (\mathbf{1.6})$$

$$CO + H_2O \rightleftharpoons CO_2 + H_2 \quad \Delta H_{298\,K} = -41.17\ kJ\ mol^{-1}; \Delta G_{298\,K} = -28.63\ kJ\ mol^{-1} \ (\mathbf{1.7})$$

$$2CH_3OH \rightleftharpoons CH_3OCH_3 + H_2O \ \Delta H_{298K} = -23.79\ kJ\ mol^{-1}; \Delta G_{298K} = -16.75\ kJ\ mol^{-1} (\mathbf{1.8})$$

Fig 1.7 shows the variation in the Gibbs Energy for the reactions **1.5-1.8**, for the temperature range of 0 to 400 °C. CO_2 hydrogenation (reaction **1.6**), is thermodynamically unfavourable for the selected temperature range. Also, CO hydrogenation (reaction 1.5) is thermodynamically favourable at temperatures below 150 °C. It is clear from Fig 1.8 that both the water gas shift (WGS) and methanol dehydration reactions; reactions **1.7** and **1.8**, respectively, are thermodynamically feasible for the selected temperature range.

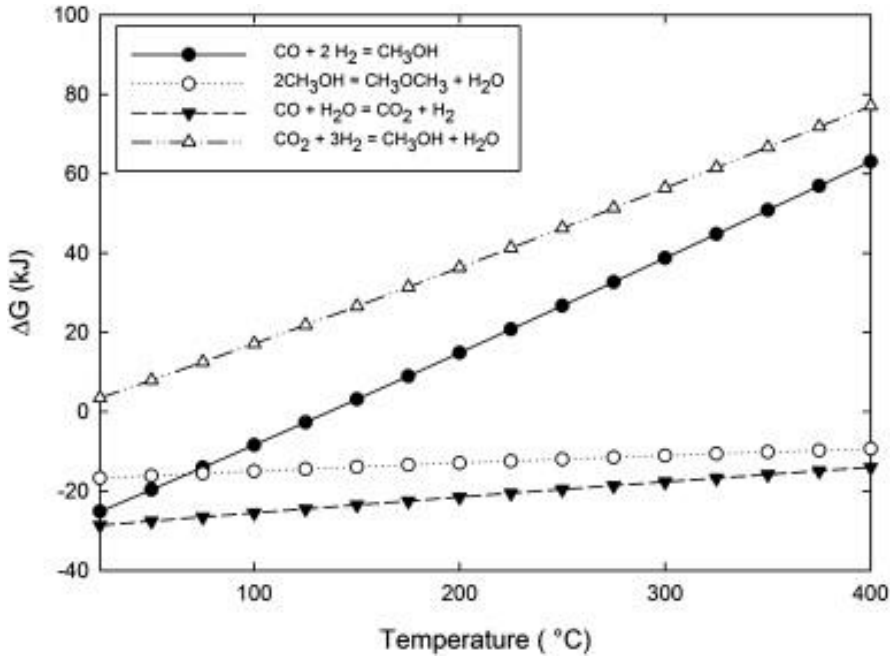

Figure 1.7 Gibbs energy of CO_2 hydrogenation (△); (●) CO hydrogenation; (○)Methanol dehydration, and (▼) WGS reactions at different temperatures.[148]

Methanol *via* hydrogenation of CO or CO_2 are exothermic, thermodynamically limited reactions, favoured at low temperatures and high pressures. Water formed by methanol dehydration can be removed by the WGS reaction. Water is believed to block the active sites for methanol consumption through competitive adsorption with methanol on the catalyst surface. The methanol dehydration reaction is an exothermic reaction which is not thermodynamically favoured at high temperature. This takes place over solid-acid catalysts including alumina[149,150], zeolites[151,152], and mixed metal oxides[153–155] with different physicochemical characteristics. In particular, DME selectivity and yield are strongly dependent on the nature of acid sites (both Lewis and Brønsted) and the textural (meso/macro porosity) and topological properties in the methanol dehydration component.

The stronger the surface acid sites of the catalyst (Lewis and Brønsted), the greater the tendency of the material to form olefins and aromatic or paraffinic hydrocarbons. This eluded to the conclusion that DME formation is related to acid sites with weak and moderate acidity. The reaction conditions, especially operating temperature, are important in determining the DME selectivity and yield. Consecutive reactions can be accelerated at temperatures greater that about 300 °C.

Alumina is a widely studied as a dehydration component in the methanol to DME reaction, with the added advantage of not catalysing the consecutive reactions to hydrocarbons. This is a result of the absence of strong acid sites. However, during the reaction methanol and water compete for the same adsorption sites on alumina such that the catalytic activity of alumina is reduced due to poisoning by water. Yaripour *et al.*[156] investigated the modification on alumina with silica, and phosphorus which enhanced the catalytic activity. An increase in silica loading in the silica modified y-alumina catalysts resulted in higher surface areas, higher surface acidity. Similarly, Ji *et al*.[157] reported the modification of alumina with a range of metal oxides (B_2O_3, ZrO_2 and SiO_2. Among the modified catalysts, only SiO_2-Al_2O_3 exhibited an improvement in catalytic performance. Sabour *et al.*[155] evaluated the effect of Si/Al (Si/Al ratio of 5-35) in a series of Al-HMS catalysts. It emerged that the rate of the methanol dehydration reaction was strongly dependent on the acidity

of catalyst employed and the order of reaction rates was: Al-HMS- 5 > Al-HMS-10 > Al-HMS-20 > Al-HMS-35 which is in the same order as the increase in acidic sites density. The most active catalyst, Al-HMS-10, exhibited an optimum yield and selectivity of 89 % and 100 %, respectively, showing excellent stability. The authors found that by decreasing Si/Al, the temperature required to reach equilibrium conversion of methanol decrease due to an increase in the number of acid sites.

A number of mechanisms have been proposed for the methanol dehydration reaction, which indicate two possible routes to DME.[146,158–161] It is thought that both Lewis acid-base pair, formed during surface dehydration, and Brønsted acid-Lewis base pair sites are active sites for the dehydration of methanol.[162] The reaction pathway, selectivity and yield are correlated to the nature and strength of the acid sites and the subsequent interaction of methanol with these sites.[163] The Langmuir-Hinshelwood mechanism, described previously, whereby two molecules of methanol adsorb onto two neighbouring acidic or basic sites which interact to produce one molecule of DME and one molecule of water.[164] This is common for alumina type catalyst where the catalytic activity for methanol dehydration is associated with the Lewis acid−Lewis base pair formed during surface dehydration. Consequently, the electron-rich oxygen anions show basic character and the electron-deficient aluminium cations show acid character.

In contrary, for acidic aluminosilicates the catalytic activity is related to the Brønsted acid-Lewis base pair. In this case, the Eley-Rideal mechanism where an interaction of methanol molecules with acidic sites only through which the acid site on the catalyst attacks the nucleophilic oxygen of the methanol molecule, is proposed.[165] Brønsted acidic sites are involved in reactions of hydrogen transfer, while their adjacent Lewis basic sites are able to stabilize carbonium or carbenium ions formed on the surface or receive protons back, regenerating the acidic site.

To elude to the acid sites responsible for the dehydration of methanol Takeguchi *et al.*[166] studied adsorption experiments with silica-alumina catalysts together with H-ZSM5 zeolite. It was found that water and NH_3 are competitively adsorbed on Lewis acid sites, whereas

adsorption of NH_3 on Brønsted acid sites was not affected by the presence of water. The authors concluded that Lewis acid–base pairs are the major active sites for methanol dehydration at atmospheric pressure, where the partial pressure of water formed is low and thus water adsorbed on acid sites is negligible. In such a case, the methanol dehydration rate on Brønsted acid sites seems to be much slower than that on Lewis acid sites. However, when considering the synthesis gas to DME reaction conditions, the partial pressure of the water formed by the dehydration of methanol is high and as such, the activity of Lewis acid sites was found to be suppressed by adsorbed water at lower temperatures. Under these conditions the Brønsted acid–Lewis base pair sites are the major active sites for the methanol dehydration reaction. Consequently, the rate limiting step in DME synthesis is determined by the acid properties, such as acid site strength and number of acid sites.

This is particularly important in context of the direct dehydrogenation of propane whereby bifunctional dehydrogenation catalysts, constituted by a coordinatively unsaturated active metal (M_{cus}^+) and an acidic support, are used. A support effect exists as Brønsted and Lewis acid sites on the support surface promote cracking while isomerization proceeds *via* Brønsted acid sites. The C-H bonds in olefins are more reactive than C-C bonds, thus catalysts that favour C-H over C-C bond cleavage are required to increase selectivity. Limited support acidity, with acid sites characterized by weak and moderate strength, is needed to avoid undesirable side reactions, such as catalytic cracking, coke formation and alkane isomerization.[87] However, in order to reach a high dispersion of the active metal on the support, Lewis acid sites and amphoteric OH groups are required.[115]

It is well known that dehydrogenation performance of catalysts is closely related to the acidic properties of the catalyst surface. Consequently, the methanol to DME reaction as an acid-catalysed reaction serves as an ideal prospective test reaction, allowing for the evaluation of the activity induced by acid sites present in pristine silica-alumina materials. Correlations and relevant deductions regarding the nature, strength and concentration of acidic sites and catalyst performance will be investigated. With this knowledge, the aim is

to construct relevant structure-activity relationships which will be applied to Pt/SiO_2-Al_2O_3 catalysts for the direct dehydrogenation of propane.

1.9 Supercritical Fluids

A supercritical fluid (SF) is defined as any substance at a temperature and pressure above its critical point, whereby the distinction between the liquid and gas phases ceases to exist, as shown in Figure 1.8. The critical point represents the highest temperature and pressure the substance can reach as both a liquid and gas in equilibrium. The boiling curve represents the gas-liquid coexistence curve whereby increasing both temperature and pressure results in the liquid becoming less dense due to thermal expansion. However, an increase in the pressure results in an increased density of the gas. Eventually, the densities of the two phases converge, becoming identical and in this state the phase boundary between liquid and gas is indistinguishable resulting in the formation of a single homogeneous phase. This is signified by the point at the end of the boiling curve, the critical point.

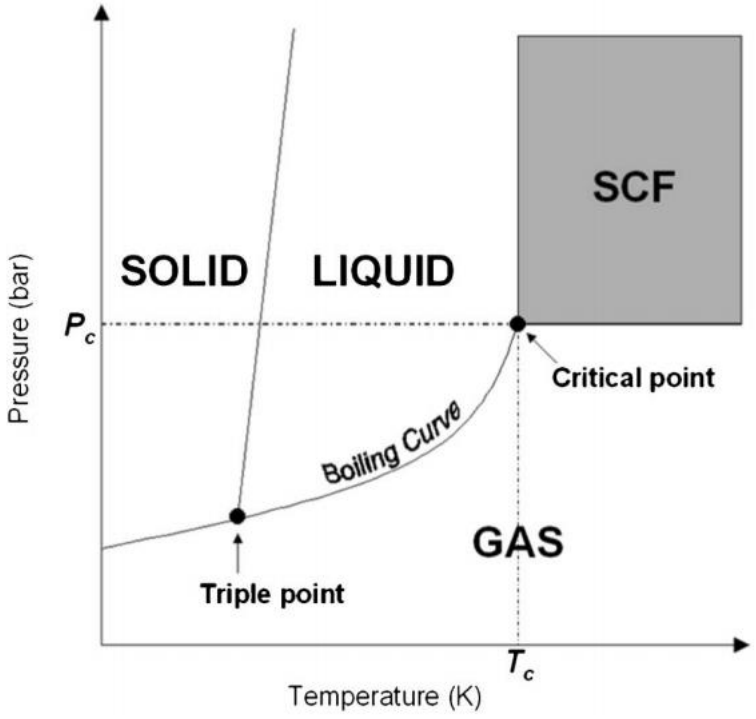

Figure 1.8: Single component Pressure-Temperature dependent phase diagram highlighting the supercritical fluid (SCF) region and the critical point.[167]

1.9.1 Properties of supercritical fluids

Supercritical fluids are considered to have physical properties commonly described as being intermediate between those of liquids and gases. As shown in Table 1.4, the viscosity of SCFs closely resembles that of gases which is substantially lower than those of conventional solvents with densities typically considerably higher than most gases, but closer to those of liquids. This allows for easier contact between phases and contributes to enhanced interphase mass transfer rates compared to conventional solvents. Consequently, SCFs have a good solubility of solutes similar to liquids with gas-like movement and diffusion properties.

Table 1.4: Comparison of physical properties of gases, liquids and SCFs.[167]

Parameter	Gas	SCF	Liquid
Density (g cm^{-3})	10^{-3}	0.1-0.9	1.0
Viscosity (g cm^{-1} s^{-1})	10^{-4}	10^{-4}	10^{-2}
Diffusivity (cm^2 s^{-1})	10^{-1}	10^{-4}	10^{-6}

Supercritical fluids, with their unusual physicochemical properties, make for interesting solvents. Another difference between SCFs and conventional solvents is their compressibility. Due to the high compressibility of fluids near the critical point, their density and dissolving power can be tuned sensitively through small changes in pressure and temperature. The solubility of a given solute is largely dependent on density of the solvent and the vapour pressure of the solute. As such, the solubility of a given solute increases with increased density of the solvent and vapour pressure of the solute. A number of studies have also reported solubility enhancement from the addition of a small amount of a volatile co-solvent which can increase the solubilisation of other solutes in the supercritical fluid.[168,169] Similarly, the use of multiple solutes can enhance solubilities.[170–172] These phenomena are known as the cosolvent and entrainer effects.

Table 1.5 contains commonly utilised SCFs for chemical reactions and syntheses, detailing their critical parameters and physical properties. Historically, the development of industrial scale reactions under supercritical conditions has been studied extensively. Common examples of such industrially relevant reactions include ammonia synthesis (BASF, 1913), methanol synthesis (BASF, 1923) and ethylene polymerisation (ICI, 1937). SCFs are applied to a number of applications, including extractions and chemical waste disposal with the most widely used substances being carbon dioxide and water.

Table 1.5: Critical properties of various SCFs.[167,173–175]

SCF	Name	Critical Temperature (°C)	Critical Pressure (bar)	Critical Density (kg m^{-3})
CO_2	Carbon Dioxide	31.1	73.9	466
H_2O	Water	374.0	220.6	322
N_2O	Nitrous Oxide	36.4	72.5	453
NH_3	Ammonia	132.4	113.2	235
CH_3OH	Methanol	239.5	80.8	273
C_2H_6	Ethane	32.2	48.7	207
C_3H_8	Propane	96.7	42.5	220
C_4H_{10}	n-butane	152.0	38.0	228
C_5H_{12}	n-pentane	196.6	33.7	232
C_6H_6	Benzene	289.5	49.2	300
SF_6	Sulfur hexafluoride	45.5	37.6	737
Xe	Xenon	16.6	58.3	1099

1.9.1.2 Supercritical CO_2

Supercritical carbon dioxide ($scCO_2$) is the most commonly used supercritical fluid for catalysis[176,177], chemical synthesis[178,179], extraction and supercritical fluid

chromatography[180,181] processes. This is due to the poor solubility for ionic and high molecular-weight organic compounds offered by $scCO_2$ coupled with the ability to dissolve and expand or extract organic solvents, thus lowering their solvation power and enabling the precipitation of solids from organic solutions. In recent years, green chemistry principles have driven the design of chemically efficient and more environmentally benign processes. This has encouraged the use of alternative solvents to traditional volatile organic compounds (VOCs).[182] Supercritical carbon dioxide in chemical processing and as a solvent is desirable as it is cheap, readily available, recyclable, chemically stable, non-polar, non-toxic and non-flammable.[169] The critical point of CO_2, indicated by the subscript '*c*' denoting the critical points of T_c= 31.1 °C and P_c = 73.9 bar, where *T* and *P* are the temperature and pressure, respectively. Above this critical pressure and temperature, CO_2 reaches a supercritical state where CO_2 is similar to a gas with a density reminiscent of a liquid.

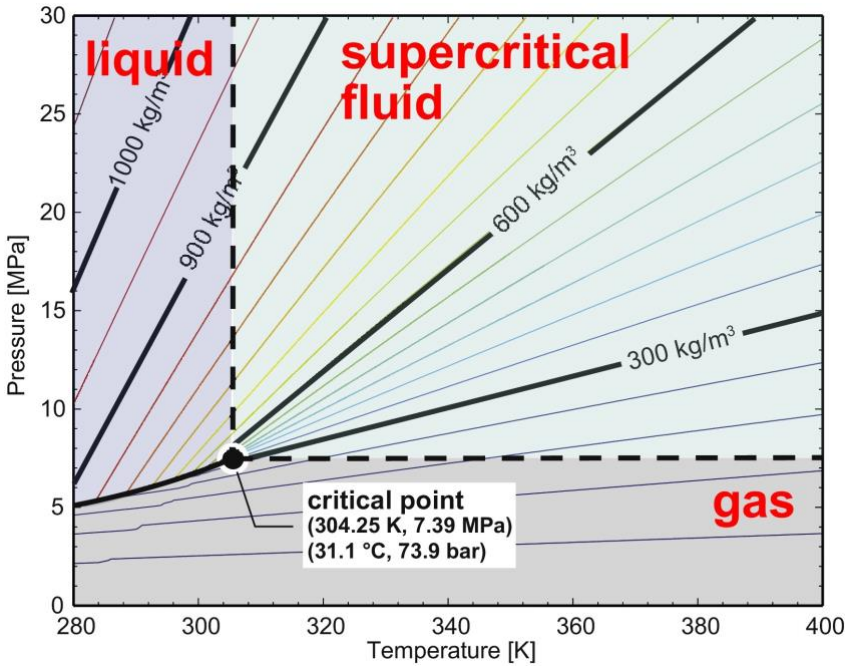

Figure 1.9: CO_2 density and phase diagram.[183]

1.9.2 $scCO_2$-Based synthesis technologies

1.9.2.2 Rapid Expansion of Supercritical Solutions (RESS)

The rapid expansion of supercritical solutions (RESS) is a method where a pressurized solution is rapidly expanded through a nozzle resulting in an extremely fast nucleation and micronization of the solute.[184–186] Mechanistically, after the dissolution of the solutes in $scCO_2$ the rapid depressurization of the solutions that follows lead to a noticeable drop in density. Subsequently leading to solute precipitation as the reduced solubility of the solutes in $scCO_2$ causes a high degree of supersaturation (typically in the order of 10^5 to 10^8). The high degree of supersaturation characterized by this method results in a high nucleation rate, and very high number of nucleation sites. This limits crystal growth, producing small particles with uniform size distributions. The adjustment of the process parameters, pressure and temperature, yields various morphologies and particle sizes in the resultant materials.[187] A requirement of this process is that the target compound has to be soluble in the SCF.

1.9.2.3 Gas Antisolvent (GAS) and Supercritical Antisolvent (SAS) Precipitation

The SCF can be utilised as an anti-solvent or as a co-antisolvent in the Gas or Supercritical anti-solvent (GAS or SAS) synthesis routes.[188–190] In both processes, a solution containing the solute is dissolved in an SCF miscible solvent. Common solvents which meet the criterion are ketones (acetone), dimethyl sulfoxide, and alcohols (methanol, ethanol, propanol). This solution, containing the requisite cations, is then introduced into the $scCO_2$, which acts as an antisolvent where the solvent is rapidly extracted by the $scCO_2$. Supersaturation is the term used to show the distance of the solute from its nucleation point. The $scCO_2$ is able to generate very high levels supersaturation, leading to high nucleation rates and smaller particles. This is due to the diffusivity of $scCO_2$ being multiple orders of magnitude greater than conventional solvents. The washing step with pure $scCO_2$ at the end of the precipitation process is also required in order to avoid the condensation of the liquid phase that would otherwise modify the precipitate and its characteristics. Given the solvent is extracted by the $scCO_2$ the product is dry from the point of

precipitation, which prevents dissolution. This is made possible by $scCO_2$'s large affinity with many organic solvents.

The GAS and SAS processes are similar, the main difference being that SAS is both a steady state and semi-continuous process. Similar to the SAS process, the GAS process involves the gradual addition of a supercritical fluid to expand a static solution until supersaturation is achieved and the solute precipitates. Once the solute is precipitated, additional supercritical fluid is added to remove residual solvent resulting in a dry precipitate upon depressurization. The atomization offers improved control of particle size distribution (PSD) in particular, the atomization of the feed solution containing the solute and solvent system with a co-axial nozzle similar to the RESS process.[191] The recovery of dry precipitates from the SAS process is achieved easily with a single depressurization, eliminating the need for complex treatments for the complete removal of contamination from liquid residues. Similar to the RESS technique, parameters important for particle design include flow rates, temperature and pressure. The process is inherently highly flexible by the alteration of preparation parameters such as temperature, pressure, flow rates and solvent injection geometries. Constituents of precursor solutions; metal salt identity and solvent type, the manipulation of which control resultant morphology, material composition, morphology and crystallinity.

1.9.3 Materials synthesis with $scCO_2$

Supercritical fluids are green and tuneable solvents which have emerged as possible alternatives to traditional organic solvents. Over recent years they have emerged as a new area of interest in materials science research, particularly in the field of micro- and nanoparticles.[192–194] In particular, as the research on the production of micro- and nanoparticles in $scCO_2$ has intensified the number of precipitation processes studied has increased. This is in part due to other SCFs' unsuitability for chemical synthesis due to their flammability (i.e., ethane, propane), high cost (i.e., CHF_3) or poor solvating power (i.e., SF_6). With synthetic chemistry in mind, the temperature-dependent miscibility with classical organic solvents as well as low polarity that results in preferential dissolution of hydrophobic compounds are advantageous.

A variety of synthesis processes using $scCO_2$ have been proposed, studied and applied to micro- and nanoparticle synthesis. Their conceptual basis relying on adjustment of the pressure and temperature or allowing rapid expansion and loss of solvent inducing the precipitation of fine, mono-dispersed particles.[194–196]

The work herein focuses on the utilisation of the use of supercritical anti-solvent (SAS) precipitation, using $scCO_2$ as an antisolvent, for the production of ASA precursors. Experimental parameters impact the resultant morphology, material composition, morphology and crystallinity. However, within the SAS system, each of the following requirements have to be fulfilled:

a. The solute needs to be soluble in the chosen solvent
b. The solvent needs to be fully miscible in the anti-solvent at the process conditions
c. The solute needs to be insoluble in the solvent-antisolvent medium

Due to the nature of the solvent-mediated method, the resultant material's physicochemical properties dependent on the thermodynamics of the SAS system. Numerous experimental studies have investigated solution-antisolvent interactions and the role of phase behaviour in controlling the morphology and dimension of precipitates.[194,197,198] The precipitation of nanoparticles occurs in a number of concurrent steps. Mixing of the solution and antisolvent is followed by the generation of supersaturation, nucleation, and growth by coagulation and condensation. Agglomeration occurs resulting in uncontrolled growth and inhomogeneous aggregated networks of particles as shown in Fig 1.10. The coagulation and condensation of the obtained particles occur simultaneously while competing for supersaturation. The high supersaturation levels inherent of the SAS methodology facilitates nanoparticle precipitation. Under such conditions, supersaturation is consumed more by nucleation relative to growth of particles and complete miscibility between the solvent system and anti-solvent is required for nanoparticle formation. Consequently, this results in the formation of amorphous precipitate.

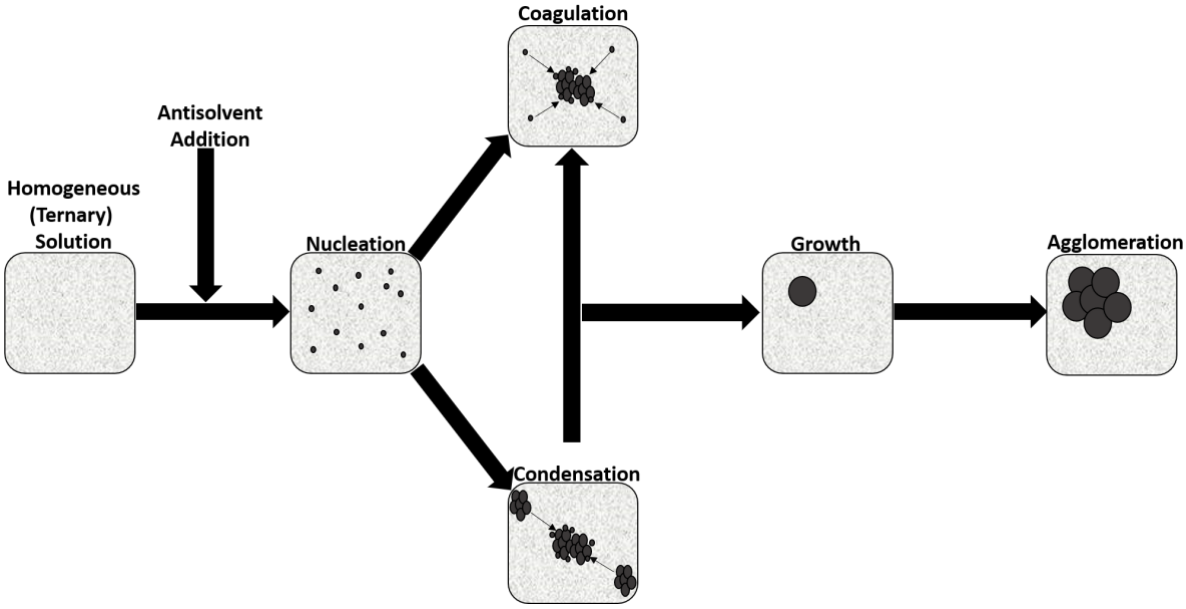

Figure 1.10: Schematic of antisolvent mediated particle precipitation process.

Moreover, the morphology of the precipitate is a function of the position of the operating point with respect to the mixture critical point (MCP) of the system. By definition, at pressures greater than the MCP, the MCP represents the pressure at which only a single supercritical phase can exist in a pressure-composition plane at a fixed temperature. The systems containing solute-solvent-antisolvent behave differently when considering key SAS operating parameters such as pressure, temperature and the solute concentration in the liquid solvent(s). Reverchon and co-workers explored the effect of the addition of a solute (Z) on the vapour-liquid equilibria (VLE) and its subsequent shift on the MCP illustrated in the phase diagram, Fig 1.11. Thus, the solute–solvent-antisolvent systems behave differently in the case of binary and ternary systems. Therefore, in order to increase the efficacy of the precipitation of nanoparticles and phase homogeneity with the SAS methodology operating at pressures higher than the critical pressure of CO_2, 72.8 bar, is paramount.

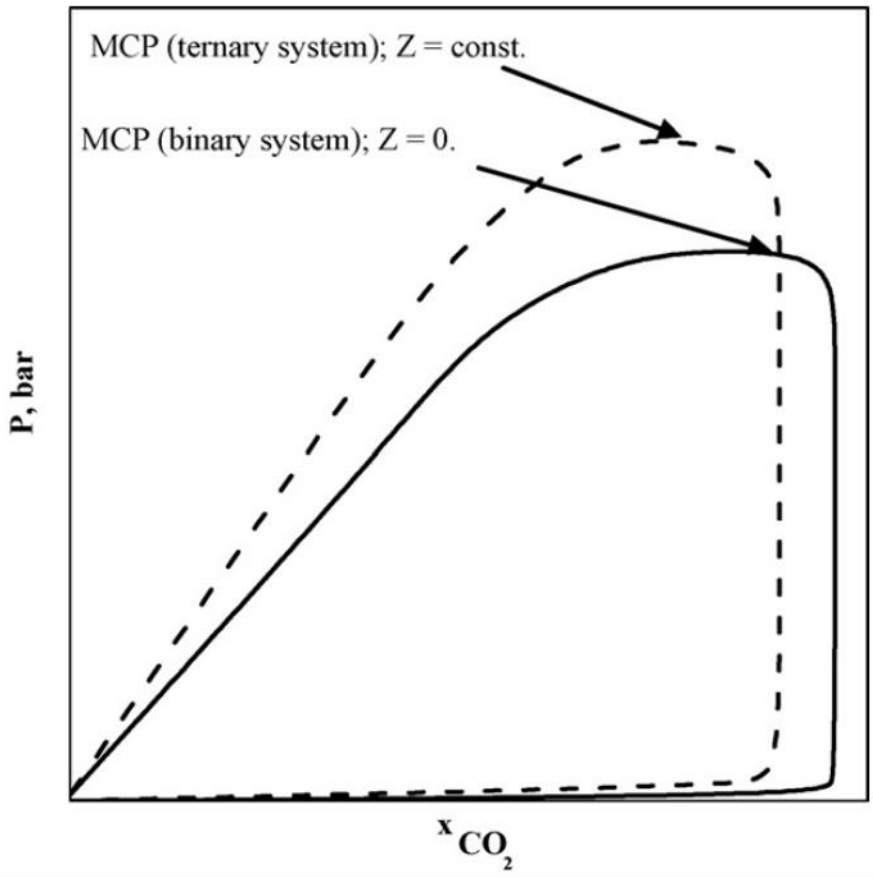

Figure 1.11: A proposed qualitative modification of the VLEs of a binary (solid line) system, when a third component (Z) is added (dotted line) at a given concentration.[195]

At this juncture, it is important to consider the effect of process conditions on the precipitation of nanoparticles. Several authors report a jet break-up and drying precipitation mechanism when microparticles are formed whereas no droplet formation, gas mixing and particle nucleation and growth, as discussed above, in the case of nanoparticle formation.[197–201] Operating at pressures above the MCP results in nanoparticle formation the surface tension vanishes at a very rapid rate such that the gas mixing prevails on the breakage of the liquid jet. In effect, no droplets are formed, and a sort of physical mixture at the nanometric level is obtained through which the precipitation of nanoparticles occurs by gas-to-particles nucleation and growth. This hypothesis is supported by experimental evidence, using light scattering analysis.[202] It was found that the transition between the multi-phase and the single-phase mixing depends on the operating pressure, as well as the viscosity and the surface tension of the solvent.

Therefore, it is fair to assume that the differences in microparticle and nanoparticle formation mechanisms by SAS are due to a complex correlation between the operating pressure and surface tension in determining droplet formation or lack thereof.

For nanoparticle formation the surface tension of the liquid injected in the precipitator approaches zero, hence no droplets are formed. The rate of this process increases with pressure. As the two mechanisms for microparticle and nanoparticle formation operate at two contiguous pressure levels, a competition occurs between jet break-up and gas mixing during the injection process which governs the observed morphology. It is therefore apparent that the observed particle morphologies are governed by the pressure of the system in relation to the ternary (solute-solvent-antisolvent) system's MCP.

1.9.4 Catalyst Preparation Using Supercritical Antisolvent (SAS) Precipitation

Considerable efforts have been made in utilising $scCO_2$ as an antisolvent for the synthesis of catalysts and catalyst components. Early stages of development were carried out at the pilot scale SAS apparatus at the University of Salerno by Reverchon and co-workers who reviewed supercritical based techniques applied to the production of polymers, superconductors, nanomaterials, and other inorganic compounds to name a few.[194–197,203,204] The reviews demonstrated the widespread applicability of supercritical based techniques.

These advancements were important steppingstones in the utilisation of $scCO_2$ in catalyst preparation. Commonly used methods of synthesis of heterogeneous catalysts often fail to meet the principles of green chemistry. For instance, the use of metal nitrates as precursors of heterogeneous catalysts which results in pollution of effluents and the formation of nitrogen oxides, which can be formed during the heat treatment and reduction of the catalysts. Similarly, the catalyst precursors of conventional mixed metal oxide or oxide-supported catalysts are initially formed either by hydrothermal synthesis, precipitation or grinding and heating. Further thermal treatment in varying atmospheres is required to

produce the final material; an energy intensive process which uses considerable amounts of solvents and generates excessive amounts of waste.

In particular, it was found that the SAS methodology showed great potential in producing precursors of high temperature superconductors; yttrium, samarium and neodymium acetates as well as nanoparticles of zinc acetate, a catalyst precursor.[205] In the case of zinc acetate, it was found that particle sizes down to 30 nm with a mean diameter of 50 nm were obtained at the optimal operating conditions. The SAS precipitated zinc acetate displayed a specific surface area of *ca.* 175 $m^2 g^{-1}$ however upon calcination at 300 °C the surface area decreased to 55 $m^2 g^{-1}$.

Amorphous or poorly crystalline high surface area metal oxides have been synthesised previously using supercritical CO_2 anti-solvent (SAS) precipitation. This approach was adopted in the synthesis of precursors to mixed metal oxides resulting in the preparation of samarium acetate.[205] It was found that an increase in solute concentration correlated with broader particle size distribution. Thermal decomposition, through calcination, produced samarium oxide particles of ca. 100 nm diameter. This translated into ethane conversion and ethene selectivity of 22 % and 58%, respectively, when tested for ethane oxidative dehydrogenation at 680 °C. Additionally, in comparison to conventionally prepared samarium oxide, the SAS prepared catalyst showed a higher ethene yield.

Similarly, Hutchings *et al*. reported a new preparative route for vanadium phosphate catalysts utilising using supercritical CO2 as an antisolvent.[206,207] In contrast to vanadium phosphates prepared using conventional methods, the SAS prepared VPO material (scVPO) was found to be wholly amorphous both before and after use as a catalyst. The specific activity appeared insensitive to the preparation method but a correlation between catalytic activity and surface area was evident. It emerged that the scVPO catalyst exhibited the highest activity, Fig 1.12. The study proved that such a material could not readily be prepared using standard methodologies and this observation prompted the study into the possible roles played amorphous phases in active catalysts. Succeeding investigations focussed on the addition of cobalt, a common promoting element for crystalline vanadium

phosphate.[208] This proved to have a poisoning effect on the amorphous vanadium phosphate prepared *via* the SAS methodology evident in reported decreased activity and selectivity for maleic anhydride. The negative effect on the catalyst performance was a consequence of the modification affecting the morphology of the material and oxidation state of vanadium.

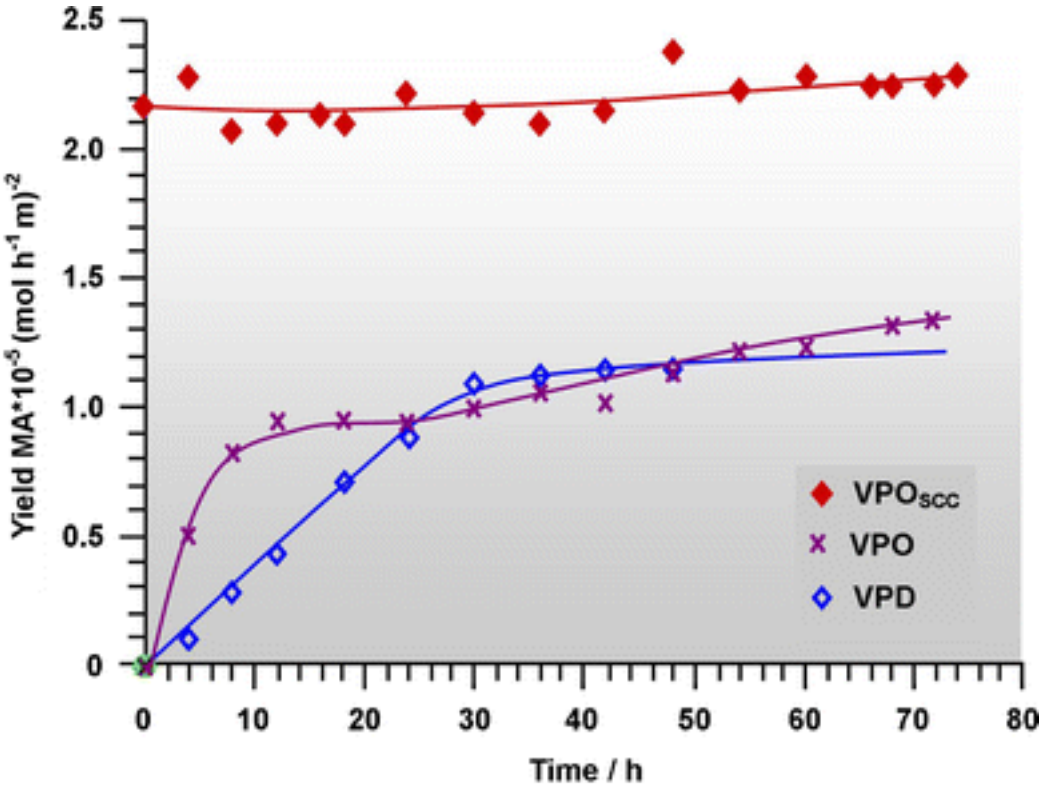

Figure 1.12: The intrinsic activity for maleic anhydride with time on stream for supercritical antisolvent prepared vanadium phosphate *via* the choice $VOHPO_4.0.5H_2O$ precursor phase, (VPO) route (◆), conventionally prepared vanadium phosphate catalyst *via* the choice $VOHPO_4.0.5H_2O$ precursor phase, (VPO) route (X) and higher surface area vanadium phosphate catalyst prepared *via* the $VOPO_4.2H_2O$ and subsequent $VOHPO_4.0.5H_2O$ active phase through heating under organic (alcohol) reflux conditions (◆). (Feed composition: 1.5% butane in air, Temperature: 400 °C).[192]

Alonso *et al*. explored the synthesis of titanium oxide *via* the SAS process, with operational temperatures in the 200 – 300 °C range.[209] The degree of crystallinity increased with

temperature such that at 200 °C the TiO_2 particles were amorphous with a specific surface area of 350 $m^2 g^{-1}$. Interestingly, operation temperatures higher than 250 °C were needed to obtain a good degree of crystallinity such that at 300 °C the specific surface area decreased to 150 $m^2 g^{-1}$. The study demonstrated the catalytic potential amorphous particles characterized with high surface areas.

Tang and co-workers explored the effect of systematic variations of operational temperature and pressure in CeO_2 preparation prior to functionalization with Au for the CO oxidation reaction.[210] After calcination, the amorphous precipitates were transformed into nanocrystalline aggregated hollow spheres with primary particles with diameter of 3-8 nm. The observed morphology was not witnessed in CeO_2 prepared *via* direct calcination (400 °C, 2 hours) of cerium acetylacetonate, referred to as $unCeO_2$. Catalyst tests revealed that the $Au/scCeO_2$ were more active than the $Au/unCeO_2$ and a standard Au/Fe_2O_3 catalyst provided by the World Gold Council, Fig 1.14.

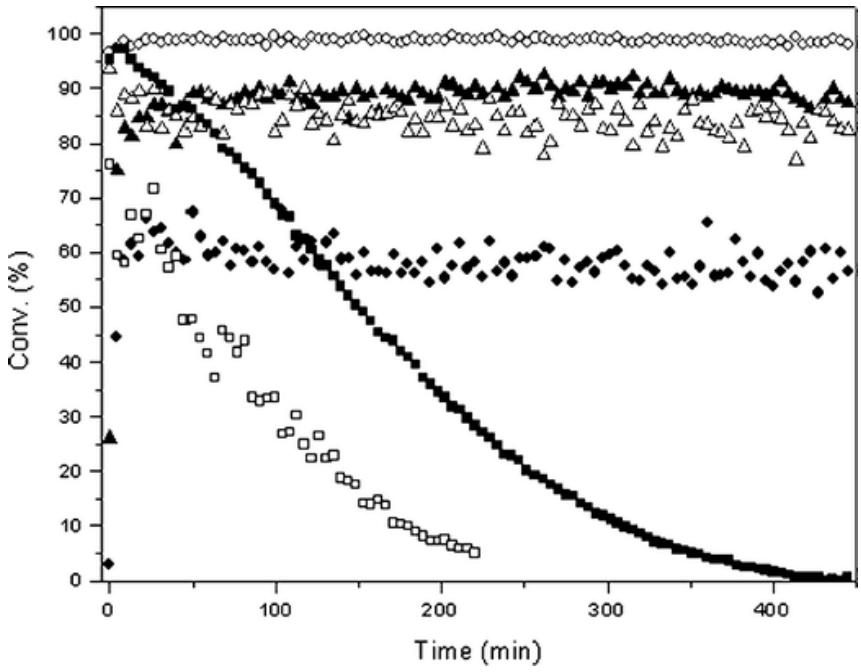

Figure 1.13: Catalytic activities for ambient CO oxidation, CO (0.5 % in synthetic air) was fed at 22.5 mL min^{-1} and passed over the catalyst (15 mg) at 25 °C: (●) $Au/unCeO_2$, (Δ) $Au/scCeO_2$-1, (○) $Au/scCeO_2$-2, (▲) $Au/scCeO_2$-3, (■) 5 wt% Au/Fe_2O_3 (supplied by World Gold Council), and (□) the deactivation of $Au/scCeO_2$-2 using high GHSV (448,000 h^{-1}).[210]

The supercritically prepared CeO_2 was thought to be able to stabilize an atomic dispersion or sub-1-nm clusters of Au aided by the high density of defects present as a result of the rapid precipitation caused by the high supersaturation in the SAS method. The authors recognized the need to improve the catalyst further because the supercritically prepared catalyst was prone to deactivation as the Au nanoparticles were not stabilized under reaction conditions.

In parallel, Miedziak *et al.* reported SAS prepared CeO_2 as a support for an Au–Pd/scCeO_2 catalyst which proved to be very active for benzyl alcoholoxidation displaying ca. 91% selectivity to the desired product, benzaldehyde.[211] The Au–Pd/scCeO_2 catalyst was approximately 4 times more active than Au–Pd/unCeO_2.

It became apparent that deposited metal (Au^0 and Pd^{2+}) species were uniformly and highly dispersed over scCeO_2, whilst discrete homogeneous Au–Pd alloy particles in the size range 50–120 nm existed on unCeO_2. Thus, differences in the reproducibility of the deposition method on the supercritically and conventionally prepared supports were observed.

The very highly dispersed Au and Pd species on the scCeO_2 support were proposed to be important for the high catalytic activity, and it is the novel surface properties of scCeO_2 that are important in controlling the high dispersion. When used for successive catalytic tests, Au–Pd/scCeO_2's activity increased considerably when compared to the fresh catalyst. However, on the second re-use it was still more active than the fresh catalyst, with a decrease in activity seen after second and third uses. In contrary, under the same treatment the Au–Pd/unCeO_2catalyst was subject to a successive loss of activity as the number of re-uses increased. Interestingly, the high activity of the scCeO_2 based catalyst was related to the morphology, Fig 1.15. The authors reported that after use the spherical morphology of nanocrystalline scCeO_2 started to increasingly break down, until the morphology started to resemble the unCeO_2 material. Simultaneously there was an increase of the metal particle size on the scCeO_2 support, as discrete Au-rich and Pd-rich bimetallic particles were formed along with a reduction of the metal content. This

investigation further proved the significance of preparing supports, utilising the supercritical antisolvent precipitation methodology, as components of highly active bifunctional catalysts.

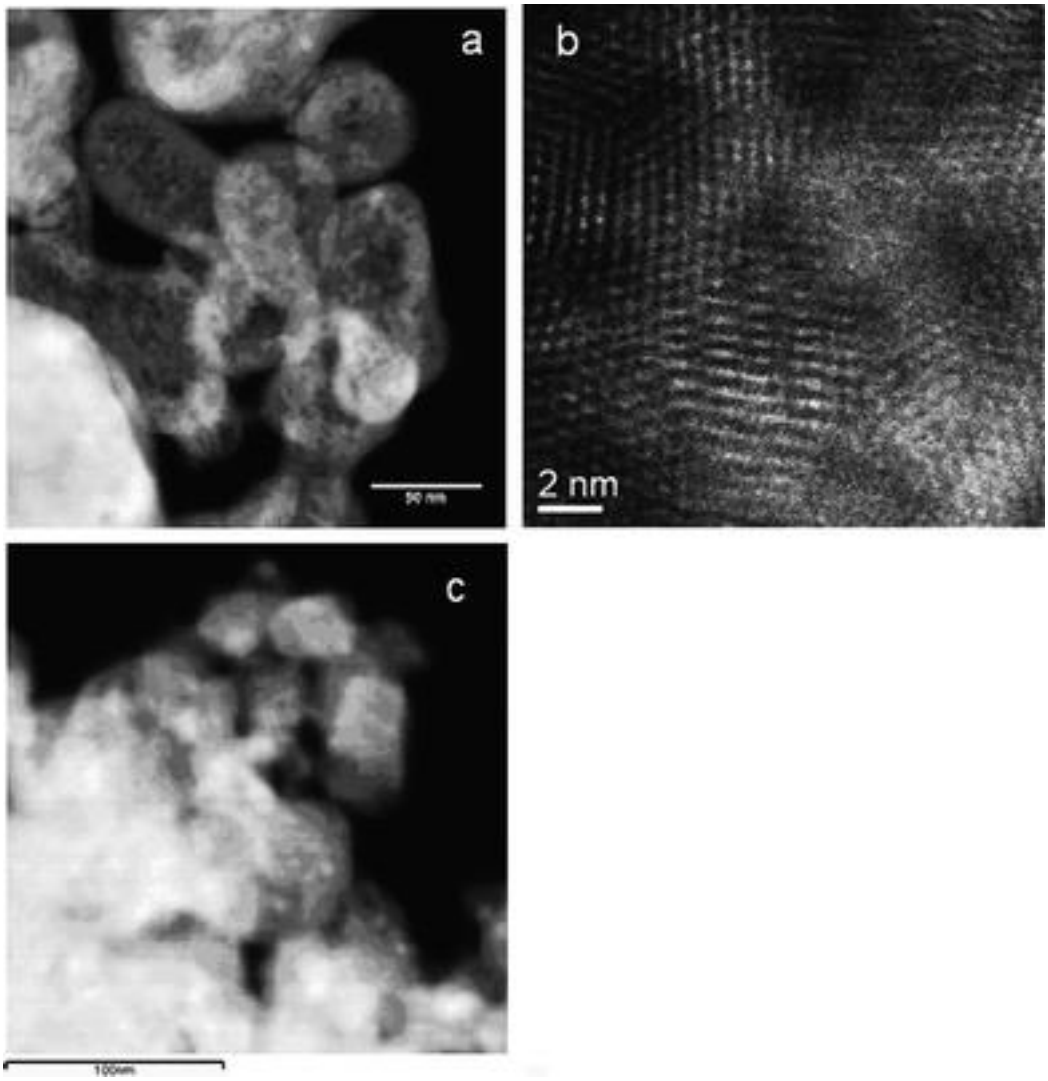

Figure 1.14: Representative ADF images showing (a) the spherical morphology of the $scCeO_2$ support, (b) the nanocrystalline nature of $scCeO_2$, and (c) the more irregular nanocrystalline morphology of the $unCeO_2$ material.[211]

Analogously, Tang *et al*. reported the use of $scCO_2$ as an antisolvent to prepare nanostructured homogeneous mixtures of Cu^{2+} and Mn^{3+} with crystallites of 10–20 nm in

diameter.[212] Following calcination, the resultant nanocrystalline Cu/MnOx with a crystalline tetragonal spinel, $CuMn_2O_4$, was formed which was more than twice as active per unit surface area as the conventional hopcalite catalysts prepared by coprecipitation for the oxidation of carbon monoxide, Fig 1.16. Most of all the supercritical antisolvent successfully produced a hopcalite phase without any mixture of other polymorphs with very high activity per unit area.

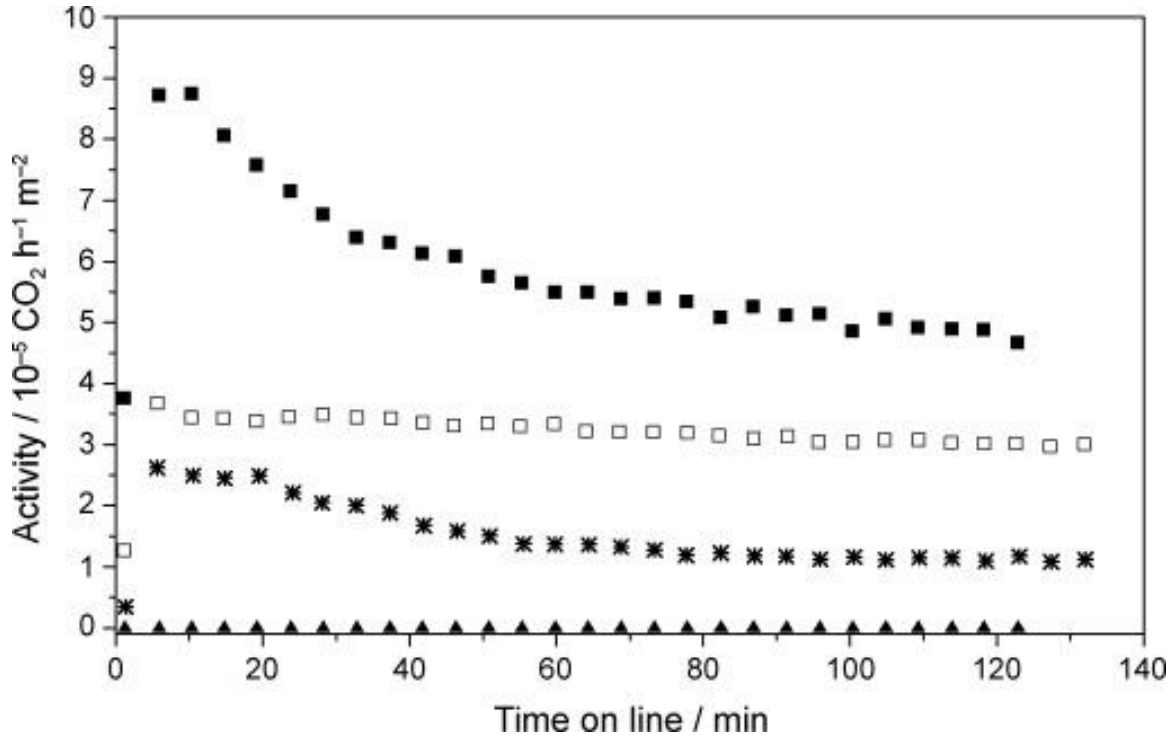

Figure 1.15: Specific catalytic activities: the CuMnOx precursor prepared by the supercritical process (▲); the CuMnOx catalyst prepared by calcination of the supercritically prepared precursor (▪); conventional hopcalite prepared by calcination of the coprecipitated precursor (✶); commercial hopcalite (□).[212]

With this knowledge, Marin and co-workers investigated the addition of water to the SAS procedure in the preparation of cobalt zinc oxide catalysts for the Fischer-Tropsch reaction.[213] The textural properties of the resultant precipitate favoured the formation of carbonates with enhanced phase separation and cobalt surface area, which was found to favour the formation of C_{5+} products. In the absence of water, the resulting catalyst

precursor was a mixture of metal acetates which upon calcination decomposed forming wurtzite type $Zn_{1-x}Co_xO$ and spinel type $Zn_xCo_{3-x}O_4$ phases.

Another related study focussed on the preparation of Fe_3O_4, NiO, CuO and Co_3O_4 *via* the SAS methodology. The authors investigated the promotional effect induced by the addition of water as a co-solvent for the formation of a carbonate precursor. It emerged in catalytic tests, for the total oxidation of propane, Co_3O_4 was found to be the most active catalyst. In particular, optimal conditions for catalyst preparation were established as a precursor solution containing 10 vol% water co-solvent followed by a 2-hour calcination at 250 °C. The resultant Co_3O_4, with BET surface area >100 m^2g, achieved 50 % propane conversion at 150 °C. It was found that the SAS prepared catalyst had considerably higher activity than a commercial 5 wt.% Pt/Al_2O_3 catalyst, Fig 1.17. This further demonstrated that a novel, nitrate free and green supercritical anti-solvent precipitation process can successfully produce highly active short chain alkane total oxidation catalysts.

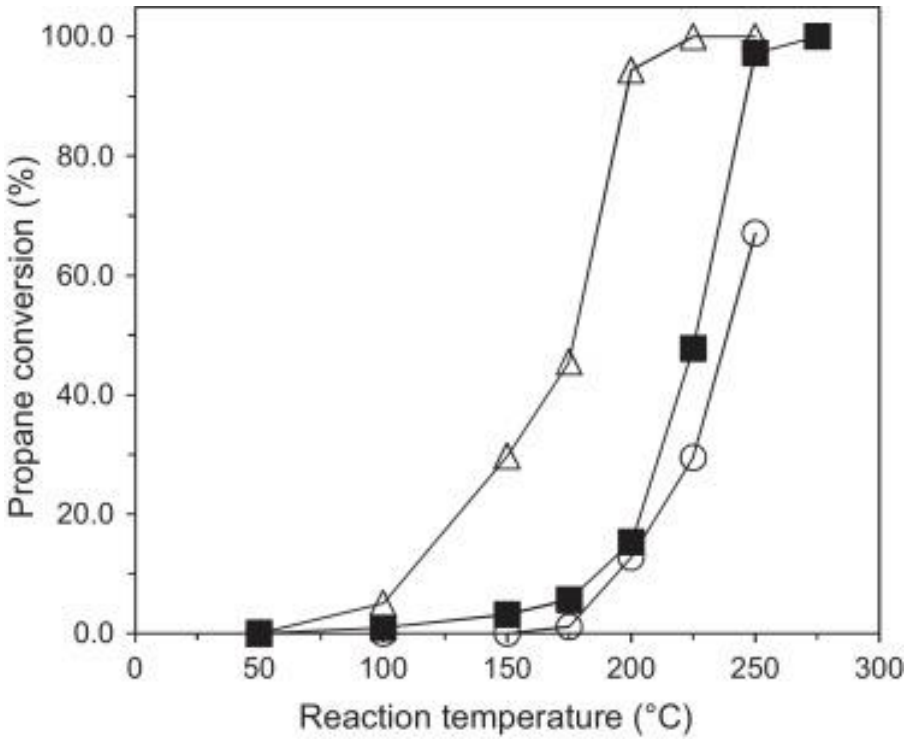

Figure 1.16: Propane conversion as a function of temperature over catalysts derived from 5 and 10% water co-solvent SAS materials calcined at 250 °C, and 5 wt% Pt/Al2O3. (■) SAS 5 vol% water derived catalyst, (▵) SAS 10 vol% water derived catalyst, (○) 5 wt% Pt/Al2O3.[214]

Using similar principles, Kondrat *et al*. reported the preparation of the amorphous hydroxycarbonate, georgeite, *via* the SAS process.[215] Utilising metal acetate salts a series of Cu, Zn and Al containing georgeite precursor materials were prepared. It became apparent that the addition of water caused a phase transformation of the resulting precipitate from a disordered mixed metal acetate to the georgeite phase. Due to miscibility issues between water and $scCO_2$ the water content was carefully controlled such that enhancing the content of georgeite in the precipitate and maintaining an optimum homogeneous system. Catalytic testing for the low temperature water gas shift (LTS) reactions alluded to the SAS prepared catalyst's superior performance in comparison to the industrial standard, both in terms of catalyst activity and stability. The authors suggested that the SAS method produces very pure zincian georgeite with a low content of sodium ions. It was postulated that this high purity may have contributed to both the high activity and the stability of the SAS prepared, zincian-georgeite-derived LTS catalyst.

In summary, extensive studies have been implemented in investigating the optimisation of numerous catalysts and catalyst components using the antisolvent mediated SAS methodology. It can be concluded that a number of experimental parameters effect the resultant material properties attributed to catalytic performance. The implications on physical properties, such as specific surface area, are known to enhance activity and improve aspects of functionalisation for various catalytic reactions. It appears that amorphous mixed metal oxides are thought to be able to stabilize an atomic dispersion or sub-1-nm clusters of metals aided by the high density of defects present as a result of the rapid precipitation caused by the high supersaturation in the SAS method. In view of SAS preparation of amorphous silica-alumina materials as catalysts and supports optimal conditions for catalyst preparation have not been established. Therefore, an extensive study of experimental and process parameters will be conducted building on knowledge gained within the research group and in literature allowing for the development of experimental methods aimed towards enhanced heterogeneous catalysts.

1.10 Aims

Thus far, the literature review has highlighted the importance of tailored design of catalyst component including using appropriate support synthesis strategies and (noble) metal deposition methods. The typical preparation methods used to achieve this have been highlighted showing the use of supported (Pt) metal catalysts in current dehydrogenation applications. In view of the fact that a number of Pt containing catalysts exhibit promising activity for the propane dehydrogenation reaction, this thesis will focus upon: (1) the design of a synthesis protocol for amorphous aluminosilicates using supercritical antisolvent precipitation, (2) advanced characterization to understand the material properties and how they differ to analagous flame spray pyrolysis and sol-gel derived materials, (3) understanding the synthesis-structure-activity relations that occur for catalytic applications, namely propane dehydrogenation and methanol to dimethyl ether reactions. Optimisation procedures for support synthesis will include varying process pressure, process temperature, solvent composition and calcination condition variations for the supercritical antisolvent method. Additionally, investigating the appropriate noble metal deposition method will be paramount in reproducibly depositing active metal species resulting in a catalyst with enhanced stability, activity and selectivity.

1.11 References

1 Z. Ma and F. Zaera, in *Encyclopedia of Inorganic and Bioinorganic Chemistry*, John Wiley & Sons, Ltd, 2014, pp. 1–16.

2 J. Wisniak, The History of Catalysis. From the Beginning to Nobel Prizes, *Educación Química*, 2010, **21**, 60–69.

3 V. Gold, Ed., *The IUPAC Compendium of Chemical Terminology: The Gold Book*, International Union of Pure and Applied Chemistry (IUPAC), Research Triangle Park, NC, 4th edn., 2019.

4 P. Flowers, K. Theopold, R. Langley and W. R. Robinson, *12.7 Catalysis - Chemistry 2e | OpenStax*, Rice University.

5 M. D. Argyle and C. H. Bartholomew, Heterogeneous Catalyst Deactivation and Regeneration: A Review, *Catalysts*, 2015, **5**, 145–269.

6 C. T. Herbschleb and F. der W. en Natuurwetenschappen, ReactorSTM, https://openaccess.leidenuniv.nl/handle/1887/17620, (accessed 23 June 2020).

7 P. Anastas and J. Warner, *Green Chemistry: Theory and Practice*, Oxford University Press, Oxford, New York, 2000.

8 R. Noyori, Pursuing practical elegance in chemical synthesis, *Chemical Communications*, 2005, **0**, 1807–1811.
9 M. A. Ali, T. Tatsumi and T. Masuda, Development of heavy oil hydrocracking catalysts using amorphous silica-alumina and zeolites as catalyst supports, *Applied Catalysis A: General*, 2002, **233**, 77–90.
10 A. Corma, M. S. Grande, V. Gonzalez-Alfaro and A. V. Orchilles, Cracking Activity and Hydrothermal Stability of MCM-41 and Its Comparison with Amorphous Silica-Alumina and a USY Zeolite, *Journal of Catalysis*, 1996, **159**, 375–382.
11 J. W. Ward, Hydrocracking processes and catalysts, *Fuel Processing Technology*, 1993, **35**, 55–85.
12 G. Busca, Acid Catalysts in Industrial Hydrocarbon Chemistry, *Chem. Rev.*, 2007, **107**, 5366–5410.
13 S. K. Maity, E. Blanco, J. Ancheyta, F. Alonso and H. Fukuyama, Early stage deactivation of heavy crude oil hydroprocessing catalysts, *Fuel*, 2012, **100**, 17–23.
14 C. Leyva, J. Ancheyta, L. Mariey, A. Travert and F. Maugé, Characterization study of NiMo/SiO2-Al2O3 spent hydroprocessing catalysts for heavy oils, *Catalysis Today*, 2014, **220–222**, 89–96.
15 R. Espinoza, C. Stander and W. Mandersloot, Catalytic conversion of methanol to hydrocarbons over amorphous or zeolitic silica-alumina, *Applied Catalysis*, 1983, **6**, 11–26.
16 Y. Matsumoto, K. Mita, K. Hashimoto and T. Tokoroyama, Preparation of silica-alumina catalyst by the sol-gel method and its activity for the Diels-Alder reaction of isoprene and acrylaldehyde, *Applied Catalysis A: General*, 1995, **131**, L1–L6.
17 A. Sachse, V. Hulea, A. Finiels, B. Coq, F. Fajula and A. Galarneau, Alumina-grafted macro-/mesoporous silica monoliths as continuous flow microreactors for the Diels–Alder reaction, *Journal of Catalysis*, 2012, **287**, 62–67.
18 T. López, M. Asomoza and R. Gómez, Catalytic properties of silico-aluminates prepared by the sol-gel method: isopropanol dehydration, *Journal of Non-Crystalline Solids*, 1992, **147–148**, 769–772.
19 K. Larmier, C. Chizallet, S. Maury, N. Cadran, J. Abboud, A.-F. Lamic-Humblot, E. Marceau and H. Lauron-Pernot, Isopropanol Dehydration on Amorphous Silica–Alumina: Synergy of Brønsted and Lewis Acidities at Pseudo-Bridging Silanols, *Angew. Chem.*, 2017, **129**, 236–240.
20 K. Hamaguchi and H. Hattori, Preparation of mesoporous silica-alumina derived from FSM-16 and its catalytic activity for cumene cracking, *React Kinet Catal Lett*, 1997, **61**, 13–19.
21 A. M. Youssef, A. I. Ahmed and S. E. Samra, Surface and acidic properties of some mixed oxide catalysts in relation to their catalytic activities, *Materials Letters*, 1990, **10**, 175–180.
22 Y. Y. Ge, Z. Q. Jia, C. G. Gao, L. L. Zhao, H. T. Li, Y. Zhang and Y. X. Zhao, SiO2-Al2O3 composite oxides with hierarchical pores as solid acid catalysts for tetrahydrofuran polymerization, *Kinet Catal*, 2013, **54**, 761–766.
23 Y. Ge, Z. Jia, H. Li, P. Gao, Y. Zhang, L. Zhao and Y. Zhao, Amorphous aluminosilicates used as acid catalysts for tetrahydrofuran polymerization, *Reac Kinet Mech Cat*, 2014, **112**, 467–475.

24 C. Yoon and D. L. Cocke, Potential of amorphous materials as catalysts, *Journal of Non-Crystalline Solids*, 1986, **79**, 217–245.
25 B. R. Goldsmith, E. D. Sanderson, D. Bean and B. Peters, Isolated catalyst sites on amorphous supports: A systematic algorithm for understanding heterogeneities in structure and reactivity, *J. Chem. Phys.*, 2013, **138**, 204105.
26 B. R. Goldsmith, B. Peters, J. K. Johnson, B. C. Gates and S. L. Scott, Beyond Ordered Materials: Understanding Catalytic Sites on Amorphous Solids, *ACS Catal.*, 2017, **7**, 7543–7557.
27 P. Hodgkinson, *Modern Methods in Solid-state NMR: A Practitioner's Guide*, Royal Society of Chemistry, 2018.
28 B. Peters and S. L. Scott, Single atom catalysts on amorphous supports: A quenched disorder perspective, *J. Chem. Phys.*, 2015, **142**, 104708.
29 C. G. Morales-Guio and X. Hu, Amorphous Molybdenum Sulfides as Hydrogen Evolution Catalysts, *Acc. Chem. Res.*, 2014, **47**, 2671–2681.
30 J. G. Howell, Y.-P. Li and A. T. Bell, Propene Metathesis over Supported Tungsten Oxide Catalysts: A Study of Active Site Formation, *ACS Catal.*, 2016, **6**, 7728–7738.
31 T. Osaki, K. Nagashima, K. Watari and K. Tajiri, Silica-doped alumina cryogels with high thermal stability, *Journal of Non-Crystalline Solids*, 2007, **353**, 2436–2442.
32 M. W. Hahn, J. R. Copeland, A. H. van Pelt and C. Sievers, Stability of Amorphous Silica–Alumina in Hot Liquid Water, *ChemSusChem*, 2013, **6**, 2304–2315.
33 C. L. Thomas, Chemistry of Cracking Catalysts, *Ind. Eng. Chem.*, 1949, **41**, 2564–2573.
34 M. W. Tamele, Chemistry of the surface and the activity of alumina-silica cracking catalyst, *Discuss. Faraday Soc.*, 1950, **8**, 270–279.
35 D. Coster, A. L. Blumenfeld and J. J. Fripiat, Lewis Acid Sites and Surface Aluminum in Aluminas and Zeolites: A High-Resolution NMR Study, *J. Phys. Chem.*, 1994, **98**, 6201–6211.
36 M. Hunger, D. Freude and H. Pfeifer, Magic-angle spinning nuclear magnetic resonance studies of water molecules adsorbed on Brønsted- and Lewis-acid sites in zeolites and amorphous silica–aluminas, *J. Chem. Soc., Faraday Trans.*, 1991, **87**, 657–662.
37 T. K. Phung and G. Busca, On the Lewis acidity of protonic zeolites, *Applied Catalysis A: General*, 2015, **504**, 151–157.
38 M. Valla, A. J. Rossini, M. Caillot, C. Chizallet, P. Raybaud, M. Digne, A. Chaumonnot, A. Lesage, L. Emsley, J. A. van Bokhoven and C. Copéret, Atomic Description of the Interface between Silica and Alumina in Aluminosilicates through Dynamic Nuclear Polarization Surface-Enhanced NMR Spectroscopy and First-Principles Calculations, *J. Am. Chem. Soc.*, 2015, **137**, 10710–10719.
39 E. J. M. Hensen, D. G. Poduval, V. Degirmenci, D. A. J. M. Ligthart, W. Chen, F. Maugé, M. S. Rigutto and J. A. R. van Veen, Acidity Characterization of Amorphous Silica–Alumina, *J. Phys. Chem. C*, 2012, **116**, 21416–21429.
40 M. Suzuki, S.-I. Hiraishi, M. Yoshimura and S. Sōmiya, Synthesis of Crystalline Mullite Fine Powders at Low Temperature by Hydrothermal Treatment of Mixed Alkoxide, *Nippon Kagaku Kaishi*, 1984, **1984**, 792–799.
41 M. Caillot, A. Chaumonnot, M. Digne, C. Poleunis, D. P. Debecker and J. A. van Bokhoven, Synthesis of amorphous aluminosilicates by grafting: Tuning the building and final structure of the deposit by selecting the appropriate synthesis conditions, *Microporous and Mesoporous Materials*, 2014, **185**, 179–189.

42 M. Caillot, A. Chaumonnot, M. Digne and J. A. Van Bokhoven, Creation of Brønsted Acidity by Grafting Aluminum Isopropoxide on Silica under Controlled Conditions: Determination of the Number of Brønsted Sites and their Turnover Frequency for m-Xylene Isomerization, *ChemCatChem*, 2014, **6**, 832–841.
43 K. Okada, T. Tomita, Y. Kameshima, A. Yasumori and K. J. D. MacKenzie, Surface Acidity and Hydrophilicity of Coprecipitated Al2O3–SiO2 Xerogels Prepared from Aluminium Nitrate Nonahydrate and Tetraethylorthosilicate, *Journal of Colloid and Interface Science*, 1999, **219**, 195–200.
44 R. Takahashi, S. Sato, T. Sodesawa, M. Shizukuishi, K. Morofuji and K. Ogura, Change in local coordination structure of aluminum cations in silica–alumina solution during coprecipitation, *Journal of Non-Crystalline Solids*, 2005, **351**, 826–832.
45 E. J. M. Hensen, D. G. Poduval, P. C. M. M. Magusin, A. E. Coumans and J. A. R. van Veen, Formation of acid sites in amorphous silica-alumina, *Journal of Catalysis*, 2010, **269**, 201–218.
46 S. Acosta, R. Corriu, D. Leclercq, P. H. Mutin and A. Vioux, Novel non-hydrolytic sol-gel route to metal oxides, *J Sol-Gel Sci Technol*, 1994, **2**, 25–28.
47 M. R. Agliullin, V. P. Talzi, N. A. Filippova, V. R. Bikbaeva, S. V. Bubennov, T. R. Prosochkina, N. G. Grigorieva, N. Narender and B. I. Kutepov, Two-step sol–gel synthesis of mesoporous aluminosilicates: highly efficient catalysts for the preparation of 3,5-dialkylpyridines, *Appl Petrochem Res*, 2018, **8**, 141–151.
48 S. Esposito, "Traditional" Sol-Gel Chemistry as a Powerful Tool for the Preparation of Supported Metal and Metal Oxide Catalysts, *Materials*, 2019, **12**, 668.
49 T. C. Keller, J. Arras, M. O. Haus, R. Hauert, A. Kenvin, J. Kenvin and J. Pérez-Ramírez, Synthesis-property-performance relationships of amorphous silica-alumina catalysts for the production of methylenedianiline and higher homologues, *Journal of Catalysis*, 2016, **344**, 757–767.
50 F. Mizukami, Y. Kiyozumi, T. Sano, S. Niwa, M. Toba and S. Shin, Effect of Solvent Diols and Ligands on the Properties of Sol-Gel Alumina-Silicas, *Journal of Sol-Gel Science and Technology*, 1998, **13**, 1027–1031.
51 P. Padmaja, K. G. K. Warrier, M. Padmanabhan, W. Wunderlich, F. J. Berry, M. Mortimer and N. J. Creamer, Structural aspects and porosity features of nano-size high surface area alumina–silica mixed oxide catalyst generated through hybrid sol–gel route, *Materials Chemistry and Physics*, 2006, **95**, 56–61.
52 Z. Wang, Y. Jiang, O. Lafon, J. Trébosc, K. Duk Kim, C. Stampfl, A. Baiker, J.-P. Amoureux and J. Huang, Brønsted acid sites based on penta-coordinated aluminum species, *Nature Communications*, 2016, **7**, 13820.
53 J. Huang, N. van Vegten, Y. Jiang, M. Hunger and A. Baiker, Increasing the Brønsted Acidity of Flame-Derived Silica/Alumina up to Zeolitic Strength, *Angewandte Chemie International Edition*, 2010, **49**, 7776–7781.
54 L. Mädler, W. J. Stark and S. E. Pratsinis, Flame-made Ceria Nanoparticles, *Journal of Materials Research*, 2002, **17**, 1356–1362.
55 J. Grothe, K. Wegner, M. Medicus, E. Schade and S. Kaskel, Tailoring Catalytic Properties of Copper Manganese Oxide Nanoparticles (Hopcalites-2G) via Flame Spray Pyrolysis, *ChemCatChem*, , DOI:10.1002/cctc.201800639.
56 R. Strobel, A. Alfons and S. E. Pratsinis, Aerosol flame synthesis of catalysts, *Advanced Powder Technology*, 2006, **17**, 457–480.

57 M. F. Williams, B. Fonfé, C. Sievers, A. Abraham, J. A. van Bokhoven, A. Jentys, J. A. R. van Veen and J. A. Lercher, Hydrogenation of tetralin on silica–alumina-supported Pt catalysts I. Physicochemical characterization of the catalytic materials, *Journal of Catalysis*, 2007, **251**, 485–496.
58 Z. Wang, Y. Jiang, A. Baiker and J. Huang, Efficient Acid-Catalyzed Conversion of Phenylglyoxal to Mandelates on Flame-Derived Silica/Alumina, *ACS Catal.*, 2013, **3**, 1573–1577.
59 J. Huang, Y. Jiang, N. van Vegten, M. Hunger and A. Baiker, Tuning the support acidity of flame-made Pd/SiO2–Al2O3 catalysts for chemoselective hydrogenation, *Journal of Catalysis*, 2011, **281**, 352–360.
60 M. A. Makarova, V. L. Zholobenko, K. M. Al-Ghefaili, N. E. Thompson, J. Dewing and J. Dwyer, Brønsted acid sites in zeolites. FTIR study of molecular hydrogen as a probe for acidity testing, *Journal of the Chemical Society, Faraday Transactions*, 1994, **90**, 1047–1054.
61 D. Barthomeuf, Zeolite acidity dependence on structure and chemical environment. Correlations with catalysis, *Materials Chemistry and Physics*, 1987, **17**, 49–71.
62 B. Burger, K. Haas-Santo, M. Hunger and J. Weitkamp, Synthesis and Characterization of Aluminium-Rich Zeolite ZSM-5, *Chemical Engineering & Technology*, 2000, **23**, 322–324.
63 A. Omegna, J. A. van Bokhoven and R. Prins, Flexible Aluminum Coordination in Alumino−Silicates. Structure of Zeolite H−USY and Amorphous Silica−Alumina, *J. Phys. Chem. B*, 2003, **107**, 8854–8860.
64 D. Tzoulaki, A. Jentys, J. Pérez-Ramírez, K. Egeblad and J. A. Lercher, On the location, strength and accessibility of Brønsted acid sites in hierarchical ZSM-5 particles, *Catalysis Today*, 2012, **198**, 3–11.
65 C. Dorémieux-Morin, P. Batamack, C. Martin, J.-M. Brégeault and J. Fraissard, Comparison of amorphous silica-alumina and highly dealuminated HY zeolite by1H high resolution MAS-NMR of solids, *Catal Lett*, 1991, **9**, 403–409.
66 J. H. de Boer, Constitution and properties of silica-alumina-catalysts, *Discuss. Faraday Soc.*, 1971, **52**, 109–112.
67 F. Leydier, C. Chizallet, D. Costa and P. Raybaud, Revisiting carbenium chemistry on amorphous silica-alumina: Unraveling their milder acidity as compared to zeolites, *Journal of Catalysis*, 2015, **325**, 35–47.
68 C. Chizallet and P. Raybaud, Acidity of Amorphous Silica–Alumina: From Coordination Promotion of Lewis Sites to Proton Transfer, *ChemPhysChem*, 2010, **11**, 105–108.
69 C. Chizallet and P. Raybaud, Pseudo-Bridging Silanols as Versatile Brønsted Acid Sites of Amorphous Aluminosilicate Surfaces, *Angewandte Chemie International Edition*, 2009, **48**, 2891–2893.
70 F. Leydier, C. Chizallet, D. Costa and P. Raybaud, CO adsorption on amorphous silica–alumina: electrostatic or Brønsted acidity probe?, *Chem. Commun.*, 2012, **48**, 4076–4078.
71 W. Daniell, U. Schubert, R. Glöckler, A. Meyer, K. Noweck and H. Knözinger, Enhanced surface acidity in mixed alumina–silicas: a low-temperature FTIR study, *Applied Catalysis A: General*, 2000, **196**, 247–260.

72 B. Xu, C. Sievers, J. A. Lercher, J. A. R. van Veen, P. Giltay, R. Prins and J. A. van Bokhoven, Strong Brønsted Acidity in Amorphous Silica−Aluminas, *J. Phys. Chem. C*, 2007, **111**, 12075–12079.
73 M. Trombetta, G. Busca, S. Rossini, V. Piccoli, U. Cornaro, A. Guercio, R. Catani and R. J. Willey, FT-IR Studies on Light Olefin Skeletal Isomerization Catalysis: III. Surface Acidity and Activity of Amorphous and Crystalline Catalysts Belonging to the SiO2–Al2O3System, *Journal of Catalysis*, 1998, **179**, 581–596.
74 G. Crépeau, V. Montouillout, A. Vimont, L. Mariey, T. Cseri and F. Maugé, Nature, Structure and Strength of the Acidic Sites of Amorphous Silica Alumina: An IR and NMR Study, *J. Phys. Chem. B*, 2006, **110**, 15172–15185.
75 C. Copéret, W.-C. Liao, C. P. Gordon and T.-C. Ong, Active Sites in Supported Single-Site Catalysts: An NMR Perspective, *J. Am. Chem. Soc.*, 2017, **139**, 10588–10596.
76 JoNlrneN, F. SrsssrNs and L. S. E. Canmcrnrr, 1985.
77 B. M. De Witte, P. J. Grobet and J. B. Uytterhoeven, Pentacoordinated Aluminum in Noncalcined Amorphous Aluminosilicates, Prepared in Alkaline and Acid Mediums, *J. Phys. Chem.*, 1995, **99**, 6961–6965.
78 M. Caillot, A. Chaumonnot, M. Digne and J. A. van Bokhoven, The variety of Brønsted acid sites in amorphous aluminosilicates and zeolites, *Journal of Catalysis*, 2014, **316**, 47–56.
79 W. O. Haag, R. M. Lago and P. B. Weisz, The active site of acidic aluminosilicate catalysts, *Nature*, 1984, **309**, 309589a0.
80 M. Bevilacqua, T. Montanari, E. Finocchio and G. Busca, Are the active sites of protonic zeolites generated by the cavities?, *Catalysis Today*, 2006, **116**, 132–142.
81 F. Leydier, C. Chizallet, A. Chaumonnot, M. Digne, E. Soyer, A.-A. Quoineaud, D. Costa and P. Raybaud, Brønsted acidity of amorphous silica–alumina: The molecular rules of proton transfer, *Journal of Catalysis*, 2011, **284**, 215–229.
82 T. K. Phung, L. Proietti Hernández, A. Lagazzo and G. Busca, Dehydration of ethanol over zeolites, silica alumina and alumina: Lewis acidity, Brønsted acidity and confinement effects, *Applied Catalysis A: General*, 2015, **493**, 77–89.
83 Z. Wang, Y. Jiang, X. Yi, C. Zhou, A. Rawal, J. Hook, Z. Liu, F. Deng, A. Zheng, M. Hunger, A. Baiker and J. Huang, High population and dispersion of pentacoordinated AlV species on the surface of flame-made amorphous silica-alumina, *Science Bulletin*, , DOI:10.1016/j.scib.2019.04.002.
84 Z. Wang, Y. Jiang, F. Jin, C. Stampfl, M. Hunger, A. Baiker and J. Huang, Strongly enhanced acidity and activity of amorphous silica–alumina by formation of pentacoordinated AlV species, *Journal of Catalysis*, 2019, **372**, 1–7.
85 Worldwide demand for propylene to rise to 130 million tonnes by 2023, says IHS, https://www.chemicals-technology.com/news/newsworldwide-demand-for-propylene-to-rise-to-130-million-tonnes-by-2023-says-ihs-4356137/, (accessed 3 January 2020).
86 Z. Nawaz, Light alkane dehydrogenation to light olefin technologies: a comprehensive review, *Reviews in Chemical Engineering*, 2015, **31**, 413–436.
87 J. J. H. B. Sattler, J. Ruiz-Martinez, E. Santillan-Jimenez and B. M. Weckhuysen, Catalytic Dehydrogenation of Light Alkanes on Metals and Metal Oxides, *Chem. Rev.*, 2014, **114**, 10613–10653.

88 D. S. Su, S. Perathoner and G. Centi, Nanocarbons for the Development of Advanced Catalysts, *Chem. Rev.*, 2013, **113**, 5782–5816.
89 F. Cavani, N. Ballarini and A. Cericola, Oxidative dehydrogenation of ethane and propane: How far from commercial implementation?, *Catalysis Today*, 2007, **127**, 113–131.
90 Z.-J. Zhao, C. Chiu and J. Gong, Molecular understandings on the activation of light hydrocarbons over heterogeneous catalysts, *Chem. Sci.*, 2015, **6**, 4403–4425.
91 V. M. T. Herauville, Catalytic Dehydrogenation of Propane, 96.
92 United States, US8563793B2, 2013.
93 United States, US4695662A, 1987.
94 United States, US5723707A, 1998.
95 Shaping the future of on-purpose propylene production, https://www.hydrocarbonprocessing.com/magazine/2017/april-2017/special-focus-petrochemical-developments/shaping-the-future-of-on-purpose-propylene-production, (accessed 9 June 2021).
96 S. Sarkaer and KBR, in *Global Refining and Petrochemicals Congress*, 2019.
97 KBR signs agreement for propane dehydrogenation project, https://www.hydrocarbonengineering.com/petrochemicals/14042021/kbr-signs-agreement-for-propane-dehydrogenation-project/, (accessed 9 June 2021).
98 United States, US11198661B2, 2021.
99 Hydrocarbon Engineering, KBR signs agreement for propane dehydrogenation project, https://www.hydrocarbonengineering.com/petrochemicals/14042021/kbr-signs-agreement-for-propane-dehydrogenation-project/, (accessed 6 May 2021).
100 United States, US10590048B2, 2020.
101 P. Praserthdam, T. Mongkhonsi, S. Kunatippapong, B. Jaikaew and N. Lim, in *Studies in Surface Science and Catalysis*, eds. C. H. Bartholomew and G. A. Fuentes, Elsevier, 1997, vol. 111, pp. 153–158.
102 J. J. H. B. Sattler, I. D. González-Jiménez, A. M. Mens, M. Arias, T. Visser and B. M. Weckhuysen, Operando UV-Vis spectroscopy of a catalytic solid in a pilot-scale reactor: deactivation of a CrOx/Al2O3 propane dehydrogenation catalyst, *Chem. Commun.*, 2013, **49**, 1518–1520.
103 J. A. Labinger and J. E. Bercaw, Understanding and exploiting C–H bond activation, *Nature*, 2002, **417**, 507–514.
104 R. H. Crabtree, Alkane C–H activation and functionalization with homogeneous transition metal catalysts: a century of progress—a new millennium in prospect, *Journal of the Chemical Society, Dalton Transactions*, 2001, **0**, 2437–2450.
105 F. Maseras, A. Lledós, E. Clot and O. Eisenstein, Transition Metal Polyhydrides: From Qualitative Ideas to Reliable Computational Studies, *Chem. Rev.*, 2000, **100**, 601–636.
106 I. Horiuti and M. Polanyi, Exchange reactions of hydrogen on metallic catalysts, *Trans. Faraday Soc.*, 1934, **30**, 1164–1172.
107 A. Iglesias-Juez, A. M. Beale, K. Maaijen, T. C. Weng, P. Glatzel and B. M. Weckhuysen, A combined in situ time-resolved UV–Vis, Raman and high-energy resolution X-ray absorption spectroscopy study on the deactivation behavior of Pt and PtSn propane dehydrogenation catalysts under industrial reaction conditions, *Journal of Catalysis*, 2010, **276**, 268–279.

108 A. Farjoo, F. Khorasheh, S. Niknaddaf and M. Soltani, Kinetic modeling of side reactions in propane dehydrogenation over Pt - Sn/γ - Al2O3 catalyst, *Scientia Iranica*, 2011, **18**, 458–464.

109 Q. Li, Z. Sui, X. Zhou, Y. Zhu, J. Zhou and D. Chen, Coke Formation on Pt–Sn/Al2O3 Catalyst in Propane Dehydrogenation: Coke Characterization and Kinetic Study, *Top Catal*, 2011, **54**, 888.

110 J. Zhu, M.-L. Yang, Y. Yu, Y.-A. Zhu, Z.-J. Sui, X.-G. Zhou, A. Holmen and D. Chen, Size-Dependent Reaction Mechanism and Kinetics for Propane Dehydrogenation over Pt Catalysts, *ACS Catal.*, 2015, **5**, 6310–6319.

111 M. Santhosh Kumar, D. Chen, J. C. Walmsley and A. Holmen, Dehydrogenation of propane over Pt-SBA-15: Effect of Pt particle size, *Catalysis Communications*, 2008, **9**, 747–750.

112 M. Santhosh Kumar, D. Chen, A. Holmen and J. C. Walmsley, Dehydrogenation of propane over Pt-SBA-15 and Pt-Sn-SBA-15: Effect of Sn on the dispersion of Pt and catalytic behavior, *Catalysis Today*, 2009, **142**, 17–23.

113 R. M. Rioux, H. Song, J. D. Hoefelmeyer, P. Yang and G. A. Somorjai, High-Surface-Area Catalyst Design: Synthesis, Characterization, and Reaction Studies of Platinum Nanoparticles in Mesoporous SBA-15 Silica, *J. Phys. Chem. B*, 2005, **109**, 2192–2202.

114 R. T. Vang, K. Honkala, S. Dahl, E. K. Vestergaard, J. Schnadt, E. Lægsgaard, B. S. Clausen, J. K. Nørskov and F. Besenbacher, Controlling the catalytic bond-breaking selectivity of Ni surfaces by step blocking, *Nature Materials*, 2005, **4**, 160–162.

115 R. M. Mironenko, O. B. Belskaya, V. P. Talsi, T. I. Gulyaeva, M. O. Kazakov, A. I. Nizovskii, A. V. Kalinkin, V. I. Bukhtiyarov, A. V. Lavrenov and V. A. Likholobov, Effect of γ-Al2O3 hydrothermal treatment on the formation and properties of platinum sites in Pt/γ-Al2O3 catalysts, *Applied Catalysis A: General*, 2014, **469**, 472–482.

116 L. Shi, G.-M. Deng, W.-C. Li, S. Miao, Q.-N. Wang, W.-P. Zhang and A.-H. Lu, Al2O3 Nanosheets Rich in Pentacoordinate Al3+ Ions Stabilize Pt-Sn Clusters for Propane Dehydrogenation, *Angewandte Chemie International Edition*, 2015, **54**, 13994–13998.

117 E. J. Jang, J. Lee, H. Y. Jeong and J. H. Kwak, Controlling the acid-base properties of alumina for stable PtSn-based propane dehydrogenation catalysts, *Applied Catalysis A: General*, 2019, **572**, 1–8.

118 Q. Yu, T. Yu, H. Chen, G. Fang, X. Pan and X. Bao, The effect of Al3+ coordination structure on the propane dehydrogenation activity of Pt/Ga/Al2O3 catalysts, *Journal of Energy Chemistry*, 2020, **41**, 93–99.

119 T. Wang, F. Jiang, G. Liu, L. Zeng, Z. Zhao and J. Gong, Effects of Ga doping on Pt/CeO2-Al2O3 catalysts for propane dehydrogenation, *AIChE Journal*, 2016, **62**, 4365–4376.

120 F. Jiang, L. Zeng, S. Li, G. Liu, S. Wang and J. Gong, Propane Dehydrogenation over Pt/TiO2–Al2O3 Catalysts, *ACS Catal.*, 2015, **5**, 438–447.

121 X. Chen, M. Ge, Y. Li, Y. Liu, J. Wang and L. Zhang, Fabrication of highly dispersed Pt-based catalysts on γ-Al2O3 supported perovskite Nano islands: High durability and tolerance to coke deposition in propane dehydrogenation, *Applied Surface Science*, 2019, **490**, 611–621.

122 W. Tolek, K. Suriye, P. Praserthdam and J. Panpranot, Effect of preparation method on the Pt-In modified Mg(Al)O catalysts over dehydrogenation of propane, *Catalysis Today*, , DOI:10.1016/j.cattod.2019.08.047.

123 L.-L. Shen, K. Xia, W.-Z. Lang, L.-F. Chu, X. Yan and Y.-J. Guo, The effects of calcination temperature of support on PtIn/Mg(Al)O catalysts for propane dehydrogenation reaction, *Chemical Engineering Journal*, 2017, **324**, 336–346.

124 X. Wu, Q. Zhang, L. Chen, Q. Liu, X. Zhang, Q. Zhang, L. Ma and C. Wang, Enhanced catalytic performance of PtSn catalysts for propane dehydrogenation by a Zn-modified Mg(Al)O support, *Fuel Processing Technology*, 2020, **198**, 106222.

125 Y. Zhang, Y. Zhou, M. Tang, X. Liu and Y. Duan, Effect of La calcination temperature on catalytic performance of PtSnNaLa/ZSM-5 catalyst for propane dehydrogenation, *Chemical Engineering Journal*, 2012, **181–182**, 530–537.

126 M. Santhosh Kumar, A. Holmen and D. Chen, The influence of pore geometry of Pt containing ZSM-5, Beta and SBA-15 catalysts on dehydrogenation of propane, *Microporous and Mesoporous Materials*, 2009, **126**, 152–158.

127 W. Wannapakdee, T. Yutthalekha, P. Dugkhuntod, K. Rodponthukwaji, A. Thivasasith, S. Nokbin, T. Witoon, S. Pengpanich and C. Wattanakit, Dehydrogenation of Propane to Propylene Using Promoter-Free Hierarchical Pt/Silicalite-1 Nanosheets, *Catalysts*, 2019, **9**, 174.

128 Y. Wang, Z.-P. Hu, X. Lv, L. Chen and Z.-Y. Yuan, Ultrasmall PtZn bimetallic nanoclusters encapsulated in silicalite-1 zeolite with superior performance for propane dehydrogenation, *Journal of Catalysis*, 2020, **385**, 61–69.

129 Z. Xu, Y. Yue, X. Bao, Z. Xie and H. Zhu, Propane Dehydrogenation over Pt Clusters Localized at the Sn Single-Site in Zeolite Framework, *ACS Catal.*, 2020, **10**, 818–828.

130 Z. Wu, B. C. Bukowski, Z. Li, C. Milligan, L. Zhou, T. Ma, Y. Wu, Y. Ren, F. H. Ribeiro, W. N. Delgass, J. Greeley, G. Zhang and J. T. Miller, Changes in Catalytic and Adsorptive Properties of 2 nm Pt3Mn Nanoparticles by Subsurface Atoms, *J. Am. Chem. Soc.*, 2018, **140**, 14870–14877.

131 L. Deng, T. Shishido, K. Teramura and T. Tanaka, Effect of reduction method on the activity of Pt–Sn/SiO2 for dehydrogenation of propane, *Catalysis Today*, 2014, **232**, 33–39.

132 L. Deng, H. Miura, T. Shishido, Z. Wang, S. Hosokawa, K. Teramura and T. Tanaka, Elucidating strong metal-support interactions in Pt–Sn/SiO2 catalyst and its consequences for dehydrogenation of lower alkanes, *Journal of Catalysis*, 2018, **365**, 277–291.

133 L. Deng, H. Miura, T. Shishido, S. Hosokawa, K. Teramura and T. Tanaka, Strong metal-support interaction between Pt and SiO2 following high-temperature reduction: a catalytic interface for propane dehydrogenation, *Chem. Commun.*, 2017, **53**, 6937–6940.

134 Z. Ji, D. Miao, L. Gao, X. Pan and X. Bao, Effect of pH on the catalytic performance of PtSn/B-ZrO2 in propane dehydrogenation, *Chinese Journal of Catalysis*, 2020, **41**, 719–729.

135 L. Wang, Y. Wang, C.-W. Zhang, J. Wen, X. Weng and L. Shi, A boron nitride nanosheet-supported Pt/Cu cluster as a high-efficiency catalyst for propane dehydrogenation, *Catal. Sci. Technol.*, 2020, **10**, 1248–1255.

136 J. Wu, L. Wang, X. Yang, B. Lv and J. Chen, Support Effect of the Fe/BN Catalyst on Fischer–Tropsch Performances: Role of the Surface B–O Defect, *Ind. Eng. Chem. Res.*, 2018, **57**, 2805–2810.

137 C. Meng, Y. Li, H. Wu, W. Wei, Y. Ning, Y. Cui, Q. Fu and X. Bao, Structural transformation of h-BN overlayers on Pt(111) in oxidative atmospheres, *Phys. Chem. Chem. Phys.*, 2018, **20**, 11013–11020.

138 S. Rimaz, L. Chen, S. Kawi and A. Borgna, Promoting effect of Ge on Pt-based catalysts for dehydrogenation of propane to propylene, *Applied Catalysis A: General*, 2019, **588**, 117266.

139 G. Sun, Z.-J. Zhao, R. Mu, S. Zha, L. Li, S. Chen, K. Zang, J. Luo, Z. Li, S. C. Purdy, A. J. Kropf, J. T. Miller, L. Zeng and J. Gong, Breaking the scaling relationship via thermally stable Pt/Cu single atom alloys for catalytic dehydrogenation, *Nature Communications*, 2018, **9**, 4454.

140 K. Xia, W.-Z. Lang, P.-P. Li, L.-L. Long, X. Yan and Y.-J. Guo, The influences of Mg/Al molar ratio on the properties of PtIn/Mg(Al)O-x catalysts for propane dehydrogenation reaction, *Chemical Engineering Journal*, 2016, **284**, 1068–1079.

141 K. Searles, K. W. Chan, J. A. Mendes Burak, D. Zemlyanov, O. Safonova and C. Copéret, Highly Productive Propane Dehydrogenation Catalyst Using Silica-Supported Ga–Pt Nanoparticles Generated from Single-Sites, *J. Am. Chem. Soc.*, 2018, **140**, 11674–11679.

142 T. H. Fleisch, A. Basu and R. A. Sills, Introduction and advancement of a new clean global fuel: The status of DME developments in China and beyond, *Journal of Natural Gas Science and Engineering*, 2012, **9**, 94–107.

143 F. Arena, G. Mezzatesta, G. Zafarana, G. Trunfio, F. Frusteri and L. Spadaro, Effects of oxide carriers on surface functionality and process performance of the Cu–ZnO system in the synthesis of methanol via CO2 hydrogenation, *Journal of Catalysis*, 2013, **300**, 141–151.

144 C. Li, X. Yuan and K. Fujimoto, Development of highly stable catalyst for methanol synthesis from carbon dioxide, *Applied Catalysis A: General*, 2014, **469**, 306–311.

145 A. Karelovic, A. Bargibant, C. Fernández and P. Ruiz, Effect of the structural and morphological properties of Cu/ZnO catalysts prepared by citrate method on their activity toward methanol synthesis from CO2 and H2 under mild reaction conditions, *Catalysis Today*, 2012, **197**, 109–118.

146 M. Xu, J. H. Lunsford, D. W. Goodman and A. Bhattacharyya, Synthesis of dimethyl ether (DME) from methanol over solid-acid catalysts, *Applied Catalysis A: General*, 1997, **149**, 289–301.

147 S. Hosseini, M. Taghizadeh and A. Eliassi, Optimization of hydrothermal synthesis of H-ZSM-5 zeolite for dehydration of methanol to dimethyl ether using full factorial design, *Journal of Natural Gas Chemistry*, 2012, **21**, 344–351.

148 S. Bhattacharya, K. B. Kabir and K. Hein, Dimethyl ether synthesis from Victorian brown coal through gasification – Current status, and research and development needs, *Progress in Energy and Combustion Science*, 2013, **39**, 577–605.

149 Z. Hosseini, M. Taghizadeh and F. Yaripour, Synthesis of nanocrystalline γ-Al2O3 by sol-gel and precipitation methods for methanol dehydration to dimethyl ether, *Journal of Natural Gas Chemistry*, 2011, **20**, 128–134.

150 A. R. Keshavarz, M. Rezaei and F. Yaripour, Preparation of nanocrystalline γ-Al2O3 catalyst using different procedures for methanol dehydration to dimethyl ether, *Journal of Natural Gas Chemistry*, 2011, **20**, 334–338.

151 L. Travalloni, A. C. L. Gomes, A. B. Gaspar and M. A. P. da Silva, Methanol conversion over acid solid catalysts, *Catalysis Today*, 2008, **133–135**, 406–412.
152 Q. Tang, H. Xu, Y. Zheng, J. Wang, H. Li and J. Zhang, Catalytic dehydration of methanol to dimethyl ether over micro–mesoporous ZSM-5/MCM-41 composite molecular sieves, *Applied Catalysis A: General*, 2012, **413–414**, 36–42.
153 R. Ladera, E. Finocchio, S. Rojas, J. L. G. Fierro and M. Ojeda, Supported niobium catalysts for methanol dehydration to dimethyl ether: FTIR studies of acid properties, *Catalysis Today*, 2012, **192**, 136–143.
154 K. Lertjiamratn, P. Praserthdam, M. Arai and J. Panpranot, Modification of acid properties and catalytic properties of AlPO4 by hydrothermal pretreatment for methanol dehydration to dimethyl ether, *Applied Catalysis A: General*, 2010, **378**, 119–123.
155 B. Sabour, M. H. Peyrovi, T. Hamoule and M. Rashidzadeh, Catalytic dehydration of methanol to dimethyl ether (DME) over Al-HMS catalysts, *Journal of Industrial and Engineering Chemistry*, 2014, **20**, 222–227.
156 F. Yaripour, F. Baghaei, I. Schmidt and J. Perregaard, Catalytic dehydration of methanol to dimethyl ether (DME) over solid-acid catalysts, *Catalysis Communications*, 2005, **6**, 147–152.
157 K.-W. Jun, H.-S. Lee, H.-S. Rho and S.-E. Park, Catalytic Dehydration of Methanol to Dimethyl Ether (DME) over Solid-Acid Catalysts, *Bulletin of the Korean Chemical Society*, 2002, **23**, 803–807.
158 G. Busca, Infrared studies of the reactive adsorption of organic molecules over metal oxides and of the mechanisms of their heterogeneously-catalyzed oxidation, *Catalysis Today*, 1996, **27**, 457–496.
159 B. C. Shi and B. H. Davis, Alcohol Dehydration: Mechanism of Ether Formation Using an Alumina Catalyst, *Journal of Catalysis*, 1995, **157**, 359–367.
160 H. Knoezinger, A. Scheglila and A. M. Watson, Dehydration of alcohols over alumina. VIII. Ether formation from the deuterated methanols CH3OH, CD3OH, CH3OD, and CD3OD, *J. Phys. Chem.*, 1968, **72**, 2770–2774.
161 P. A. Clayborne, T. C. Nelson and T. C. DeVore, Temperature programmed desorption-FTIR investigation of C1–C5 primary alcohols adsorbed on γ-alumina, *Applied Catalysis A: General*, 2004, **257**, 225–233.
162 Y. Tavan, S. H. Hosseini, M. Ghavipour, M. R. Khosravi Nikou and A. Shariati, From laboratory experiments to simulation studies of methanol dehydration to produce dimethyl ether—Part I: Reaction kinetic study, *Chemical Engineering and Processing: Process Intensification*, 2013, **73**, 144–150.
163 S. R. Blaszkowski and R. A. van Santen, Theoretical Study of the Mechanism of Surface Methoxy and Dimethyl Ether Formation from Methanol Catalyzed by Zeolitic Protons, *J. Phys. Chem. B*, 1997, **101**, 2292–2305.
164 V. A. MATYSHAK, T. I. KHOMENKO, G. I. LIN, I. N. ZAVALISHIN and A. Y. ROZOVSKII, Surface species in the methyl formate-methanol-dimethyl Ether-γ-Al2O3 system studied by in situ IR spectroscopy, *Kinet. catal*, 1999, **40**, 269–274.
165 Z. Qinwei and D. Jingfa, Studies on the properties of water in and conversion of methanol into dimethyl ether on H3PW12O40, *Journal of Catalysis*, 1989, **116**, 298–302.

166 T. Takeguchi, K. Yanagisawa, T. Inui and M. Inoue, Effect of the property of solid acid upon syngas-to-dimethyl ether conversion on the hybrid catalysts composed of Cu–Zn–Ga and solid acids, *Applied Catalysis A: General*, 2000, **192**, 201–209.
167 In *Alternative Solvents for Green Chemistry*, 2013, pp. 115–148.
168 J. M. Dobbs, J. M. Wong, R. J. Lahiere and K. P. Johnston, Modification of supercritical fluid phase behavior using polar cosolvents, *Ind. Eng. Chem. Res.*, 1987, **26**, 56–65.
169 C. A. Eckert, B. L. Knutson and P. G. Debenedetti, Supercritical fluids as solvents for chemical and materials processing, *Nature*, 1996, **383**, 313–318.
170 R. M. Lemert and K. P. Johnston, Chemical complexing agents for enhanced solubilities in supercritical fluid carbon dioxide, *Ind. Eng. Chem. Res.*, 1991, **30**, 1222–1231.
171 J. G. Van Alsten and C. A. Eckert, Effect of entrainers and of solute size and polarity in supercritical fluid solutions, *J. Chem. Eng. Data*, 1993, **38**, 605–610.
172 E. Ruckenstein and I. Shulgin, Entrainer effect in supercritical mixtures, *Fluid Phase Equilibria*, 2001, **180**, 345–359.
173 P. W. Bridgman, Change of Phase under Pressure. I. The Phase Diagram of Eleven Substances with Especial Reference to The Melting Curve, *Phys. Rev.*, 1914, **3**, 153–203.
174 G. M. Schneider, Carbon Dioxide – International Thermodynamic Tables of the Fluid State, Bd. 3. Von S. Angus, B. Armstrong und K. M. de Rerrck. Pergamon Press Ltd., Oxford–New York 1976. 1. Aufl., XXVII, 385 S., zahlr. Abb. u. Tab., geb., DM 172,50, *Chemie Ingenieur Technik*, 1977, **49**, 594–594.
175 International Thermodynamic Tables of the Fluid State - 1st Edition, https://www.elsevier.com/books/international-thermodynamic-tables-of-the-fluid-state/angus/978-0-08-022373-5, (accessed 16 April 2020).
176 F. M. A. Geilen, T. vom Stein, B. Engendahl, S. Winterle, M. A. Liauw, J. Klankermayer and W. Leitner, Highly Selective Decarbonylation of 5-(Hydroxymethyl)furfural in the Presence of Compressed Carbon Dioxide, *Angewandte Chemie International Edition*, 2011, **50**, 6831–6834.
177 P. Licence, J. Ke, M. Sokolova, S. K. Ross and M. Poliakoff, Chemical reactions in supercritical carbon dioxide: from laboratory to commercial plant, *Green Chem.*, 2003, **5**, 99–104.
178 P. Lozano, Enzymes in neoteric solvents: From one-phase to multiphase systems, *Green Chem.*, 2010, **12**, 555–569.
179 E. J. Beckman, Supercritical and near-critical CO2 in green chemical synthesis and processing, *The Journal of Supercritical Fluids*, 2004, **28**, 121–191.
180 E. Reverchon and I. De Marco, Supercritical fluid extraction and fractionation of natural matter, *The Journal of Supercritical Fluids*, 2006, **38**, 146–166.
181 S. M. Pourmortazavi and S. S. Hajimirsadeghi, Supercritical fluid extraction in plant essential and volatile oil analysis, *Journal of Chromatography A*, 2007, **1163**, 2–24.
182 O. US EPA, Basics of Green Chemistry, https://www.epa.gov/greenchemistry/basics-green-chemistry, (accessed 10 June 2018).
183 C. Li and L. Laloui, Coupled multiphase thermo-hydro-mechanical analysis of supercritical CO2 injection: Benchmark for the In Salah surface uplift problem, *International Journal of Greenhouse Gas Control*, 2016, **51**, 394–408.
184 D. W. Matson, J. L. Fulton, R. C. Petersen and R. D. Smith, Rapid expansion of supercritical fluid solutions: solute formation of powders, thin films, and fibers, *Ind. Eng. Chem. Res.*, 1987, **26**, 2298–2306.

185 D. W. Matson, R. C. Petersen and R. D. Smith, The preparation of polycarbosilane powders and fibers during rapid expansion of supercritical fluid solutions, *Materials Letters*, 1986, **4**, 429–432.
186 J. W. Tom and P. G. Debenedetti, Particle formation with supercritical fluids—a review, *Journal of Aerosol Science*, 1991, **22**, 555–584.
187 B. Helfgen, M. Türk and K. Schaber, Hydrodynamic and aerosol modelling of the rapid expansion of supercritical solutions (RESS-process), *The Journal of Supercritical Fluids*, 2003, **26**, 225–242.
188 J. O. Werling and P. G. Debenedetti, Numerical modeling of mass transfer in the supercritical antisolvent process: miscible conditions, *The Journal of Supercritical Fluids*, 2000, **18**, 11–24.
189 S.-D. Yeo, G.-B. Lim, P. G. Debendetti and H. Bernstein, Formation of microparticulate protein powder using a supercritical fluid antisolvent, *Biotechnology and Bioengineering*, 1993, **41**, 341–346.
190 P. M. Gallagher, M. P. Coffey, V. J. Krukonis and N. Klasutis, in *Supercritical Fluid Science and Technology*, American Chemical Society, 1989, vol. 406, pp. 334–354.
191 E. Reverchon, G. Caputo and I. De Marco, Role of Phase Behavior and Atomization in the Supercritical Antisolvent Precipitation, *Ind. Eng. Chem. Res.*, 2003, **42**, 6406–6414.
192 G. J. Hutchings, Catalyst Synthesis Using Supercritical Carbon Dioxide: A Green Route to High Activity Materials, *Top Catal*, 2009, **52**, 982–987.
193 S. A. Kondrat and S. H. Taylor, in *Catalysis*, 2014, pp. 218–248.
194 E. Reverchon, Supercritical antisolvent precipitation of micro- and nano-particles, *The Journal of Supercritical Fluids*, 1999, **15**, 1–21.
195 E. Reverchon, I. De Marco and E. Torino, Nanoparticles production by supercritical antisolvent precipitation: A general interpretation, *The Journal of Supercritical Fluids*, 2007, **43**, 126–138.
196 E. Reverchon and R. Adami, Nanomaterials and supercritical fluids, *The Journal of Supercritical Fluids*, 2006, **37**, 1–22.
197 E. Reverchon, Supercritical-Assisted Atomization To Produce Micro- and/or Nanoparticles of Controlled Size and Distribution, *Ind. Eng. Chem. Res.*, 2002, **41**, 2405–2411.
198 E. Reverchon and I. De Marco, Mechanisms controlling supercritical antisolvent precipitate morphology, *Chemical Engineering Journal*, 2011, **169**, 358–370.
199 C. S. Lengsfeld, J. P. Delplanque, V. H. Barocas and T. W. Randolph, Mechanism Governing Microparticle Morphology during Precipitation by a Compressed Antisolvent: Atomization vs Nucleation and Growth, *J. Phys. Chem. B*, 2000, **104**, 2725–2735.
200 E. Reverchon, R. Adami, G. Caputo and I. De Marco, Spherical microparticles production by supercritical antisolvent precipitation: Interpretation of results, *The Journal of Supercritical Fluids*, 2008, **47**, 70–84.
201 V. Prosapio, I. De Marco and E. Reverchon, Supercritical antisolvent coprecipitation mechanisms, *The Journal of Supercritical Fluids*, 2018, **138**, 247–258.
202 E. Reverchon, E. Torino, S. Dowy, A. Braeuer and A. Leipertz, Interactions of phase equilibria, jet fluid dynamics and mass transfer during supercritical antisolvent micronization, *Chemical Engineering Journal*, 2010, **156**, 446–458.

203 E. Reverchon, G. Della Porta, A. Di Trolio and S. Pace, Supercritical Antisolvent Precipitation of Nanoparticles of Superconductor Precursors, *Ind. Eng. Chem. Res.*, 1998, **37**, 952–958.

204 E. Reverchon, G. Della Porta, D. Sannino and P. Ciambelli, Supercritical antisolvent precipitation of nanoparticles of a zinc oxide precursor, *Powder Technology*, 1999, **102**, 127–134.

205 E. Reverchon, G. Della Porta, D. Sannino, L. Lisi and P. Ciambelli, in *Studies in Surface Science and Catalysis*, eds. B. Delmon, P. A. Jacobs, R. Maggi, J. A. Martens, P. Grange and G. Poncelet, Elsevier, 1998, vol. 118, pp. 349–358.

206 G. J. Hutchings, J. K. Bartley, J. M. Webster, J. A. Lopez-Sanchez, D. J. Gilbert, C. J. Kiely, A. F. Carley, S. M. Howdle, S. Sajip, S. Caldarelli, C. Rhodes, J. C. Volta and M. Poliakoff, Amorphous Vanadium Phosphate Catalysts from Supercritical Antisolvent Precipitation, *Journal of Catalysis*, 2001, **197**, 232–235.

207 G. J. Hutchings, J. A. Lopez-Sanchez, J. K. Bartley, J. M. Webster, A. Burrows, C. J. Kiely, A. F. Carley, C. Rhodes, M. Hävecker, A. Knop-Gericke, R. W. Mayer, R. Schlögl, J. C. Volta and M. Poliakoff, Amorphous Vanadium Phosphate Catalysts Prepared Using Precipitation with Supercritical CO2 as an Antisolvent, *Journal of Catalysis*, 2002, **208**, 197–210.

208 J. Antonio Lopez-Sanchez, J. K. Bartley, A. Burrows, C. J. Kiely, M. Hävecker, R. Schlögl, J. Claude Volta, M. Poliakoff and G. J. Hutchings, Effects of cobalt additive on amorphous vanadium phosphate catalysts prepared using precipitation with supercritical CO 2 as an antisolvent, *New Journal of Chemistry*, 2002, **26**, 1811–1816.

209 E. Alonso, I. Montequi, S. Lucas and M. J. Cocero, Synthesis of titanium oxide particles in supercritical CO2: Effect of operational variables in the characteristics of the final product, *The Journal of Supercritical Fluids*, 2007, **39**, 453–461.

210 Z.-R. Tang, J. K. Edwards, J. K. Bartley, S. H. Taylor, A. F. Carley, A. A. Herzing, C. J. Kiely and G. J. Hutchings, Nanocrystalline cerium oxide produced by supercritical antisolvent precipitation as a support for high-activity gold catalysts, *Journal of Catalysis*, 2007, **249**, 208–219.

211 P. J. Miedziak, Z. Tang, T. E. Davies, D. I. Enache, J. K. Bartley, A. F. Carley, A. A. Herzing, C. J. Kiely, S. H. Taylor and G. J. Hutchings, Ceria prepared using supercritical antisolvent precipitation: a green support for gold–palladium nanoparticles for the selective catalytic oxidation of alcohols, *J. Mater. Chem.*, 2009, **19**, 8619–8627.

212 Z.-R. Tang, C. D. Jones, J. K. W. Aldridge, T. E. Davies, J. K. Bartley, A. F. Carley, S. H. Taylor, M. Allix, C. Dickinson, M. J. Rosseinsky, J. B. Claridge, Z. Xu, M. J. Crudace and G. J. Hutchings, New Nanocrystalline Cu/MnOx Catalysts Prepared from Supercritical Antisolvent Precipitation, *ChemCatChem*, 2009, **1**, 247–251.

213 R. P. Marin, S. A. Kondrat, T. E. Davies, D. J. Morgan, D. I. Enache, G. B. Combes, S. H. Taylor, J. K. Bartley and G. J. Hutchings, Novel cobalt zinc oxide Fischer–Tropsch catalysts synthesised using supercritical anti-solvent precipitation, *Catal. Sci. Technol.*, 2014, **4**, 1970–1978.

214 R. P. Marin, S. A. Kondrat, R. K. Pinnell, T. E. Davies, S. Golunski, J. K. Bartley, G. J. Hutchings and S. H. Taylor, Green preparation of transition metal oxide catalysts using supercritical CO2 anti-solvent precipitation for the total oxidation of propane, *Applied Catalysis B: Environmental*, 2013, **140–141**, 671–679.

215 S. A. Kondrat, P. J. Smith, P. P. Wells, P. A. Chater, J. H. Carter, D. J. Morgan, E. M. Fiordaliso, J. B. Wagner, T. E. Davies, L. Lu, J. K. Bartley, S. H. Taylor, M. S. Spencer, C. J. Kiely, G. J. Kelly, C. W. Park, M. J. Rosseinsky and G. J. Hutchings, Stable amorphous georgeite as a precursor to a high-activity catalyst, *Nature*, 2016, **531**, 83.

2 Experimental

2.1 Materials

All reagents, solvents and gases used during this project are presented in Table 2.1. In each case they were used as received without further purification, unless otherwise stated. Deionised water was generated in-house.

Table 2.1: List of reagents, solvents and gases used for catalyst material preparations, characterization, and catalyst testing procedures.

Material	**Supplier**	**Purity Grade**
Aluminium acetylacetonate	Sigma Aldrich	≥99 %, ReagentPlus
Aluminium nitrate	Sigma Aldrich	≥98 %
Tetraethylorthosilicate	Sigma Aldrich	≥98 %
Silicon tetraacetate	Sigma Aldrich	≥98 %
Zeolite ZSM-5	Zeolyst International	Ammonium form, (Si/Al=11.5)
Platinum acetylacetonate	Sigma Aldrich	≥99.98 %,
Tetraammineplatinum nitrate	Sigma Aldrich	≥50 % Pt basis
Chloroplatinic acid hexahydrate	Sigma Aldrich	≥37.5, Pt basis
Tetraammineplatinum hydroxide hydrate	Sigma-Aldrich	≥59 % Pt basis
Yttrium aluminium oxide	Sigma Aldrich	99 %
Tetramethylsilane	Sigma Aldrich	≥99 %, NMR Grade
Water	Sigma Aldrich	HPLC Grade
Ethanol	Sigma Aldrich	≥99.8 %, Absolute
Methanol	Sigma Aldrich	≥99.8 %, Absolute
Poly vinyl alcohol (M_w: 9,000-10,000)	Sigma Aldrich	80 % hydrolyzed

Ammonia solution	Fisher Scientific	35 % NH_4OH, certified AR
Sodium Borohydride	Sigma Aldrich	≥98 %,
Carbon dioxide (CO_2)	BOC Gases	CP Grade
Argon (Ar)	BOC Gases	99.9995 %
Nitrogen (N_2)	BOC Gases	99.999 %
Propane	BOC Gases	99.2 %
Pyridine	Sigma Aldrich	99.8 %, anhydrous

2.2 Aluminosilicate Preparation:

A number of aluminosilicates and catalytic materials were synthesised during the course of this project. Synthesis strategies, characterization techniques and testing methods will be discussed in this chapter. Examples of each procedure are provided.

2.3 Supercritical anti-solvent (SAS) precipitation

2.3.1 SAS aluminosilicate preparation

A series of amorphous aluminosilicates were prepared using a bespoke apparatus, consisting of a CO_2 pump, back pressure regulator (BPR) and heat exchanger manufactured by Waters, assembled by Sci-Med. Appropriate amounts of various silicon metal salts and aluminium acetylacetonate, shown in Table 1.1, were dissolved in a mixed aqueous-organic (ethanol and varying amounts of HPLC grade water) solvent. SAS experiments were performed using the apparatus illustrated in Figure 2.1a.

Contact between the $scCO_2$ and prepared solutions was achieved through a co-axial nozzle which was characterized by an inner and outer tube. This configuration supplied the prepared solution in the inner tube (diameter = 1 mm) and the $scCO_2$ through the surrounding outer tube (diameter = 4.95 mm), Figure 2.1b. Liquid CO_2 was cooled to -2 °C and then pumped through the system *via* a temperature-programmed heat exchanger, through the outer part of a coaxial nozzle into a precipitation vessel at a set point pressure

(100-140 bar) and mass flow rates (35 g min^{-1}). The liquid mixture was delivered to the precipitator through the inner segment of stainless-steel nozzle by a HPLC pump at a standard flow rate of 6.5 ml min^{-1}.

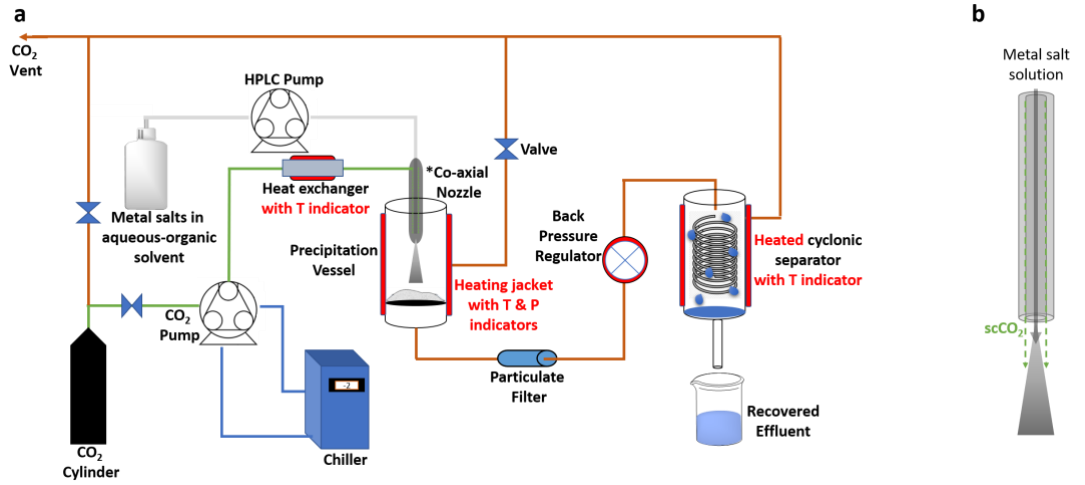

Figure 2.1: (a) Schematic of Sci-med SAS apparatus with flow indications for CO_2 (green), coolant (blue), prepared solution (grey) and ventilation (orange). Cross sectional illustration of co-axial nozzle (b) is included with interactions between the antisolvent (green) and prepared solution (grey).

The resulting precipitate was collected on a stainless-steel frit (pore diameter of 7 µm). A particulate filter (pore diameter of 0.5 µm) located downstream to the precipitation vessel was used to collect any material with dimensions less than 7 µm in diameter. The CO_2-solvent mixture passed down stream through a BPR and cyclonic separator which rapidly cooled, condensed and separated the two components recovered as an effluent. Following precipitation, sequential 30 min purges of the system with the CO_2-solvent mixture and CO_2 were carried out under the reaction conditions. The system was then de-pressurized down to atmospheric pressure and the precipitate recovered and calcined in flowing air at 600 °C (1 °C min^{-1} ramp rate) for 6 h.

2.3.2 Sol-gel aluminosilicate preparation

Sol-gel is an established technique utilised widely used for the preparation of ASAs due to its ability to control homogeneity and final product microstructure from cheap starting reagents as described in Figure 2. 2. The synthesis of systematically varied ASAs was conducted based on the procedure from Agluillin and co-workers.[1] In a typical synthesis, tetraethylorthosilicate (14 g), and an appropriate amount of aluminium nitrate were added to a solution of deionised water (12 ml) and ethanol (28 ml) at 60 °C. The solution was maintained at 60 °C for 20–30 h, with vigorous stirring until the gel point was reached. Following this, aqueous ammonia solution (6.3 g) was added to the gel with vigorous stirring. The resultant gel was maintained at 25 °C for 24 h. Then, all prepared gels were subjected to stepwise thermal treatment at various temperatures and isothermal periods: 50 °C (12 h), 150 °C (24 h) and 650 °C (4 h), in a static air atmosphere with a heating rate of 5 °C min^{-1}.

2.3.3 Flame Spray Pyrolysis aluminosilicate preparation

As previously described in **Chapter 1.6.1.3** the FSP technique is the current state-of-the-art ASA preparation strategy. This strategy offers the production of novel, thermally stable, scalable amorphous phases in a single step without the need for various post-treatment filtration, washing, drying and calcination processes. Due to the short residence and experimental time this methodology has the capacity for scale up due to its energetically sustainable conditions. Systematically varied FSP ASA materials, with varying Si/Al (Si/Al = 1, 4 and 10), were obtained from Department of Chemistry, Università degli Studi di Milano. Through this collaboration we were able to use the strategy previously reported in literature by the Baiker *et al*.[2] In this strategy, a solution containing appropriate amounts of methanol, acetic acid, tetraethylorthosilicate and aluminium acetylacetonate were introduced through a nozzle and nebulized by O_2. The resulting spray was ignited by a methane/oxygen flame and the resulting material was recovered.

2.3.4 Zeolite Activation

Zeolite ZSM-5 with acidity (SiO_2/Al_2O_3 = 22), included in the materials list, was used as a support. Commercial zeolites were purchased from Zeolyst International. Prior to exchange, ammonium (NH^{4+}) was transformed to the acidic (H^+) form by calcination for 5 h at 550 °C (10 °C/min) in flowing air.

2.4 Supported metal catalyst preparation

2.4.1 Incipient wetness impregnation (IWI)

A series of monometallic Pt-based catalysts with 1 wt. % Pt were prepared by IWI. Prior to impregnation, the pore volume of the support was determined by adding the solvent dropwise until no loose material was observed. The desired mass of $Pt(NH3)_4(NO_3)_2$ (0.1241 g) was dissolved in an amount of deionized H_2O corresponding to the support's pore volume. To ensure homogeneous impregnation, the Pt precursor solution was added dropwise to the support maintaining mixing, with a glass rod, until a paste was formed. The exchange procedure was followed by a drying step at 110 °C for 16 hours and calcination for 3 hours at 550 °C (10 °C/min) in static air.

2.4.2 Chemical vapour impregnation (CVI)

1 wt. % Pt monometallic catalysts were prepared by CVI. Prior to exchange, a known mass of the ASA (typically 1 g) was heat treated at 150 °C for 30 min under continuous vacuum. Subsequently, the dried support (≈ 1 g) was added to the desired mass (0.0203 g) of $Pt(acac)_2$. Following physical mixing of the metal precursor and support, the dry mixture was transferred to a Schlenk flask and heated to sublimation- deposition temperature (150 °C) under continuous vacuum (*ca.* 10-5 mbar) for 2 hours. The sample was then allowed to cool to ambient temperature.

2.4.3 Sol-immobilization

Desired quantities of $H_2PtCl_6.6H_2O$ (0.0184 mol) were added to deionised water (800 mL g^{-1} of catalyst prepared) and stirred. To this solution, polyvinyl alcohol (metal/ PVA = 0.65

weight ratio, weight average molecular weight Mw = 9000–10 000 g mol^{-1}, 80% hydrolysed) was added. Subsequently, $NaBH_4$ ($NaBH_4$/metal (mol/mol) = 5) was then introduced. After 30 minutes of sol generation, the colloid was immobilised by adding the support (0.99 g) and the solution was acidified to pH 2 (0.1 M, H_2SO_4) under vigorous stirring. After 1 hour, the slurry was filtered, and the catalyst was washed thoroughly with distilled water and dried at 110 °C for 16 h.

2.4.4 Charge enhanced dry impregnation (CEDI)

The CEDI approach is a method used to synthesize supported metal nanoparticles which combines the simplicity of incipient wetness impregnation with the small particle size obtained from electrostatic adsorption of metal precursors onto an oxide support. With considerations into the surface chemistry of the support the charge-enhanced dry impregnation method (CEDI), first introduced by Cao *et al.* and *Zhu et al.*, has undergone significant development leading to high dispersion and surface loading.[3,4] For context, incipient wetness impregnation or pore filling, often suffers from sub-optimum metal precursor-support interaction during metal deposition, which usually leads to extensive sintering and poor distribution of the metal phase after pre-treatment. To utilise the CEDI strategy, the support's point zero charge (PZC), which is easily found with pH shift measurements, the BET surface area, and the water-accessible pore volume are required. The latter two properties determine the surface loading at dry impregnation, where the surface loading is defined as follows:

$$SL\ (m^2\ L^{-1}) = \frac{BET\ surface\ area\ (m^2\ g^{-1})}{Pore\ volume\ (L^{-1}\ g^{-1})} \qquad (1)$$

Table 2.2: Textural properties of the series of SAS-, FSP-, SG-synthesized ASAs and commercial ZSM5

Support	**Surface area**	**Pore volume normalised per gram (ml g^{-1})**	**Surface loading (x10^3 m^2 L^{-1})**
SAS-1	90	4.0	22.5
SAS-4	44	4.0	11.0
SAS-10	58	3.5	16.6
FSP-1	167	6.0	27.8
FSP-4	267	6.5	41.1
FSP-10	231	6.5	35.5
SG-1	395	2.0	197.5
SG-4	402	2.0	201.0
SG-10	411	2.5	164.4
H-ZSM5	323	1.5	215.3

2.4.4.1 Point of Zero Charge (PZC) calculations:

The point of zero charge for a given particle surface is the pH at which that surface has a net neutral charge. This is important in the context of amorphous aluminosilicate materials where varying degrees of homogeneity in Si-Al mixing can result in silica and alumina domains. In addition, acid sites are generated at the interface between silica and alumina whereby the density of the hydroxyl groups provide surface for electrostatic adsorption. However, due to the differing nature of the individual oxides, the level of atomic (Si and Al) dispersion, and composition (Si/Al) the surface charge varies. Therefore, a range of pH values where metal precursor ions with certain charge types would preferentially adsorb onto one oxide relative to the other exist. On the oxide surface the surface hydroxyl groups protonate or deprotonate as a function of the solution pH. At low pH, the surface is positively charged; on the other hand, at high pH, the surface is negatively charged. Using a pH shift model, (Fig 2.2), the difference in the nature and selectivity of metal adsorption with respect to the pH and type of precursor ions can be deduced.

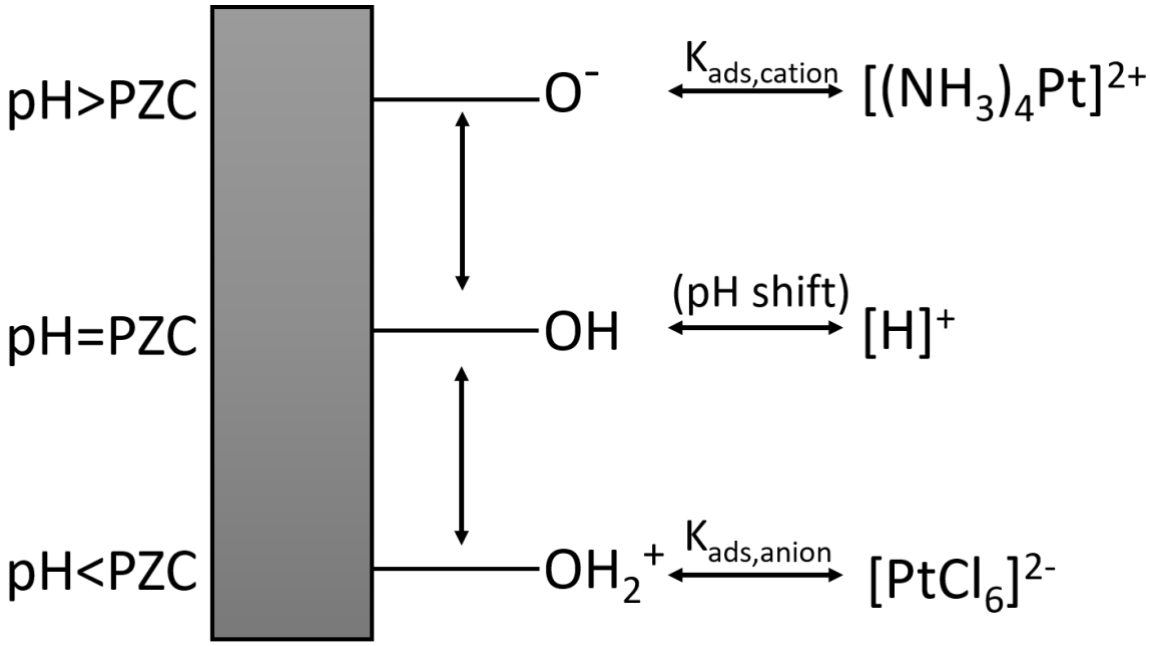

Figure 2.2: Components of surface charging, metal adsorption, proton transfer and the electrostatic adsorption mechanism.

At higher pH, away from their respective PZCs, negative surface potentials over silica and alumina enable them to adsorb cationic $[Pt(NH_3)_4]^{2+}$.

In order to determine the PZC for a given ASA, the following procedure was followed: A series of 10 ml solutions with different initial (pre-adsorption) pH values, pH 1 - 14, were prepared from serial dilutions of 0.1M NaOH or HCl stock solutions, as required. A standard pH electrode (Orion 3-star benchtop) was used with three-point calibration (pH 4, 7, and 10) through appropriate buffer solutions, to record the pH of the solution. The support (0.1 g) was then added in powder form to each solution, and the resulting slurry was thoroughly mixed for 15 min in a glass vial equipped with a magnetic stirrer. After 15 min, the final pH (adsorption pH) was recorded. This was followed by filtration and drying the of the resultant slurry in a vacuum oven at room temperature, for 16 h.

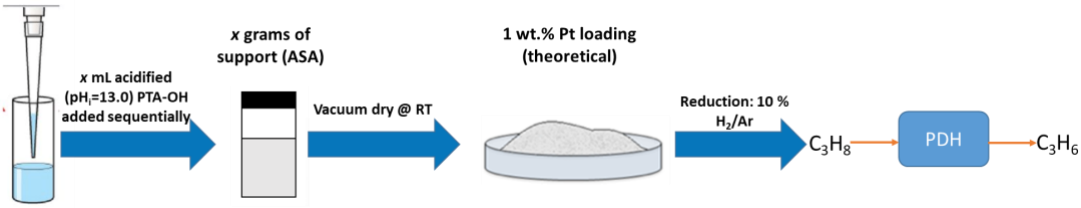

Figure 2.3: Schematic of the charge enhanced dry impregnation procedure for catalyst synthesis.

For CEDI method, an impregnating solution containing metal precursor complex with the desired concentration that would yield the desired, 1 wt.%, metal loading was prepared. In each case freshly prepared solutions of tetraammineplatinum(II) hydroxide hydrate, (0.84 μmol m^{-2}) were used. Based on PZC studies, the pH of this impregnating solution was adjusted to target the pH of maximum adsorption. All pH adjustments were done using either dilute HCl or NaOH solutions. Following pH adjustment, the impregnating solution was added dropwise to support placed in a 10 ml vial. After adding each drop of impregnating solution, the vial was vigorously mixed with a glass rod for homogeneous distribution and pH equilibration. Once the impregnating solution was completely added the resulting sample was dried for 16h at 30 °C in a vacuum oven. Prior to use the catalyst was reduced *in situ* at 350 °C for 1 h with 10 vol.% H_2/Ar (total flow rate = 50 ml min^{-1}).

2.5 Characterisation Techniques

2.5.1 Brunner Emmett Teller (BET) isotherm

BET theory uses the adsorption of non-reactive gases to probe the surface area and pore volume of a solid sample. Several inert adsorbate gases such as N_2, Ar and He are used to determine surface area using BET methods depending on the solid sample. Typically, a known mass of solid sample is outgassed, exposed to a quantity of probe gas at 77K (in the case of Ar and N_2) leading to adsorption onto the solid surface forming an equilibrium between surface bound and free probe gas. The correlation between the gaseous pressure and the quantity of gas adsorbed by the solid sample is termed an adsorption isotherm. The BET isotherm method can be used to determine the surface area of a sample by

determining the amount of adsorbate gas corresponding to a monolayer coverage at the surface. This is achieved using a modification to the Langmuir adsorption model, detailed in **equation 2**:

$$\frac{1}{v\left[\left(\frac{P_0}{P}-1\right)\right]} = \frac{1}{V_m c} + \frac{(c-1)}{v_m c} \times \frac{p}{p_0} \qquad (2)$$

Where:

p = Equilibrium pressure

p_0 = Saturation pressure

v = Adsorbed gas volume

v_m = Monolayer adsorbed gas volume

c = the BET constant, otherwise defined as

$$c = e \times \left(\frac{E_1 - E_L}{RT}\right) \qquad (3)$$

Where:

E_1 = Heat of adsorption for one monolayer

E_L = The heat of liquification

T = Temperature

R = Gas constant

An adsorption/desorption isotherm, yielded from plotting *v vs* p/p_0, conveys the change in volume expressed as a change in pressure. The BET approximation is a linear expression of the form *y = mx + c,* thus it is only applicable for surface area determination in the linear range measured in from adsorption isotherm as the $p/p_0 = 0.05 – 0.35$ range.

The classification of adsorption isotherms, as proposed by the IUPAC, categorises the six types of adsorption isotherms as illustrated in Fig 2.3. Type I isotherms are obtained for microporous adsorbents with a high proportion of exposed surface present within the micropores and a significantly smaller fraction of external surfaces for additional adsorption. Non-porous adsorbents with strong fluid wall attractive forces have characteristic Type II isotherms whereby the low p/p_0 region indicates monolayer coverage. Subsequent increase of the pressure denotes multilayer adsorption. Type III isotherms are associated with weak substrates where the heats of adsorption are lower than the adsorption heat of liquefaction. Type IV isotherms display similarities with Type II

isotherms, but the monolayer-multilayer adsorption isotherms in this case are represent mesoporous adsorbents and similarly the low p/p_0 region indicates complete coverage of the first monolayer. Additional pressure increases result in filling of the pores through a capillary (pore) condensation process (at $p/p_0 > ca.$ 0.2). Type V isotherms signify weak adsorbate-adsorbent interactions observed with specific porous adsorbents, similar to Type II isotherms, with a hysteresis loop similar to Type IV isotherms. Non-porous materials characterised by stepwise multilayer adsorption are represented by Type VI isotherms.

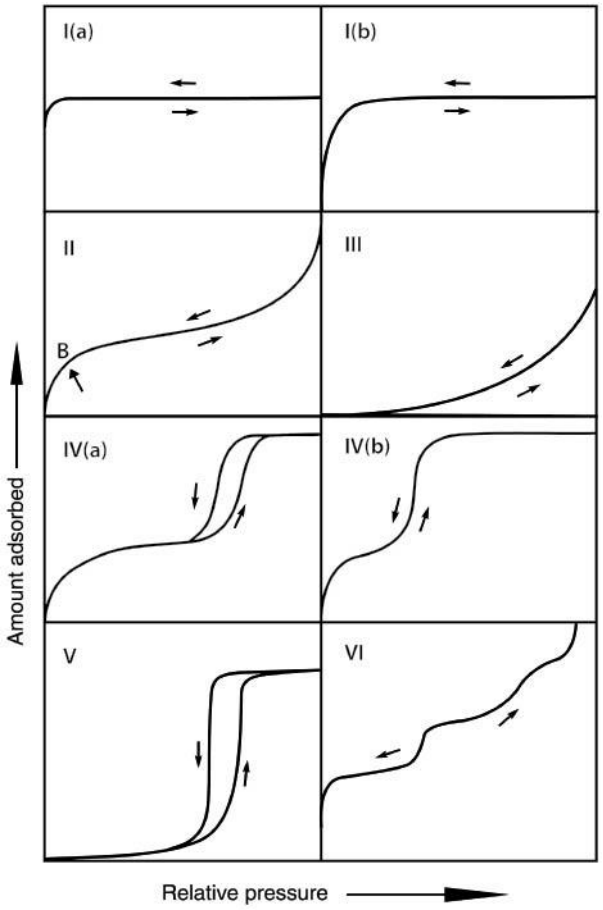

Figure 2.4: IUPAC classification of adsorption isotherms.[5]

The aforementioned capillary condensation is usually accompanied by adsorption-desorption hysteresis which occur when there is a difference between adsorption and desorption curves of the isotherms. This allows for additional analysis of pore size and structure. Based on IUPAC classification four types of adsorption desorption hysteresis loops exist and are denoted as H1, H2, H3, H4 and H5 (Fig 2.4). Porous materials possessing

cylindrical pores open at both ends are characterized by a type H1 hysteresis loop. Materials with complex pore structures consisting of pores with ill-defined shape and broad pore size distribution are characterized by a type H2 hysteresis loop. The type H3 hysteresis loop is observed for aggregates of plate-like particles which give rise to slit-shaped pores. Complex bimodal structures, consisting of both micropores (<2 nm) and mesopores (2-50 nm) often associated with narrow slit-like pores, are defined by a type H4 hysteresis loop. H4 loops have more pronounced uptake at low p/p_0 which is usually often associated with the filling of micropores. The type H5 hysteresis loop's distinctive form is associated with materials with pore structures characterized by both open and partially blocked pores.

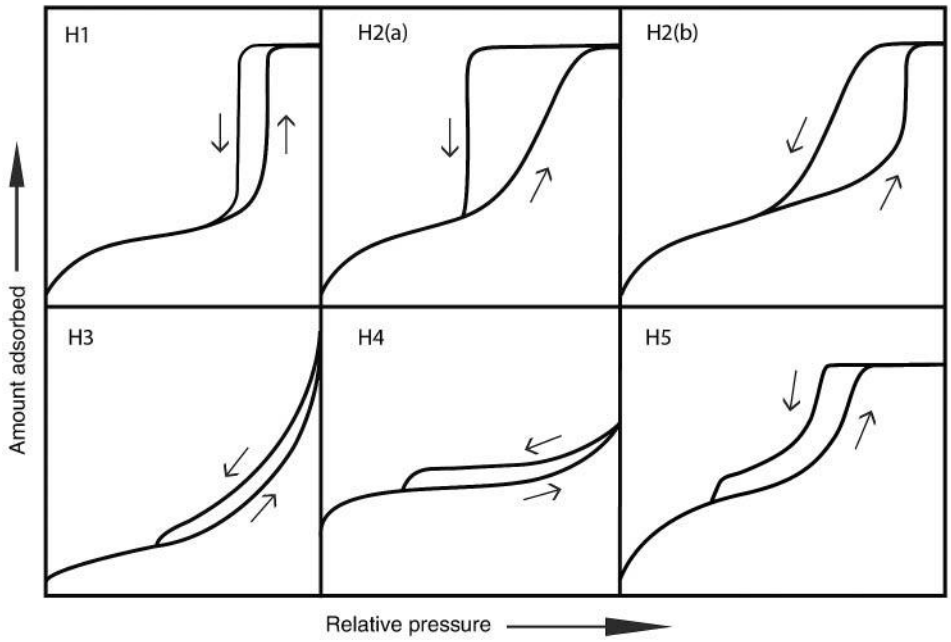

Figure 2.5: IUPAC classification of hysteresis loops.[5]

In the context of this work, in order to model materials that contain a combination of micro and mesopores, it is necessary to maximize *v* values in this p/p_0 range. Information on the physical properties is possible through examining pore volume and pore size distribution.

BET analysis was performed on a Micromeritics 3Flex surface characterization analyser using a multipoint Ar adsorption method. Prior to use, the solid samples were degassed (200 °C, 6 h) under vacuum. Adsorption isotherms were obtained at 77 K and analysed using

BET methods. Additional analysis of the adsorption isotherms by the DFT method allowed the pore sizes and volumes of various aluminosilicates to be measured.

2.5.2 Powder X-Ray Diffraction (XRD)

X-ray diffraction is a bulk analysis technique based on the elastic scattering of X-ray photons by atoms in crystalline, ordered structures. For a powdered sample, the XRD pattern is acquired using stationary X-ray source and a moveable detector, which records the intensity of the diffracted X-rays as a function of the angle, 2Θ between the incident and diffracted X-rays. The interaction between the incident monochromatic X-rays, a Cu Kα source, with the crystal lattice leads to the production of X-ray diffraction patterns as the X-rays are scattered by neighbouring atoms which results in either constructive or destructive interference. The scattered, in-phase, monochromatic X-rays give rise to constructive interference and satisfy the Bragg relation (Fig 2.5 and Equation 4).

$$n\lambda = 2d \sin(\Theta) \qquad (4)$$

Whereby:

n = Order of reflection (an integer)

λ = Wavelength of incident X-ray radiation

d = the distance between two lattice planes

Θ = Angle of diffraction between incident and scattered radiation

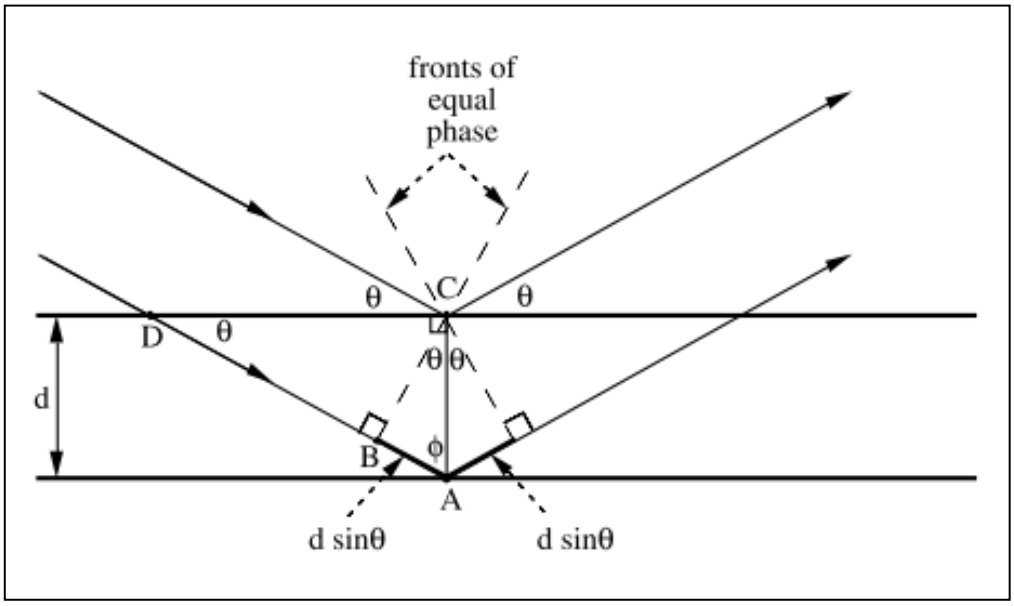

Figure 2.6: Reflection of X-rays in a crystalline material as defined by Bragg's Law.

The ability to record a diffraction pattern of a powder relies the condition that at any given time a number of individual crystallites will be orientated at the correct angle to allow constructive interference to occur, and thus produce a diffraction pattern. Rotation of the sample during analysis can be used to enhance the number of particles that contribute to the diffraction pattern. The random orientation of the crystallites in a powdered sample results in a diffraction cone otherwise referred to as the Debye-Scherrer diffraction ring. Consequently, the crystallite size of a particular phase can be calculated using the Debye-Scherrer equation (equation 5).

$$\beta_K = K\lambda/(d_{hkl}\cos\Theta) \qquad (5)$$

Where:

d_{hkl} = Crystallite size

β_K = Peak width

K = Shape factor

λ = Wavelength of radiation used

Θ = Peak position

Though XRD analysis is a powerful tool for crystallite size and phase analysis it encounters limitations when there is a lack of sufficient long-range order rendering it unsuitable for

the detailed study of amorphous materials. Moreover, sufficiently small particles (>5 nm) are problematic as they fall below the XRD detection limit. In such cases, measured peaks become ill-defined resulting in broad peaks that merge into the background signal.

XRD Analysis was performed on a (θ-θ) PANalytical X'pert Pro powder diffractometer equipped with a Ni filtered CuK_α radiation source operating with an applied accelerator voltage of 40 keV and a current of 40 mA. Patterns were recorded over the range 10-80 ° 2θ using a step size of 0.016 °. Analysis was performed using a back filled sample holder or with the sample dispersed on a silicon wafer when limited sample was available. The produced patterns were compared against reference patterns from the international centre for diffraction data (ICDD).

2.5.3 X-ray Photoelectron Spectroscopy

XPS is a surface-specific technique based on the photoelectric effect which provides information on the elemental composition and oxidation states of atoms present in a given material. The photoionization of the sample occurs as the constituent atoms absorb photons with sufficient energy and wavelength, hν, where h is Planck's constant, from a monochromatic X-ray source. This is followed by the displacement of a core or valence electrons with a specific binding energy (E_B) from the atom characterized by a specific kinetic energy (E_K).

$$E_K = h\nu-(E_B-\phi) \qquad (6)$$

The work function (ϕ) is an important consideration given that for the process to take place the ionisation energy must be greater than or equal to the work function. The binding energy characteristic to the specific emitted element can be determined by measuring the kinetic energy of an emitted photoelectron. The intensity of each peak recorded is proportional to the amount of emitted electrons while the binding energy of each peak relies on the oxidation state and local environment of the sample. An XPS spectrum is therefore a plot of the intensity of emitted photoelectrons as a function of their binding energy. This allows for the determination of the elemental composition of a given sample.

X-ray photoelectron spectroscopy (XPS) measurements were performed using a Thermo Scientific K-α^+ spectrometer. The samples were analysed using a monochromatic Al X-ray source operating at 72 W (6 mA at 12 kV), with the signal averaged over an oval-shaped area of approximately 600x400 µm in dimension. Data were recorded at pass energies of 150 eV for survey scans and 40 eV for high resolution scans with a 1.0 eV and 0.1 eV step size, respectively. Charge neutralisation of the sample was achieved using a combination of both low energy electrons and argon ions (less than 1 eV energy) which gave a C1s binding energy of 284.8 eV. All data were analysed using CasaXPS (v2.3.20) using Scofield sensitivity factors and an energy exponent of -0.6.

2.5.4 Thermogravimetric Analysis (TGA)

TGA is an analytical technique which measures changes in mass as a function of temperature or time under a variable gas atmosphere (i.e. Air, N_2). The technique can be combined with Differential scanning calorimetry (DSC) with the obtained TGA profile revealing the nature of the decomposition and phase changes with either absorption (endothermic) or evolution (exothermic) of heat measured. The TGA profile provides valuable qualitative and quantitative information as volatile products result in mass loss while oxidation or adsorption results in mass gain. When compared to reference materials, deduced observed mass changes at precise temperatures are associated with characteristic mass changes for specific adsorbents and known phases. This leads to the identification and quantification of adsorbents or species existent in a given sample. Therefore, the TGA profile provides information on decomposition, transformations and other reactions that occur as the temperature ramp is applied.

TGA analysis was carried out to study the material's thermal stability and the fraction of volatile components which decompose upon thermal treatment by monitoring the weight change that occur due to heating at a constant rate. In the context of the amorphous silica-alumina and their precursors, this information aided the determination of the temperature required for calcination of the precursor to the final mixed metal oxide material.

TGA was performed using a Labsys TG-DTA/DSC analyser. 10-60 mg of the sample was loaded into alumina crucibles, heated from ambient temperature to 700 °C (at 10 °C min^{-1}) in a flow of synthetic air or N_2 (50 ml min^{-1}) and held for 10 min before cooling. For each specified run, a blank run was first carried out and the results were subtracted from the relevant data to remove buoyancy effects. Mass losses were recorded as a percentage of the total mass of the sample.

2.5.5 Ammonia Temperature Programmed Desorption (NH_3-TPD)

TPD determines the amount and strength of adsorbed species on a given solid sample based on its desorption temperature and is an extremely powerful tool for screening total acid site strength, concentration, and density in solid acid catalysts. In a TPD experiment, residual moisture is removed from solid samples through a purge at an elevated temperature then adsorbate gas is adsorbed on the solid sample at low temperature and flushed with an inert gas to remove excess adsorbate gas. The thermal pre-treatment ensures the removal of any residual water or solvent. Following adsorption only the adsorbed species remain on the solid sample and throughout this thesis, 10 % NH_3/He adsorbate gas was used. Then the sample is sequentially heated firstly at constant temperature to remove physisorbed adsorbate species, and secondly linearly in an inert gas flow to remove chemisorbed adsorbate species. The outlet gas is monitored on-line with a thermoconductivity detector (TCD). Finally, TPD profiles are obtained by plotting the signals from the TCD as a function of temperature whereby the intensity of the TPD peak is dependent on the number of adsorbed adsorbates on the material surface. The total number of acid sites were calculated according to equation 7:

$$\text{Acidity } (NH_3\ \mu\text{mol}\ g^{-1}) = \frac{\left(\frac{Integrated\ area}{NH_3\ Response\ Factor}\right)}{g_{catalyst}} \qquad (7)$$

Ammonia temperature programmed desorption (NH_3-TPD) was carried out on a ChemBET TPD Quantachrome equipped with a TCD. Each sample (50 mg) was place in a quartz U-tube and underwent a pre-treatment under He flow (50 ml min^{-1}) for 1 h, at 400 °C with a heating ramp of 10°C min^{-1}. After cooling, to 30 °C, the sample was saturated with 10% NH_3/He (50 ml min^{-1}) for 15 min. After purging with He for 1 h at 100 °C the sample was

cooled to 30 °C, the temperature was ramped from 30-900 °C, with a heating ramp of 10°C min^{-1}, under a He atmosphere (50 ml min^{-1}). The TCD signal of the desorbed ammonia was used to evaluate the ammonia uptake.

2.5.6 Scanning Electron Microscopy (SEM)

SEM is a powerful analytical technique which allows for the observation of elemental compositions, structure and morphology of materials. The improved resolution is due to a short wavelength, highly focussed beam of accelerated electrons which scans the surface of the sample generating 2D images of small areas. In SEM, when the electron beam is focussed on an area of a sample known as the interaction volume and the interaction produces a 'teardrop'-shaped interaction volume. A number of interactions occur between the incident electrons and the material surface**.**

Backscattered electrons (BSEs), produced from the elastic scattering of electrons from the surface of the sample, are high energy electrons whose intensity are dependent on the atomic number and the electron beam acceleration voltage. The inelastic scattering of electrons causes the emission of low energy, secondary electrons (SEs) from the sample surface which are characterized by low depth penetration. The SEs detected in a serial manner to provide topological and morphological imaging information meanwhile BSEs provide compositional contrast between elements.

2.5.6.1 Energy Dispersive X-Ray Spectroscopy (EDX)

EDX is an analytical technique used to identify the elemental compositional of materials and catalysts from spatially resolved x-rays emitted from the interaction of the primary electron beam with the sample. The scattering of electrons results in the formation of electron holes and the concurrent emission of X-rays as the electron holes are filled. The formed x-rays' energies correspond to the energy difference between the two shells and the intensity and energy of the x-rays are compared to the emission spectra of known elements.

2.5.7 Transmission Electron Microscopy (TEM)

TEM uses electron accelerating voltage for the microstructural characterisation of materials including and not limited to lattice spacings, crystallinity and morphologies. This is made possible by several operating modes with brightfield and darkfield microscopy being the most useful forms of diffraction contrast imaging. Similar to SEM, this type of microscopic technique uses high energy, primary beam of electrons that pass through the condenser to produce parallel rays that impinge on the sample.

A bright field image is generated based on diffraction contrast in brightfield imaging mode which detects electrons not diffracted by the sample producing a two-dimensional projection of the sample depending on differences in crystallinity. On the contrary, the dark field imaging mode generates images obtained from the diffracted electron beam. Using the De Broglie wavelength (equation 8) from the wavelike characteristic of the incident filament and accelerated electrons, elucidates the comparability of the wavelength to atomic dimensions:

$$\lambda = h/p = h/(mv) \qquad (8)$$

Where:

λ = de Broglie wavelength of an electron

p = momentum of an electron

h = Planck's constant (6.6×10^{-34} Kg m^2 s^{-1})

m = the mass of an electron (9.1×10^{-31} Kg)

v = velocity of an electron (typically in the 1×10^6 m s^{-1} range)

Intensifying the operating voltage increases the spatial resolution, with point-to-point resolutions in the sub nanometre range achievable with voltages approaching 400 keV. The intensity of diffracted electrons across a thin specimen, namely the diffraction contrast, is measured and shown as a two-dimensional representation of the material's microstructure.

This method provides exceptionally high magnification and allows of both images and diffraction patterns from individual samples by variations in the intermediate lens'

excitation. This operation allows for the detector to view a selected area electron diffraction (SAED) pattern which can be interpreted both qualitatively and quantitatively to specific crystal phases and orientations.

2.5.8 Magic Angle Spinning Nuclear Magnetic Resonance (MAS-NMR) Spectroscopy:

MAS-NMR is a solid-state spectroscopic technique that provides information on the chemical environment of atoms and allows for structural determination of a given material. The technique can be applied to multiple atomic nuclei in heterogeneous materials, provided the nuclei possess an uneven number of protons and/or neutrons. The atomic nuclei spin about an axis resulting in an induced magnetic moment. Nuclear spin is quantized by the quantum number I, with characteristic integer or half-integer values dependent on the number of unpaired protons and neutrons in the nuclei of interest. In the absence of an applied external magnetic field the nuclei are oriented randomly in equal population in two possible degenerate spin states referred to as α and β spin states ($m_s = +1/2$, $m_s = -1/2$). There are 2I + 1 levels associated with the nuclear spin and when placed in an external magnetic field of strength H_0, the nuclei adopt one of two orientations either aligning with (lower energy, α spin state) or aligning against (higher energy, β spin state) with the external magnetic field. These different energy states afford the necessary conditions for spectroscopy as irradiation of solid samples with a radiofrequency pulse excites a lower energy state nucleus to the higher energy state. The magnetic field is held constant, and a radiofrequency (RF) pulse of short duration excites all nuclei simultaneously. This pulse covers a range of frequencies, and each individual nucleus absorbs the required frequency to spin flip such that α nuclei spin flip to the β spin state in resonance with the applied radiation, hence the terminology nuclear magnetic resonance. The relaxation phenomenon transpires whereby the nuclei return to their original lower energy state and a pulse of radiofrequency electromagnetic radiation is emitted from the sample and measured. As the nuclei relax, they produce a complex Free Induction Delay (FID) signal. This signal is mathematically processed by a Fourier Transformation operation decomposing the time-domain signal (intensity-vs-time) into its constituent frequencies (intensity-vs-frequency).

In heterogeneous solid samples, the electronic distribution is different around each nucleus, depending on the presence of electron-donating or electron-withdrawing groups around it, polarity of bonds or hybridization of attached atoms. Therefore, each nucleus experiences a slightly different magnetic field according to its chemical environment which results in a small variation in the resonant frequency of each nucleus. This explains the presence of multiple peaks for each type of nucleus, through which unique electronic environments give each nucleus a characteristic resonance frequency. In particular, by focusing on a small frequency window specific to individual nuclei provides structural information on the chemical surroundings of a nucleus. In doing so, identification of the local environment and dynamics (coordination number and geometry) is possible as each type has a characteristic chemical shift. However, in solid samples line broadening effects influence the NMR spectra and are eliminated by rapid spinning (10 kHz) about the *magic spinning angle* (Θ = 54.7°). This action mimics the rapid molecular motions in liquid samples permitting higher resolution spectra to be obtained.

Conventional 1D spectra are plots of intensity vs frequency however for certain nuclei, such as ^{27}Al, 1D spectra are too difficult to analyse because of signal overlap. Two dimensional (2D) homonuclear correlation spectroscopy identifies correlations between nuclei of the same type. Homonuclear 2D NMR experiments are *de facto* better resolved. In 2D NMR, intensity is plotted as a function of two frequency coordinates F1 (x-axis) and F2 (y-axis). This allows additional resolution of the spectrum in the second dimension. Moreover, peaks are displayed as contour plots in which the intensity is represented by contour plots, each of which are correlation signals representing coupling interactions between two different nuclei.

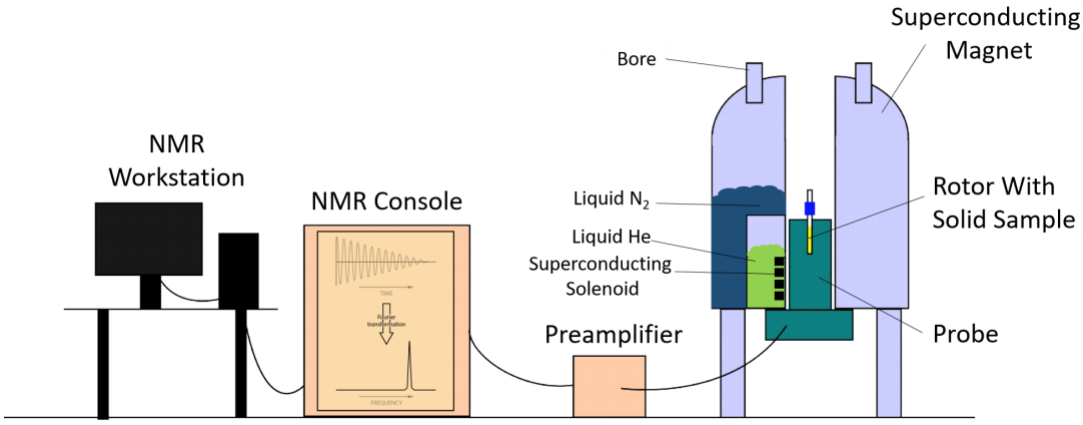

Figure 2.7: Schematic of the NMR instrument used for multinuclear MAS NMR experiments.

One dimensional (1D) ^{27}Al and ^{29}Si MAS-NMR measurements were performed during this study to assess the local structure of a number of amorphous silica-alumina materials with structure-performance relationships relating to the non-oxidative dehydrogenation of propane in mind. Samples were run on a Bruker Avance III NMR spectrometer (9T) operating at frequencies of 400 MHz controlled by the Bruker Topspin™ software. Tetramethylsilane (TMS) was used as an external Si reference and an aqueous solution of 0.5 M aluminium nitrate [$Al(NO_3)_3$] as an external Al standard reference.

Additional analysis of the connectivity within the solid samples through tracing of the J-coupling between various aluminium environments was investigated further with two-dimensional multi-quantum MAS NMR (2D MQMAS NMR). ^{27}Al 2D MQMAS NMR spectra of the samples were measured with a Bruker Avance III NMR spectrometer (9T) operating at frequencies of 400 MHz with an Yttrium aluminium oxide (YAG) external standard reference. Experiments were conducted under MAS conditions, using a Bruker 7-mm H-X double-resonance probe head and zirconia rotors with Kel-F® caps spun in air at 10 kHz at 298 K, using a previous method.[6] NMR line shape analyses were conducted using the Bruker Topspin™ software.

2.5.9 Fourier Transform Infrared (FTIR) spectroscopy

2.5.9.1 Pyridine adsorption based Diffuse Reflectance Infrared Fourier-Transform Spectroscopy (Pyridine-DRIFTS)

Diffuse reflectance infrared Fourier-transform spectroscopy (DRIFTS) is a surface localised spectroscopic method capable of providing chemical and structural information for numerous materials. When incident radiation interacts with the molecules in a given sample, they selectively absorb radiation of specific wavelengths causing a change of dipole moment. This results in the transfer of the vibrational energy levels of the molecules from the ground state to the excited state, a transition which has a characteristic vibrational energy and thus frequency. The number and intensity of the resultant absorption peaks are related to the number of vibrational freedoms and change of dipole moments, respectively. The incident radiation can be absorbed, penetrate the sample or is reflected in which case the random orientation of crystallites and particles within a powdered solid sample generates diffuse reflectance causing reflection in all directions. The reflected infrared radiation is measured and transition energies corresponding to changes in vibrational energy states for many functional groups located in the mid-IR range (4000-40 cm^{-1}) allow for identification of specific functional groups based on absorption bands in this region. In the context of this project, employing this technique serves as a viable route to distinguishing between Lewis and Brønsted acidities using suitable probe molecules. Pyridine, a basic probe molecule, is commonly used for qualitative and quantitative assessment of the strength, nature and concentration of surface acidity. Electron donation capabilities on the nitrogen atom give rise to a number of electron pair acceptor sites due to the dual Lewis and Brønsted base character of pyridine, **Fig 2.7**. **Table 2.2** summarizes the IR characteristics namely the range of vibrational modes, ν_{8a}, ν_{8b}, ν_{19a}, ν_{19b}, and positions associated with the interaction of adsorbed pyridine on different adsorption sites on acidic materials. The qualitative assessment of the nature and strength of acid sites is evaluated by inspection of the frequency of the ring vibrations which increase with respect to strengthening of the bonds as well as the temperature(s) pyridine desorption occurs.

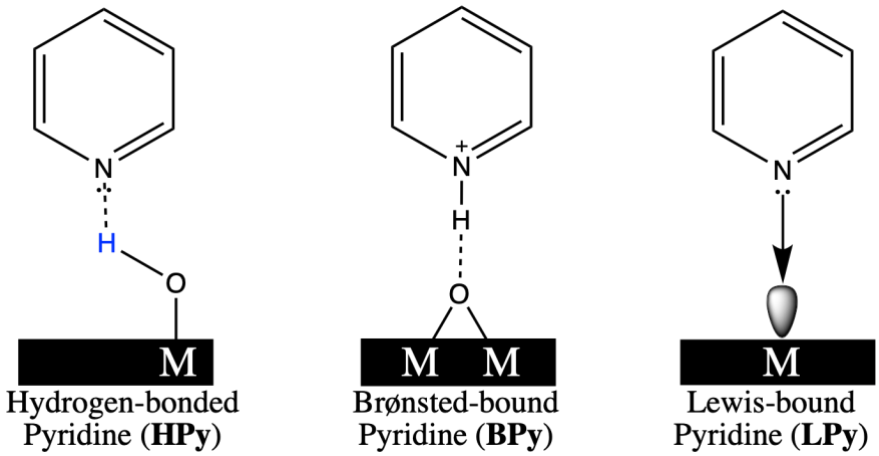

Figure 2.8: Configuration of pyridine adsorbed species on metal oxide surfaces.

In a Pyridine-DRIFTS experiment powdered solid samples are initially activated, under vacuum and elevated temperature, to dehydrate the surface of the material. This is particularly important considering the hygroscopic nature of aluminosilicates at atmospheric conditions. The solid sample is then cooled, a background spectrum is taken before exposing the solid sample to pyridine vapour until saturation, monitored *in situ* by a mercury cadmium telluride (MCT) detector on the DRIFT spectrometer. Preceding recording the IR spectra, the solid sample is outgassed at the same temperature in order to eliminate physisorbed pyridine molecules. This avoids undesirable spectral contributions on the *v*CCN frequency region of interest for acid site identification and distinguishment, 1400-1700 cm^{-1}, of chemisorbed species. Indications of available Brønsted acid sites, typically surface-OH groups as well as coordinated H_2O molecules, are the result of the protonation of pyridine molecules into pyridinium ions (BPy). Lewis acid sites, surface exposed coordinatively unsaturated metal sites, are formed through coordination of pyridine molecules to the surface (LPy). Hydrogen-bonded pyridine molecules (HPy) are formed through coordination with available surface O-H groups which are H-bond donor sites. The acid strength distribution can be determined through monitoring the desorption of pyridine as a function of temperature. Spectral interpretation assigns the vibrational frequencies of the infrared (*v*8a, *v*8b and v19a, v19b absorptions for the Bpy, LPy and HPy species, **Table 2.2**.

Table 2. 3: Assignment of infrared modes of pyridine as determined from model metal oxide systems.[7]

Mode	Symmetry	Wavenumber (cm^{-1})		
		Protonated Py (BPy)	Coordinated Lewis Adduct Py (LPy)	Hydrogen bonded Py (HPy)
ν_{8a}	A_1	1640	1633-1600	1600-1590
ν_{8b}	B_2	1620	1580	1590-1580
ν_{19a}	A_1	1500-1485	1503-1488	1490-1485
ν_{19b}	B_2	1540	1460-1447	1447-1440

DRIFTS measurements were recorded from 4000–1000 cm^{-1} at a spectral resolution of 4 cm^{-1} (64 scans) on a Bruker Tensor 27 spectrometer fitted with a mercury cadmium telluride (MCT) detector cooled by liquid N_2. A sample was loaded into the Praying Mantis high-temperature (HVC-DRP-4) *in situ* cell before exposure prior to evacuation under vacuum (pressure lower than 10^{-6} mbar) at 400 °C for 1 h. A background spectrum was recorded at 150 °C under N_2 flow (30 mL min^{-1}). The sample was then exposed to pyridine (8 mL) by the isothermal saturator (14.0 °C) under N_2 flow (30 mL min^{-1}) at 150 °C for 30 min. Excess adsorbate was removed by outgassing at 150 °C for 1 h prior to recording spectra.

2.5.9.2 Attenuated Total Reflectance (ATR)

The ATR technique is highly surface sensitive and is based on internal reflection where the infrared beam is totally reflected inside an ATR crystal which is well suited for evaluating strongly absorbing samples. At each point of reflection in the ATR crystal, an evanescent wave is created perpendicular to the surface of the ATR crystal. In order to achieve total reflection, the angle of incidence must be greater than the critical angle (**equation 9**):

$$\theta_{critical} = \sin^{-1}\left(\frac{n_2}{n_1}\right) \qquad (9)$$

Where:

θ = Critical angle

n_1 = ATR crystal refractive index

n_2 = Sample refractive index

An additional requirement for total reflection is that the ATR crystal must have a higher refractive index than the solid sample. Under these conditions, the infrared beam undergoes total internal reflection at the interface between the optically dense ATR crystal and optically rare solid sample. At the ATR crystal-solid sample interface, the evanescent field decays with distance from the crystal surface and has components in all spatial directions. The evanescent field is present at each interaction of the infrared beam with the interface and the solid material is sampled at each reflection. The intensity of the reflection is attenuated in any case where an infrared absorbing medium is in contact with the ATR crystal. According to equation 10 the amplitude of the evanescent wave's electric field declines exponentially with distance from the surface of the ATR crystal:

$$E = E_0 e^{-z/d_p} \qquad (10)$$

Where:

E = Electric field after exponential decline

E_0 = Electric field prior to exponential decline

z = Distance from ATR crystal surface

d_p = Penetration depth

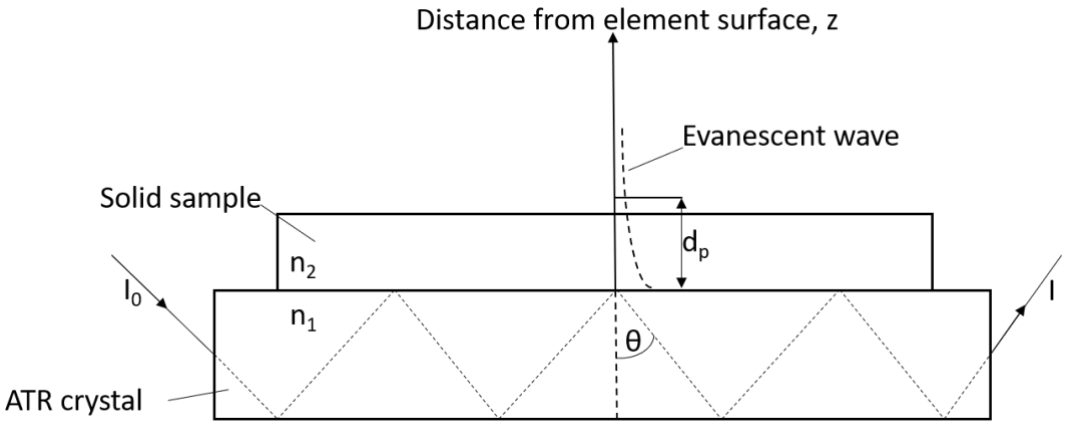

Figure 2. 9: Schematic of the ATR technique.

The penetration depth is indicative of the reach of the electric field from the surface of the ATR crystal and is typically in the micrometre to nanometre range which is ideal for surface analysis. It is approximated according to equation 12:

$$d_p = \frac{\lambda_1}{2\pi(\sin^2\theta - n_{21}^2)^{0.5}} \quad (12)$$

Where:

λ_1 = Wavelength of the infrared radiation inside the ATR crystal

θ = Angle of incidence

n_{21} = Ratio of the refractive indices

2.5.10 Microwave Plasma Atomic Emission Spectroscopy (MP-AES)

MP-AES is an atomic emission technique widely used to quantitatively determine the elemental composition of liquid samples. The technique currently offers simultaneous multi-analyte determination of elements, with detection limits at the ppm (parts per million) level. Typically, a sample is irradiated by an excitation source and the valence electrons of the constituent elements in the sample are excited to higher energy levels. As the valence electrons return to their ground states, they emit light in a characteristic pattern of wavelengths – an emission spectrum, which are directed into a scanning monochromator and recorded by a charge coupled device (CCD) detector. Microwave plasma (MP) is a high temperature source for atomic emission generated from nitrogen extracted from compressed air by a nitrogen generator through the microwave energy from an industrial magnetron. Plasmas composed of diatomic molecules have lower electron densities, which results in a greater interaction between the plasma and the sample aerosol.

In a MP-AES experiment, the nitrogen-based plasma is formed through a nitrogen-containing water trap and gas filter to the torch. An axial magnetic field and radial electric field focus at the torch and the result is a plasma which is able to reach temperature nearing *ca*. 5000 °C. Under these conditions, the liquid sample is injected with a high degree of control and accuracy *via* a peristaltic pump, nebulized to an aerosol in the spray chamber before being transported to the plasma where it dries, decomposes and is subsequently

atomised. In a standard procedure, commercially available calibration standards (typically 1000 ppm), are diluted to the required concentration and the response recorded.

In the context of this project MP-AES is an important tool for the determination of elemental composition, elemental ratios, leaching, and metal loadings in numerous heterogeneous catalysts and their constituents. Microwave Plasma Atomic Emission Spectroscopy (MP-AES) was used to determine the metal loading of the as-prepared catalysts and to evaluate metal concentration in solution in effluents recovered from mixed metal oxide synthesis.

Analysis was performed on an Agilent 4100 MP-AES equipped with a standard glass concentric nebulizer and cyclonic spay chamber. Elemental analysis was conducted by digesting the material (100 mg) in aqua regia (1 ml) to ensure total metal dissolution followed by dilution with distilled water (9 ml) prior to analysis. Depending on the analysis the signal response was recorded at two characteristic emission wavelengths for Si (251.6 nm, 288.2 nm) and Al (394.4 nm, 396.2 nm) and the resultant concentrations averaged. For the prepared catalysts, Pt weight loadings were measured by digesting the catalyst (100 mg) in aqua regia (1 mL) for 24 h to ensure total metal dissolution followed by dilution with distilled water (9 mL) prior to analysis. The signal response was recorded at two characteristic emission wavelengths for Pt (265.9 nm, 306.5 nm) and the resultant concentrations averaged. The concentration response of Si, Al and Pt were calibrated using commercially obtained stock reference standards, in all cases $r^2 > 0.999$.

2.6 Catalyst Testing

2.6.1 Propane Dehydrogenation

The gas phase non-oxidative dehydrogenation of propane was carried out fixed-bed flow quartz reactor. Propane, nitrogen, hydrogen and argon were connected to the reactor and controlled by individual mass flow controllers (MFC) (MKS). The reactor was loaded with 100 mg of catalyst (sieve fraction 212-300 μm), firmly packed between two plugs of quartz wool. Prior to the experiments the catalysts were reduced *in-situ* at 350 °C for 1 h in flow

of 10% H_2/Ar (50 ml min^{-1}). Then, H_2 was replaced by the PDH reaction mixture of C_3H_8: N_2: Ar, with a volumetric ratio of 5:5:90 at a total flow of 50 ml min^{-1}. The weight hourly space velocity (WHSV) was calculated as 12 h^{-1}. The product gases were analysed by an on-line GC (Agilent) equipped with a thermal conductivity (TCD) and flame ionization (FID) detectors, and HayesepQ column (2.44 m length and 2 mm internal diameter, allowing the separation of hydrocarbons up to C_3). Propane conversion (X) and product selectivity (S) were calculated according to Eqs. (1) and (2), respectively.

$$X_{C_3H_8}(\%) = \left[\frac{n^{in}_{C_3H_8} - n^{t}_{C_3H_8}}{n^{i}_{C_3H_8}}\right] \times 100\% \qquad (13)$$

$$S_i(\%) = \left[\frac{\beta_i}{\beta_{C_3H_8}}\right] \mathrm{x} \left[\frac{n^{t}_{i}}{n^{in}_{C_3H_8} - n^{t}_{C_3H_8}}\right] \times 100\% \qquad (14)$$

Where:

n^{in} is the molar flow of gas phase components initially (mol min^{-1})

n^{t} is the molar flow of gas phase components at specific sampling times (mol min^{-1})

β is the number of carbon atoms in product molecules (i.e. 1 for C_1 products, 2 for C_2 products, 3 for C_3 products). The coke selectivity was calculated, as the unaccounted carbon, after the sum of all the observed products was considered.

2.6.2 Methanol-to-DME

Catalytic performance tests for the methanol-to-DME reaction were carried out in a fixed-bed flow quartz microreactor system under atmospheric pressure and under isothermal conditions of 275 °C. For each test 100 mg of catalyst (sieve fraction 200 μm), was outgassed in a flow of pure nitrogen at 200 °C for 1 h. Methanol was introduced into the reactor *via* a N_2 bubbler placed in an isothermal saturator (11 °C), maintaining an total vapour pressure of 58.6 mmHg. The total flow rate was varied in efforts to obtain isoconversion of *ca.* 20 %. All inlet and outlet lines to the reactor (after the saturator) were heated at 150 °C, to prevent condensation in the lines. The reaction products were analysed using a gas chromatograph (Agilent) equipped with a methanizer and FID detector. The activity was calculated according to the following equation:

$$MeOH\ Conversion = \left[\frac{MeOH\ moles_{initial} - MeOH\ moles_{final}}{MeOH\ moles_{initial}}\right] \times 100\% \qquad (15)$$

The DME selectivity was calculated as a ratio (expressed in mole %) between the content of carbon in the product, DME, and the sum of carbon content corresponding to all observed organic products in the reaction:

$$DME\ Selectivity = \left[\frac{2DME\ moles}{(nCO_2\ moles + nCO\ moles + FA\ moles + 2DME\ moles)}\right] \times 100\% \quad (16)$$

2.7 References

1 M. R. Agliullin, V. P. Talzi, N. A. Filippova, V. R. Bikbaeva, S. V. Bubennov, T. R. Prosochkina, N. G. Grigorieva, N. Narender and B. I. Kutepov, Two-step sol–gel synthesis of mesoporous aluminosilicates: highly efficient catalysts for the preparation of 3,5-dialkylpyridines, *Appl Petrochem Res*, 2018, **8**, 141–151.

2 J. Huang, N. van Vegten, Y. Jiang, M. Hunger and A. Baiker, Increasing the Brønsted Acidity of Flame-Derived Silica/Alumina up to Zeolitic Strength, *Angewandte Chemie International Edition*, 2010, **49**, 7776–7781.

3 C. Cao, G. Yang, L. Dubau, F. Maillard, S. D. Lambert, J.-P. Pirard and N. Job, Highly dispersed Pt/C catalysts prepared by the Charge Enhanced Dry Impregnation method, *Applied Catalysis B: Environmental*, 2014, **150–151**, 101–106.

4 X. Zhu, H. Cho, M. Pasupong and J. R. Regalbuto, Charge-Enhanced Dry Impregnation: A Simple Way to Improve the Preparation of Supported Metal Catalysts, *ACS Catal.*, 2013, **3**, 625–630.

5 M. Thommes, K. Kaneko, A. V. Neimark, J. P. Olivier, F. Rodriguez-Reinoso, J. Rouquerol and K. S. W. Sing, Physisorption of gases, with special reference to the evaluation of surface area and pore size distribution (IUPAC Technical Report), *Pure and Applied Chemistry*, 2015, **87**, 1051–1069.

6 B. V. Padlyak, N. A. Sergeev, M. Olszewski and P. Stępień, The MAS NMR study of solid solutions based on the YAG crystal, *Nukleonika*, 2015, **60**, 417–421.

7 E. B. Wilson, The Normal Modes and Frequencies of Vibration of the Regular Plane Hexagon Model of the Benzene Molecule, *Phys. Rev.*, 1934, **45**, 706–714.

3 Understanding the synthesis of amorphous silica-alumina (ASA) *via* supercritical anti-solvent precipitation (SAS)

3.1 Introduction

The objective of this investigation was to develop and optimize a method for the preparation of homogeneous amorphous silica-alumina (ASA) materials, at low Si/Al ratios, *via* tailored supercritical anti-solvent (SAS) precipitation using supercritical CO_2. Amorphous silica-alumina (ASA) are heterogeneous compounds that contain a silica-alumina mixed phase as well as aluminium clusters and pure silica zones. They exhibit interesting surface chemistry which makes them of particular interest in heterogeneous catalysis.[1–3] Amorphous materials are disordered and cover a continuous range of compositions, as they are not constrained by a crystalline structure. This makes it possible to selectively tune their macroscopic properties.[4] In order to achieve this, a strategy to control nucleation and precipitation, which is affected by numerous parameters and conditions, had to be established. During this process the following experimental parameters were evaluated:

- Solvent composition
- Process temperature
- Process pressure
- Post-synthesis thermal treatment conditions
- Silicon and aluminium metal precursors

These parameters are known to have an effect on the precipitation process and resultant material properties.[5–7] In view of the application of these materials as components in bifunctional catalysts for the direct dehydrogenation of propane, a number of systematically different materials were prepared. As solid acid catalysts, their catalytic behaviour is usually attributed to their acid properties which arise from the functionalisation of silica by alumina resulting in aluminium atoms which are tetra- (Al^{IV}), penta- (Al^{V}) or hexacoordinated (Al^{VI}).[8–10]

It is commonly understood that ASAs are characterized by Brønsted acid sites of a lower density and strength in comparison to their crystalline counterparts.[11–14] This is accounted

for by differences in the silanol O to Al bond distance, which is much shorter (1.8–2.0 Å) in the case of zeolites compared to ASAs (2.94–4.43 Å).[15] The bulk and surface heterogeneity depend on the synthesis method and the Si/Al ratio. Variations in the synthesis method and other experimental conditions can influence the mixing between components of the amorphous silica alumina (ASA).

To achieve materials with different structural properties the elemental distribution, the Si/Al was altered and the following structural descriptors were identified using advanced characterisation techniques:

- Homogeneity: Homogeneous dispersion of silicon and aluminium
- Surface acidity: Type, strength, concentration, and density
- Atomic scale structure: Aluminium and silicon coordination environments
- Textural and morphological properties: BET surface area, porosity, crystallinity

The aim was to gain a fundamental understanding of the synthesized materials with the intention of contextualizing the influence of different structural descriptors on the observed catalytic performance. Different synthetic approaches yield ASA with systematic differences in porosity, morphology, composition, Al speciation and elemental distribution which directly influences acidity.[16] Thus, other analogous materials were synthesized as benchmarks to the SAS methodology, including traditional wet-chemistry (sol-gel) and state-of-the-art (FSP) methodologies, previously discussed in **Chapter 1.3**. In particular, overcoming the limitations of the sol-gel technique and potential synergies with the FSP technique were targeted throughout the optimization studies. To achieve this, a methodical experimental design was applied to determine the optimum synthesis conditions. The choice of the aforementioned experimental parameters was based upon information available in literature, and the experience acquired within the research group on mixed metal-oxide synthesis, detailed in **Chapter 1.5**.

3.2 Solution Precursor Selection: Effect of (Silicon and Aluminium) Metal Precursors

Supercritical Antisolvent Precipitation (SAS) process continues to show strong potential for forming nanoparticles with the current challenge of enhancing homogeneity and controlling crystallinity. These are considered important metrics in bypassing limitations observed with sol-gel processing allowing for improved surface acidity and density of defect sites. In this process, the simultaneous mass transfer between supercritical CO_2 and the organic solvent supersaturates the solutes resulting in precipitation out of solution. In view of mixed metal oxide synthesis, the solution containing the constituent metal precursors dissolved in an organic solvent requires homogenization and stabilization prior to injection into the supercritical fluid. Consequently, different chemical compounds were considered as metal precursors including silicon and aluminium alkoxides, acetylacetonates and acetates.

Visual indications of gel formation in the solution containing both Al-$(acac)_3$, and TEOS were seen. Solution stability, indicated by gel or precipitate formation upon aging, was much improved with the combination of aluminium acetylacetonate, Al-$(acac)_3$, and silicon tetraacetate. This was evident in complete dissolution of both metal precursors in solution. It is well understood that both silicon metal precursors are reported as equally utilisable precursors which react in ethanol in the absence of water to form silica gel and ethyl acetate.[17–20]

Metal alkoxides, the building blocks for materials obtained by sol-gel processing, are understood to have issues relating to chemical reactivity of the molecular precursors.[21] Additionally, the choice of molecular precursors influences the final microstructure of the resultant material. As such, the order of addition of the metal precursors was important. With this knowledge, the solubility tests revealed considerably better solution stability when the aluminium precursor was added to the solvent system, containing 5 vol% H_2O/C_2H_5OH, followed by the silicon precursor.

Initially, the SAS process follows a similar approach to the sol-gel method approach due to the requirement for complete dissolution of appropriate Si and Al metal precursors in an

appropriate mixed aqueous-organic solvent. To examine the Al and Si metal content lost during SAS precipitation, the SAS effluents from the metal solutions, with 1:1 atomic ratios of Si and Al (nominal Si/Al = 1), were recovered and analysed for Al and Si ppm levels using MP-AES analysis (Table 3.1). This is a useful metric indicative of metal precursor miscibility in $scCO_2$ under supercritical conditions. Of these, effluents collected and analysed from solutions containing the combination of aluminium acetylacetonate, Al-$(acac)_3$, and silicon tetraacetate were the most promising.

The MP-AES analysis shows a noticeable decrease in metal present in the recovered effluent when Al-$(acac)_3$, and silicon tetraacetate were used. The entrainer effect and lower reactivity towards hydrolysis are characteristic of multidentate ligands which are hydrolytically more stable than alkoxo ligands.[22] Analysis of the effluent after the precipitation of Al-$(acac)_3$, and TEOS precursors results in the presence of 50% of the Si content. This is attributed to alkoxide instability in their corresponding alcoholic derivatives which is known to lead to a high tendency of oligomerization of metal alkoxides in their solutions prior to the hydrolysis step. The result being complex oligomeric and polymeric structures of metal alkoxides-hydrolysis products, applicable under supercritical conditions.[23]

Experimentally, the addition of water in the solvent system was paramount as no precipitate was produced in the pure organic solvent. Since the two combinations of metal precursors yield different findings, it demonstrates that the choice of metal precursors drastically influences the precipitation dynamics. After careful consideration of the solubility and resultant yield (**Table 3.1**) all future experimental studies were based on solutions containing Al-$(acac)_3$, and silicon tetraacetate.

Table 3.1: MP-AES analysis of SAS effluents obtained from using various combinations of aluminium and silicon metal precursors to determine yields.

Iteration	Metal Precursors	Solvent Composition (*x* vol%)[A]	Solubility Limit (ppm)[B]	Metal in effluent (%)[C]
1	Aluminium acetylacetonate	5	416	8.3
	Silicon Tetraacetate		433	10.6
2	Aluminium Acetylacetonate	5	416	8.3
	Tetraethyl Orthosilicate		2022	49.6

A: *x* vol.% H_2O/C_2H_5OH solvent composition

B: Based on solubility tests conducted in 500 ml total solution volume, representing the concentration of Si and Al in the recovered effluent

C: Calculated from the comparison of metal concentration in initial solution relative to metal concentration present in the recovered effluent

The SAS precipitate was investigated further with thermogravimetric (TGA/DTA) analyses to probe the influence of temperature on thermal evolution in the precipitate. The results are presented in, Fig 3.1.

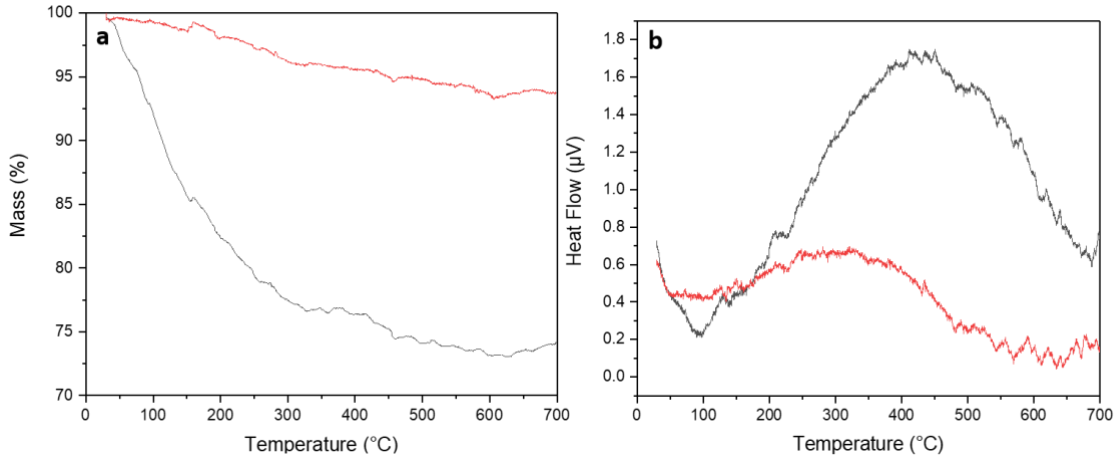

Figure 3.1: (a) TGA and (b) DTA profiles of as-precipitated SAS prepared ASA precursor (---) and resultant ASA (---).

Thermal profiles recorded from the precipitate show a three-stage decomposition pattern. The first stage is characterized with a 14.8 % mass loss, occurring up to 154 °C, which corresponds with the desorption of physisorbed water and ethanol accounting for the greatest rate of mass loss. The corresponding DTA profile displays an endothermic peak at 96 °C. The second stage, occurring up to 361 °C, is associated with the removal of volatile organics and chemisorbed water with an associated mass loss of 7.0 %. The DTA curve corroborates this process with a broad exothermic peak centred at 414 °C. The final stage, levelling out at 631 °C, is assigned to dehydroxylation reactions which corresponds with a 3.4 % mass loss and a corresponding endothermic peak in the DTA profile at 688 °C. It is expected that the formation of heterometallic (M-O-M') complexes occurs and central metal atoms are coordinated by hydroxo-, oxo-, and aqua-groups. Subsequent thermal treatment causes the dehydration of such metal oxide precursors leading to irregular amorphous oxide structures.

Following calcination, the resultant ASA's thermal profile exhibits a continuous decomposition with the total mass loss amounting to 7%. The DTA profile displays a broad endothermic peak centred at 85 °C attributed to the desorption of physisorbed water. The weight loss above *ca*. 200 °C is ascribed to dehydration and dehydroxylation reactions. This is supported by the exothermic peak centred at 322 °C.

A comparison of the TGA/DTA profile and total mass loss of the SAS precipitate with commercially obtained aluminium silicate hydroxide, aluminium hydroxide hydrate showed no similarities in the thermal profiles, Fig 3.2. Given the associated mass loss (*ca*. 25%) this can be assumed to be the direct result of the elimination of water molecules thus rendering hydroxyaluminosilicate as a viable precursor to the final mixed metal oxide. Therefore, using the TGA/DTA analysis, 600 °C was chosen as an appropriate calcination temperature.

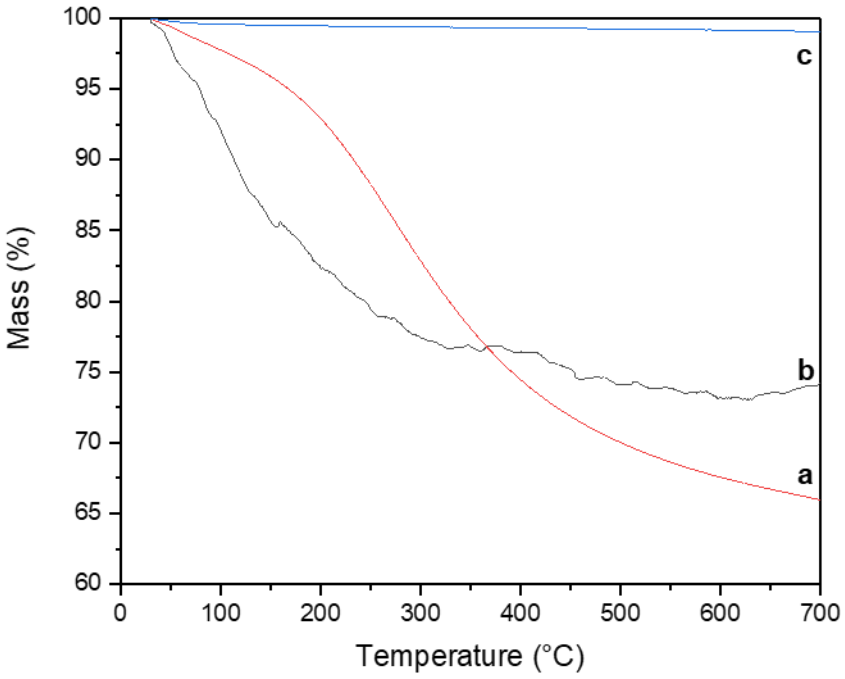

Figure 3.2: TGA profiles of (a) aluminium hydroxide hydrate, (b) SAS prepared ASA precursor and (c) aluminium silicate hydroxide.

The amorphous nature of the ASAs was confirmed by XRD patterns, Fig 3.3. The broad XRD peak detected at 2θ = 20-30° indicates amorphous silica. Absence of peaks corresponding to crystalline polymorphs of SiO_2 and Al_2O_3 further indicates that aluminium species are well dispersed in the amorphous silicon oxide network. This is an indication of effective thermal decomposition processes required for mixed metal oxide synthesis.

To induce crystallinity and probe thermal stability in the materials further, the calcination temperature was increased to 900 °C. The two calcined samples were labelled 'SAS-a', with a representing the respective calcination temperatures.

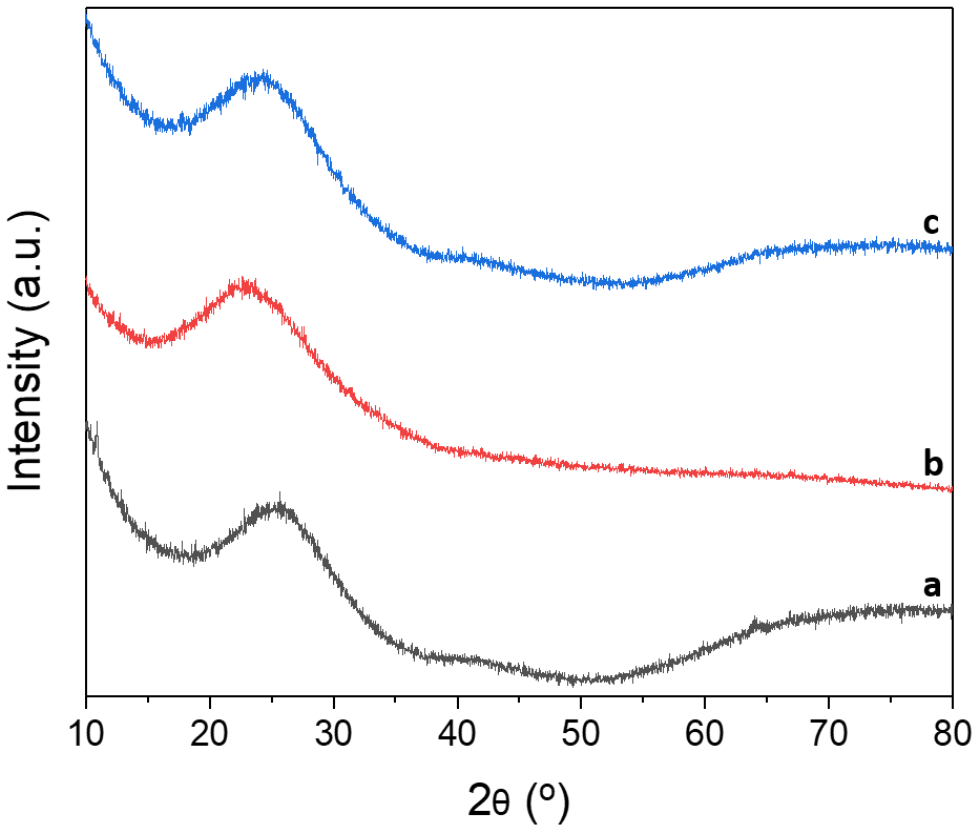

Figure 3.3: X-ray diffraction patterns of (a) ASA-PC; (b) SAS-600; (c) SAS-900

The higher calcination temperature had no effect on the resultant XRD profiles. XRD analyses performed on the untreated precipitate and on the calcined SAS particles revealed both were amorphous. This indicates that the material did not crystallize irrespective of post thermal treatment, Fig 3. This is significant in the context of industrial applications as high thermal stability is a prerequisite for catalyst components for the non-oxidative propane dehydrogenation reaction. Therefore, it is concluded that silica-alumina materials prepared using the SAS methodology are amorphous in nature, constituted by a random array of coordinated silica and alumina structures.

Surface areas of the precursor and calcined material were measured using BET analysis to analyse the effect of thermal treatment (Table 3.2). For the SAS-600 precursor, a BET surface area of 134 m^2 g^{-1} was observed. Comparison of the BET surface areas after calcination showed that the ASA resulted in a lower surface area (26 m^2 g^{-1}). The SAS

material has a lower BET surface area after calcination, which is consistent with the assumption that complete decomposition of the precursor to the metal oxide occurs.

Table 3.2: BET surface area of SAS-600 before and after calcination treatment. BET constant, C, values are calculated from the intercept and gradient values and indicate the strength of adsorbate-adsorbent interactions.

Precursor surface area		**Calcined surface area**	
$m^2\ g^{-1}$	**C value**	**$m^2\ g^{-1}$**	**C value**
134	35	26	17

In order to elucidate structural information, FTIR spectroscopy was used. The FTIR/ATR spectra of the samples calcined at 600 °C and 900 °C are presented in Fig 3.4. The 400-1200 cm^{-1} region, which contains all the important $\nu_{Al\text{-}O}$ and $\nu_{Si\text{-}O}$ related absorptions due to surficial groups, is presented. Both SAS-600 and SAS-900 display a sharp absorption peak centred at 1058 cm^{-1}, corresponds to the asymmetric stretching of Si-O-Si or Si-O which is typical for four coordinate silica (SiO_4).[24] The absorption peak at 430 cm^{-1} is known to be the consequence of the deformation mode of Si-O-Si, usually ascribed to the formation of amorphous silica. Meanwhile, the red-shifted shoulder appearing at the higher wavenumber of this absorption indicates the presence of Al-O-Si through cross condensation of Al and Si moieties.[25]

The stretching and bending modes of AlO_6 and AlO_4 moieties are expected in the 500-750 cm^{-1} and 750-850 cm^{-1} regions, respectively. Therefore, for both materials calcined at 600 °C and 900 °C, the absorption peaks centred at 678 cm^{-1} and 806 cm^{-1} are attributed to $\nu_{Al\text{-}O}$ of AlO_6 and $\nu_{Al\text{-}O}$ of AlO_4, respectively. The shoulder at 865 cm^{-1}, from the bending vibration of Si-OH groups, indicates the presence of Si-OH groups in both materials.[26] The presence of ν_{OH} of Si-OH at 3375 cm^{-1} in the spectra also confirms this argument. The aforementioned peaks corresponding to AlO_6 and AlO_4 sites are broad indicating general structural disorder.[27] This is in agreement with XRD analysis, and further suggests the disordered distribution of both AlO_6 and AlO_4 sites.

FTIR/ATR analysis of the ASA precursor reveals a few clear differences. Firstly, a number of surface hydroxyls were observed. The presence of the more prominent ν_{OH}, broad adsorption centred at 3300 cm^{-1} and shoulder peak observed at 890 cm^{-1} confirm this proposition. Moreover, the bands observed in the 1590-1290 cm^{-1} spectral region, ascribed to a mixture of ν_{C-C}, $\nu_{C=O}$, ν_{C-O} and ν_{C-C} vibrations become less pronounced with thermal treatment. The nature of this decreased intensity in the above-mentioned bands upon calcination further supports the formation of the mixed oxide as suggested by TGA/DTA and BET analysis. Additionally, the absorption at 1630 cm^{-1} represents the scissoring mode of physisorbed water and decreases in intensity following calcination.

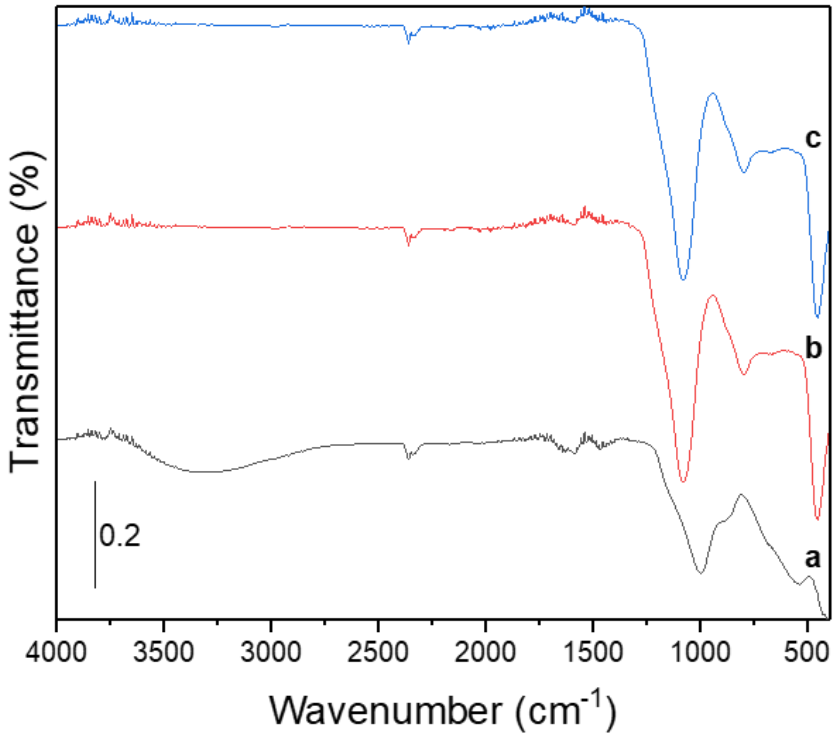

Figure 3. 4: FTIR spectrum of the as prepared (a) ASA precursor, (b) 600 ˚C and (c) 900 ˚C calcination treatment.

The SAS methodology produces precursors to ASA oxides through careful selection of Si and Al molecular precursors. It was concluded that to maximise material yield, the reactant

stoichiometries had to be carefully considered. Other considerations included the order of addition of the molecular precursors in a solvent system consisting of ethanol and water at 5:95 by volume, respectively, based on the lack of stability in pure organic solvents. Obtained precursor solutions were subject to careful control in the order of addition, drawing similar principles to those applied in sol-gel processing. The precipitate, consisting of a hydroxy-aluminosilicate precursor, were converted to thermally stable, amorphous mixed metal oxide upon post-thermal treatment, irrespective of temperature. Thus, the SAS method is highly advantageous and offers success in forming homogeneous amorphous aluminosilicates, at the micro and atomic scale.

The disordered, highly defective nature of the mixed metal oxide is confirmed by combined XRD and FTIR/ATR analysis. Additionally, the material prepared with a nominal Si/Al of 1 display structural disorder which is reflected in a number of pseudo-bridging Si-OH groups, present in FSP synthesized ASAs and high proportion of AlO_5 not present in crystalline counterparts.[28,29] This has implications on the surface acidity, which will be discussed in detail in proceeding sections an important characteristic for possible applications to acid-catalysed reactions.

3.3 The role of supercritical experimental parameters

To investigate the influence of different experimental parameters on the solvating power of the antisolvent and the precipitation mechanism, different experimental parameters were investigated.

3.3.1 Effect of process pressure

The process pressure of the solvent-CO_2 system determines the efficiency of the precipitation process due to its potential impact on the solvating properties of scCO_2. The chosen process pressures, 100-140 bar, ensured CO_2 was supercritical, which is required for faster mass transfer and droplet supersaturation in the presence of the antisolvent. With the absence of sufficient information relating to the mixture critical point (MCP) it was assumed this pressure range would sufficiently accelerate several associative processes resulting in faster Al and Si precipitation with more uniform dispersion. The

unusual physical properties and tuneability of $scCO_2$ while in the supercritical state, at constant temperature, is such that the solvating power of the fluid increases with increasing pressure.

In order to investigate the effect of the process pressure on the morphological, compositional and crystallinity characteristics of the ASA material a study was carried out with solutions precipitated at several pressures. The exact process pressures with the results of the specific surface area, total pore volume and Si/Al of the synthesized and calcined materials are presented in Table 3.3.

Table 3.3: Physical properties of the different samples with the variation of process pressure.

	Experimental Factor					**Material Property**		
	P/bar	**T/°C**	**Solvent Composition /xvol% H_2O**	**Calcination T/ °C**	**Calcination ramp rate/ °C min^{-1}**	**BET surface area /m^2 g^{-1}**	**Pore volume /cm^3 g^{-1}**	**Si/Al**
SAS-P100	100	40	5	600	5	28	0.09	1.0
SAS-P120	120	40	5	600	5	26	0.09	1.0
SAS-P140	140	40	5	600	5	19	0.07	1.1

Inspection of the specific surface area revealed a general trend in that the surface area decreased with increasing process pressure. The same trend was evident for the porosity, as anticipated. Interestingly, the EDX analysis (Table 3.3) also revealed a slight decrease in the Si/Al ratio with an increase in process pressure indicating negligible preferential precipitation of Si at 140 bar. This phenomenon can likely be related to the previously mentioned pressure induced supersaturation, mass transfer effect. It is possible that non-ideal mixing under supercritical conditions, suggested by Werling and Debenedetti, may be occurring.[30] The sensitivity of the antisolvent-solvent ($scCO_2$-5 vol.% H_2O/C_2H_5OH) as the

MCP is approached, from either the subcritical or the supercritical regime, is one of many determining factors contributing to differences in mass transfer. Additionally, Reverchon and co-workers reported the need for higher pressures as additional solute is introduced into the SAS system since the MCP shifts to higher pressures.[31]

Previous experimental studies showed the disappearance of the liquid surface tension of fluid jets injected in high pressure carbon dioxide concluding that at completely miscible conditions, where the solution and CO_2 mixture are above the MCP, the surface tension vanishes resulting in a "gas like" jet.[31–33] As a result, at pressures slightly above the MCP one phase mixing is favoured. Additionally, product morphologies and their relation to the phase behaviour of the system, especially the high pressure vapour liquid equilibrium (VLE) have been studied concluding that at completely developed supercritical conditions, much higher than the MCP, nanoparticles are methodically produced.[31,33,35]

In this work, the MCP was not explored but knowledge obtained from literature suggests that the choice of solvent and process pressure is also key due to its effect on the MCP. Finally, the mass transfer effects between the solute, solvent and antisolvent at supercritical conditions govern the precipitation mechanism with a: (i) diffusion-limited regime that produces a precipitation front and; (ii) nucleation-limited regime inside a whole homogenously-mixed droplet.[30,36]

No apparent morphological differences were observed with SEM analysis, Fig 3.5**.** This suggests control of both morphology and composition at the micrometre and sub-micrometre scale irrespective of process pressure. At 100-140 bar, the maximum droplet size is fairly consistent under isothermal supercritical conditions and is less sensitive to temperature. The solvent-antisolvent mixture is supercritical for all the pressure conditions studied. Therefore, the extent of swelling, and thus particle diameter is limited due to the small difference in density between $scCO_2$ and the cosolvent-solute solution.

The FTIR/ATR findings (Fig 3.6) confirmed the presence of SiO_4, AlO_4 and AlO_6 species evident in the $\nu_{Al\text{-}O}$ and $\nu_{Si\text{-}O}$ absorptions centred at 1040-1060 cm^{-1}, 790-810 cm^{-1} and 660-

680 cm^{-1} spectral regions, respectively. The presence of Si-O-Al through cross-condensation is confirmed by the shoulder 1060 cm^{-1} to the peak appearing at higher wavenumber. In the mixed metal oxide precursors of both SAS-P100 and SAS-P120 materials, surface hydroxyls are observed. Broad adsorption centred in the 3500-3300 cm^{-1} region and shoulder peak observed at 890 cm^{-1} attributed to ν_{OH} of Si-OH absorptions confirmed the presence of surface hydroxyls.

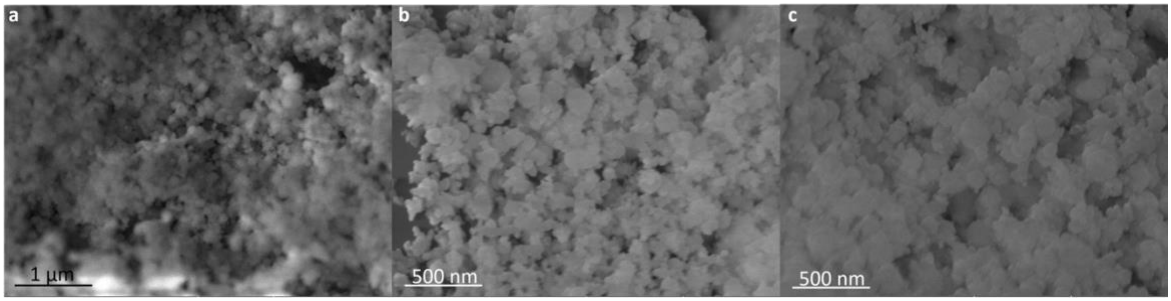

Figure 3.5: SEM images of a) SAS-P100; b) SAS-P120 and c) SAS-P140 materials after calcination revealing similarities in aggregated spherical morphology irrespective of process pressure.

In the IR spectrum, the bands observed at frequencies of 1589 cm^{-1} and at frequencies of 1500-1290 cm^{-1} are assigned ν_{C-C} coupled with a mixture of $\nu_{C=O}$, ν_{C-O} and ν_{C-C} vibrations, respectively. Thermal treatment also induces the release of volatile organics which is manifested in the decreased intensity of the associated bands in the FTIR spectra of ASA-100 and ASA-120. These peaks become less prominent upon calcination which suggests that the mixed oxide precursors of ASA-100 and ASAS-120 when heated to 600 °C undergo a greater degree of dehydroxylation.

It is widely understood that the absorption at 1630 cm^{-1} represents the scissoring mode of physisorbed water and decreases in intensity following calcination. However, for the SAS-140 ASA and its precursor there are no drastic peak shifts, appearances, or disappearances observed in the “material fingerprint” region (400−1500 cm^{-1}). It is unclear whether this is an indication of no thermally induced structural changes. The thermal treatment does result in a shift and greater intensity of the 660-680 cm^{-1} band, which is due to AlO_6 polyhedra, to a higher wavenumber. Interestingly, no absorption peak attributed to AlO_4

polyhedra is present in the SAS-140 ASA. This implies thermal treatment initiates crosslinking of SiO_4 and AlO_6 species.

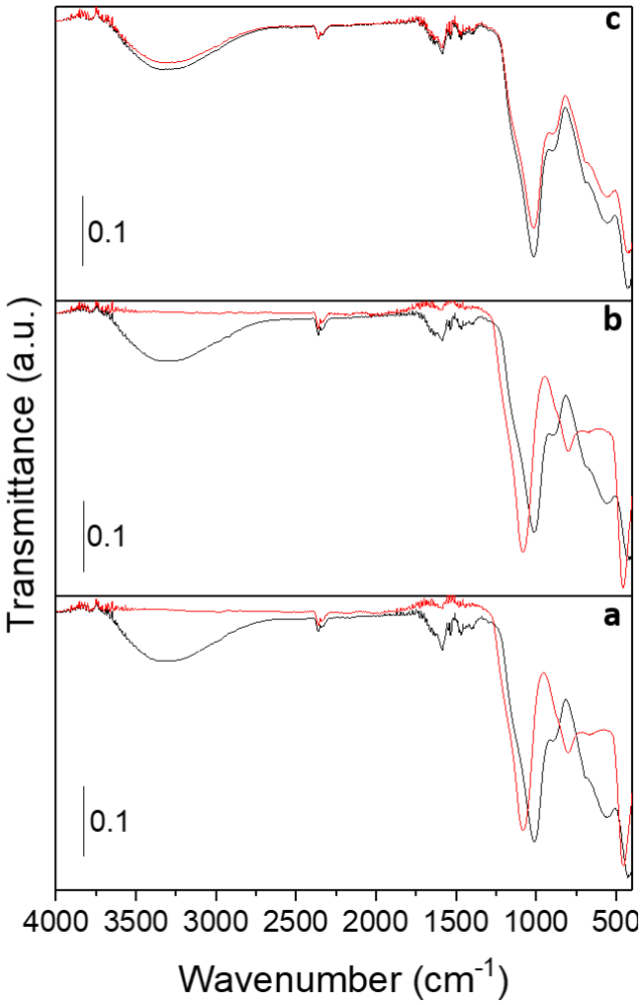

Figure 3.6: FTIR spectrum of the ASA precursors (---) and corresponding calcined ASAs (---) prepared at a) 100 bar; b) 120 bar and; c) 140 bar antisolvent process pressure.

3.3.2 Effect of Operating Temperatures

The solvation properties of $scCO_2$ are affected by temperature. In the antisolvent method, the formation of a single supercritical phase is the key step for the successful production of nanoparticles. Previous studies have shown the influence of several process parameters on particle diameter and particle size distribution.[37,38] Early work on the development of this process for the production metal oxide nanoparticles by Reverchon, Caputo and De Marco using a yttrium acetate and dimethyl sulfoxide model system reported sub-micron

yttrium acetate with mean diameters of 0.28 to 50 μm.[39] Variations in the operating pressure and temperature altered the MCP. Therefore, much like process pressure, the temperature is a key determinant required to vary dimensions and morphologies in the final product.

In this section, the effect of varying the process temperature was presented in order to evaluate the optimum temperature required to further enhance the solvating power of the antisolvent as well as any further insights relevant to material design. The results of the specific surface area, total pore volume and Si/Al of the calcined materials are presented in Table 3.4. The specific surface area and corresponding total pore volume data revealed variations otherwise not seen to the same degree with systematic variations in the process pressure. Under constant pressure, increasing the temperature decreases the density of the antisolvent. The results presented here also suggest the importance of the MCP for SAS operation. In particular, the possible connection between solvent–antisolvent phase behaviour and resultant particle characteristics. This is due to the surface area trend which is as follows: SAS-T35>SAS-T50>SAS-T40 (Table 3.4).

Due to the complexity of the trend, this experimental relationship and dependence is difficult to rationalise. Previous studies have ascribed faster mass transfer and a higher degree of droplet supersaturation as causations for higher nucleation rates and smaller particles.[30,32] The observed surface area and total pore volume's dependence on process temperature somewhat explains the experimental trend. However, the solvent-antisolvent mass transfer alone does not determine textural and morphological properties of the final product.

The results of the EDX analysis, presented in Table 3.4, show an inverse relationship between the process temperature and the Si/Al. Consequently, it was assumed that in order to achieve the theoretical composition, nominal Si/Al of 1, an appropriate process temperature of 40 °C was required. This is based on experimental data which suggests that the lower process temperature, 35 °C, results in slight Si enrichment in the final material. On the contrary, the higher process temperature, 50 °C, results in a measured Si/Al value

than is 25% below the nominal Si/Al. The temperature dependent inhomogeneity in the metal distribution the solvating power of the antisolvent, causing preferential precipitation of Si at higher temperature.

Table 3.4: Effect of process temperature on resultant material properties.

Sample	Experimental Factor						Material Property		
	Pressure (bar)	Temperature (°C)	Solvent Composition (vol%)	Injection Velocity	Calcination Temperature (°C)	Calcination Ramp rate (°C min^{-1})	BET surface area (m^2 g^{-1})	Pore volume (cm^3 g^{-1})	Si/Al
SAS-T35	120	35	5	6.5	600	5	67	0.04	1.1
SAS-T40	120	40	5	6.5	600	5	26	0.09	1.0
SAS-T50	120	50	5	6.5	600	5	35	0.02	0.7

SEM analysis portrays the dense networks of submicron diameter spherical aggregates and ruptured spheres present for SAS-T35 and SAS-T40 (Fig 3.7a-b). It is fair to assume that the differences in the particle diameters and the presence of ruptured spheres, inherent to the SAS methodology, are possible causes of the observed low specific surface areas. Noticeable differences in bulk morphology are observed when the process temperature is increased to 50 °C, in **Fig 3.7-c**. Therefore, the resultant materials' morphology display sensitivity to the process temperature. This is a consequence of changes in the precipitation mechanism whereby droplets near the MCP are more sensitive to operating conditions than systems at temperatures, and pressures, far from criticality.

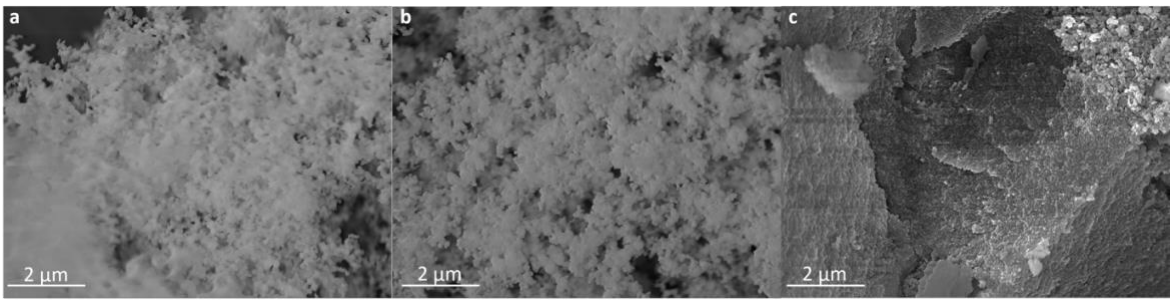

Figure 3.7: SEM micrographs of ASA materials produced at (a) 35 °C; b) 40 °C and (c) 50 °C process temperatures after calcination revealing similarities in aggregated spherical morphology irrespective of process temperature in the 35-40 °C region and mix of morphology when process temperature is varied to 50 °C.

FTIR/ATR analysis was carried out on the SAS prepared materials to prior to and after calcination to evaluate the structural changes. All materials were calcined using the standard set of conditions: 600 °C using a ramp rate of 5 °C min^{-1} and held for 6 h in a synthetic flowing air environment. For the precursors, the findings confirmed the presence of organic content, most likely originating from the residual acetate and acetylacetonate ligands, in the 1590-1290 cm^{-1} spectral region. These bands are assigned to ν_{C-C} coupled with a mixture of $\nu_{C=O}$, ν_{C-O} and ν_{C-C} vibrations, respectively. The presence of the ν_{OH} of Si-OH absorptions characterized by the broad adsorption centred at 3300 cm^{-1} and shoulder peak observed at 890 cm^{-1} suggested the existence of several hydroxyl groups. Upon calcination, spectra of the SAS-T35, SAS-T40 and SAS-T50 ASAs were moderately different particularly in terms of the relative intensities of the aforementioned bands. This indicates thermally induced dehydroxylation as well as combustion of residual organic compounds.

Moreover, whilst FTIR/ATR analysis of the calcined materials shows the presence SiO_4, AlO_4 and AlO_6 species evident in the associated ν_{Al-O} and ν_{Si-O} absorptions, the relative proportion of these absorptions differed (Fig 3.8). The relative intensity of the AlO_6 and AlO_4 bands expected in the 500-750 cm^{-1} and 750-850 cm^{-1} regions, respectively, is greater and is shifted to higher wavenumber by *ca.* 80 cm^{-1} in the case of SAS-T50. This is possibly a result of the higher Al content which in turn would result in stronger Si-Al-O linkages, evident in

the 1160 cm^{-1} shoulder peak. This structural change is a possible rationale for the observed variations in the SEM and EDX analysis.

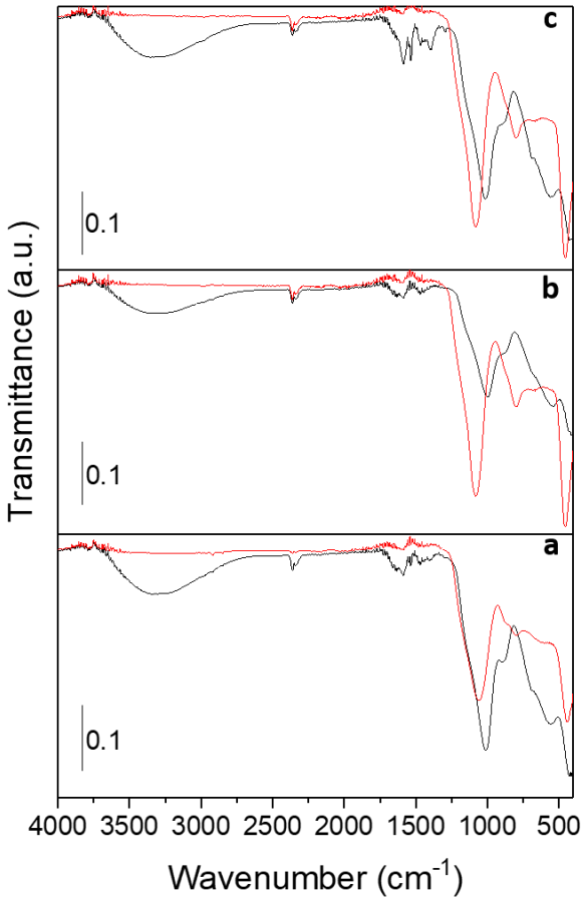

Figure 3.8: FTIR spectrum of the ASA precursors, denoted PC, (---) and corresponding calcined (---) ASAs prepared at a) 35 °C; b) 40 °C and; c) 50 °C antisolvent process pressure.

Moreover, MP-AES analysis was conducted in order to verify the conclusions drawn from the EDX and FTIR/ATR findings. Similar to the process pressure studies, the effluents generated from the synthesis procedure were collected and analysed for Si and Al concentrations, Table 6.

Table 3.5: MP-AES analysis of SAS effluents obtained from using various process temperatures to determine yields.

Material	Metal in solution (ppm)[A]		Yield (mol %)[B]
	Al	Si	
SAS-T35	3.0	7.4	91.1
SAS-T40	1.2	3.0	91.0
SAS-T50	1.3	3.2	95.3

A: Effluent collected and diluted in distilled water, based on a 1:10 (Effluent:H_2O) ratio prior to MP-AES analysis, after a supercritical antisolvent precipitation experiment with experimental parameters of; Pressure: 100-140 bar, Temperature: 40 °C, Solution Injection Velocity: 6.5 ml min^{-1}

B: Yields were calculated on a molar basis and corrected for the observed Si and Al from the recovered effluents.

For the SAS-T35, SAS-T40 and SAS-T50 materials, it is clear that a negligible amount of silicon and aluminium metal present in the effluent confirms the near complete precipitation of the metals. This result implies the increased preferential miscibility of the silicon metal in the antisolvent with increasing temperature. It therefore suggests that in order to achieve the required metal molar ratio, temperatures not exceeding 40 °C may be required.

3.3.3 Impact of calcination conditions

Literature comparisons show that SAS prepared amorphous silica alumina materials are characterized by lower surface areas in comparison to commercial counterparts and other synthetic methods. Calcination results in a redistribution of the surface aluminium species, an important process in determining the surface acidity. The diffusion of aluminium into the silica network generates the necessary $Si^{4+} \rightarrow Al^{3+}$ substitutions to induce Brønsted acidity.

Thus far, changing the operating conditions has had a small effect on the morphology of the calcined nanostructures such that their surface area and porosity are not yet satisfactory. Both properties can be tuned *via* calcination. At the same time, calcination process parameters such as temperature, ramp rate and atmospheric gas composition can be modified in order to reduce the micro- and nanosphere growth rate as well. The calcination temperature was varied and discussed with no change in the crystallinity observed.

In evaluating methods to further optimise material properties the calcination conditions were explored. An ideal candidate was the material synthesized using the following conditions: 120 bar, 40 °C, Solution Injection Velocity: 6.5 ml min^{-1}. The calcination conditions (600 °C held for 6 h in a synthetic flowing air environment) were maintained changing only the ramp rate from 5 °C min^{-1} to 1 °C min^{-1}. BET analysis revealed an increase in the surface area from 26 to 90 m^2g^{-1}, Table 3.7. The modification in the calcination ramp rate had a positive effect on the material's porosity, evident in the increased total pore volume of the resultant ASA.

Table 3.6: Physical properties of the different samples prepared *via* the variation of calcination conditions and the effect on the resultant material properties.

Sample	Experimental Factor						Material Property		
	Pressure (bar)	Temperature (°C)	Solvent Composition (vol%)	Injection Velocity	Calcination Temperature (°C)	Calcination Ramp rate (°C min^{-1})	BET surface area (m^2 g^{-1})	Pore volume (cm^3 g^{-1})	Si/Al
SAS-R-1	120	40	5	6.5	600	1	90	0.12	1.0
SAS-R-5	120	40	5	6.5	600	5	26	0.09	1.0

The materials calcined with the ramp rate of 5 °C min^{-1} presented the lowest surface area most likely due to the unsuccessful removal of residual volatile organics. On the contrary,

the material calcined with the modulate ramp rate, 1 °C min^{-1}, presented the higher surface area due to complete removal of residual volatile organic compounds. SEM analysis, used to further investigate morphological differences, reported similarities in the bulk morphological features of the resultant ASAs, Fig 3.9.

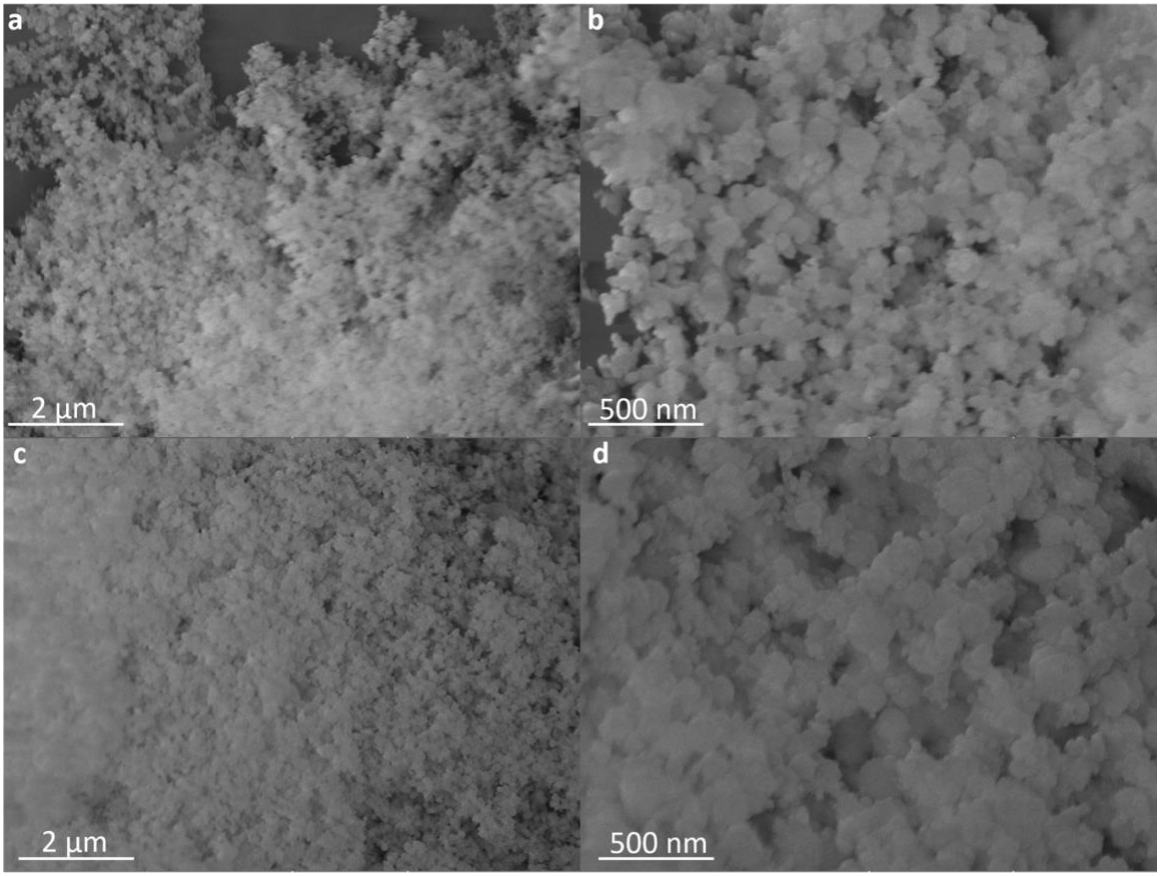

Figure 3.9: SEM micrographs of ASA materials calcined with calcination ramp rates of (a-b) 5 °C min^{-1}; and (c-d) 1 °C min^{-1} at 600 °C.

The thermal treatment is suggested to enhance the isomorphous substitution of aluminium and is a facile approach easily applicable in the preparation of the resultant ASAs.[40] The results indicate that the calcination process parameters, especially ramp rate, directly affects the structure of the resultant material. Therefore, the calcination ramp rate is one strategy in increasing the surface area which in the context of catalytic applications is a desirable structural parameter in a support of a bifunctional catalyst. Particularly, when functionalized, higher surface area supports are required to achieve high dispersion.

3.3.4 Conclusions of material optimization studies

At this point it is important to appreciate the fundamental chemical processes occurring under supercritical conditions in particular expanding on the previously discussed precipitation mechanisms (Chapter 1.5.1). This in turn could contribute towards the rational design of amorphous aluminosilicate preparation. Droplet behaviour under supercritical conditions is sensitive to, variations in the pressure and temperature. Therefore, the effect of temperature and pressure on mass transfer, and its importance in SAS operation, is clearly seen.

Reverchon and De Marco ascribed liquid jet break-up and surface tension vanishing at supercritical conditions as the processes in competition to produce spherical microparticles or nanoparticles.[41] Similarly, supersaturation is mainly consumed by nucleation and growth of particles. These processes occur simultaneously. It is therefore important to discuss these effects in context to the findings reported herein.

The observed morphological features, typically aggregated networks of sub-micron diameter particles with non-uniform dimensions, are largely consistent irrespective of experimental conditions. In order to produce sub-micron particles with narrow size distribution it is paramount to create uniform spatial concentration distribution in solution and a high degree of supersaturation. Thus, it is possible the observed non-uniformity in particle dimensions in the resultant ASAs stems from possible negligible insolubility or solute stability during the SAS preparation. Visual indications of the solute-solvent solution have not alluded to this. However, in the case of high process temperatures, for instance 50 °C, observed morphological differences originate from droplet behaviour under supercritical conditions. Droplets near the MCP are more sensitive to operating conditions than systems at temperatures, and pressures, far from the MCP. Reverchon and co-workers attributed morphological modifications to the superimposition of fast crystallization kinetics that can produce rough surfaces, nanocrystalline surfaces and spherical geometry collapse.[35]

Interestingly, as eluded by elemental analysis (see the Appendix), the resultant ASAs are largely homogeneous achieving the nominal Si/Al in most cases, with the exception of high process temperatures (50 °C). This suggests that the high super-saturation levels achieved in the SAS preparation of ASAs enables access to more intimately mixed metal oxides. Therefore, it is clear that preparation of ASA precursors by SAS precipitation is complex particularly given the limited knowledge on the MCP. Overall, this work has paved the way forward for further optimisation studies of the procedure.

3.4 Effect of water content

Hutchings and co-workers reported the addition of water co-solvent into the metal acetate solution in the preparation of hopcalite catalyst precursors using the SAS process.[42] The authors discovered that water addition changed the precipitation mechanism resulting in a change in particle morphology and the nature of the material produced. Similarly, Kondrat *et al*. conducted a similar study for the synthesis of zincian georgeite.[43] It emerged that systematic variations in the volumetric ratio between water and ethanol in the mixed (aqueous-organic) solvent, a component of the precursor solution, had a significant effect. The authors reported differences in the type and mixture of phases, crystallinity, chemical composition as well other physical and structural properties. In both studies, the inclusion of water in the precursor solution resulted in the formation of metal hydroxycarbonate species with the absence of water producing metal hydroxy-acetates. In each case highly disordered precipitates were produced following thermal treatment. These findings imply that optimum precipitation and facilitation of atomically mixed metal precipitates can be achieved in the presence of water in the SAS process.

Supersaturation is the driving force in precipitation in the SAS process. Thus far, experimental studies have revealed the requirement of water in the precipitation mechanism which may involve another process such as hydrolysis. Further studies within the same group resulted in a proposed anionic ligand exchange reaction generating carbonate anions which displace the acetate ligand, in the presence of water.[44] The authors reported the formation of the thermodynamically favoured hydroxycarbonate. In view of

further optimizing the synthesis strategy, and using the information gained on the synthesis procedure to this point, it was important to optimize the water content in the co-solvent.

A series of SAS materials were prepared with different concentrations of water present in the organic solvent. To elucidate the influence on water on subsequent precipitation the water content (by volume) in the organic solvent were systematically varied to 1%, 5 %, 7.5 % and 10 %. For brevity, these materials are denoted 'SAS-x%'. The corresponding surface area, pore volume and The BET surface areas, pore volumes and Si/Al are presented in Table 3.7

Table 3.7: Textural properties determined from Ar physisorption, Si/Al ratio determined from EDX analysis and surface acidity for a series of SAS ASAs synthesized with varying water concentration in the initial solvents.

Sample	Si/Al	BET surface area/ $m^2\ g^{-1}$	Pore volume/ $cm^3\ g^{-1}$	Acid site concentration/ $x10^{-4}$ mmol g^{-1}	Acid site density/ $x10^{-4}$ mmol m^{-2}
SAS-1%	1.0	11	0.09	3.3	0.3
SAS-5%	1.0	90	0.10	183	2.0
SAS-7.5%	1.0	98	0.12	600	6.1
SAS-10%	1.3	128	0.07	120	0.9
H-ZSM5	11.5	323	0.16	510	1.6

Incremental increases in the water content from 1 vol.% to 5 vol.% resulted in a near nine-fold increase in specific surface area from 11 $m^2\ g^{-1}$ to 90 $m^2\ g^{-1}$. A further 2.5 % increase in water content, totalling 7.5 vol.%, marginally increased the specific surface area to 98 $m^2\ g^{-1}$ with the largest surface area, 128 $m^2\ g^{-1}$, observed with the addition of 10 vol.% of water.

SEM analysis conducted to investigate bulk morphologies of the SAS-x% materials revealed a highly aggregated network of non-uniform spherical agglomerates. Interestingly, the diameters of the spheres increased with water content. The SAS-1%, SAS-5% and SAS-7.5% ASAs displayed sub-micron diameter spheres, Fig 3.10**.**

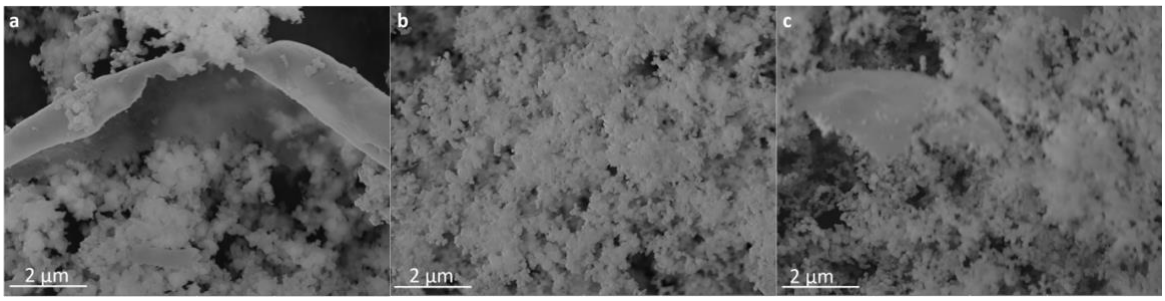

Figure 3.10**:** SEM micrographs of ASA materials produced with (a) 1 vol%; (b) 5 vol% and;(c) 7.5 vol% in water content in the aqueous-organic solvent system revealing spherical network of aggregates of varying diameter and ruptured microspheres.

However, the SAS-10% (Fig 3.11) ASA displayed a complex network of larger micrometre diameter spheres populated with an aggregated network of non-uniform spherical agglomerates. This phenomenon has been previously ascribed to differences in the mass density between the solute-solvent and the antisolvent.[41] Droplet behaviour has implications on the particle size. Droplets swell when the solute-solvent's mass density is greater than that of the antisolvent. Based on the SEM analysis this is suggested in the case of SAS-10%. On the contrary, sub-micron spheres are observed in materials with starting solutions constituted by water contents in the solvent up to 7.5 vol.%.

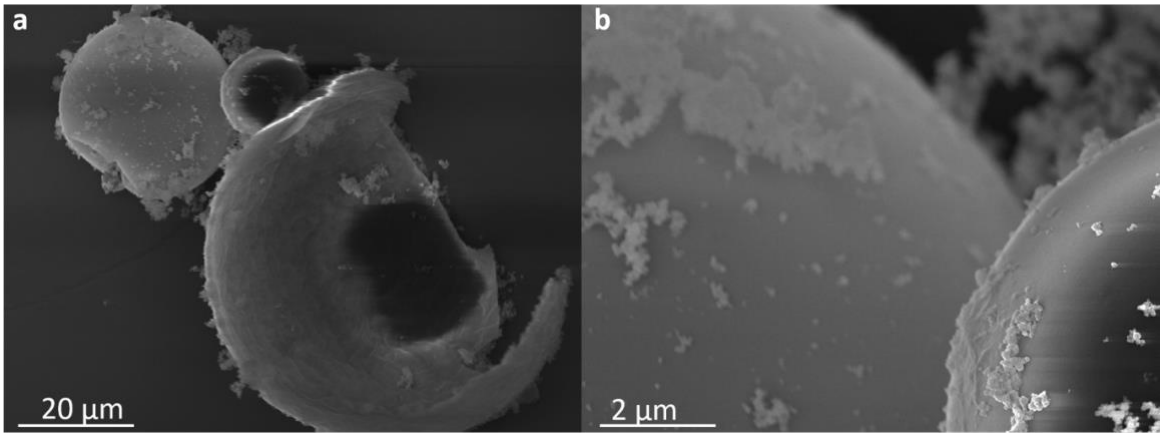

Figure 3.11: SEM micrographs of ASA materials produced with 10 vol% water content in the aqueous-organic solvent system revealing (a) microspheres of varying diameter with (b) the presence of a number of nano-diameter spherical aggregates.

Compositional analysis was conducted using EDX analysis. EDX analysis, reported composition similarities between the SAS-1%, SAS-5% and SAS-7.5% ASAs. The nominal and measured Si/Al in these ASAs were identical indicating bulk homogeneity on a micrometre scale, Table 3.8. However, the Si/Al of SAS-10% ASA suggested compositional differences to the above-mentioned materials displaying a Si/Al; indicative of a negligibly Si-enriched material.

Due to the resolution limitations of SEM analysis, TEM analysis was conducted to further investigate morphological properties of the resultant ASAs. Representative TEM micrographs of SAS-5% are shown in Figure 3.12 a-b. A network of aggregated nanospheres with non-uniform diameter as well as another “cloud” like, non-spherical morphology.

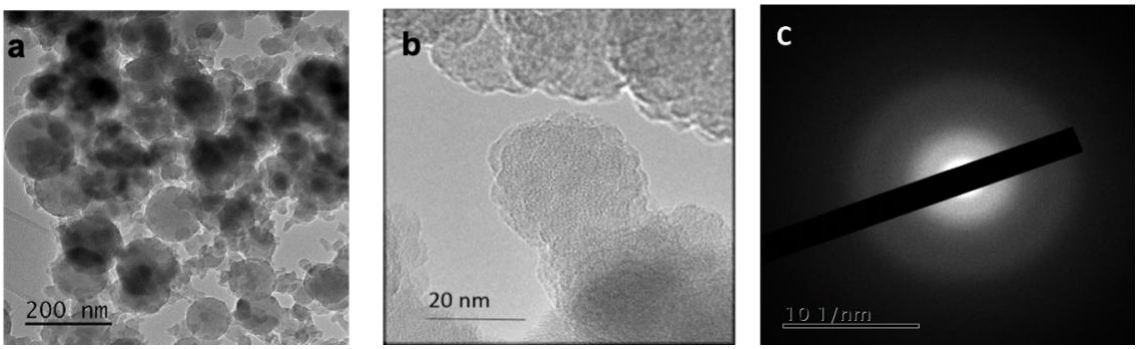

Figure 3.12: TEM micrographs of (a-b) SAS-5% displaying amorphous characteristics and (c) a SAED pattern also suggesting an amorphous material due to its diffuse rings.

The two different morphologies point to differences in the precipitation mechanisms. The morphological changes are attributed to supersaturation as well as the superimposition of fast crystallization kinetics that can produce spherical geometry collapse. Moreover, SAED analysis revealed that ASAs retained their amorphous character due to the absence of lattice fringes, Figure 3.12-c. Additionally, no nanocrystallinity was evident. In summary, the wholly amorphous and heterogeneity of the phase composition of ASA synthesis with SAS precipitation was confirmed by TEM. The TEM results are in good agreement with the observations of SEM and XRD results.

Through extensive characterization and knowledge gained from the above investigations the effect of these parameters on the resultant materials, the most impactful parameter, water content in the solvent system, was chosen.

At the present stage of this work, the major challenges requiring attention concern the enhancement of the low surface areas that characterize SAS materials. To date surface areas typically in the range 11-128 $m^2 g^{-1}$. The surface acidity is an important factor that influences the materials' catalytic applications. NH_3-TPD and pyridine-DRIFTS are two key characterisation methods that have been used to quantify the concentration and distinguish the types of acid sites present. After observing and quantifying the physical effects of changing a number of process parameters, the resulting surface acidity was explored with basic probe molecules.

For a quantitative determination of the total acid site concentration (Brønsted and Lewis acidity), NH_3-TPD has been used and the TPD curves are presented. The acid site strength is based on the peak position, Fig 3.13. The overall acidity, based on the integrated area of the desorption peak together with the total density of acid sites, normalised by the respective surface areas, are reported in Table 8.

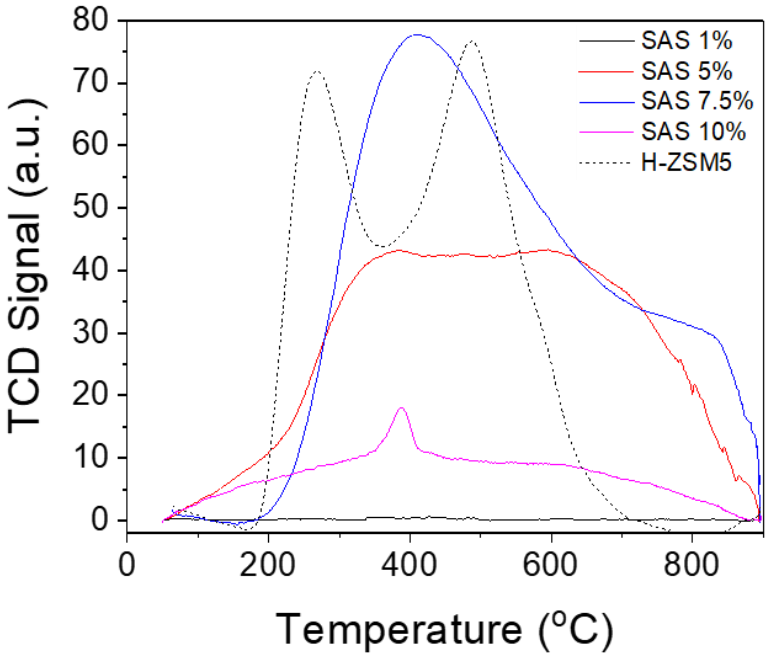

Figure 3.13: NH_3-TPD curves of SAS 1-10% materials and H-ZSM-5.

The TPD curves are asymmetric, it can be concluded that different solid-acid catalysts exhibited three types of acid sites: weak acid sites (130–290 °C), acid sites with moderate strength (290–540 °C) and strong acid sites (540–900 °C).

The weak acid sites are ascribed to weak Lewis acid sites, $Al(OH)_2^+$, $Al(OH)^{2+}$, weakly acidic hydroxyls, terminal Si-OH and adsorbed ammonia on non-acidic sites.[45] The high temperature peak is attributed to strong (Brønsted and Lewis) acid sites. Brønsted acid sites in ASAs are hydroxyl groups coordinated with trigonal aluminium atoms and can be converted to Lewis acid sites by dehydration at high temperatures. Due to the complex surface structure and overlapping features in the TPD curves the moderate strength acid sites are anticipated to have hybrid characteristics of both weak and strong sites. It is likely that the acid sites formed are hydroxyl groups and Lewis acid sites of various structures with numerous configurations. Perras *et al.*, suggested that ASAs constitute predominantly of a mixture of numerous pseudo-bridging silanols as well as a small fraction of bridging silanols.[46]

The overall acidity varies for the SAS-x% materials and so too do the temperatures at which NH_3 desorbs, evident in the different peak maxima. This implies varying distribution as well as strength in the acid sites, a product of the heterogeneous nature of the surface. SAS-7.5% displayed significantly greater acidity than the other SAS-x% materials. These findings suggest that the physical properties of these ASAs, such as specific surface area, pore volume as well as overall acidity, can be easily modified through systematic variation of water content. In particular, the lack of NH_3 adsorption in the SAS-1% is due to its low surface area and thus lower concentration of acid sites in comparison to the other SAS-x% materials. This approach provides a highly flexible route to a range of novel catalytic materials.

Pyridine-DRIFTS further probed the surface acidic properties of the SAS-x% materials by evaluating the ν_{CCN} frequency region, 1400-1700 cm^{-1}, due to the range of vibrational modes (ν_{8a}, ν_{8b}, ν_{19a}, ν_{19b}, and positions associated with the interaction of adsorbed pyridine on different adsorption sites on acidic materials. Characteristic bands in the resultant Pyridine-DRIFTS spectra (Fig 3.14) feature bands at *ca.* 1450 and 1545 cm^{-1} which indicate pyridine coordinated to LASs and the chemisorption of pyridine on strong BASs, respectively.[47] Meanwhile, the IR bands at around 1620 cm^{-1} and 1640 cm^{-1} are characteristic of pyridine coordinated to LAS and BAS, respectively. It is generally accepted that the bands at higher frequency represent LASs and BASs of a higher relative acid strength.[8] Also, a band located around 1490 cm^{-1} is common to both adsorbed species (LAS and BAS) and an additional band centred around 1600 cm^{-1} is generally assigned to hydrogen-bonded pyridine.

Analysis of the 1650-1425 cm^{-1} region allowed for the evaluation of the broad adsorption bands at *ca.* 1545 cm^{-1}, and 1450 cm^{-1} corresponding to BAS and LAS, respectively. Due to the experimental setup, direct comparison of the species present was only possible on a qualitative level. It is apparent that the SAS-1% material contains a lower distribution of acid sites (Fig 3.14-a) in comparison to the other SAS-x% materials. As the water content is increased an inverse relationship is observed between the concentration of Lewis and Brønsted acid sites.

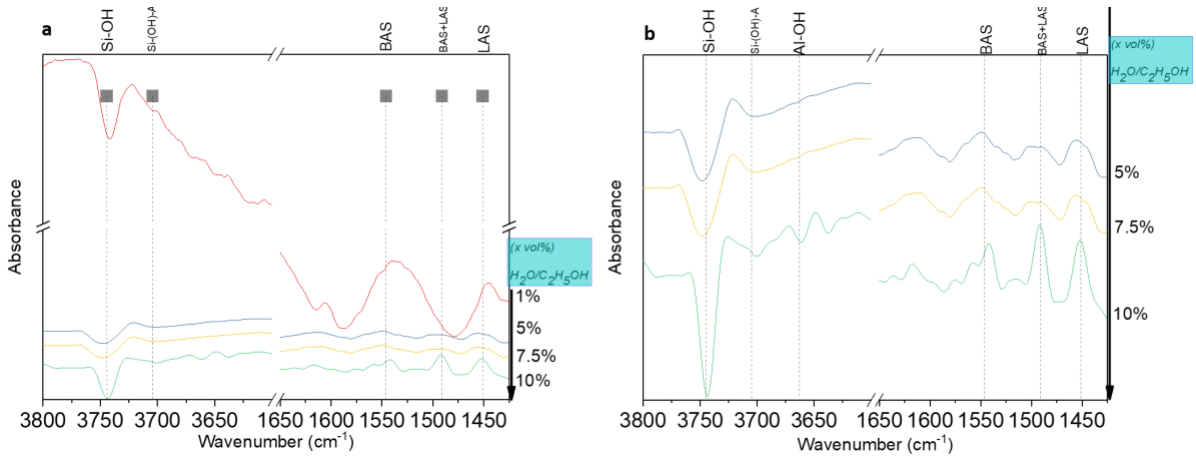

Figure 3.14: DRIFTS spectra of pyridine adsorption of (a) 1-10% H_20/C_2H_5OH SAS ASA materials and; (b) (i) 5-10% H_20/C_2H_5OH SAS ASA materials spanning 1650-1425 cm^{-1} and 3800-3600 cm^{-1} spectral regions.

Analysis of the OH stretching region of the SAS-x% materials are in close agreement with previous literature reports, and show the expected major bands at 3690 cm^{-1} and 3745 cm^{-1} attributed to silanols, hydrogen bonded with other silanols ($Si\text{-}OH_H$) and isolated hydroxyls, respectively.[8,50,9] The latter is a key component of strong BAS sites. However, the presence of a number of absorptions attributed to BAS and LASs with a number of characteristic frequencies which directly correlate to varying acid site strengths. This synergy is consistent between TPD and DRIFTS analysis. This is in agreement with literature reports which state the heterogeneous nature of the surface acid sites of ASAs.[40,51] The authors report a large concentration of Brønsted acid sites, a small fraction of which were of zeolitic strength, and Lewis acid sites of varying acidity.

Likewise other studies report synergy between the Brønsted and Lewis acidic sites not observed in crystalline zeolites, known as a pseudo-bridging silanols (PBS).[52] In fact, two pseudo-bridging silanol groups exist (PBS-Al and PBS-Si).[53] Thus, the BAS strength in ASAs does not compare to that of crystalline zeolites which makes them particularly useful in selective hydrocracking reactions.[54,55] These properties of SAS synthesized ASAs make them potentially ideal supports for acid-catalysed reactions.

3.4.1 MAS NMR assisted structural studies

Multinuclear MAS NMR studies were conducted to further investigate the local coordination environments present in the SAS ASAs. The motivation was to investigate the homogeneity with insights targeted towards gaining a further understanding of the atomic scale coordination environment and synergies with the surface acidity.

One-Dimensional ^{29}Si Magic Angle Spinning Nuclear Magnetic Resonance (^{29}Si 1D MAS NMR) spectra of several SAS prepared silica-aluminas, varying only in the water concentration in the solvent system are presented in Fig 3.15. The assignments of the ^{29}Si NMR spectra are listed in Table 3.8. The ^{29}Si 1D MAS NMR spectra's line width and isotropic chemical shift (δ_{iso}) features have been used to identify the local silicon coordination environment present. A large degree of heterogeneity has been found in both cases. The resonance at -108 ppm in the ^{29}Si NMR spectra of the reference material, SiO_2, is attributed to the Q^4 site present in accordance with previous studies.[56,57]

The resultant resonances suggest the presence of aluminosilicates with a three-dimensional framework, consisting of Q^4 [$(SiO)_4Si$] units with partial substitution of some silicon atoms by aluminium. This is supported by the fact that the ^{29}Si NMR isotropic chemical shift is governed by the number of the nearest neighbour Al atoms, and subsequent number of adjacent aluminate tetrahedra, around Si or by the number of Si-O-(Si, Al) bridges occurring in the structure.[58] The ^{29}Si MAS NMR spectra displayed heterogeneity in silicon environments attributed to Q^4 groups with similar degrees of aluminium substitution in the SAS materials. A regular paramagnetic shift accompanies increasing substitution of silicon by aluminium in the Q^4 units, causing line broadening. This phenomenon has been previously attributed to the homogeneous distribution of Si and Al and the more aluminium that is located around silanol groups, the stronger the induced electron density from the OH groups.[57,59] This generates the strong acid sites.

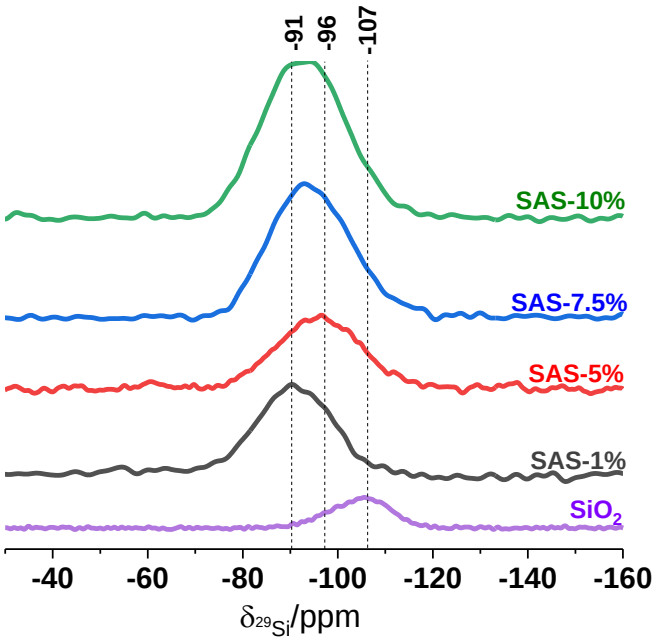

Figure 3.15: ^{29}Si CP/MAS NMR spectra of SAS-1%, -5%, -7.5%, 10% and silica

This is in agreement with previous studies whereby systematic variations in peak positions and widths with composition are closely related to the extent of ordering of Si and Al cations.[60] After incorporation with aluminium, the resonances slightly deviated to higher frequencies for the SAS materials. This is in agreement with numerous studies.[61,62]

Table 3.8: Isotropic ^{29}Si chemical shift ranges (relative to TMS) for Q^4 units in SAS ASAs and SiO_2.

Sample	**δ (ppm)**	**Assignment**
SAS 1% SA	-90.4	Q^4(4Al)/ Q^4(3Al)
	-94.2	
SAS 5% SA	-93.1	Q^4(3Al)/ Q^4(2Al)
	-96.4	
	-101.7	
SAS 7.5% SA	-93.3	Q^4(3Al)/ Q^4(2Al)
	-97.0	
SAS 10% SA	-94	Q^4(3Al)/ Q^4(2Al)

	-97	
SiO_2	-104	Q^4(4Si)
H-ZSM5 (23)	-104	Q^4(1Al)
	-110	Q^4(4Si)

This is not evident in the zeolitic sample (Fig 3.16) is characterized by more orderly Si/Al distribution with two more resolved peaks present at -109 ppm and -104 ppm representing the Q^4 and a shoulder Q^4(1Al) silicate species, respectively. The origin of the latter is caused by replacement of silicon by aluminium in the second coordination sphere. This is manifested in the ASAs, which contain several inequivalent Q^4 units due to different degrees of aluminium substitution a causation of the aluminium molar fraction.

However, it is understood that the formation of Brønsted acid sites differs in amorphous and crystalline aluminosilicates.[52,63] In zeolites, high aluminium content in the framework can reduce the strength of bridging hydroxyls because of the change in electronegativity. Thus, all the SAS-x% materials have a suggested disordered distribution of Si and Al atoms in the framework which corroborates the aforementioned FTIR/ATR and XRD analyses.

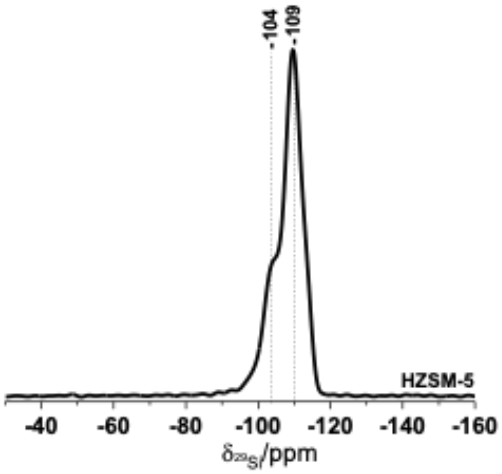

Figure 3.16: ^{29}Si CP/MAS NMR spectra of H-ZSM5 (Si/Al = 11)

3.4.2 Structural studies of ASAs by ^{27}Al MAS NMR

For greater molecular insights One-Dimensional ^{27}Al Magic Angle Spinning Nuclear Magnetic Resonance (1D MAS NMR) was utilised. ^{27}Al 1D MAS NMR a powerful tool for elucidating local geometries at Al sites in molecular and solid-state systems because they are typically associated with specific NMR signatures. Commonly, the overall symmetry of the polyhedra and the Al–O distance is indicated by the resonance position and line width, as well as the nature of the second coordination sphere.

Three characteristic asymmetric peaks with isotropic chemical shifts (δ_{iso}) of 4, 30 and 55 ppm which can be attributed to octahedral (Al^{VI}/AlO_6), pentahedral (Al^{V}/AlO_5) and tetrahedral (Al^{IV}/AlO_4) species, respectively.[64] All the signals show a large distribution in isotropic chemical shifts and therefore they are not well resolved. This reflects the topological distribution of aluminium atoms in the disordered amorphous, SAS synthesized, silica−alumina material. This further validates the suggested disorder and from FT-IR and XRD analysis. In crystalline materials, like zeolites, the bond angles are well defined, leading to a smaller distribution in NMR parameters and relatively sharper and more symmetric resonances. As anticipated by previous studies, the AlO_5 seems to be present exclusively in amorphous silica-alumina with the highest proportion of this site correlating compositionally with the highest Al content.[11,65]

Each signal is also associated with signal broadening associated with site inhomogeneity and the quadrupolar nature of the nuclei (I = 5/2) which results in an additional interaction with the electric field gradient.

Fig 3.17 shows the ^{27}Al MAS NMR spectra of the SAS prepared ASAs and alumina. All spectra exhibit three main signals with isotropic chemical shifts in the range of 0-10 ppm, 20-30 ppm and 50-60 ppm. The signals at 50-60 ppm and 0-10 ppm are unambiguously assigned to Al^{IV} and Al^{VI} species, respectively.[66] The third signal (20-30 ppm) is ascribed to a Al^{V} centre which is commonly observed in oxides obtained by sol-gel routes and more recently FSP routes.[15,28,59,67] In silica-aluminas, Al^{V} species have previously been considered to be primarily related to the interface between the segregated aluminium oxide domains and the amorphous silica alumina phase.[68,69]

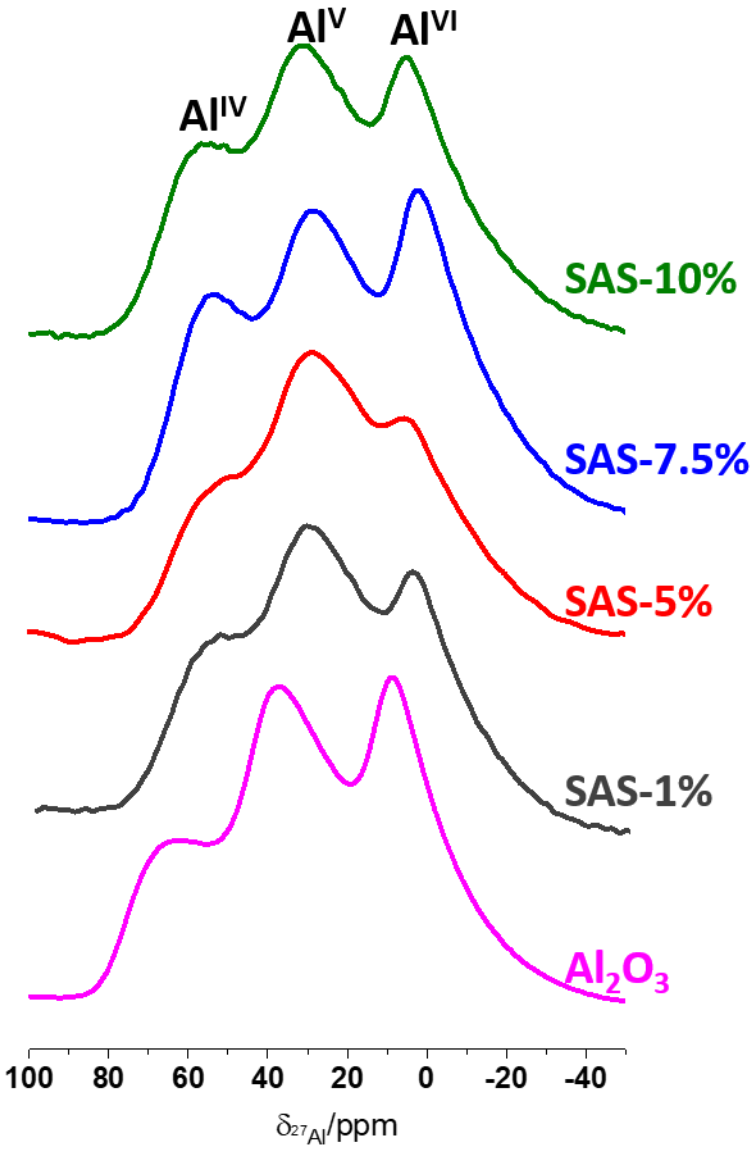

Figure 3.17: ^{27}Al MAS NMR spectra of SAS-1%, -5%, -7.5%, 10% and alumina

However, further analysis using two-dimensional ^{27}Al multiple-quantum magic angle spinning (MQ MAS) is required to obtain a definitive picture of the local structure of the Al^{3+}.[15] The unsaturated Al^{3+} cations with pentahedral coordination have been attributed to a new type of BAS-Al^{V} which show comparable acidity and structural similarities to BAS-Al^{IV}. It is also generally accepted that surface Al^{3+} centres with unsaturated coordination are the important anchoring sites for maintain high dispersion and thermally stability of the catalytically active phase.[70,71] This unique structure could account for the formation of

highly dispersed and stabilised oxide-supported metal catalysts. With this consideration the SAS 7.5 and 10% show greater promise than the FSP material.

3.5 Conclusions

This work has demonstrated a systematic approach to the antisolvent method for ASA synthesis by investigating a number of experimental variables. The implementation of this in material design is promising in our targets to match or surpass current state-of-the-art amorphous silica-alumina, as several properties are largely tuneable *via* the antisolvent method.

The SAS methodology was able to control the bulk morphology and composition when compositional parameters were systematically evaluated, showing morphological similarities to sol-gel and FSP ASAs. On an atomic level the SAS ASAs have similarities to FSP synthesized ASAs, albeit distinguished only by the distribution of environments present. Such minute differences occur in the observed acid sites. The performance of acid-catalysed reactions is largely dictated by the acidic features such as the type, amount, strength, ratio and local environment of acid sites. However, the SAS process remains more effective in controlling compositional features resulting in synergies to ASAs produced *via* FSP processing. However, current lack of understanding would hinder the ability to fully exploit the potential of the synthesis protocol at an industrial scale currently.

It is important to appreciate the importance of the choice metal precursors and solvent composition both of which may require further investigation. In view of optimizing the technique, other process parameter and their effect on the efficacy of the process are to be evaluated further in more detail. Based on the knowledge gained, a more systematic approach to future work can be adopted with the view of further optimizing the undesirably low surface areas and slight inhomogeneity currently observed. Therefore, subsequent studies are required to maximise the full potential of the technique and the resultant mixed metal oxides.

A systematic study investigating the effect water content in the solvent system as an experimental parameter was undertaken. This has led to non-porous materials, characterized by homogeneity in Si and Al on a micrometer scale, with a high proportion of Al(IV) and Al(V) sites resulting in high acid site concentration; a direct result of pseudo-bridging silanols.

Varying the water content in the solvent system, proved to be effective in tuning a number of physical properties of the resultant ASAs. The tuneable nature of the antisolvent method was evident in the variations in the reported specific surface areas and acid site concentrations. Additionally, TEM analysis showed the amorphous nature of the SAS materials, with no observed nanocrystallinity.

The ^{29}Si MAS NMR spectra displayed heterogeneity in silicon environments attributed to Q^4 groups with similar degrees of aluminium substitution in the SAS materials, in agreement with previous FTIR/ATR findings. This is indicative of several inequivalent silicate species which are formed in SAS prepared ASAs. A regular paramagnetic shift accompanies increasing substitution of silicon by aluminium in the Q^4 units, causing line broadening. This phenomenon has been previously attributed to an irregular Si/Al distribution.[57]

Though three signals appear attributed to tetra-, penta- and octahedrally coordinated Al species, the Al^V species can be distinguished as the main difference between amorphous and crystalline aluminosilicates. However, the ^{27}Al MAS NMR spectra shows a high proportion of coordinatively unsaturated Al^V in the SAS materials. This Al^V species is significant catalytically as it is proposed to enhance Brønsted acidity possessing coordinatively unsaturated surface centres on the support for anchoring noble metal atoms for efficient catalyst design.[28] Additional importance on these sites includes their role as anchoring sites for metal species, maintaining high dispersion and sinter resistance of the catalytically active phase.

3.6 References:

1 C. Yoon and D. L. Cocke, Potential of amorphous materials as catalysts, *Journal of Non-Crystalline Solids*, 1986, **79**, 217–245.

2 B. R. Goldsmith, E. D. Sanderson, D. Bean and B. Peters, Isolated catalyst sites on amorphous supports: A systematic algorithm for understanding heterogeneities in structure and reactivity, *J. Chem. Phys.*, 2013, **138**, 204105.
3 B. R. Goldsmith, B. Peters, J. K. Johnson, B. C. Gates and S. L. Scott, Beyond Ordered Materials: Understanding Catalytic Sites on Amorphous Solids, *ACS Catal.*, 2017, **7**, 7543–7557.
4 P. Hodgkinson, *Modern Methods in Solid-state NMR: A Practitioner's Guide*, Royal Society of Chemistry, 2018.
5 E. Alonso, I. Montequi, S. Lucas and M. J. Cocero, Synthesis of titanium oxide particles in supercritical CO2: Effect of operational variables in the characteristics of the final product, *The Journal of Supercritical Fluids*, 2007, **39**, 453–461.
6 J. Jung and M. Perrut, Particle design using supercritical fluids: Literature and patent survey, *The Journal of Supercritical Fluids*, 2001, **20**, 179–219.
7 S. A. Kondrat and S. H. Taylor, in *Catalysis*, 2014, pp. 218–248.
8 G. Crépeau, V. Montouillout, A. Vimont, L. Mariey, T. Cseri and F. Maugé, Nature, Structure and Strength of the Acidic Sites of Amorphous Silica Alumina: An IR and NMR Study, *J. Phys. Chem. B*, 2006, **110**, 15172–15185.
9 H. Koller and M. Weiss, Solid state NMR of porous materials : zeolites and related materials, *Top Curr Chem*, 2012, **306**, 189–227.
10 E. Lam, A. Comas-Vives and C. Copéret, Role of Coordination Number, Geometry, and Local Disorder on 27Al NMR Chemical Shifts and Quadrupolar Coupling Constants: Case Study with Aluminosilicates, *J. Phys. Chem. C*, 2017, **121**, 19946–19957.
11 E. J. M. Hensen, D. G. Poduval, V. Degirmenci, D. A. J. M. Ligthart, W. Chen, F. Maugé, M. S. Rigutto and J. A. R. van Veen, Acidity Characterization of Amorphous Silica–Alumina, *J. Phys. Chem. C*, 2012, **116**, 21416–21429.
12 C. Dorémieux-Morin, P. Batamack, C. Martin, J.-M. Brégeault and J. Fraissard, Comparison of amorphous silica-alumina and highly dealuminated HY zeolite by1H high resolution MAS-NMR of solids, *Catal Lett*, 1991, **9**, 403–409.
13 J. H. de Boer, Constitution and properties of silica-alumina-catalysts, *Discuss. Faraday Soc.*, 1971, **52**, 109–112.
14 F. Leydier, C. Chizallet, D. Costa and P. Raybaud, Revisiting carbenium chemistry on amorphous silica-alumina: Unraveling their milder acidity as compared to zeolites, *Journal of Catalysis*, 2015, **325**, 35–47.
15 Z. Wang, Y. Jiang, O. Lafon, J. Trébosc, K. Duk Kim, C. Stampfl, A. Baiker, J.-P. Amoureux and J. Huang, Brønsted acid sites based on penta-coordinated aluminum species, *Nature Communications*, 2016, **7**, 13820.
16 T. C. Keller, J. Arras, M. O. Haus, R. Hauert, A. Kenvin, J. Kenvin and J. Pérez-Ramírez, Synthesis-property-performance relationships of amorphous silica-alumina catalysts for the production of methylenedianiline and higher homologues, *Journal of Catalysis*, 2016, **344**, 757–767.
17 B. K. Coltrain, L. W. Kelts, N. J. Armstrong and J. M. Salva, Silicon tetraacetate as a sol-gel precursor, *J Sol-Gel Sci Technol*, 1994, **3**, 83–90.
18 S. Acosta, R. Corriu, D. Leclercq, P. H. Mutin and A. Vioux, Novel non-hydrolytic sol-gel route to metal oxides, *J Sol-Gel Sci Technol*, 1994, **2**, 25–28.

19 Y.-F. Lin and J.-W. Kuo, Mesoporous bis(trimethoxysilyl)hexane (BTMSH)/tetraethyl orthosilicate (TEOS)-based hybrid silica aerogel membranes for CO2 capture, *Chemical Engineering Journal*, 2016, **300**, 29–35.
20 B. Tan and S. E. Rankin, Study of the Effects of Progressive Changes in Alkoxysilane Structure on Sol−Gel Reactivity, *J. Phys. Chem. B*, 2006, **110**, 22353–22364.
21 S. Esposito, "Traditional" Sol-Gel Chemistry as a Powerful Tool for the Preparation of Supported Metal and Metal Oxide Catalysts, *Materials*, 2019, **12**, 668.
22 P. D. Lickiss, in *Encyclopedia of Inorganic Chemistry*, American Cancer Society, 2006.
23 R. Sui, A. S. Rizkalla and P. A. Charpentier, Synthesis and Formation of Silica Aerogel Particles By a Novel Sol−Gel Route in Supercritical Carbon Dioxide, *J. Phys. Chem. B*, 2004, **108**, 11886–11892.
24 S. L. Warring, D. A. Beattie and A. J. McQuillan, Surficial Siloxane-to-Silanol Interconversion during Room-Temperature Hydration/Dehydration of Amorphous Silica Films Observed by ATR-IR and TIR-Raman Spectroscopy, *Langmuir*, 2016, **32**, 1568–1576.
25 P. Padmaja, K. G. K. Warrier, M. Padmanabhan, W. Wunderlich, F. J. Berry, M. Mortimer and N. J. Creamer, Structural aspects and porosity features of nano-size high surface area alumina–silica mixed oxide catalyst generated through hybrid sol–gel route, *Materials Chemistry and Physics*, 2006, **95**, 56–61.
26 J. K. West and L. L. Hench, A PM3 molecular orbital model of silica rings and their vibrational spectra, *Journal of Non-Crystalline Solids*, 1994, **180**, 11–16.
27 H. Yoshino, K. Kamiya and H. Nasu, IR study on the structural evolution of sol-gel derived SiO2 gels in the early stage of conversion to glasses, *Journal of Non-Crystalline Solids*, 1990, **126**, 68–78.
28 Z. Wang, Y. Jiang, X. Yi, C. Zhou, A. Rawal, J. Hook, Z. Liu, F. Deng, A. Zheng, M. Hunger, A. Baiker and J. Huang, High population and dispersion of pentacoordinated AlV species on the surface of flame-made amorphous silica-alumina, *Science Bulletin*, , DOI:10.1016/j.scib.2019.04.002.
29 Z. Wang, Y. Jiang, F. Jin, C. Stampfl, M. Hunger, A. Baiker and J. Huang, Strongly enhanced acidity and activity of amorphous silica–alumina by formation of pentacoordinated AlV species, *Journal of Catalysis*, 2019, **372**, 1–7.
30 J. O. Werling and P. G. Debenedetti, Numerical modeling of mass transfer in the supercritical antisolvent process: miscible conditions, *The Journal of Supercritical Fluids*, 2000, **18**, 11–24.
31 E. Reverchon, I. De Marco and E. Torino, Nanoparticles production by supercritical antisolvent precipitation: A general interpretation, *The Journal of Supercritical Fluids*, 2007, **43**, 126–138.
32 E. Reverchon, Supercritical antisolvent precipitation of micro- and nano-particles, *The Journal of Supercritical Fluids*, 1999, **15**, 1–21.
33 E. Torino, I. De Marco and E. Reverchon, Organic nanoparticles recovery in supercritical antisolvent precipitation, *The Journal of Supercritical Fluids*, 2010, **55**, 300–306.
34 C. S. Lengsfeld, J. P. Delplanque, V. H. Barocas and T. W. Randolph, Mechanism Governing Microparticle Morphology during Precipitation by a Compressed Antisolvent: Atomization vs Nucleation and Growth, *J. Phys. Chem. B*, 2000, **104**, 2725–2735.

35 E. Reverchon, R. Adami, G. Caputo and I. De Marco, Spherical microparticles production by supercritical antisolvent precipitation: Interpretation of results, *The Journal of Supercritical Fluids*, 2008, **47**, 70–84.
36 F. Chávez, P. G. Debenedetti, J. J. Luo, R. N. Dave and R. Pfeffer, Estimation of the Characteristic Time Scales in the Supercritical Antisolvent Process, *Ind. Eng. Chem. Res.*, 2003, **42**, 3156–3162.
37 E. Reverchon, C. Celano, G. D. Porta, A. D. Trolio and S. Pace, Supercritical antisolvent precipitation: A new technique for preparing submicronic yttrium powders to improve YBCO superconductors, *Journal of Materials Research*, 1998, **13**, 284–289.
38 E. Reverchon, G. Della Porta, A. Di Trolio and S. Pace, Supercritical Antisolvent Precipitation of Nanoparticles of Superconductor Precursors, *Ind. Eng. Chem. Res.*, 1998, **37**, 952–958.
39 E. Reverchon, G. Caputo and I. De Marco, Role of Phase Behavior and Atomization in the Supercritical Antisolvent Precipitation, *Ind. Eng. Chem. Res.*, 2003, **42**, 6406–6414.
40 W. Daniell, U. Schubert, R. Glöckler, A. Meyer, K. Noweck and H. Knözinger, Enhanced surface acidity in mixed alumina–silicas: a low-temperature FTIR study, *Applied Catalysis A: General*, 2000, **196**, 247–260.
41 E. Reverchon and I. De Marco, Mechanisms controlling supercritical antisolvent precipitate morphology, *Chemical Engineering Journal*, 2011, **169**, 358–370.
42 Z.-R. Tang, S. A. Kondrat, C. Dickinson, J. K. Bartley, A. F. Carley, S. H. Taylor, T. E. Davies, M. Allix, M. J. Rosseinsky, J. B. Claridge, Z. Xu, S. Romani, M. J. Crudace and G. J. Hutchings, Synthesis of high surface area CuMn2O4 by supercritical anti-solvent precipitation for the oxidation of CO at ambient temperature, *Catal. Sci. Technol.*, 2011, **1**, 740–746.
43 S. A. Kondrat, P. J. Smith, P. P. Wells, P. A. Chater, J. H. Carter, D. J. Morgan, E. M. Fiordaliso, J. B. Wagner, T. E. Davies, L. Lu, J. K. Bartley, S. H. Taylor, M. S. Spencer, C. J. Kiely, G. J. Kelly, C. W. Park, M. J. Rosseinsky and G. J. Hutchings, Stable amorphous georgeite as a precursor to a high-activity catalyst, *Nature*, 2016, **531**, 83.
44 P. J. Smith, S. A. Kondrat, J. H. Carter, P. A. Chater, J. K. Bartley, S. H. Taylor, M. S. Spencer and G. J. Hutchings, Supercritical Antisolvent Precipitation of Amorphous Copper–Zinc Georgeite and Acetate Precursors for the Preparation of Ambient-Pressure Water-Gas-Shift Copper/Zinc Oxide Catalysts, *ChemCatChem*, 2017, **9**, 1621–1631.
45 G. Tonetto, J. Atias and H. de Lasa, FCC catalysts with different zeolite crystallite sizes: acidity, structural properties and reactivity, *Applied Catalysis A: General*, 2004, **270**, 9–25.
46 F. A. Perras, Z. Wang, T. Kobayashi, A. Baiker, J. Huang and M. Pruski, Shedding light on the atomic-scale structure of amorphous silica–alumina and its Brønsted acid sites, *Phys. Chem. Chem. Phys.*, 2019, **21**, 19529–19537.
47 M. E. Z. Velthoen, S. Nab and B. M. Weckhuysen, Probing acid sites in solid catalysts with pyridine UV-Vis spectroscopy, *Phys. Chem. Chem. Phys.*, 2018, **20**, 21647–21659.
48 L. F. Isernia, FTIR study of the relation, between extra-framework aluminum species and the adsorbed molecular water, and its effect on the acidity in ZSM-5 steamed zeolite, *Materials Research*, 2013, **16**, 792–802.

49 F. Jin and Y. Li, A FTIR and TPD examination of the distributive properties of acid sites on ZSM-5 zeolite with pyridine as a probe molecule, *Catalysis Today*, 2009, **145**, 101–107.

50 R. Buzzoni, S. Bordiga, G. Ricchiardi, C. Lamberti, A. Zecchina and G. Bellussi, Interaction of Pyridine with Acidic (H-ZSM5, H-β, H-MORD Zeolites) and Superacidic (H-Nafion Membrane) Systems: An IR Investigation, *Langmuir*, 1996, **12**, 930–940.

51 G. Crépeau, V. Montouillout, A. Vimont, L. Mariey, T. Cseri and F. Maugé, Nature, Structure and Strength of the Acidic Sites of Amorphous Silica Alumina: An IR and NMR Study, *J. Phys. Chem. B*, 2006, **110**, 15172–15185.

52 C. Chizallet and P. Raybaud, Pseudo-Bridging Silanols as Versatile Brønsted Acid Sites of Amorphous Aluminosilicate Surfaces, *Angewandte Chemie International Edition*, 2009, **48**, 2891–2893.

53 K. Larmier, C. Chizallet, S. Maury, N. Cadran, J. Abboud, A.-F. Lamic-Humblot, E. Marceau and H. Lauron-Pernot, Isopropanol Dehydration on Amorphous Silica–Alumina: Synergy of Brønsted and Lewis Acidities at Pseudo-Bridging Silanols, *Angew. Chem.*, 2017, **129**, 236–240.

54 B. Xu, C. Sievers, J. A. Lercher, J. A. R. van Veen, P. Giltay, R. Prins and J. A. van Bokhoven, Strong Brønsted Acidity in Amorphous Silica−Aluminas, *J. Phys. Chem. C*, 2007, **111**, 12075–12079.

55 D. G. Poduval, J. A. R. van Veen, M. S. Rigutto and E. J. M. Hensen, Brønsted acid sites of zeolitic strength in amorphous silica - alumina, *Chemical Communications*, 2010, **46**, 3466–3468.

56 H. He, J. Guo, J. Zhu, P. Yuan and C. Hu, 29Si and 27Al MAS NMR spectra of mullites from different kaolinites, *Spectrochim Acta A Mol Biomol Spectrosc*, 2004, **60**, 1061–1064.

57 E. Lippmaa, M. Maegi, A. Samoson, G. Engelhardt and A. R. Grimmer, Structural studies of silicates by solid-state high-resolution silicon-29 NMR, *J. Am. Chem. Soc.*, 1980, **102**, 4889–4893.

58 JoNlrneN, F. SrsssrNs and L. S. E. Canmcrnrr, 1985.

59 J. Huang, N. van Vegten, Y. Jiang, M. Hunger and A. Baiker, Increasing the Brønsted Acidity of Flame-Derived Silica/Alumina up to Zeolitic Strength, *Angewandte Chemie International Edition*, 2010, **49**, 7776–7781.

60 S. K. Lee and J. F. Stebbins, The degree of aluminum avoidance in aluminosilicate glasses, *American Mineralogist*, 1999, **84**, 937–945.

61 X. Qu, Z. Zhao and X. Zhao, Microstructure and characterization of aluminum-incorporated calcium silicate hydrates (C–S–H) under hydrothermal conditions, *RSC Advances*, 2018, **8**, 28198–28208.

62 S. Komarneni, R. Roy, D. M. Roy, C. A. Fyfe, G. J. Kennedy, A. A. Bothner-By, J. Dadok and A. S. Chesnick, 27Al and29Si magic angle spinning nuclear magnetic resonance spectroscopy of Al-substituted tobermorites, *J Mater Sci*, 1985, **20**, 4209–4214.

63 A. Corma, Inorganic Solid Acids and Their Use in Acid-Catalyzed Hydrocarbon Reactions, *Chem. Rev.*, 1995, **95**, 559–614.

64 E. Lam, A. Comas-Vives and C. Copéret, Role of Coordination Number, Geometry, and Local Disorder on ^{27} Al NMR Chemical Shifts and Quadrupolar Coupling Constants: Case Study with Aluminosilicates, *The Journal of Physical Chemistry C*, 2017, **121**, 19946–19957.

65 Z. Wang, T. Li, Y. Jiang, O. Lafon, Z. Liu, J. Trébosc, A. Baiker, J.-P. Amoureux and J. Huang, Acidity enhancement through synergy of penta- and tetra-coordinated aluminum species in amorphous silica networks, *Nature Communications*, 2020, **11**, 225.
66 M. P. J. Peeters and A. P. M. Kentgens, A 27Al MAS, MQMAS and off-resonance nutation NMR study of aluminium containing silica-based sol-gel materials, *Solid State Nuclear Magnetic Resonance*, 1997, **9**, 203–217.
67 M. E. Smith, Application of27Al NMR techniques to structure determination in solids, *Appl. Magn. Reson.*, 1993, **4**, 1–64.
68 E. J. M. Hensen, D. G. Poduval, V. Degirmenci, D. A. J. M. Ligthart, W. Chen, F. Maugé, M. S. Rigutto and J. A. R. van Veen, Acidity Characterization of Amorphous Silica–Alumina, *J. Phys. Chem. C*, 2012, **116**, 21416–21429.
69 B. M. De Witte, P. J. Grobet and J. B. Uytterhoeven, Pentacoordinated Aluminum in Noncalcined Amorphous Aluminosilicates, Prepared in Alkaline and Acid Mediums, *J. Phys. Chem.*, 1995, **99**, 6961–6965.
70 J. H. Kwak, J. Hu, D. Mei, C.-W. Yi, D. H. Kim, C. H. F. Peden, L. F. Allard and J. Szanyi, Coordinatively Unsaturated Al3+ Centers as Binding Sites for Active Catalyst Phases of Platinum on γ-Al2O3, *Science*, 2009, **325**, 1670–1673.
71 L. Shi, G.-M. Deng, W.-C. Li, S. Miao, Q.-N. Wang, W.-P. Zhang and A.-H. Lu, Al2O3 Nanosheets Rich in Pentacoordinate Al3+ Ions Stabilize Pt-Sn Clusters for Propane Dehydrogenation, *Angewandte Chemie International Edition*, 2015, **54**, 13994–13998.

4 Comparison of SAS, FSP and Sol-gel prepared ASAs

As previously discussed, a series of ASAs materials have been synthesized using the SAS methodology with $scCO_2$ as the antisolvent. Through the knowledge gained from the experimental study and extensive characterization, the solvent composition (*x* vol.% H_2O/CH_3OH) and calcination ramp rate had the greatest influence on the desired physicochemical properties. These factors circumvented the low surface areas that typically characterize SAS synthesised materials.

With the non-oxidative propane dehydrogenation reaction in mind the surface acidity has also been identified as a key structural parameter determining catalytic performance. Compositional differences, such as varying the Si/Al, modulate and systematically vary the acid site concentration, type and strength.

Other than the SAS methodology, other considerations are the synthesis strategy with the equally novel flame spray pyrolysis (FSP) and traditional sol-gel (SG) methodologies governing the ability to tune the structural, textural, and morphological properties in their own right. In efforts to contextualise the current findings these synthesis methods have been employed evaluating the degree of homogeneity mixed on the micro- and atomic scale. The aim is to provide a detailed account of similarities and variations in the structural, textural, and morphological features of the resultant mixed metal oxides considering homogeneity, based on Si and Al atomic dispersion, and surface acidity.

Several ASAs solid acids with different Al/(Al+Si) molar ratios simplified for brevity to Si/Al ratios, ranging from 1, 4, 10 to 20, were synthesized using the SAS methodology. Analogous materials were synthesized *via* the FSP technique in collaboration with the University of Milan as well as the sol-gel (SG) technique. For the purpose of this discussion these materials will be denoted as SAS-x, FSP-x and SG-x, where x refers to the nominal Si/Al ratio.

To understand the effects of the preparation strategy on the texture of the different ASAs, the Ar adsorption-desorption isotherms were compared, Fig 4. 1**.**

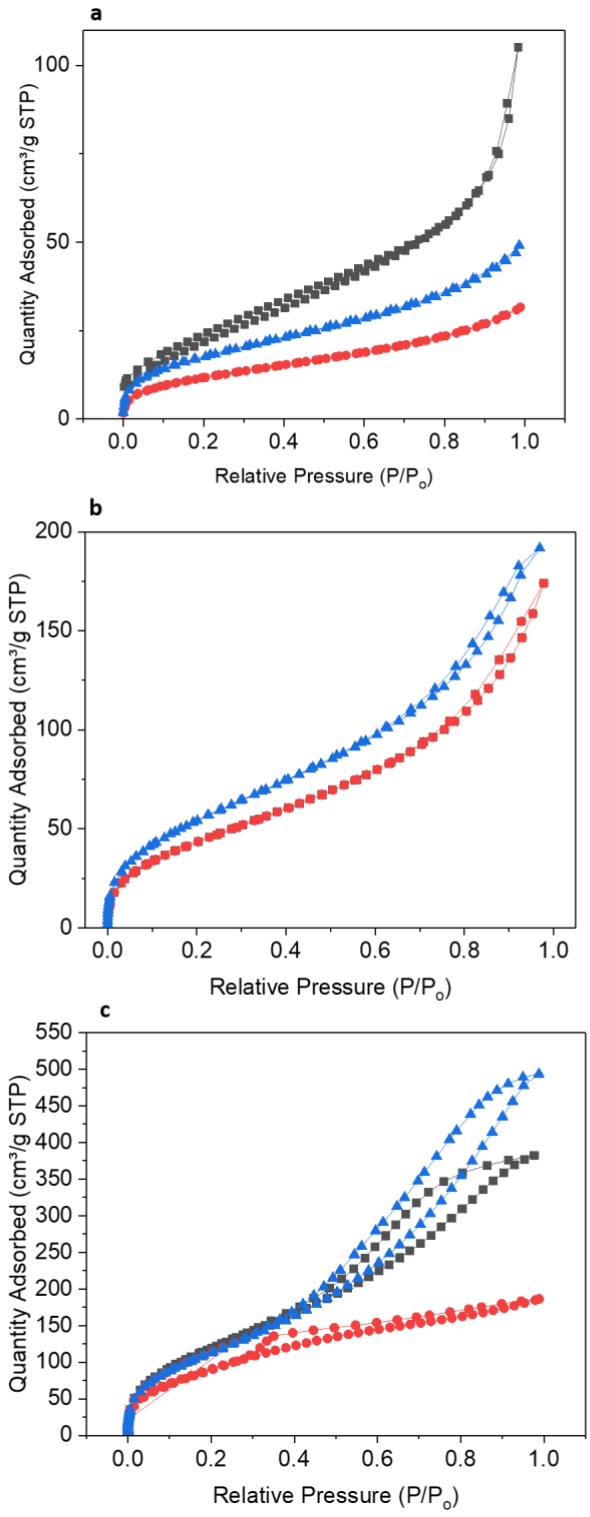

Figure 4.1: Ar adsorption-desorption isotherms of (a) SAS; (b) FSP and; (c) SG ASA oxides with Si/Al of 1 (---), 4 (---) and 10 (---).

The SAS-x and FSP-x materials exhibit a type II isotherm with a type H4 hysteresis loop, which is characteristic of non-porous materials that are common for flame aerosol synthesized nanoparticles.[1,2] On the contrary, the SG ASAs with Si/Al of 1 and 10 exhibit a type IV isotherm with a type H1 hysteresis loop, which is characteristic of mesoporous materials with cylindrical pore channels with relatively narrow pore size distribution. The SG-4 (Si/Al=4) ASA has a different pore structure as signified by the type H4 hysteresis loop.

As shown in Fig 4. 1, irrespective of the samples, the Ar uptake in the low-pressure region ($P/P_o<0.1$) is quite low, indicating a low proportion of micropores. However, further comparing the SAS-x and FSP-x ASAs it is clear that the higher Ar uptake with increasing P/P_o, in the 0.65-0.99 region indicates the presence of mesopores with the H4-type hysteresis loop suggesting the presence of slit-like pores. In the case of the SAS materials, the decreased Ar uptake is reflective of the lessened total pore volume and BET surface areas as displayed in Table 4. 1. This trend is consistent for the FSP and SG materials such that the total pore volume and BET surface areas trend generally increases as follows: SAS-x<FSP-x<SG-x. In the SG-x materials, a high Si content appears beneficial in attaining a high specific surface area. However, this finding is not consistently applicable for both SAS-x and FSP-x materials.

Table 4.1: Physical properties of the different samples with the variations in synthesis strategy and composition.

Sample	**Si/Al**	**BET surface area ($m^2 g^{-1}$)**	**Pore volume ($cm^3 g^{-1}$)**
SAS-1	1.8	98	0.10
SAS-4	6.2	44	0.04
SAS-10	13.5	58	0.06
FSP-1	1.2	140	0.10
FSP-4	4.0	146	0.11
FSP-10	10.5	172	0.11
SG-1	0.7	390	0.47
SG-4	4.6	309	0.22
SG-10	11.9	391	0.57

4.1 Nanometre Scale Morphology

Analogous SAS, FSP and SG calcined materials with nominal Si/Al ratio of 1 were further analysed using HRTEM and SAED to determine the nanometre scale morphology. It is clear that, in the case of the SAS-1 material the presence of a network of spherical agglomerates, with mean diameters of *ca.* 70 nm ± 27 nm is evident (Fig 4. 2 a-b). This corroborates the spherical agglomerates found at the micrometre scale by SEM analysis.

Further, on a 20 nm scale there is no presence of nanocrystallinity denoted by the lack of lattice fringes. The SAED analysis further supports the XRD and HRTEM findings suggesting the formation of a wholly amorphous mixed metal oxide. SAED observations suggested that no nanocrystallinity exists on a nano and sub-nanometre scale. The lattice spacings further illustrate the lack of ordered, crystalline planes evident in the overall broad peak, characteristic of largely amorphous materials.

In view of investigating the effect of different preparation methods on the crystal structure and morphology of silica-alumina support materials further HRTEM and SAEDP analysis of analogous FSP and sol-gel synthesized materials was conducted, Fig 4. 2 d-f. Both FSP-1 and SG-1 materials displayed marked morphological and textural similarities. HRTEM images showed a network of spherical agglomerates with a 'cloud'-like morphology accompanied by the compact arrangement of small primary particles.

Further analysis revealed mean diameters of *ca.* 8 nm ± 4 nm, for FSP-1 and significantly smaller, indiscernible primary particles in the SG-1 material. This interpretation is consistent with numerous studies relating to FSP synthesized amorphous silica-alumina. Meanwhile, the coherent packing assortment permits the low total pore volume in the complex pore architecture determined by argon sorption studies, Fig 4. 1**.** This is a consequence of the principles of nucleation and crystal growth is the FSP methodology's precipitation mechanism which are characteristically governed by short residence times and high process temperatures.

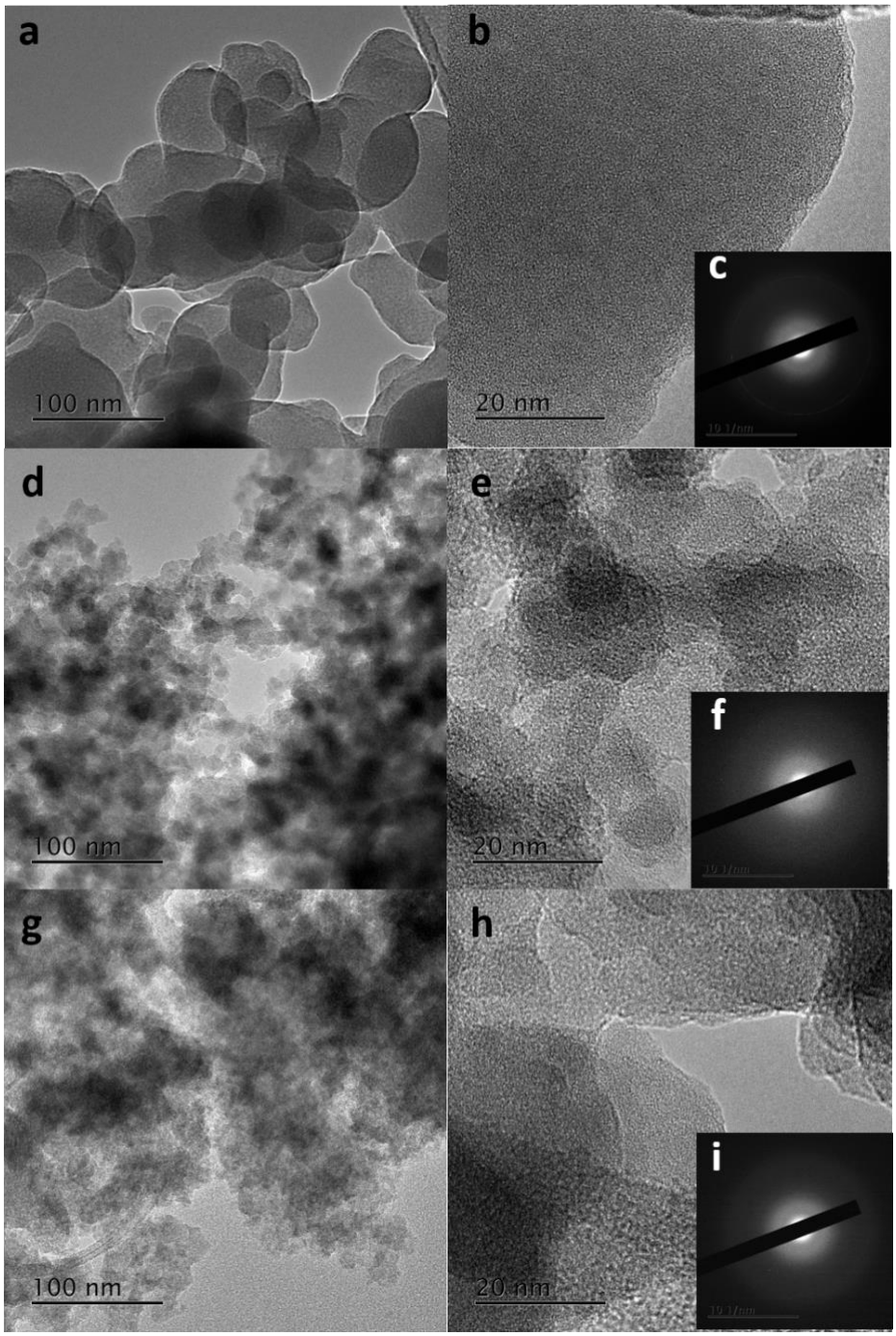

Figure 4. 2: HRTEM micrographs of (a-b) SAS1; (d-e) FSP 1 and; (g-h) SG 1 ASA materials displaying amorphous characteristics and SAED patterns of (c) SAS1; (f) FSP 1 and; (i) SG 1 ASA materials also suggesting an amorphous material due to the diffuse rings.

Contrary to SAS and FSP supported materials, the HRTEM of the SG-1 material displays indiscernible primary particles on a nanometre scale. The platelet-like morphology accompanied by the compact arrangement of the small primary particles result in the

observed high surface areas. In agreement with literature, the formation of aerogels with high BET surface areas and well-defined pore diameters can be obtained using sol-gel processing.[3] Consequently, the observed differences in specific surface areas for analogous ASA materials directly correlate with crystallite size, as anticipated.

In all cases, the SAED patterns exhibit extended broad and diffuse rings. Qualitative interpretation of the SAED patterns provide an informative insight into coordination environments. The previous FTIR/ATR findings report both a disordered network of AlO_6 and AlO_4 polyhedra linked to SiO_4 polyhedra in the SAS synthesized ASAs. This deduction is true for previously analysed materials with equimolar Al and Si, and a nominal Si/Al ratio of 1.

4.2 Structural analysis

4.2.1 Bulk structural analysis

The FT-IR spectra of systematically different SAS, FSP and sol-gel materials with nominal Si/Al ratios ranging from 1-10 are presented in Fig 4. 3. With a specific focus on the 400-1200 cm^{-1} region, which contains all the important $\nu_{Al\text{-}O}$ and $\nu_{Si\text{-}O}$ related absorptions, all the samples give comparatively broad spectra. This indicates the general disorderliness and disordered distribution of AlO_6 and AlO_4 sites irrespective of the synthesis method. In particular, the intensities of the sharp absorption peaks centred in the 1040-1060 cm^{-1} spectral region correspond to the asymmetric stretching of Si-O-Si or Si-O which is typical of four coordinate silica (SiO_4).

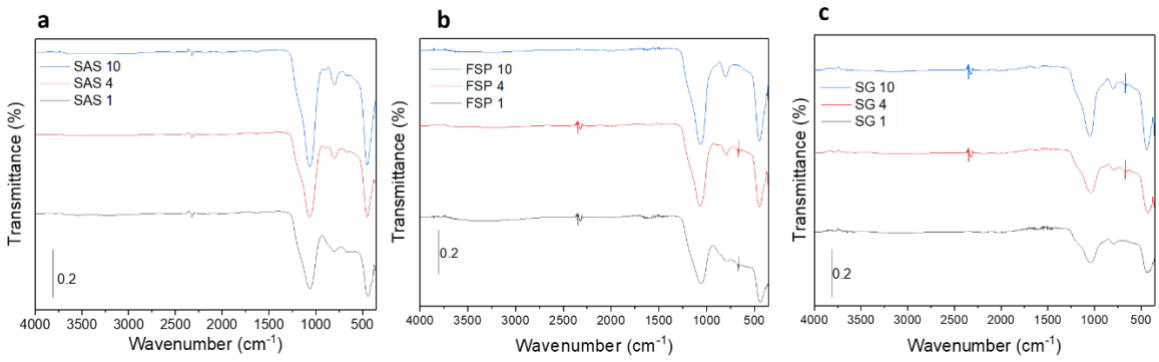

Figure 4.3: FTIR spectra of (a) SAS 1-10; (b) FSP 1-10 and; (c) SG 1-10 ASA materials.

As the Al concentration decreases, the intensity of this absorption peak progressively increases compared absorption peaks related to Al sites. This is supported by the concurrent increase in intensity of the absorption peaks in the 430-450 cm^{-1} spectral region which are known to be the consequence of the deformation mode of Si-O-Si. This absorption is usually ascribed to the formation of amorphous silica. This is characteristic of Si-O-Si and, its higher intensity in materials with higher nominal Si/Al ratios, can be attributed to the higher content of silica in the material. Additionally, irrespective of synthesis method and composition the absorption peaks centred at 1040-1060 cm^{-1} have shoulder peaks which appear at higher wavenumber to this absorption.

This feature indicates the presence of Al-O-Si formed through cross condensation of Al and Si moieties with the intensity of these absorption peaks increasing in the order of Si/Al: 1<4<10. The peaks in the 790-805 cm^{-1} and 670–686 cm^{-1} spectral regions are ascribed to ν_{Al-O} of AlO_4 and AlO_6, respectively. The increased intensity of the absorption peak associated with the AlO_4 site is an indication of the presence of a higher proportion of this tetrahedral unit. As expected, the intensity of this absorption peak corresponds with the Si/Al.

Generally, the relative proportion of AlO_4 is independent of silicon content such that the incorporation of silica increases the tetrahedral condensation in the materials increasing the tetrahedral condensation and thus favouring tetrahedrally coordinated Al. An opposing trend is seen for the proportion of AlO_6 which decreases progressively with an increase in silica content. The shoulder seen in the 875-895 cm^{-1} spectral region, for all the samples irrespective of composition, arises from the bending vibration of Si-OH groups.

For both *SAS-x* and *FSP-x* materials the intensity of the shoulder peak is greatest. This could be due to the higher distribution of types of silanols present which give rise to more Si-OH functions. This is an inherent property of homogeneous, FSP synthesized ASAs, which display a complex surface structure characterized by a range of silanols with varying configurations.[4–6] The presence of broad, asymmetric, overlapping ν_{OH} absorption bands of Si-OH in the 3200-3220 cm^{-1} and 3510-3550 cm^{-1} regions also confirms this argument.

Additionally, a less intense absorption peak at higher wavenumber in the 3740-3770 cm^{-1} region is attributed to the stretching mode of isolated silanols.[7]

Importantly, the presence of absorption peaks in the 1620-1640 cm^{-1} spectral region attributed to the bending mode of water molecules, are expected due to the hygroscopic nature of the ASAs. This upholds the TGA analysis' attribution of the majority of the mass loss to the removal physisorbed water in all the studied ASAs.

4.2.2 Surface structure analysis

The analysis of the surface composition reveals interesting differences between SAS, FSP and sol-gel support materials. EDX analysis (*see* Figs 7. 1-3) evidences the FSP-x materials' increased bulk homogeneity, at low Si/Al ratios; a consequence of the greater degree of intimate mixing of heterometallic species *via* the process' high temperatures and short residence times. On the contrary, greater dissimilarity between the nominal and measured Si/Al ratios is observed in both *SAS-x* and *SG-x* materials. This is attributed to the increased number of experimental variables and reaction steps, requiring meticulous monitoring throughout typical ASA preparations, which are incorporated within both the SAS and sol-gel techniques.

Additionally, the difference in the nominal and measured Si/Al in the SG-x ASAs is accounted for by phase separation phenomena reported at low Si/Al values in sol-gel processing of mixed metal oxides.[8] As previously mentioned, the variability in the final microstructure is governed by a number of factors. Prior to the gel point (in acidic medium) the hydrolysis and condensation of both Si and Al molecular precursors occurs at different rates. This is heightened by differences in hydrolysis and condensation rates between Si and Al precursors. This reactivity originates from differences in electronegativity, steric and inductive effects. Resultantly, the condensation reaction proceeds at an increased rated compared to the hydrolysis reaction for the Si precursor.[9]

The result is a complex mixture consisting of silica gel with colloidally dispersed aluminium nitrate. An amorphous aluminium hydroxide precipitate is formed from aluminium

containing acidic solutions by a base, in parallel.[10,11] However, following calcination this is undetectable by XRD analysis due to the lack of long-range order and concentration gradients consisting of extended SiO_2 and Al_2O_3 domains, respectively. This is suggestive of the fact that any segregated phases must be highly localized.

The subsequent basic aqueous environment facilitates the formation of stable heterometallic bonds in the secondary particles. This limitation in the sol-gel technique is not relevant to the FSP method as elemental analysis with EDX reveals compositionally more homogeneous materials. It is important to also note the similarity of the SAS method to the sol-gel method under continuous conditions (Table 4. 2), a process carried out to increase the yield per pass. However, XPS analysis of analogous ASAs demonstrates the surface-level homogeneity of both SAS-x and FSP-x which display equivalent Si/Al ratios to the nominal values.

Differences in the theoretical and measured Si/Al of the analogous SG ASA is accounted for by the previously discussed phase separation phenomena at low Si/Al.[8] In addition, the FSP-x and SAS-x materials are characterized by high amounts of surface carbon. This is not attributed to adventitious carbon but rather possible carbon surface impurities characteristic of the synthesis methods.

Table 4. 2: Compositional analysis of analogous SAS, FSP and SG ASAs based on XPS and EDX analysis

Sample	$Si/Al_{nominal}$	Concentration (At. %)				Si/Al	
		O	Si	Al	C	XPS	EDX
FSP-1	**1**	**50.4**	**9.5**	**9.7**	**26.1**	**1.0**	**1.2**
SAS-1	**1**	**55.0**	**12.8**	**13.1**	**19.1**	**1.0**	**1.8**
SG-1	**1**	**66.9**	**10.8**	**13.7**	**8.6**	**0.7**	**0.7**

4.2.3 Local structure analysis

However, due to limitations in FTIR/ATR and EDX analysis, 1D ^{27}Al MAS NMR and 2D ^{27}Al MQMAS were used to determine the Al speciation, distribution and the second

coordination sphere (Fig 3.21)**.** The spectra for *SAS-1* and *FSP-1* are characterized by line broadening in the three characteristic asymmetric peaks with isotropic chemical shifts (δ_{iso}) of 4, 30 and 55 ppm attributed to octahedral (Al^{VI}/AlO_6), pentahedral (Al^{V}/AlO_5) and tetrahedral (Al^{IV}/AlO_4) species, respectively.

Irrespective of the preparation method the largest fraction of aluminium is incorporated in the pentahedral environment which is believed to be responsible for the occurrence of surficial Brønsted acid sites (BAS-Al^{V}). This type of Brønsted acid site is known to co-exist with strong Brønsted acid sites originating from Al^{IV}, formed independent of an alumina phase, with high population at low Si/Al. Subsequent decrease in the Al content leads to the incorporation of Al in a tetrahedral environment and subsequent decrease in both penta- and octahedrally coordinated aluminium.

Deconvolution of the 2D ^{27}Al MQMAS spectra, verified the aforementioned trend observed in the 1D ^{27}Al MAS NMR. According to the isotropic chemical shifts in the F_1 and F_2 axis three strong signals at (70,61), (44,37) and (15,17) were assigned to Al^{IV}, Al^{V} and Al^{VI} species, respectively, an indication of the three distinct Al environments in analogous FSP and SAS materials with the highest Al content. It is important to note that, due to the hygroscopic nature of the materials and the sample packing in air, the relative proportions of the different Al sites are influenced by the level of hydration. From the MQMAS NMR spectra it can be concluded that the line broadening observed in the ^{27}Al MAS NMR spectra is due to both a distribution in isotropic chemical shifts and a distribution in quadrupole coupling constants. However, the latter is beyond the scope of this study at this time.

This reflects the topological distribution of aluminium atoms in the disordered ASA materials. In crystalline materials, like zeolites, the bond angles are well defined, leading to a smaller distribution in NMR parameters.

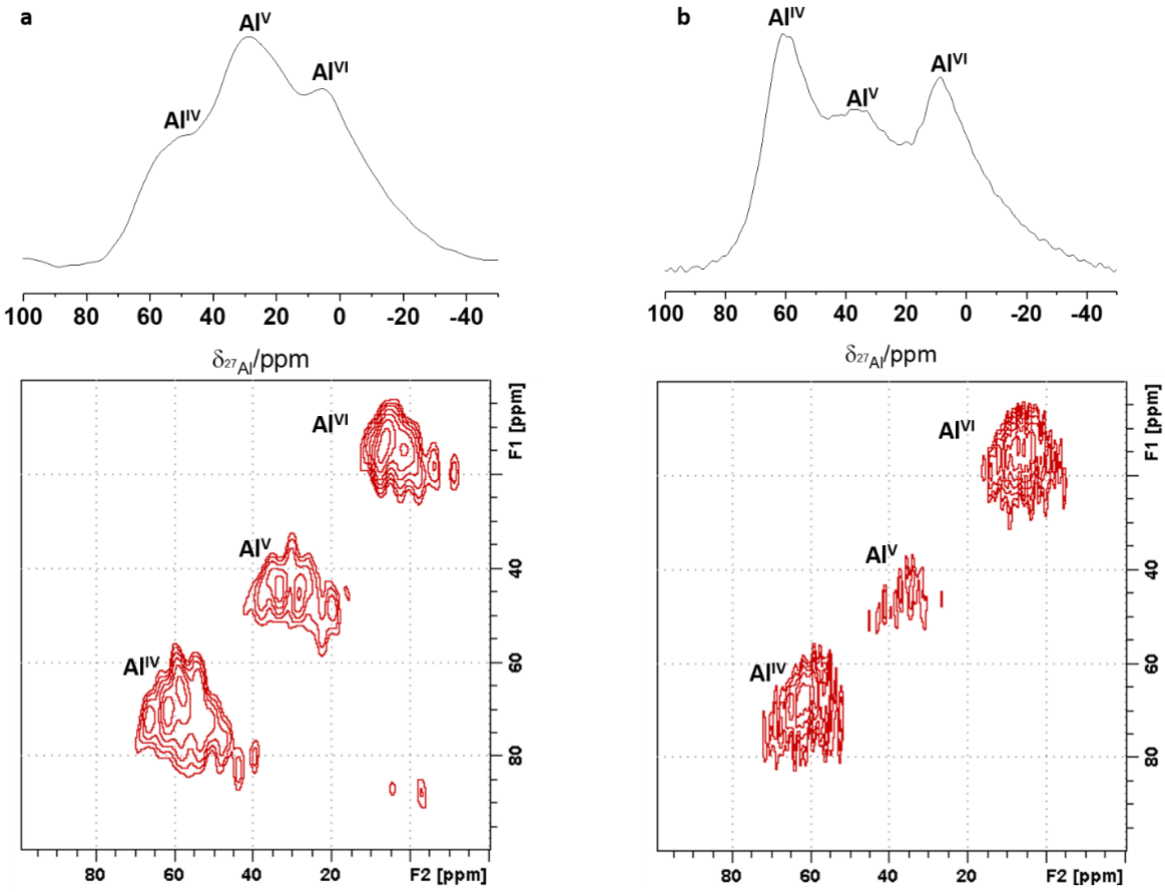

Figure 4.4: 1D ^{27}Al MAS NMR (top) and 2D ^{27}Al MQMAS NMR (bottom) spectra of (a) SAS-1 and (b) FSP-1 ASAs.

Irrespective of the preparation method the largest fraction of aluminium is incorporated in the tetrahedral and pentahedral environments which are believed to be responsible for the occurrence of Brønsted acid sites. The Al^{V} based Brønsted acid site (BAS-Al^{V}) is known to co-exist with strong Brønsted acid sites originating from Al^{IV} (BAS-Al^{IV}) formed independent of an alumina phase, with high population at low Si/Al. Subsequent decrease in the Al content leads to the incorporation of Al in a tetrahedral environment and subsequent decrease in both penta- and octahedrally coordinated aluminium. It is important to note that, due to the hygroscopic nature of the materials and the sample packing in air, the relative proportions of the different Al sites are influenced by the level of hydration. This is in agreement with reports by Wang *et al.* on FSP-synthesised aluminosilicates who report the partial hydrolysis of highly dispersed Al^{V}-O-Si sites, preferentially located on the surface and thus accessible to guest molecules.[12] With increasing aluminium content, a fraction of

the Al^{V} species were formed inside the bulk of the particles resulting in greater stabilization and unavailability for hydrolysis. With this knowledge, it is assumed that Al^{IV} are available on the surface of the support materials but not in high concentration. Equally, partial hydrolysis of Al^{IV} occurs to a lesser extent due to the low concentration of surface Al^{IV} species (shown by the monotonic decrease in the corresponding resonance).

This corroborates the 1D ^{27}Al MAS NMR. As shown in Fig 4. 4, further compositional modification results in the disappearance of both signals corresponding to both Al^{V} and Al^{VI} species. This effect is easily seen by superficial inspection in the F_1 and F_2 projections of the Al^{V} and Al^{VI} resonances. Comparing the ^{27}Al MAS NMR spectra, it can be seen that the fraction of octahedrally coordinated species is higher when the aluminium concentration is higher. This observation is congruent with the previous report that Al^{V} species are surface-enriched species existing in high concentrations at high Al content, with partial hydrolysis of Al^{V}, resulting in Al^{VI} in the hydrated state. This corroborates the aforementioned FT-IR analysis. Similarly, partial hydrolysis of Al^{IV} occurs to a lesser extent due to the low concentration of surface Al^{IV} species (shown by the monotonic decrease in the corresponding resonance).

Accordingly, as there are no cross peaks between all three types of Al coordination, it is reasonable to assume the Al^{V} and Al^{IV} sites are primarily coordinated to silicon sites. This in agreement with Loewenstein's rule and previous studies on similar FSP derived materials.[13] With catalyst design in mind, minimizing the formation of an extended alumina phase or Al^{VI} species during synthesis can maximise the dispersion of Al atoms and the generation of framework Al^{IV}, and surface Al^{V} species for optimal surface acidity is highly desirable. Due to the highly defective structure of silica−alumina, the formation of reversible aluminium species is expected and has been reported to occur more readily than in zeolites.[14]

A comparison between spectra of SAS-*x* (Fig 4. 5a) and FSP-*x* (Fig 4. 5b) indicate that the amount of reversible aluminium species is an inverse function of the aluminium concentration. Both ATR-IR and MAS NMR analyses suggest the possibility that even if the

total acidity is due to Brønsted type acid sites, different types of hydroxyl groups, other than the hydroxyl group of a Brønsted acid are also present on the surface of the SAS and FSP synthesized amorphous silica-aluminas.

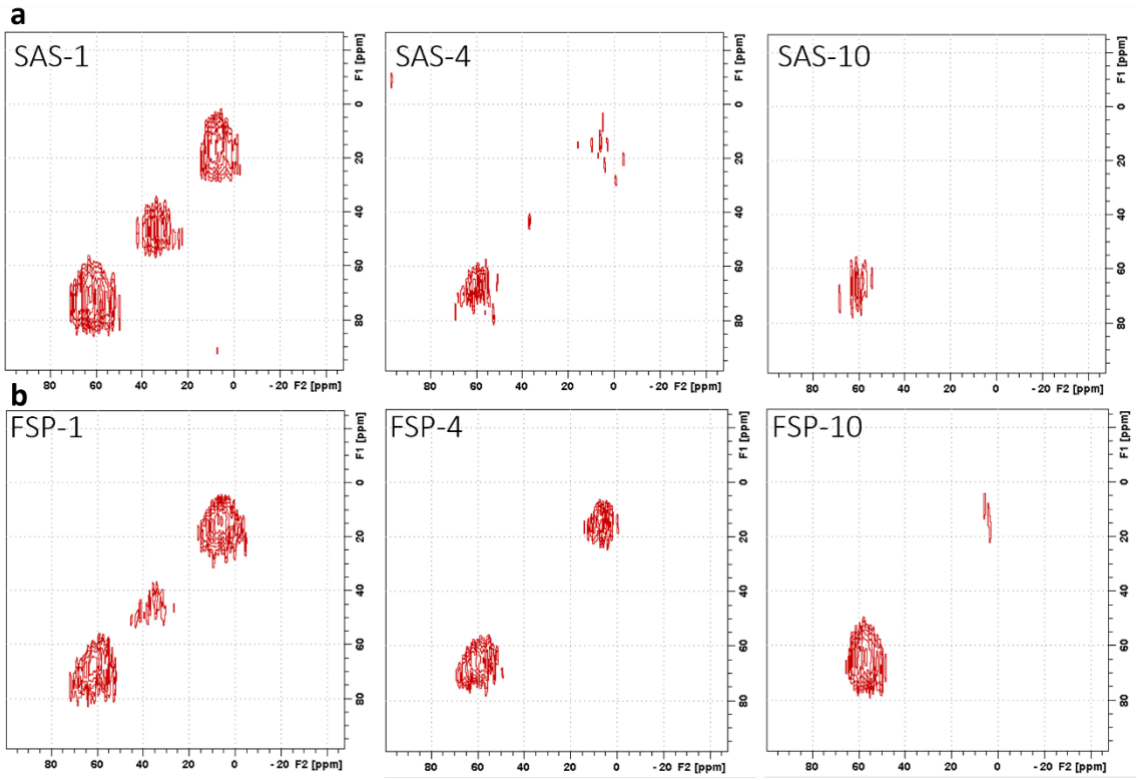

Figure 4.5: 2D ^{27}Al MQMAS NMR spectra of (a) SAS-*x* and (b) FSP-*x* ASAs.

4.2.4 Surface acidity analysis

NH_3-TPD has been used to quantify total acidity (Brønsted and Lewis acidity) and the acid strength based on the peak position. Figure 4. 6 displays the TPD curves with the total acid site concentrations and densities summarized in Table 3.12. Regardless of synthesis method the TPD curve intensities, associated with the amount of NH_3 adsorbed, increase in the order of Si/Al: 10 < 4 < 1. The SAS materials contain a high density of acid sites, a consequence of their characteristically lower surface areas, Table 4. 3. As previously discussed, the TPD curves are asymmetric and can be decomposed into three contributions corresponding to weak acid sites (Low Temperature peak), medium acid sites (Moderate Temperature peak) and strong acid sites (High temperature peak).

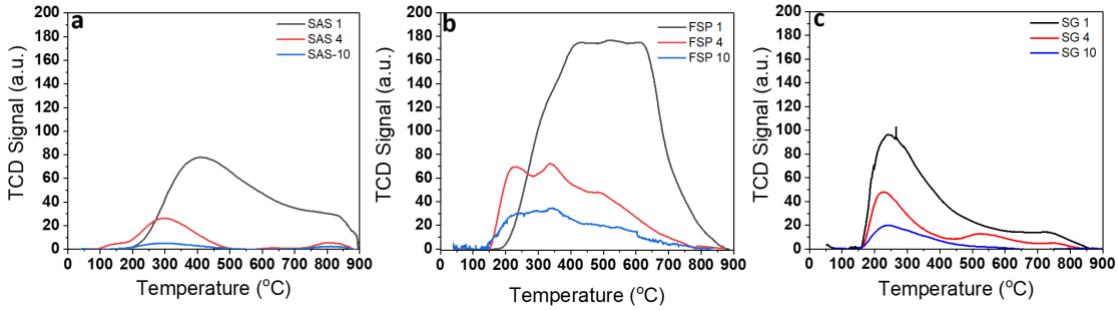

Figure 4.6: NH_3-TPD profile of (a) SAS 1-10; (b) FSP 1-10 and (c) SG 1-10 ASA materials.

For both SAS and FSP materials, medium surface acidity forms the highest portion of the total acidity. As anticipated, increasing the aluminium content increases the acid site concentration and the amount of strong acid sites. This is indicated by the increase in intensity of the high temperature component of the NH_3-TPD profile. Weak, medium and strong acidity peaks in FSP-1 TPD profile appear at marginally lower temperatures than those of analogous SAS material, implying weaker strength of these sites in the former.

In all cases, the total acidity clearly decreases as the nominal aluminium concentration decreases. The acidity decrease seems to originate mostly from the low temperature peak which is assigned to weak Lewis and Brønsted acid sites whereas the high temperature peak decreases only slightly. Interestingly, the acid site distribution does not change largely, with the highest proportion of sites ascribed to medium strength acid sites. Moreover, the NH_3-TPD profiles show that the sol-gel materials displayed a greater total number of acid sites with respect to their analogous SAS and FSP materials.

Table 4. 3: Acid properties of SAS-*x*, FSP-*x* and SG-*x* samples determined by NH_3-TPD.

Sample	Acid site concentration (x10^{-4} mmol g^{-1})	Acid site density (x10^{-4} mmol m^{-2})
SAS-1	600	6.1
SAS-4	121	2.8
SAS-10	27	0.5
FSP-1	1380	9.9
FSP-4	478	3.3
FSP-10	238	1.4
SG-1	463	1.2
SG-4	188	0.6
SG-10	73	0.2

A method often used to determine the acidity of supports and catalysts is Diffuse Reflectance Fourier Transform Infrared Spectroscopy with adsorbed pyridine e(Pyridine-DRIFTS). The lone-pair electrons of nitrogen are involved in different types of interactions with the surface acid sites. This technique is used to further differentiate the various acid sites present allowing for a clearer assessment of the nature and evolution of the acidity with thermal treatment.

As previously discussed, three modes of adsorption have been observed: (i) protons transfer at BASs (pyridinium ions); (ii) electrons transfer at LASs (molecularly coordinated pyridine); and (iii) hydrogen bonding to surface hydroxy groups. Each mode of adsorption displays IR spectra peaks at different wavelengths allowing for their identification and distinguishment. Pyridine, coordinated with the surface LAS, yields a peak at 1450 cm^{-1}, protonated pyridine on the surface BAS a peak at 1540 cm^{-1}. A combination of both LAS and BAS also yields a peak at 1490 cm^{-1} and an additional band centred around 1600 cm^{-1} is generally assigned to hydrogen-bonded pyridine.

Fig 4.7 shows the DRIFTS spectra of SAS, FSP and sol-gel materials after pyridine adsorption at 150 °C, followed by thermal treatment at 400 °C. Lewis (1450 cm^{-1}) and Brønsted (1545 cm^{-1}) bands are clearly observed. The evolution of the intensities of these peaks with desorption temperature (150 °C, 400 °C) was used to qualitatively evaluate the amount of total and strong acid sites.

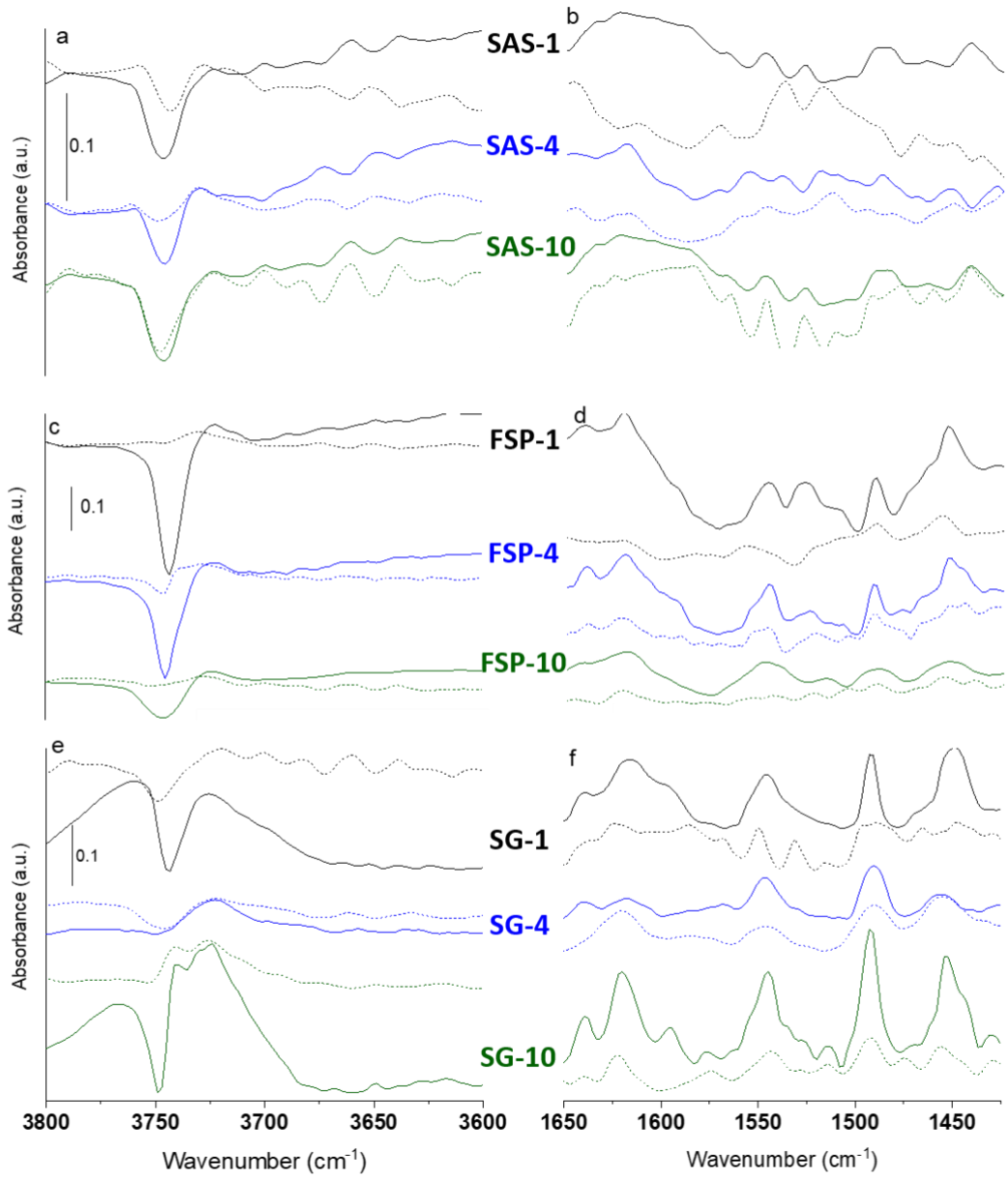

Figure 4. 7: DRIFTS spectra of total (full line) and strong (dashed lines) acid sites in the Lewis and Brønsted acid site stretching region (1650-1400 cm^{-1}) for (b) SAS-x; (d) FSP-x; and (f) SG-x and the corresponding hydroxyl (OH) stretching region (3800-3600 cm^{-1}) for (a) SAS-x; (c) FSP-x; and (e) SG-x ASA materials.

The DRIFTS spectra display characteristic bands of Brønsted acid sites at 1540 cm^{-1} with the intensity of these absorption peaks increasing in the order of Si/Al: 10<4<1. Both bands at *ca.* 1540 cm^{-1} and 1640 cm^{-1}, characteristic of the ν_{19b} and ν_{19a} ring vibrations of pyridinium ions, indicating the chemisorption of pyridine on strong Brønsted acid sites (BAS) increase in intensity. This is in part due to dehydration of physisorbed and chemisorbed water forming additional Brønsted acid sites. With regards to the Lewis acid sites, the opposite trend exists. This is evidenced in the decreased intensity of the bands at *ca.* 1450 cm^{-1} and 1620 cm^{-1} corresponding to the ν_{8a} and ν_{19b} modes, respectively, of pyridine coordinated to Lewis acid sites (LAS). The negative peak centred in the 3750-3740 cm^{-1} region of the ν_{OH} stretching region represents the removal of OH groups. This is a direct consequence of the formation of pyridinium ions. On close inspection, the SAS materials displayed bands at 3650 cm^{-1}, 3670 cm^{-1} and 3710 cm^{-1} assigned to extra-framework AlOH (EFAL) possessing intermediate acidic character and OH stretching vibrations of silanols, hydrogen bonded with other silanols (Si-OH_H), respectively.[8,17,9] The absence of the band corresponding to extra-framework AlOH in the FSP materials suggests the greater level of homogeneous mixing of Si and Al inherent to this method.

With this insight, semi-quantitative evaluation of the ratio of BAS and LAS sites for the SAS, FSP and sol-gel materials is presented, Fig 4. 8. This method is based on the integrated band intensities of the two bands of the ν_{8a} modes and ν_{19b} ring vibrations of pyridinium ions at 1450 cm^{-1} and 1540 cm^{-1}.

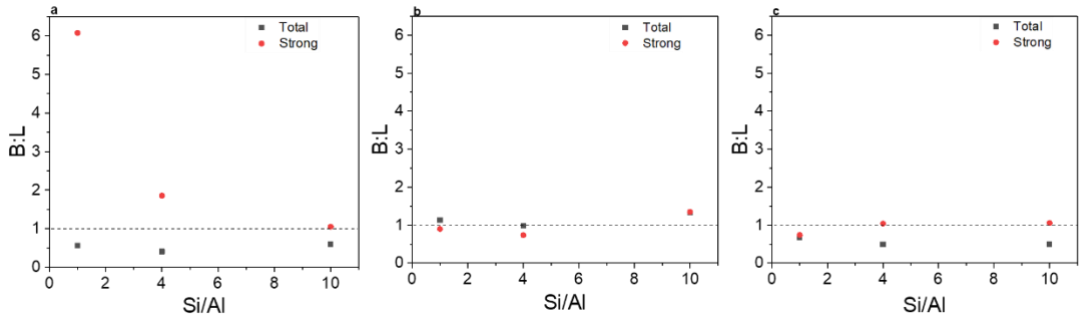

Figure 4. 8: Ratio of total and strong Brønsted and Lewis acid sites as a function of Si/Al in (a) SAS 1-10; (b) FSP 1-10 and; (c) SG 1-10 ASA materials.

Figure 4. 8 illustrates the compositional dependency of the B:L, total and strong acid sites whereby the SAS-1 material displays the highest measured B:L (B:L=6). The B:L ratio is governed by surface acid site properties of the catalysts whereby the SAS-1 displays enhanced strong Brønsted acidity and the highest overall B:L ratio after thermal treatment. This consideration is important given the high temperatures employed in the non-oxidative propane dehydrogenation reaction. Among the different roles of supports, the most relevant are (i) dispersing the active phase of the catalyst, (ii) increasing metal surface area and (iii) improving the catalytic performance through interactions between the metal and support. In addition, a balance of BASs and LASs is key for propane activation and enhancement of propene selectivity. This is valid in the case of a high proportion of Brønsted acid sites which can induce further propene deep dehydrogenation as well as side reactions such as hydrogenolysis, cracking, aromatization and isomerization.[18–20]

It is important to note that the B:L is dependent on the Si/Al and a B:L>0 represents a greater relative proportion of strong BASs with respect to strong LASs. In comparison, the analogous SG and FSP materials display an opposing trend with the highest B:L corresponding with the highest Si/Al. Noticeable differences in B:L values of strong acid sites exist. The presence of mixed BASs and LASs of varying strength in the SAS-*x*, FSP-*x* and SG-*x* materials are a direct consequence of dehydration and dehydroxylation reactions.

4.3 Methanol-to-Dimethylether (DME): Catalytic Performance of FSP-ASAs

Contrary to the propane dehydrogenation reaction, the methanol-to-DME (MTD) reaction is exothermic and is thus not thermodynamically favoured at high temperatures. To further evaluate and understand the effect of the surface acidity on acid-catalysed reactions on a series of ASA materials, the MTD reaction was chosen as a model reaction. With this in mind, a synergy between the MTD reaction and Pt-based catalysts applied for the PDH reaction, would provide useful insights.

The FSP-synthesized ASAs were examined using the methanol-to-DME reaction as a test reaction. The catalytic performances of FSP synthesized ASAs tested for methanol dehydration to DME under isothermal (275 °C) and iso-conversion (*ca.* 20%) conditions

were investigated (*see* Appendix Figs 7. 4-5). Similar to the dehydrogenation of propane, reactant conversion, product distribution and yield are strongly dependent on the surface acidity (nature, strength, distribution and concentration) and textural properties (BET total surface area).

Under isothermal conditions the methanol conversion coincides directly with the catalysts' surface acidity. This illustrates the influence of compositional differences whereby low Si/Al ratios and higher acid site concentrations correspond to enhanced methanol conversion.

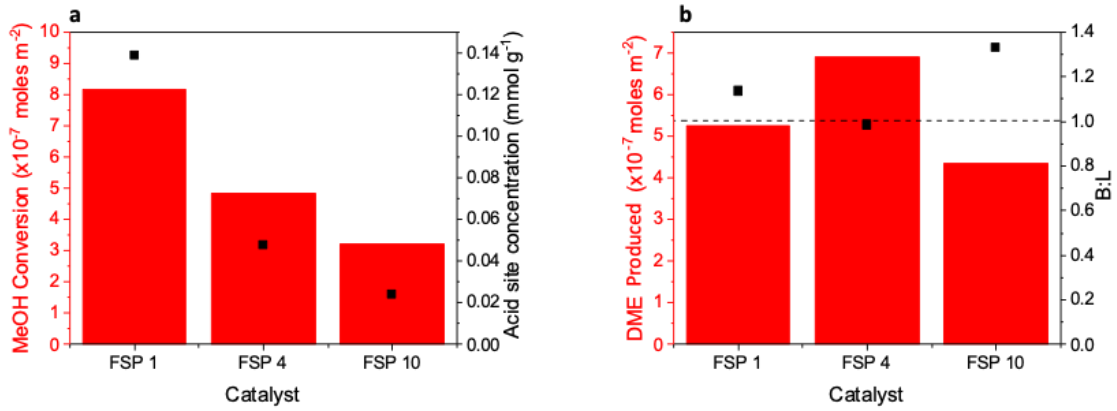

Figure 4.9: Correlations between (a) converted methanol per unit area and acid site concentration; and (b) DME production per unit area and ratio of surficial acid site, for FSP-synthesized ASAs with systematically varied Si/Al ratios.

It is evident that the methanol conversion increases with decreasing Si/Al ratio which is consistent with findings by Jiang and co-workers.[21] This result implies the role of the acid sites in the catalytic dehydration of methanol to DME given the FSP catalysts exhibit similar surface areas. Thus, the observed differences can be ascribed to the surface acidity. Upon evaluation of the surface area normalized production of DME (Fig 4. 9b) the trend is more ambiguous decreasing in the following order: FSP 4 > FSP 1 > FSP 10. The variable nature of the produced DME insinuates the concerted action of Brønsted and Lewis acid sites which at an optimal composition (moderate Si/Al) leads to a bifunctional acid catalyst. This further corroborates surface acidity requirements pertinent for optimal PDH activity.

Additionally, Takeguchi *et al*. reported that the rate of methanol dehydration rates was slower on Brønsted acid sites relative to Lewis acid sites.[22] With this knowledge, the experimental findings demonstrate that acid-base pair sites that bind mildly to the reactant are needed to exhibit enhanced dehydration activity while not poisoning the catalyst surface.

Comparison of the ratio of surface Brønsted and Lewis (B:L) acid sites was conducted to further examine the influence and synergism of the nature of the acid sites on the surface area normalized produced DME. Figure 4. 9b illustrates that B:L is pertinent to DME formation and yield. The dependence of the produced DME at iso-conversion of methanol on the BAS/LAS (B:L) ratio indicates that at a low B:L ratio, the DME formation is enhanced. The lowest B:L ratio (0.98), attributed to FSP 4, displays the largest production of DME. This corresponds to a balance in the relative proportion of surficial Brønsted and Lewis acid sites.

In the case of FSP 1 and FSP 10 which have B:L ratios of 1.13 and 1.33, respectively, an incremental rise in the B:L results in decreases in normalized DME selectivity. It is fair to assume that the influence of the balance in the acid sites has a profound effect on product distribution. This further demonstrates that FSP-synthesized ASAs with moderate proportion and strength BASs along with lower B:L ratios are highly selective for generating DME.

Further evaluation of the effect of the surface area normalized acid site density and yield of DME, is highly informative. DME yield is favoured by moderate acid site density and not favoured by the high acid site density, Fig 4. 10. After a two-hour reaction time the resulting DME yield decreases in the order: FSP 4 > FSP 10 > FSP 1. Thus, it fair to imply that the rate limiting step in DME synthesis is determined by acid properties such as the acid site strength and number of acid sites.

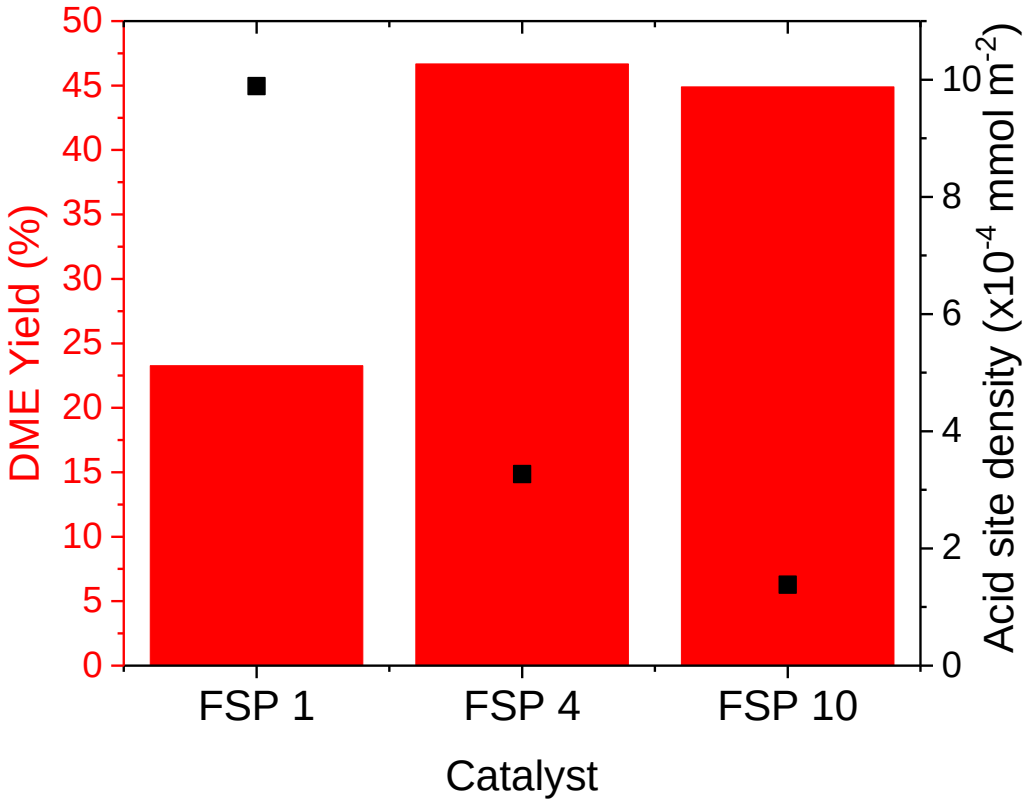

Figure 4.10: Correlations between initial DME yield and acid site density, for FSP-synthesized ASAs with systematically varied Si/Al ratios under iso-conversion conditions.

The results indicated the possibility of synergy between the Brønsted and Lewis acid sites in methanol dehydration to DME. It is clear that compositional and microstructural differences, modulated through systematic variations in Si/Al ratios, directly impact catalytic performance.

However, coking and other secondary reactions occur on sites with strong acidity a direct consequence of the complex distribution of surface acid site strength resulting in the decrease of DME yield and catalyst deactivation. The low DME yield over FSP 1 was due to a higher amount of surficial strong acid sites which induced the deactivation of the catalyst and the decrease in DME yield. Additionally, water is another reaction product known to deactivate the catalyst through competitive adsorption on the active sites.

This is particularly important in context of the direct dehydrogenation of propane whereby bifunctional dehydrogenation catalysts, constituted by a coordinatively unsaturated active metal (M_{cus}^{+}) and an acidic support, are utilised. A support effect exists as Brønsted and Lewis acid sites on the support surface promote cracking while isomerization proceeds *via* Brønsted acid sites. The C-H bonds in alkenes are more reactive than C-C bonds, thus catalysts that favour C-H over C-C bond cleavage are required to increase olefin selectivity. Limited support acidity, with moderate strength acid sites, is needed to avoid undesirable side reactions. However, in order to reach a high dispersion of the active metal on the support, Lewis acid sites and amphoteric OH groups are often required.[23]

4.4 Conclusions

This work has demonstrated that ASA mixed metal oxides can be readily made by the SAS method and similar acid site concentrations to the state-of-the-art FSP ASAs can be obtained. Through extensive characterization microstructural, textural and morphological similarities of the SAS- and FSP-synthesized ASAs have been realised.

The SAS methodology was able to control the bulk morphology and composition when compositional parameters were systematically evaluated, showing morphological similarities to sol-gel and FSP synthesized ASAs. On an atomic level the SAS ASAs have similarities to FSP synthesized ASAs, albeit distinguished only by the distribution of environments present. Such minute differences occur in the observed acid sites. The performance of acid-catalysed reactions is largely dictated by the acidic features such as type, amount strength and local environments acid sites. However, the SAS process remains more effective in controlling compositional features resulting in synergies to ASAs produced *via* FSP processing but current lack of understanding would hinder the ability to fully exploit the potential of the synthesis protocol at an industrial scale currently.

With respect to the MTD reaction the structural descriptors described above jointly contribute to the high catalytic activity, DME selectivity, and DME yield of the catalyst with moderate surface acidity. These insights can be applied to the direct dehydrogenation of propane whereby an intermediate acid-base strength of the active site is also required. The

balance in acid sites (B:L) appears to be pertinent to desired product (DME) yield and catalyst productivity, which is maximised an intermediate Si/Al (Si/Al = 4). Increasing the Si/Al in bifunctional catalysts results in improvements in dehydrogenation activity by decreasing the C-H activation barriers of the kinetically favoured concerted mechanism.

4.5 References

1 Z. Wang, Y. Jiang, A. Baiker and J. Huang, Efficient Acid-Catalyzed Conversion of Phenylglyoxal to Mandelates on Flame-Derived Silica/Alumina, *ACS Catal.*, 2013, **3**, 1573–1577.

2 B. Schimmoeller, F. Hoxha, T. Mallat, F. Krumeich, S. E. Pratsinis and A. Baiker, Fine tuning the surface acid/base properties of single step flame-made Pt/alumina, *Applied Catalysis A: General*, 2010, **374**, 48–57.

3 S. Esposito, "Traditional" Sol-Gel Chemistry as a Powerful Tool for the Preparation of Supported Metal and Metal Oxide Catalysts, *Materials*, 2019, **12**, 668.

4 C. Chizallet and P. Raybaud, Pseudo-Bridging Silanols as Versatile Brønsted Acid Sites of Amorphous Aluminosilicate Surfaces, *Angewandte Chemie International Edition*, 2009, **48**, 2891–2893.

5 K. Larmier, C. Chizallet, S. Maury, N. Cadran, J. Abboud, A.-F. Lamic-Humblot, E. Marceau and H. Lauron-Pernot, Isopropanol Dehydration on Amorphous Silica–Alumina: Synergy of Brønsted and Lewis Acidities at Pseudo-Bridging Silanols, *Angew. Chem.*, 2017, **129**, 236–240.

6 J. Huang, N. van Vegten, Y. Jiang, M. Hunger and A. Baiker, Increasing the Brønsted Acidity of Flame-Derived Silica/Alumina up to Zeolitic Strength, *Angewandte Chemie International Edition*, 2010, **49**, 7776–7781.

7 Y. Matsunaga, H. Yamazaki, T. Yokoi, T. Tatsumi and J. N. Kondo, IR Characterization of Homogeneously Mixed Silica–Alumina Samples and Dealuminated Y Zeolites by Using Pyridine, CO, and Propene Probe Molecules, *J. Phys. Chem. C*, 2013, **117**, 14043–14050.

8 E. J. M. Hensen, D. G. Poduval, V. Degirmenci, D. A. J. M. Ligthart, W. Chen, F. Maugé, M. S. Rigutto and J. A. R. van Veen, Acidity Characterization of Amorphous Silica–Alumina, *J. Phys. Chem. C*, 2012, **116**, 21416–21429.

9 J. Sjöblom, S. E. Friberg and A. Amran, Reaction Between Aluminum Nitrate Nonahydrate and Tetraethoxysilane in Ethanol, *Journal of Dispersion Science and Technology*, 1995, **16**, 31–50.

10 A. N. Mukhamed'yarova, O. V. Nesterova, K. S. Boretsky, J. D. Skibina, A. V. Boretskaya, S. R. Egorova and A. A. Lamberov, Influence of the Obtaining Method on the Properties of Amorphous Aluminum Compounds, *Coatings*, 2019, **9**, 41.

11 K.-T. Hwang, H.-S. Lee, S.-H. Lee, K.-C. Chung, S.-S. Park and J.-H. Lee, Synthesis of aluminium hydrates by a precipitation method and their use in coatings for ceramic membranes, *Journal of the European Ceramic Society*, 2001, **21**, 375–380.

12 Z. Wang, Y. Jiang, X. Yi, C. Zhou, A. Rawal, J. Hook, Z. Liu, F. Deng, A. Zheng, M. Hunger, A. Baiker and J. Huang, High population and dispersion of pentacoordinated AlV species on the surface of flame-made amorphous silica-alumina, *Science Bulletin*, , DOI:10.1016/j.scib.2019.04.002.

13 F. A. Perras, Z. Wang, T. Kobayashi, A. Baiker, J. Huang and M. Pruski, Shedding light on the atomic-scale structure of amorphous silica–alumina and its Brønsted acid sites, *Phys. Chem. Chem. Phys.*, 2019, **21**, 19529–19537.
14 A. Omegna, J. A. van Bokhoven and R. Prins, Flexible Aluminum Coordination in Alumino−Silicates. Structure of Zeolite H−USY and Amorphous Silica−Alumina, *J. Phys. Chem. B*, 2003, **107**, 8854–8860.
15 L. F. Isernia, FTIR study of the relation, between extra-framework aluminum species and the adsorbed molecular water, and its effect on the acidity in ZSM-5 steamed zeolite, *Materials Research*, 2013, **16**, 792–802.
16 F. Jin and Y. Li, A FTIR and TPD examination of the distributive properties of acid sites on ZSM-5 zeolite with pyridine as a probe molecule, *Catalysis Today*, 2009, **145**, 101–107.
17 R. Buzzoni, S. Bordiga, G. Ricchiardi, C. Lamberti, A. Zecchina and G. Bellussi, Interaction of Pyridine with Acidic (H-ZSM5, H-β, H-MORD Zeolites) and Superacidic (H-Nafion Membrane) Systems: An IR Investigation, *Langmuir*, 1996, **12**, 930–940.
18 Z.-J. Zhao, C. Chiu and J. Gong, Molecular understandings on the activation of light hydrocarbons over heterogeneous catalysts, *Chem. Sci.*, 2015, **6**, 4403–4425.
19 A. Farjoo, F. Khorasheh, S. Niknaddaf and M. Soltani, Kinetic modeling of side reactions in propane dehydrogenation over Pt - Sn/γ - Al2O3 catalyst, *Scientia Iranica*, 2011, **18**, 458–464.
20 Q. Li, Z. Sui, X. Zhou, Y. Zhu, J. Zhou and D. Chen, Coke Formation on Pt–Sn/Al2O3 Catalyst in Propane Dehydrogenation: Coke Characterization and Kinetic Study, *Top Catal*, 2011, **54**, 888.
21 S. Jiang, J.-S. Hwang, T.-H. Jin, T. Cai, W. Cho, Y.-S. Baek and S.-E. Park, Dehydration of Methanol to Dimethyl Ether over ZSM-5 Zeolite, *Bulletin of the Korean Chemical Society*, 2004, **25**, 185–189.
22 T. Takeguchi, K. Yanagisawa, T. Inui and M. Inoue, Effect of the property of solid acid upon syngas-to-dimethyl ether conversion on the hybrid catalysts composed of Cu–Zn–Ga and solid acids, *Applied Catalysis A: General*, 2000, **192**, 201–209.
23 R. M. Mironenko, O. B. Belskaya, V. P. Talsi, T. I. Gulyaeva, M. O. Kazakov, A. I. Nizovskii, A. V. Kalinkin, V. I. Bukhtiyarov, A. V. Lavrenov and V. A. Likholobov, Effect of γ-Al2O3 hydrothermal treatment on the formation and properties of platinum sites in Pt/γ-Al2O3 catalysts, *Applied Catalysis A: General*, 2014, **469**, 472–482.

5 Supported Pt-based catalysts for the non-oxidative propane dehydrogenation (PDH) reaction

5.1 Introduction

The catalytic dehydrogenation of propane typically requires bifunctional catalysts comprising of an acidic support and active component such as noble metals (Chapter 1.3). Several commercialised processes utilise Pt-based catalysts where the support and Pt nanoparticles provide the necessary acidity and dehydrogenation functions.

Propane dehydrogenation, displays site (acid site) and size (platinum nanoparticle size) dependency both of which significantly influence the activity, selectivity, and stability with added implications on the reaction pathway.[1] Under the reaction temperatures commonly applied (See Chapter 1, Table 1.2), instantaneous and continuous catalyst deactivation is a persistent and insurmountable issue. For instance, under typical reaction conditions side reactions such as hydrogenolysis, cracking, aromatization and isomerization are thermodynamically and kinetically favoured.[1–3] It is understood that large Pt ensembles, a result of sintering, and Brønsted acid sites favour the numerous side reactions.[4] [5,6] [7–9]

Therefore, it is necessary to study and correlate the particle size effects induced by the catalytic design and preparation techniques with the aim of enhancing the understanding of the relevant structure–performance relationships. Additionally, the preparation of Pt-based catalysts with the smallest possible nanoparticle size and distribution, maximizes metal utilization. Moreover, a comprehensive review of Pt-based catalysts (Chapter 1.B) has proved that unique catalytic properties are attributed to smaller, isolated, and uniformly dispersed Pt nanoparticles.

The efficacy of the catalyst preparation method was measured based on the resultant particle size, particle size distribution, dispersion and thermal stabilization. At this juncture, an accompanying systematic study was carried out to determine the best possible method for the immobilization of Pt onto the acidic (ASA) support.

5.2 Platinum deposition method development

In heterogeneous catalysis, the synthesis of supported metal nanoparticles is usually aimed at producing smaller particles. This is to efficiently utilize the metal, exposing more atoms, optimizing the number of active sites for a desired reaction. Conventional such as, incipient wetness impregnation (IWI) methods of catalyst synthesis often use simple impregnation of the support with a solution of the metal precursor.[10] This usually fails to produce well dispersed particles and results in a wide particle size distribution. Other methods such as chemical vapour impregnation (CVI) offer metal deposition through the application of volatile precursors, which react and decompose on the support surface to produce the desired supported metal catalyst.

This study was initiated to reproducibly design highly dispersed metal catalysts and ultimately allow for a better understanding of the role of various parameters on reaction activity and selectivity. To do so Charge Enhanced Dry Impregnation, or CEDI, a pore filling analog to IWI, which involves adjusting the pH of the precursor solution and the colloidal, sol-immobilisation (sol), techniques were systematically evaluated.

After synthesis a microscopy (HRTEM) study was undertaken to assess the efficacy of each method. As control samples, a set of catalysts were prepared *via* the IWI and CVI whereby appropriate platinum salts were supported on FSP synthesized ASA (Si/Al=1) to form 1 wt.% Pt/SiO_2-Al_2O_3, denoted, Pt/FSP-1.

5.2.1 Control Catalysts: IWI and CVI Pt-based Catalysts

Initially, a set of control Pt-based catalysts were prepared *via* IWI and CVI techniques. HRTEM micrographs of both reduced IWI and CVI prepared catalysts display non-uniform Pt dispersion with large agglomerates dominating, Fig 5. 1. Average Pt particle sizes of the IWI and CVI catalysts were measured with characteristic values in the ranges of *ca.* 10-40 nm and *ca.* 30-60 nm, respectively. Possible considerations of the non-uniform and broad particle size distribution can be attributed to weaker metal-support interactions between

the Pt salts and support resulting in adverse changes in Pt dispersion after drying, calcination, and reduction processes.

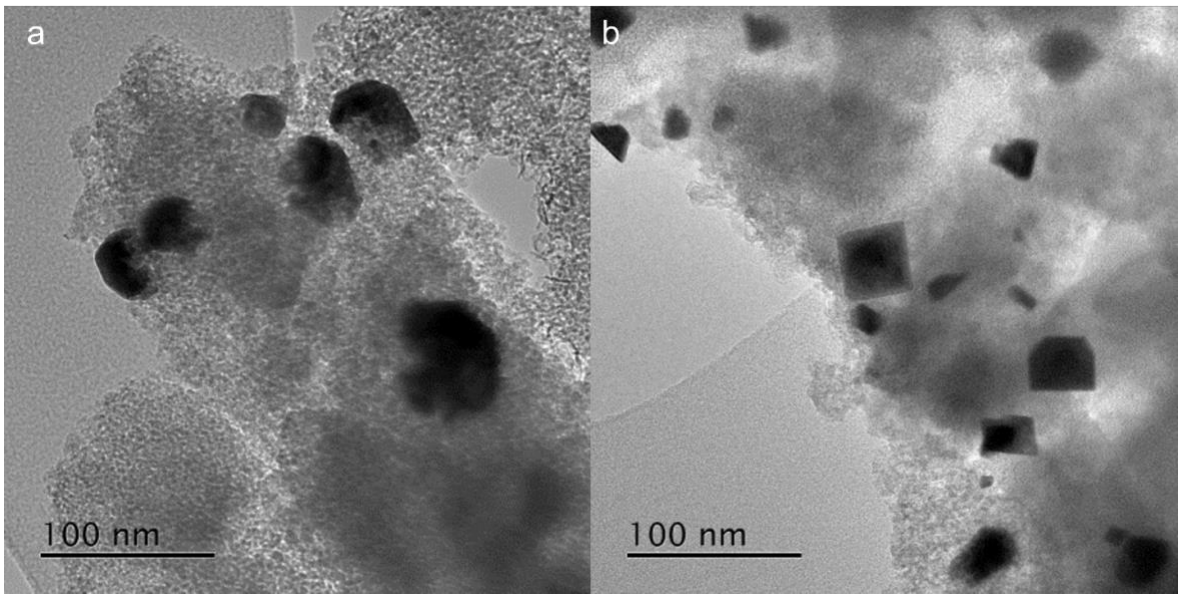

Figure 5.1: HRTEM micrographs of Pt (1 wt.%) deposited onto FSP-1 *via* (a) IWI and; (b) CVI deposition methods.

In theory by optimizing the conditions to obtain the strongest interaction between support and precursor the migration of metal is lessened during thermal treatment, resulting in smaller catalysts.

5.3 Sol-immobilisation for Pt-based Catalyst Synthesis

It was anticipated that the sol immobilisation method, involving the deposition of pre-formed ligand stabilized nanoparticles onto an oxidic support, would offer the greatest control of the resulting nanoparticle morphology, size, and size distribution. Inherent to the sol immobilisation is the reduced effect of support surface chemistry and morphology on particle size of nanoparticles, relative to other catalyst preparation methods. Experimental parameters within the sol immobilisation can be tuned to control particle size and shape. Such factors include the nature and choice of the reducing agents, solvents and stabilizing polymers.[11,12] A systematic study was conducted with a solution containing

hexachloroplatinic acid, $PtCl_6^{2-}$, stabilized with polyvinyl alcohol (PVA) and supported on FSP synthesized ASA (Si/Al=1) to form 1 wt.% Pt/SiO_2-Al_2O_3.

5.3.1 Effect of Experimental Parameters

5.3.1.1 Drying Procedure and Support Slurry

In comparison to the IWI and CVI catalysts the sol-derived catalysts display smaller, Pt nanoparticles with a narrow size distribution (2.7 ± 0.9 nm), Fig 5. 2. However, a degree of preferential agglomeration emerged with the resultant clustering appearing on certain areas of the support surface. The influence of the reducing agent, changes to the preparation strategy, support synthesis strategy and nature of the support were investigated.

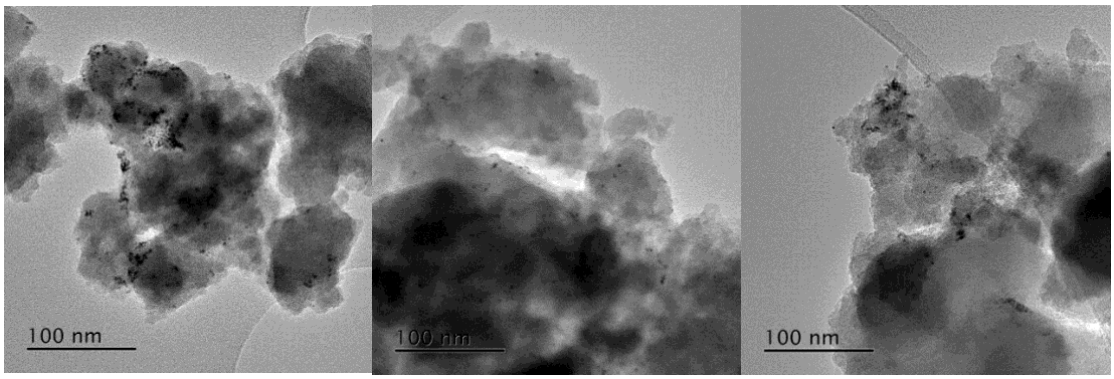

Figure 5.2: HRTEM micrographs of Pt/FSP-1 prepared *via* sol immobilisation and dried at room temperature.

The support being suspended in solution as a slurry prior to Pt deposition, increasing the platinum to reducing agent ratio or a room temperature post-synthesis drying approach appeared to not resolve the preferential deposition.

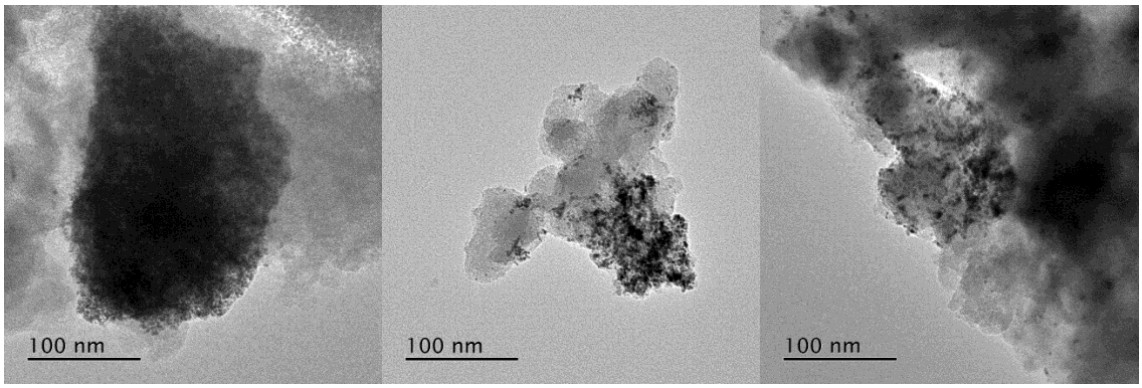

Figure 5 3:HRTEM images of Pt deposited onto FSP-1 *via* sol immobilisation in which the support was suspended in solution prior to adding the H_2PtCl_6 solution.

The room temperature dried catalyst initially appears to circumvent the observed clustering phenomena to an extent, Fig 5. 2. However, on closer inspection multiple HRTEM images show there to be less Pt on the support and the clustering seems to still be present.

5.3.1.2 Reductant Concentration and ASA Support

The expectation was that increasing the $NaBH_4$:Pt ratio would induce faster reduction of the Pt complex ions and nuclei formation pertinent to formation of small homogeneous nanoparticles.[12] Thus, the influence of the reduction and thermally induced particle growth would be lessened. Contrary to reports in literature the clustering persisted in an identical preferential manner to the drying procedure and support suspension as a slurry.

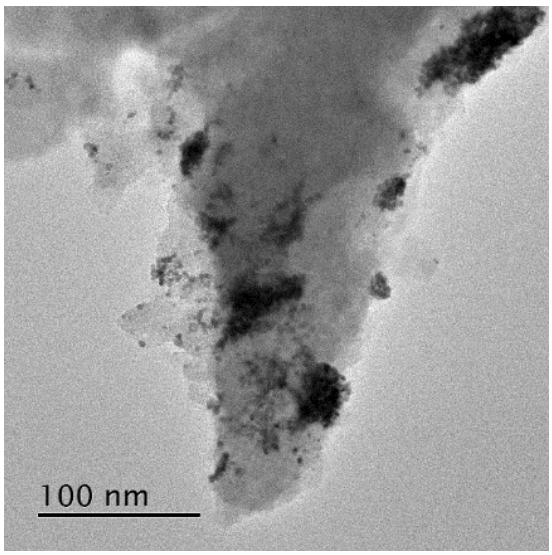

Figure 5.4: HRTEM image of Pt deposited onto FSP-1 *via* sol immobilisation in which the $NaBH_4$:Pt ratio was 16.

For a more robust analysis of the effect of the support synthesis strategy, an analogous catalyst was prepared with Pt deposited on sol-gel synthesized ASA (Si/Al=1), denoted Pt/SG-1 for brevity. Similarly, no observable differences in clustering were seen on Pt/SG-1 relative to Pt/FSP-1 under an analogous sol-immobilisation preparation. The extent of the clustering made it difficult to accurately determine the particle size and size distribution. HRTEM images displayed clear preferential deposition of Pt nanoparticles onto specific support areas, Fig 5.5. This suggested that the preferential clustering was not due to a contaminant introduced in the support preparation, or that the contaminant was present in both samples, which seems unlikely given the difference in precursors/conditions used.

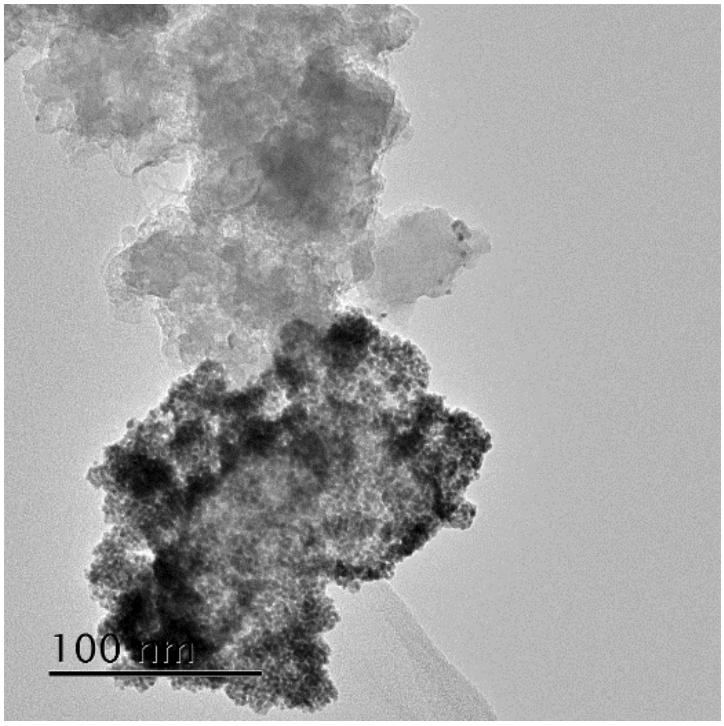

Figure 5.5: HRTEM image of Pt deposited on SG-1 *via* sol-immobilisation.

XPS analyses were performed to evaluate the effect of preparation method on the surface elemental composition and Pt clustering. As illustrated in Table 5.1 Pt/SG-1 was characterized by a slightly lower Si/Al ratio, relative to the nominal value, and less surface carbon than Pt/FSP-1. This is expected as the combustion of the atomised precursor spray in the FSP process can result in the formation and deposition of carbon on the metal oxide surface. With the sol-gel process in mind, it is important to recognize the effect of the aging,

drying and subsequent heat treatment steps on the lower carbon content. Thus, both the more homogeneous elemental distribution and higher surface carbon content are likely due to the greater control inherent to the FSP method and incomplete combustion of organics due to the short residence time.

Table 5.1: Atomic concentration (at. %) of elements on the support surface and Si/Al determined by XPS.

Catalyst	**Nominal Si/Al ratio**	**Concentration / at. %**				**Si/Al**
		O	Si	Al	C	
Pt/FSP-1	1	50.4	9.5	9.7	26.1	1.0
Pt/SG-1	1	66.9	10.8	13.7	8.6	0.7

5.3.1.3 Nature of Support

At this juncture the issue of preferential deposition of Pt on the sol-derived supported catalyst was probed further, exploring the influence of the nature of the support. Initially, Pt was deposited onto commercially obtained SiO_2 and TiO_2. This was also to try and rule out the possibility of the Pt particles agglomerating in the solution before being deposited on the support. HRTEM images displayed well dispersed Pt particles on SiO_2 and TiO_2 with more easily distinguishable, and uniform Pt particles present relative to analogous Pt/ASA catalysts, Fig 5. 6.

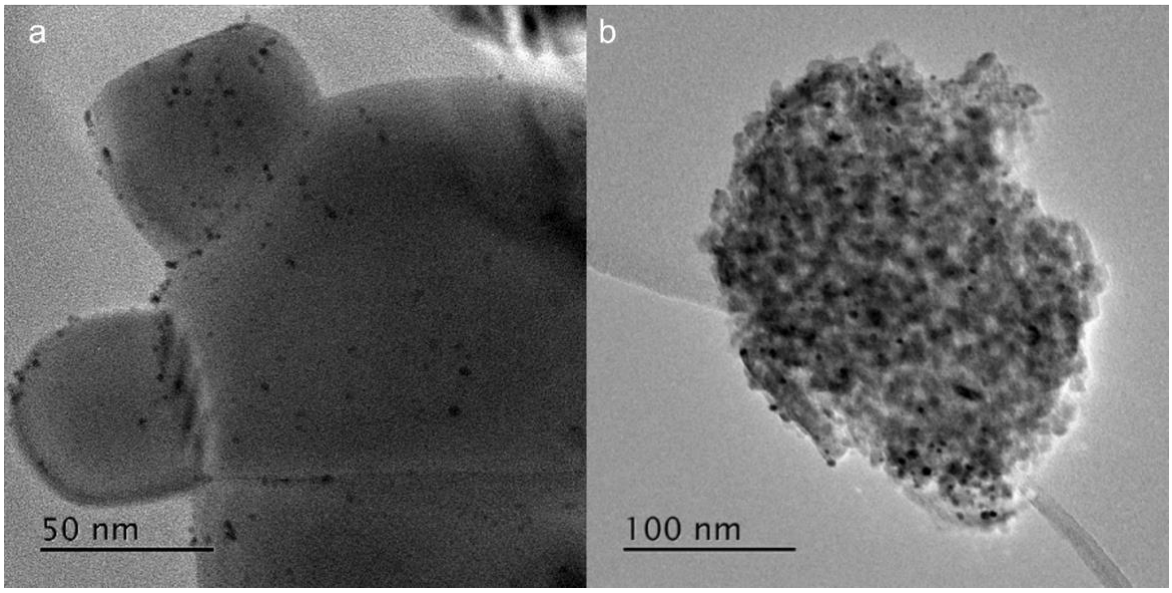

Figure 5.6: HRTEM images of (a) Pt/TiO_2; and (b) Pt/SiO_2 prepared *via* sol immobilisation.

A possible rationale is the effect of surface acidity and surface structure as Brønsted acid sites are the main distinguishing factor between the SiO_2-Al_2O_3, SiO_2 and TiO_2 supports utilised. Further, direct comparison of Pt deposited on SiO_2 and TiO_2 reveal less clustering in the latter thus suggesting an additional effect from the reducibility of the oxide support which permits strong metal support interactions after metal deposition and upon reduction. The images display no evidence of clustering of the Pt particles, which means that the clustering problem is a result of the ASA support itself, rather than the preparation method.

5.3.1.4 Thermal and Reflux Removal Methods

Further, the effect of the approach to remove the protective ligand, Polyvinyl Alcohol (PVA) was also investigated. Several PVA removal methods were explored including calcinations at various temperatures (200 °C, 300 °C, 400 °C). However, the removal of the stabilizing polymer is challenging with thermal, oxidative approaches known to lead to an increase in the size of the nanoparticles.[13] Lopez-Sanchez *et al*. evaluated a facile, solvent extraction approach for the removal of stabilizer-ligands from supported gold and gold-palladium nanoparticles without significantly affecting nanoparticle size and structure.[14] It is also well known that the partial or complete removal of the ligand can enhance metal-support interactions thus improving activity, selectivity to desired products and catalyst durability.

Consequently, a comparable facile approach involving a heated (90 °C) reflux in water under various time intervals (30, 60, and 120 minutes) was utilised.

The average particle size increased as the calcination temperature increased, likely due to sintering. The particle size also increased with longer reflux times and reflux solution temperatures. Particle size distribution analysis shows little statistical difference in 200 °C and 300 °C post-synthesis calcinations as the particle size and size distribution display no statistical difference. However, further increase in the calcination temperature, 400 °C, result in a larger particle size and less uniformity in particle size.

Table 5.2: Pt particle size and particle size distribution as measured from HRTEM images of post-synthesis thermal and reflux-based stabilizer removal techniques after using the sol-immobilisation method for metal deposition.

Treatment Method	Average Particle Diameter (nm)	Standard Deviation
Calcined at 200 °C	2.4	0.8
Calcined at 300 °C	2.2	0.9
Calcined at 400 °C	4.1	3.4
30 min reflux	2.4	1.4
60 min reflux	2.2	0.8
120 min reflux	3.3	1.2

This data suggests a trend, however, is not as reliable as typical particle counting. This is due to the Pt on the support depositing preferentially, resulting in heavy clustering and making it difficult to differentiate between separate, clustered and sintered particles. More importantly, the data suggests that to retain the structure of the Pt particles there is no need for subsequent thermal treatment in excess of 300 °C. Though no direct evidence of the complete removal of PVA, the particle size and size distribution of the 200 °C, 300 °C removal methods and 30–60-minute reflux conditions show similarity to the aforementioned data (2.7 ± 0.9 nm) illustrated in Fig 5. 2. Additionally, the treatment of

supported sol-derived nanoparticles with hot water under reflux for relatively short time periods is an equally effective approach.

5.4 Charge Enhanced Dry Impregnation (CEDI) for Pt-based Catalyst Synthesis

The charge-enhanced dry impregnation (CEDI) method, first introduced by Cao *et al.* and Zhu *et al.,* has undergone significant development leading to high dispersion and surface loading.[15,16] As previously discussed, (Chapter 2.4.4) this approach combines the simplicity of incipient wetness impregnation with the small particle size obtained from electrostatic adsorption of metal precursors onto oxidic supports. A plethora of studies have investigated the optimization of the method with reports of ultrasmall, isolated metal nanoparticles with particle sizes lower than 2 nm typical of the CEDI method.[17–19] The main aim of the current work was to deposit Pt in a reproducible way across different ASA supports, ensuring small particle size, particle size distribution and high dispersion throughout. To circumvent limitations previously encountered by the sol-immobilization technique, a series of Pt-based catalysts were prepared using the CEDI method and characterized thoroughly.

5.5 CEDI Method Development: Point of Zero Charge (PZC) Determination

With the CEDI approach effective metal deposition requires an interaction between the electrostatically charged surface, and oppositely charged metal precursor ions.[15,20,21] This electrostatic interaction is controlled by the pH of the solution.[22] This enables the ability to buffer aqueous solutions to their oxides' respective Point of Zero Charge (PZC), and in the case of mixed metal oxides this represents charge neutrality of the oxide surface. The concept of charging of metal oxide surfaces stems from the fact that these oxides have a high proportion of hydroxyl groups of differing speciation and location. The resulting strong electrostatic interaction establishes strong metal-support interactions which improves metal dispersion in the final catalyst. Therefore, knowledge of the Point of Zero Charge (PZC) of the support is crucial in carrying out this catalyst preparation technique. Figure 5.7 displays representative values for analogous SAS, FSP and sol-gel synthesized ASAs.

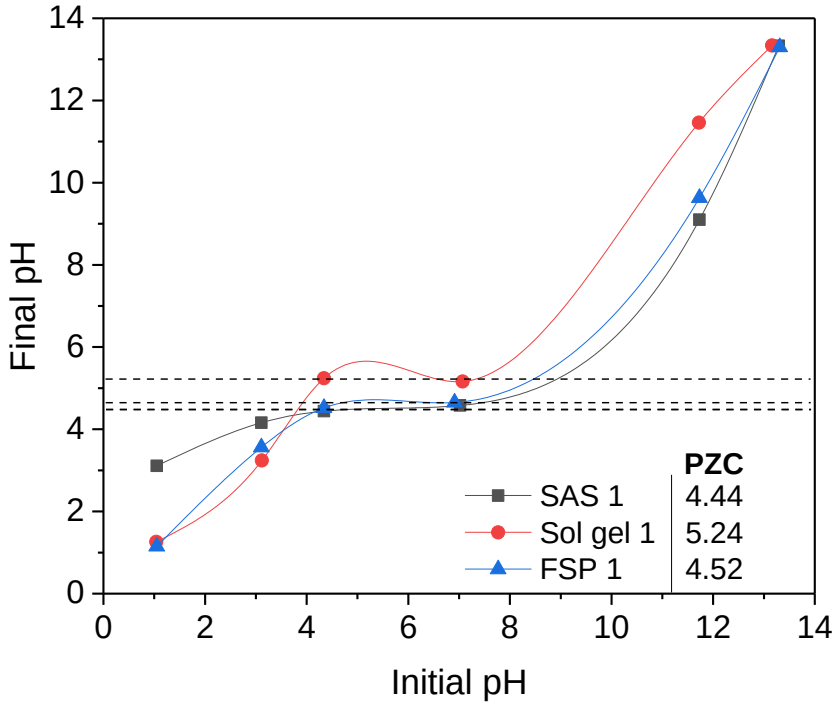

Figure 5.7: Determined PZC of (black) SAS-1, (blue) FSP-1 and (red) SG-1 supports.

5.5.1 CEDI Prepared Pt-based Catalysts: 0.5 wt.% Pt Loading

Initially, a series of Pt-based catalysts were prepared *via* the CEDI approach with tetraammineplatinum (II) hydroxide hydrate (PTA), under iso-metal loading (0.5 wt.%). The appropriate pH for maximal $Pt(NH_3)_4^{2+}$ adsorption and metal uptake as well as PTA concentration on silica-alumina has previously been reported as pH 11 and 0.84 µmol m^{-2}.[23] Thus for the purpose of this study the aqueous solution was adjusted to pH 11 to enhance the electrostatic adsorption of metal precursor ions on the support. Comparisons of the nominal and measured metal loading were conducted with MP-AES and ICP-OES analysis. The results from both techniques indicated negligible variation in Pt loading irrespective of the support preparation method.

Table 5. 3: Determination of elemental analysis of Pt-based catalysts, with nominal metal loading of 0.5 wt.%, by multiple techniques (MP-AES and ICP-OES).

Catalyst[a]	**Pt loading (%)**	
	MP-AES	ICP-OES
0.5Pt/SAS-1	0.54	0.49
0.5Pt/FSP-1	0.51	0.45
0.5Pt/SG-1	0.50	0.47
0.5Pt/SG-4	0.46	0.41
0.5Pt/SG-10	0.43	0.45

a: For simplicity, catalyst labelling is in the format (Weight loading, %) Pt/(Support synthesis technique)-(Support nominal Si/Al value)

Further, representative SEM analysis using secondary electron and backscattered electron imaging modes of the reduced catalyst, Pt/SG-4, are included in Fig 5. 8. A combination of the CEDI catalyst preparation technique and subsequent reduction procedure yielded small particle size, with high dispersion. This has been previously attributed to strong electrostatic adsorption which establishes a stronger interaction between the support and metal precursor, and decreased mobility of Pt species in the final catalyst.[19]

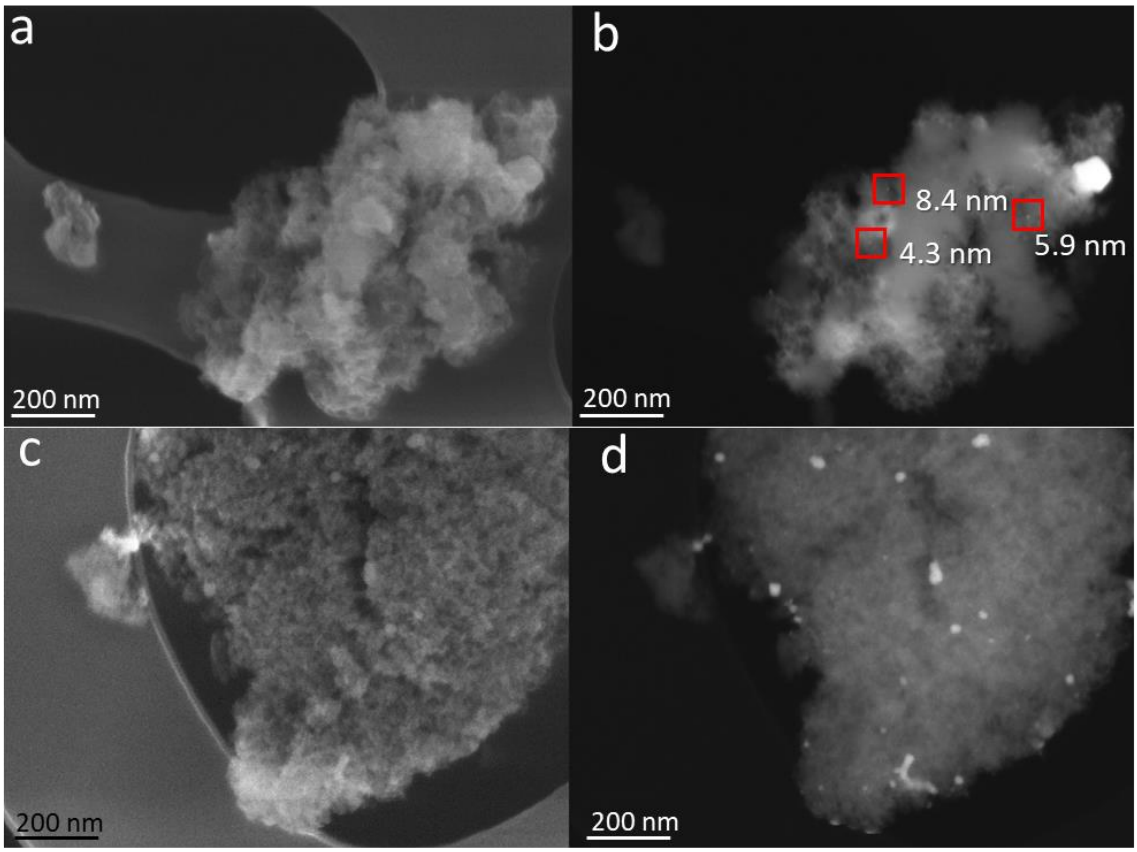

Figure 5.8: SEM images of reduced Pt/SG-4 under (a), (d) Secondary electron; and (b), (d) backscattered electron image modes.

The average diameter of 300 Pt particles was determined as 22.9 nm, with a standard deviation of 14.2 nm. Though the particles were larger than previous sol-immobilisation catalysts which were characterized by particle sizes of below 10 nm in diameter, the dispersion was improved. It is important to note that a discrepancy in particle size counting would likely occur with Pt particles with diameters below 10 nm due to the resolution of the FEG-SEM. With this in mind, TEM analysis of subsequent catalysts would solve this discrepancy.

5.6 CEDI Prepared Pt-based Catalysts: 1 wt.% Pt Loading

At this stage and to circumvent limitations, in Pt clustering, previously encountered by the sol-immobilization technique analogous Pt-based catalysts were prepared *via* the CEDI approach with the PTA, precursor under iso-metal loading (1 wt.%). Upon metal deposition, well dispersed Pt particles were observed on analogous SAS, FSP, and SG prepared support materials (Fig 5.9). Quantitative analysis revealed negligible statistical differences in the resultant catalysts, a consequence of the control offered by the CEDI preparation method. It is important to note that negligible experimental and human error in the particle counting on ImageJ exists which has been considered. The clustering behaviour in IWI, CVI and sol-derived catalyst was avoided by using the CEDI method. A possible rationale being stronger bonding between the Pt metal species and support such that it is difficult to induce the migration of metal species over the support during the reduction process.

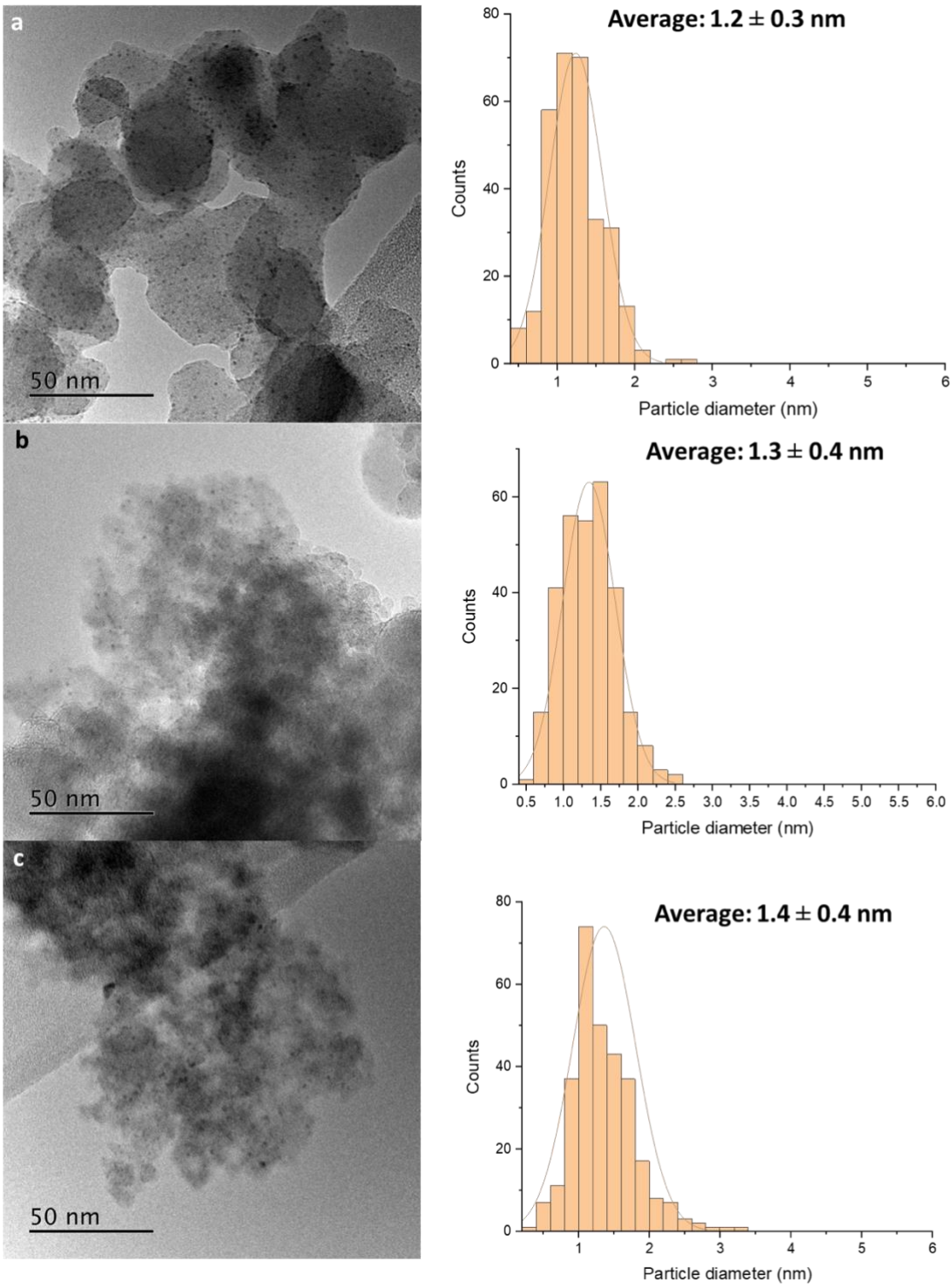

Figure 5.9: HRTEM image and particle distribution analysis of CEDI prepared and reduced (a) Pt/SAS-1, (b) Pt/FSP-1, and (c) Pt/SG-1 catalysts.

However, the applicability of the CEDI method was applied to a crystalline aluminosilicate support, H-ZSM5. The CEDI derived and reduced Pt/H-ZSM5 catalyst ensured small particle size, particle size distribution and high dispersion, Fig 5. 10.

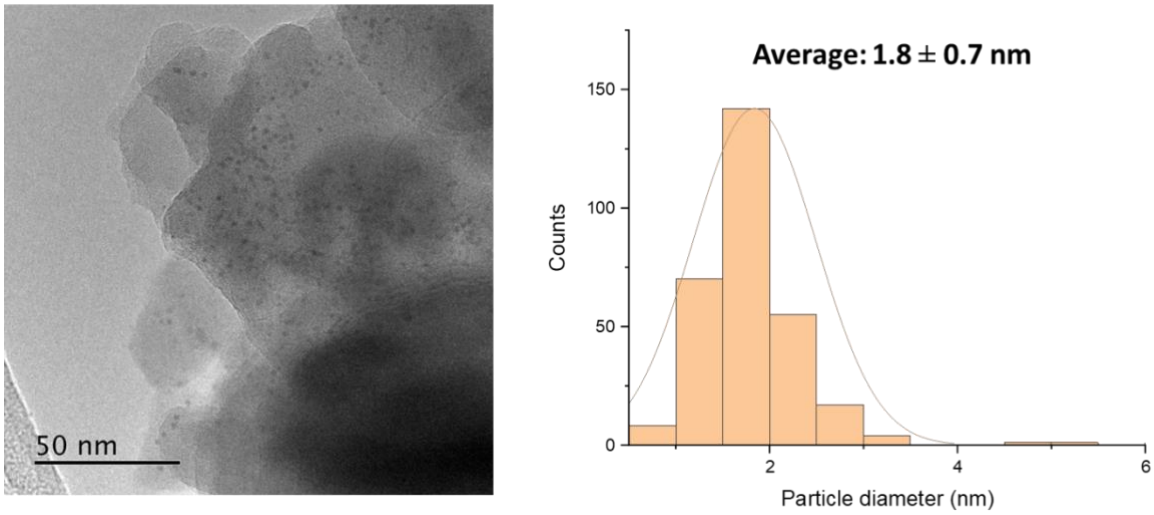

Figure 5.10: HRTEM image and particle distribution analysis of CEDI prepared, and reduced Pt/H-ZSM5 catalyst.

The main aim of the work was to deposit Pt in a reproducible way across different ASA supports. This was confirmed in the HRTEM images (*see* Appendix Figs 7. 16-21**)** and the accompanying particle size and size distribution data on the systematically varied supports illustrated in Table 5. 4.

Table 5.4: Particle sizes and size distributions of Pt-based, CEDI prepared and reduced catalysts with systematically varied supports.

Catalyst	**d_{TEM} (nm)**
Pt/FSP-1	1.3 ± 0.4
Pt/FSP-4	1.7 ± 0.6
Pt/FSP-10	2.4 ± 0.7
Pt/SAS-1	1.2 ± 0.3
Pt/SAS-4	1.3 ± 0.4
Pt/SAS-10	*Not available
Pt/SG-1	1.4 ± 0.4
Pt/SG-4	1.3 ± 0.4
Pt/SG-10	1.1 ± 0.3
Pt/H-ZSM 5	1.8 ± 0.7
Pt/FSP-SiO_2	*Not available

*Note: Due to a lack of catalyst material available for characterization after testing due to restrictions with the supercritical equipment and material availability from the external partner (See Chapter 2.2).

5.6 CEDI Prepared Catalysts Thermal Stabilization Studies:

Thermal stabilisation studies were also carried out, testing the stability of CEDI deposited Pt particles on CEDI prepared Pt/FSP-4 after various thermal treatments presented in Table 5. 5.

Table 5.5: Particle sizes and size distributions of CEDI deposited Pt on ASA after various heat treatments with the intention of removing the stabilizer while maintaining narrow and uniform particle size and size distribution.

Treatment Method	d_{TEM} (nm)
300 °C Calcination	4.9 ± 1.3
300 °C Calcination and Reduction	4.1 ± 1.3
600 °C Calcination	7.6 ± 2.5
600 °C Calcination and Reduction	5.9 ± 3.3

Table 5. 5 shows the effect of heat treatments on the CEDI deposited Pt-based catalysts. In all cases the average Pt particle sizes and size distributions are larger than those of the above mentioned reduced, and uncalcined catalysts. The reduction process appears to help in minimising the sintering of the Pt particles. The 600 °C calcined samples also show significantly larger Pt particles than even the 300 °C example. Simonsen *et al.* confirmed that Otswald ripening is responsible for the sintering of Pt under oxidative atmospheres.[24] Since Pt is known to form a volatile oxide, the authors suggested that this Pt oxide constitutes the mobile phase responsible for Pt sintering. The increase in calcination temperature results in the weakening of metal-support interactions and aggregation of Pt particles; this situation also favours the broader size distribution evidenced in Table 3. This effect is not present in the reduced catalysts as H_2 treatment, at high temperature, induces stronger metal support interactions particularly in the case of non-reducible oxides as supports.[25] As illustrated in Table 4.4, these Pt nanoparticles are stable to treatment in the reduction conditions.

X-ray diffraction patterns for the (SiO_2-Al_2O_3) support and all prepared catalysts are shown in Fig 7. 28 (*see* Appendix). The diffraction peaks of Pt species are not detected for all the reduced catalysts as their small particle size and low concentration fall below the XRD detection limit. The exception in this regard is the Pt/FSP-1 catalyst which displays reflections attributed to both Pt(200) and Pt (220) with 2 values of 46.4° and 67.5°, respectively. The additional diffraction peak, with 2θ value of 39.6°, was attributed to XRD

sample holder. Moreover, no diffraction peaks characteristic of Pt nanocrystallites exist for all the catalysts thus it is fair assume that well dispersed, small nanoparticles are formed. This assumption is in accordance with the TEM observations.

In summary, the CEDI process has improved the dispersion of the Pt particles greatly, and now produces reliable, well dispersed, and stable Pt particles, which correlates with an increase in activity. The thermal stability studies have suggested an instability under calcination conditions, however, under the reductive conditions of the propane dehydrogenation reaction the Pt particles appear very stable.

5.7 CEDI prepared ASA catalyst for Propane Dehydrogenation (PDH)

5.7.1 Systematically varied CEDI catalysts: On the role of support synthesis method

In this section, the catalytic activity of supported monometallic (1 wt.% Pt) catalysts, prepared *via* the CEDI approach, were evaluated for the PDH reaction and the results are shown in Fig 5.11. The influence of the surface acidity on activity was investigated by varying Al/(Al+Si) molar ratios in the supports of the Pt-based catalysts otherwise simplified to Si/Al ratios of 1, 4 and 10. This gave a set of systematically different catalysts which, for brevity, were denoted Pt/A-*x*, where A is the support synthesis strategy and *x* is the nominal Si/Al.

Initially catalytic activity was examined over 200 minutes time-on-stream (TOS). A comparison of initial activity, measured at 25 minutes TOS, displayed propane conversions of 34.8 %, 43.3 % and 92.3 % for Pt/SAS-1, Pt/SAS-4 and Pt/SAS-10, respectively. The loss in activity with time correlates with Si/Al (Figure 5.11). This is exemplified in percentage reduction of propane conversions of 67.8 %, 84.5 % and 86.8 % over 200 min TOS for Pt/SAS-1, Pt/SAS-4, and Pt/SAS-10, respectively. As indicated in Fig 5. 11-a, the initial activity of the Pt/SAS-10 catalyst exceeds the calculated thermodynamic equilibrium conversion of 54.6 %. This is attributed to initial propane adsorption on the catalyst surface as well as consecutive reactions which appear to be more prevalent in the initial stages of the reaction.

Despite the influence Si/Al can have on activity, it is curious to see the less drastic effect of the support preparation method has on altering the activity in the case of the Pt/FSP-*x* and Pt/SG-*x* catalysts. Both sets of catalysts displayed lower initial propane conversions, appearing to reach steady state conditions at a faster rate than analogous Pt/SAS-*x* catalysts in the initial stages of the reaction. Over the 200 TOS, the Pt/FSP-*x* and Pt/SG-*x* catalysts displayed moderate, stable activity throughout the 200-minute reaction, with negligible observable deactivation.

However, no linear trend between activity and Si/Al was observed for the Pt/SAS-*x* and Pt/FSP-*x* catalysts such that the catalytic performance of the Pt/FSP-*x* catalysts decreased inexplicably with Si/Al in the following order: Pt/FSP-4 > Pt/FSP-10 > Pt/FSP-1. Similarly, the Pt/SAS-X catalysts exhibited similar behaviour with reported propane conversions at 200 min TOS of 11.2 %, 6.7 % and 12.2 % for the Pt/SAS-1, Pt/SAS-4 and Pt/SAS-10 catalysts, respectively. This translated to the following activity trend in the Pt/SAS-*x* catalysts: Pt/SAS-10 > Pt/SAS-1 > Pt/SAS-4. As illustrated in Fig 5. 11 e-f**,** the Pt/SG-*x* catalysts followed a similar activity trend to the FSP-based Pt catalysts such that the activity trend decreased in the following order: Pt/SG-1 > Pt/SG-4 > Pt/SG-10.

However, once the reaction reached steady state conditions, the Pt/SAS-x catalysts displayed similar propane conversion values to analogous FSP and SG-based catalysts. Therefore, it is fair to assume that moderate aluminium content, and thus surface acidity in the catalysts is pertinent to increased catalyst activity in the case of the Pt/SAS-*x* and Pt/FSP-*x* catalysts. The variability in these observations is unexpected but can be rationalised to morphological and microstructural differences induced by the support preparation methods.

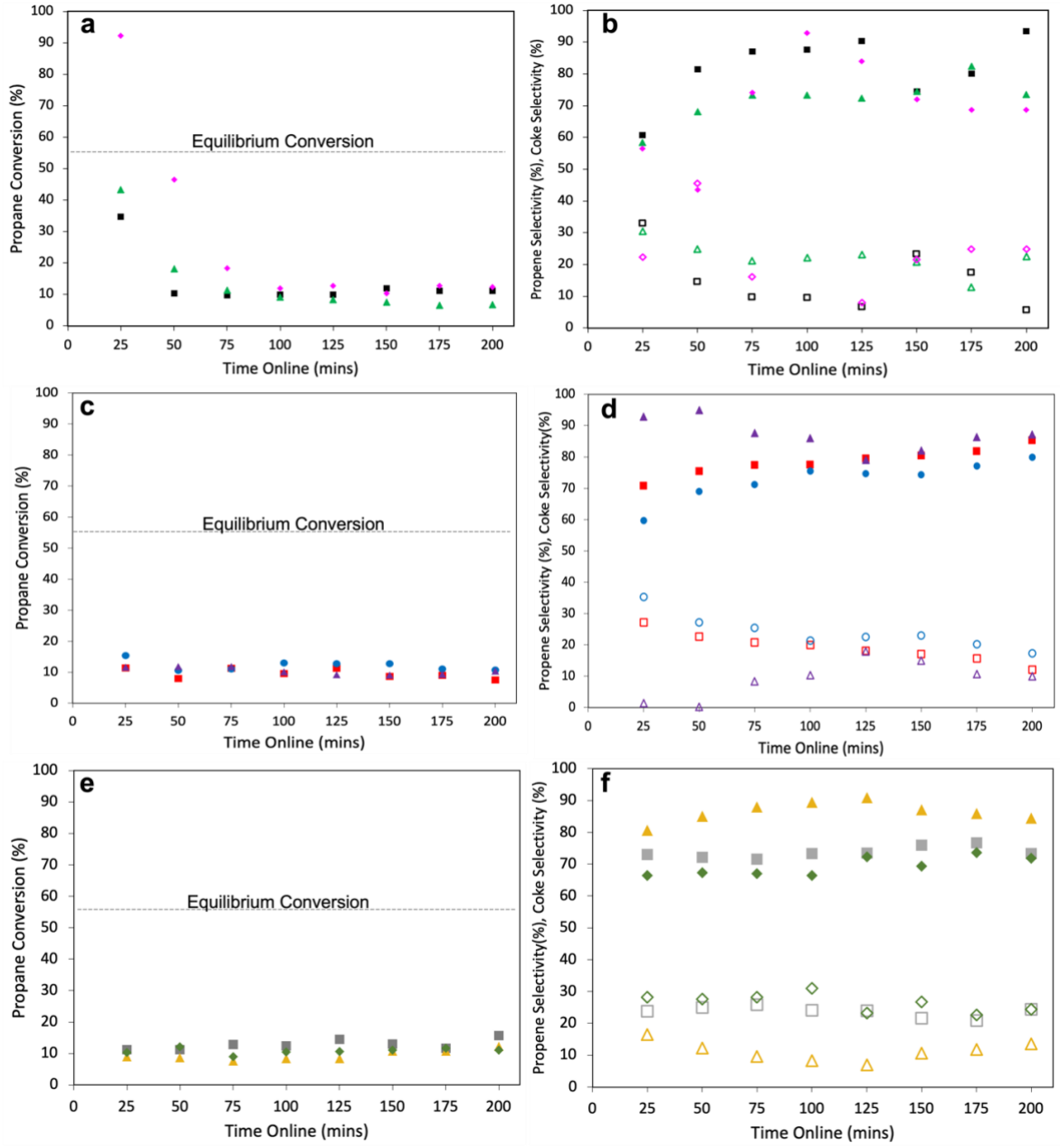

Figure 5.11: (a) Conversion of C_3H_8; and (b) selectivity to C_3H_6 (full symbols) and Coke (hollow symbols) for Pt/SAS-1 (■), Pt/SAS-4 (▲), Pt/SAS-10 (◆); (c) Conversion of C_3H_8; and (d) selectivity to C_3H_6 (full symbols) and Coke (hollow symbols) for Pt/FSP-1 (■), Pt/FSP-4 (●), Pt/FSP-10 (▲); (e) Conversion of C_3H_8; and (f) selectivity to C_3H_6 (full symbols) and Coke (hollow symbols) for Pt/SG-1 (■), Pt/SG-4 (▲) and Pt/SG-10 (◆) catalysts.

The observed product distribution indicates that as the reaction progresses the degree of coking decreases irrespective of microstructural and surface acidity characteristics. In

addition to propene being the most prominent product, negligible amounts of ethene, ethane, methane and toluene side products are present, Table 5. 6. Though desired product (propene) selectivities were important to consider, catalyst performance was measured against two key metrics: propene yield and propene productivity. When considered, initial performance for all tested catalysts demonstrated linear correlations between Si/Al, propene yield and propene productivity, Fig 5. 12.

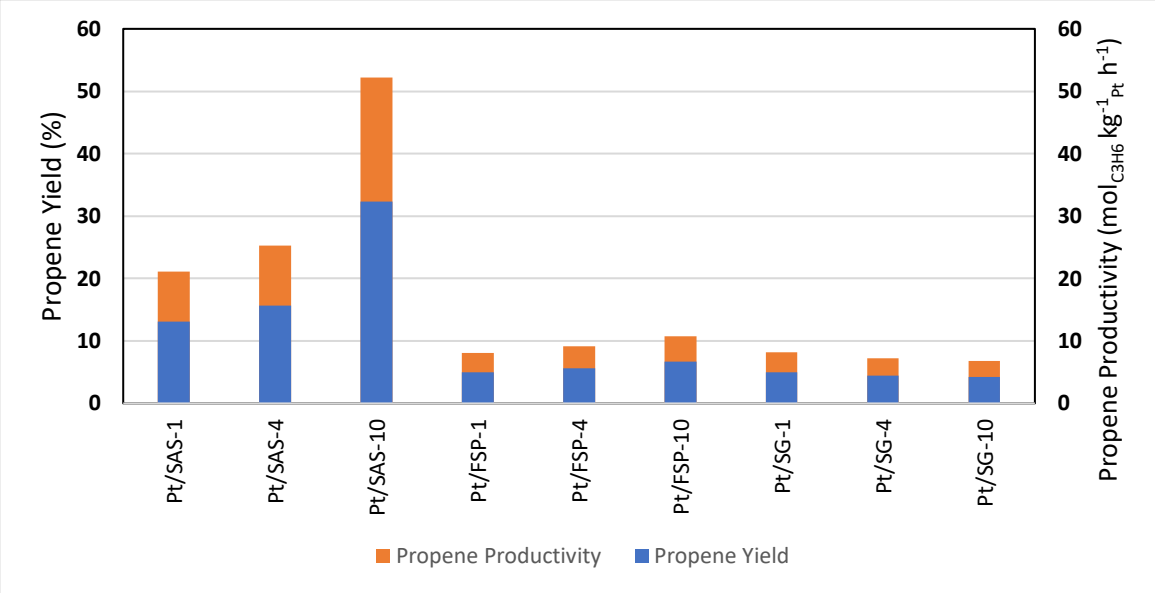

Figure 5. 12: Initial propene yield and propene productivity for all tested catalysts.

It is clear that the use of SAS-prepared ASAs as supports are highly beneficial to the activity displayed by the Pt/SAS-*x* catalysts, given the order-of-magnitude increase in the initial propane yield and propene productivity compared to analogous Pt/FSP-x and Pt/SG-*x* catalysts. Much like the Pt/SAS-x catalysts, the Pt/FSP-x catalysts display increased propene yield and propene productivity with increasing Si/Al, owing to the high level of control offered by the support synthesis method and subsequent microstructural consistencies. An opposing trend was observed for the Pt/SG-x catalysts.

Interestingly, after 200 minutes TOS, Pt/SAS-1 exhibited the highest propene yield and production rates of 6.5%, and 10.4 mol_{C3H6} $kg^{-1}{}_{Pt}$ h^{-1}, respectively. It was noted at this stage the relative stability in the Pt/FSP-*x* catalysts and contrastingly the large susceptibility to

deactivation of the Pt/SAS-*x* catalysts (Table 5.6). Sequential improvements in catalytic performance correlating with Si/Al were observed on the Pt/FSP-1, Pt/FSP-4, Pt/FSP-10 catalysts. It is stressed at this point that although this is the first report of Pt-based catalysts on SAS-synthesized supports with considerable performance, the observed deactivation requires attention.

5.7.2 On the role of support surface acidity and crystallinity

Further, under the reaction conditions used here (600 °C, 100 mg, 5 % C_3H_8 in 5 % N_2 and Ar, balance, WHSV: 12 h^{-1}), Pt/FSP-SiO_2 converted 26.4 % of the propane to propene (77.0 %), ethene (1.5%), methane (1.0 %), trace of amounts of ethane (0.1 %), and benzene (0.4%). On the other hand, though identical propane conversion (26.1 %) was observed over Pt/H-ZSM5 after 200 min TOS marked differences in selectivity to propene (17.7 %), ethene (32.7 %), methane (8.0 %) and ethane (0.8 %) as by-products. Sattler and co-workers outline that the observed activity and product distributions can originate from thermal cracking, isomerization, and polymerization of adsorbed propene.[26] The differences in coke selectivity between Pt/FSP-SiO_2 (19.9 %) and Pt/H-ZSM5 (40.8 %) suggest the existence of two active centres, metal nanoparticles and surface acid sites. Based on the Horiuti-Polanyi mechanism, it is fair to assume that strong, Brønsted acid sites interact with adsorbed, migrated propene and soft coke (propylidene) generated on Pt undergoing polymerization, condensation, and cyclisation.

Pt/ZSM-5 displayed the lowest observed catalytic performance as expected due to the higher density and strength of acid sites characteristic of crystalline aluminosilicates which are a detriment to catalyst performance. This verified the previous running hypothesis relating moderate surface acidity with increased catalyst performance, evident in the ASA supported Pt-based catalysts.

Table 5. 6: Conversion of propane and product distribution after 200 min on-stream for the various catalysts.

Catalyst	C_3H_8 Conversion (%)	Selectivity (%)						Propene Yield (%)	Productivity ($mol_{C3H6}\ kg_{cat}^{-1}\ h^{-1}$)
		C_3H_6	C_2H_4	C_2H_6	CH_4	Toluene	Coke		
Pt/SAS-1	11.2	93.5	0	0	0.5	0.5	5.6	10.4	6.5
Pt/SAS-4	6.7	73.5	2.0	1.2	1.2	0.9	22.4	4.9	3.0
Pt/SAS-10	12.2	68.6	3.8	0.3	1.8	0.8	24.7	8.4	5.2
Pt/FSP-1	7.5	85.3	2.2	0	0	0.5	12.1	7.6	4.7
Pt/FSP-4	16.6	76.0	1.9	0	0.7	0.4	21.1	8.5	5.3
Pt/FSP-10	16.6	89.7	2.0	0	0.7	0.5	7.0	14.9	9.2
Pt/SG-1	15.7	73.4	0.4	1.2	0	0.6	24.4	11.8	7.4
Pt/SG-4	12.3	84.5	1.1	0	0.4	0.5	13.5	10.4	6.5
Pt/SG-10	11.0	71.9	1.8	0	1.4	0.6	24.3	7.9	4.9
Pt/FSP-SiO_2	26.4	77	1.5	0.1	1.0	0.4	19.9	20.3	12.6
Pt/ZSM-5	26.4	17.7	32.7	0.8	8.0	0	40.8	4.1	2.6

Additionally, a few important aspects of the reaction pathway can be concluded from the data presented in Table 4.6. The fact that the selectivity to the C_3 product is typically greater than that of C_1 and C_2 products implies that the activation of C-H bond and a weaker binding strength of propene predominates, with low activity for C-C bond rupture. This implies the lower prevalence of hydrogenolysis and cracking pathways. However, the noticeable selectivity to coked products suggests complete cracking of propane can occur leading to sequential aromatization and isomerization reactions. This can be attributed to different Pt surface site heterogeneity and catalyst surface acidity, which will be discussed in more detail in the subsequent sections.

5.7.3 Long term iso-conversion PDH testing:

A more conclusive comparison of the catalysts was conducted over a period of 16 hours. Propene yield and propene productivity were used as indicators of the catalyst performance under iso-conversion. These conditions were selected to operate the system at a conversion level, of around 10 %, far from equilibrium thus representing differential conditions.

Over a 16-hour reaction time, the Pt/SAS-*x* catalysts deactivated in accordance with the catalyst's Si/Al ratio evident in the monotonical decrease in propane conversion in the first 2 hours (Fig 5. 12a). The highest initial activity is observed for Pt/SAS-10 (92.3%), followed by Pt/SAS-4 (42.2%) and Pt/SAS-1 (34.8%). Additionally, the rate of deactivation is as follows: Pt/SAS-1 > Pt/SAS-4 > Pt/SAS-10 which is due to the higher concentration of Brønsted acid sites, with decreasing Si/Al, which promote cracking and coke formation. From the relationship between catalytic activity and Si/Al ratio, it can be concluded that the rate of deactivation is dependent on the surface acidity. It is clear from this difference the ability of the active Brønsted acid sites to protonate propane. Conversely, no correlation was found between support surface area (*see* Table 4. 10) and catalyst activity. This is demonstrated by the Pt/SAS-*x* catalysts which display comparable catalytic performance to analogous Pt/FSP-X and Pt/SG-X catalysts after steady state conditions are reached, despite the latter having higher surface areas.

The lower activity and rate of deactivation achieved by increasing Si/Al can be attributed to differences in the strength, nature and concentration of active sites inducing lower uptake of propane. This is in line with the kinetic perspective of the dehydrogenation reaction whereby higher initial reaction rates can be ascribed to different heat of propane adsorption, and energetic barriers between propene dehydrogenation and desorption.[27,28] With this knowledge, it is fair to assume that the lower heat of adsorption with increasing Si/Al can lead to differences in surficial propane coverage and subsequent activity per active site. However, an appropriate temperature programmed desorption experiment to elucidate the coverage dependant desorption kinetics between the tested catalysts is beyond the scope of this study.

Contrary to previously demonstrated data (Fig 5. 11a-d), the long-term propene selectivities showed a large amount of variability particularly after steady state conditions were achieved. The exact cause is unclear but possible rationales can be attributed to the resultant morphology, elemental, microstructural properties characteristic of the support synthesis and Pt surface site heterogeneity. Further analysis revealed that although at points propene selectivity did fluctuate slightly, this did not lead to variability in the propene productivity. Similar trends in catalyst performance were observed in both Pt/SAS-*x* and Pt/FSP-*x* catalysts over the 16-hour reaction time with the catalysts characterised by moderate acidity displaying the highest performance (Fig 5.13 and Fig 5.14).

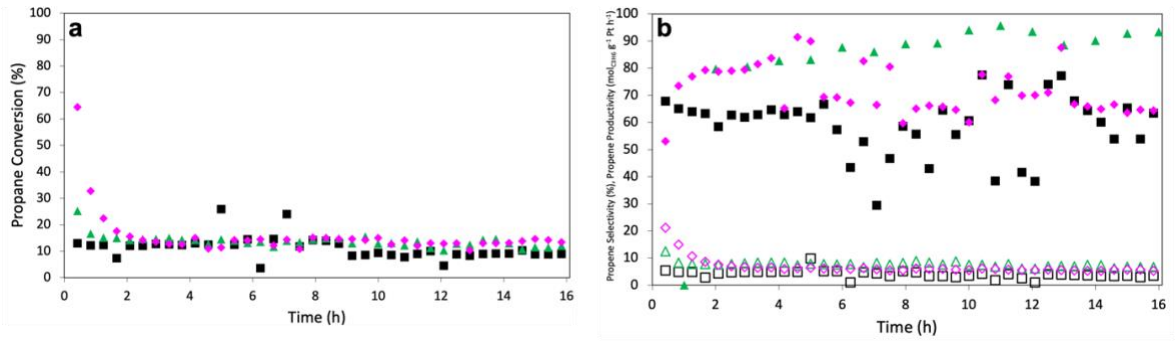

Figure 5.13: (a) Conversion of C_3H_8; and (b) selectivity to C_3H_6 (full symbols) and C_3H_6 productivity (hollow symbols) for Pt/SAS-1 (■), Pt/SAS-4 (▲), Pt/SAS-10 (◆).

As illustrated in Fig 5.13b, after 16 hours TOS Pt/SAS-4 exhibited the highest propene yield and productivity of 11.5 %, and 7.1 mol_{C3H6} kg^{-1}_{Pt} h^{-1}, respectively. Similarly, among the Pt/FSP-*x* catalysts Pt/FSP-4 exhibited the highest propene yield and productivity of 10.8 %, and 6.7 mol_{C3H6} kg^{-1}_{Pt} h^{-1}, respectively. Notable also is that this anticipated weaker adsorption of propene obtained on the Pt-based catalysts characterized by higher Si/Al ratios, resulted in the prevention of the deep dehydrogenation of propene to propylidene, a model precursor for coked products.

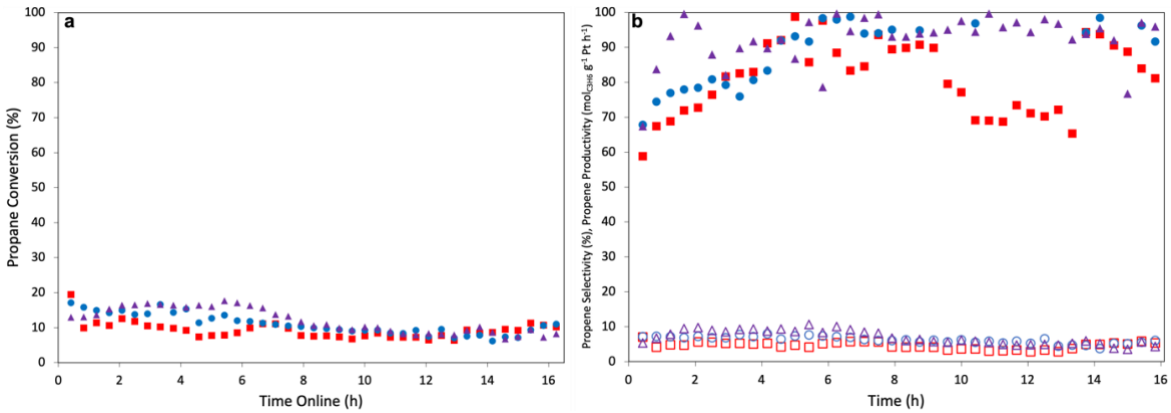

Figure 5.14: (a) Conversion of C_3H_8; and (b) selectivity to C_3H_6 (full symbols) and C_3H_6 productivity (hollow symbols) for Pt/FSP-1 (■), Pt/FSP-4 (●), Pt/FSP-10 (▲).

Moreover, the ASA-supported Pt catalysts significantly reduced the amount of coke formation, particularly on the active sites which diminished the catalytic deactivation otherwise observed in the zeolitic analogue (See Appendix, Fig 7. 35). This is a highly significant result as it shows a fourfold improvement in the rate of formation of propene in both Pt/SAS-10 and Pt/FSP-10 catalysts relative to Pt/H-ZSM5.

Based on these observations it was noteworthy that the SAS synthesized ASAs could provide similarities in key structural features to the FSP synthesized counterparts that may be beneficial to catalysis. In view of this a large amount of work was undertaken to determine the key structural features pertinent to the observed catalyst performance.

5.8 Understanding the role of the support in non-oxidative propane dehydrogenation

5.8.1 On the role of surface site heterogeneity

The catalytic performance also depends on the geometric and electronic properties of the active sites. The electronic properties of the various Pt/SiO_2-Al_2O_3 catalysts, before and after long-term PDH testing, were characterized by XPS. The most intense photoemission lines of Pt are attributed to Pt 4f. The Pt 4f XPS spectra of all the catalysts exhibited doublet peaks corresponding to a spin-orbit splitting of Pt $4f_{7/2}$ and Pt $4f_{5/2}$ states, in accordance with the NIST X-Ray Photoelectron Spectroscopy database.[29]

Table 5.7: Particle size, size distribution and ratio of Pt active sites provided by HRTEM and XPS analysis of all tested catalysts.

Catalyst	REDUCED		POST REACTION	
	d_{TEM} (nm)	Pt^{2+}/Pt^0	d_{TEM} (nm)	Pt^{2+}/Pt^0
Pt/SAS-1	1.2 ± 0.3	1.7	4.8 ± 3.8	0.8
Pt/SAS-4	1.3 ± 0.4	1.4	2.1 ± 0.8	0.8
Pt/SAS-10	*Not available	*Not available	1.4 ± 0.4	0.8
Pt/FSP-1	2.4 ± 0.7	1.5	2.2 ± 0.8	0.8
Pt/FSP-4	1.2 ± 0.3	2.0	1.6 ± 0.4	0.8
Pt/FSP-10	1.3 ± 0.4	1.1	1.9 ± 0.7	0.8
Pt/SG-1	1.4 ± 0.4	1.4	4.5 ± 1.7	0.8
Pt/SG-4	1.3 ± 0.4	1.2	3.0 ± 1.4	0.8
Pt/SG-10	1.1 ± 0.3	0.6	3.6 ± 1.4	0.8
Pt/H-ZSM5	1.8 ± 0.7	*Not available	2.4 ± 1.0	*Not available

***Note: Due to a lack of catalyst material available for characterization after testing due to restrictions with the supercritical equipment and material availability from the external partner (See Chapter 2.2).**

However, an intense Al 2p photoemission peak overlapped with the Pt $4f_{5/2}$ peak with binding energy (BE) in the 73-77 eV range. As to Pt, only metallic platinum (Pt^0) is observed when considering the Pt $4f_{7/2}$ peaks with BE values in the 70.2-70.9 eV and 71.3-71.9 eV ranges. Additionally, the Pt $4f_{5/2}$ peaks of the reduced catalysts, prior to testing, could be resolved into two components with binding energies of 74.7-75.2 eV and 73.6-74.2 eV, assigned to the presence of Pt^{2+} and Pt^0 species, respectively.

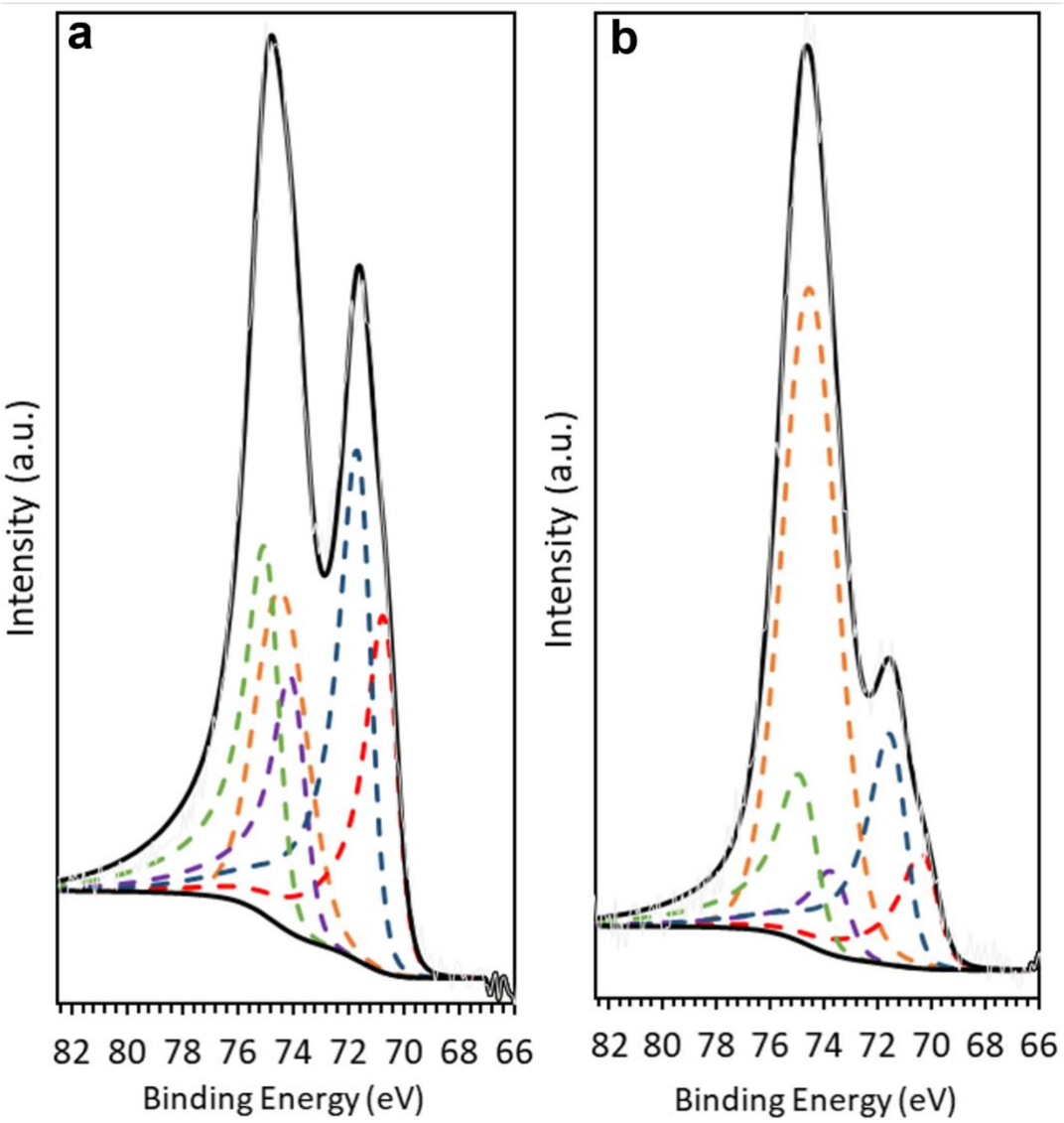

Figure 5. 15: XPS spectra of the Al2p (---) and Pt 4f (---Pt $4f_{7/2}$ ^{0}, ---Pt $4f_{7/2}$ $^{2+}$, ---Pt $4f_{5/2}$ ^{0}, ---Pt $4f_{5/2}$ $^{2+}$) regions of reduced (a) Pt/SAS-4 and (b) Pt/FSP-4 catalysts.

The Pt^{2+}/Pt^{0} ratios calculated based on the combined spectral contribution of both Pt $4f_{7/2}$ and Pt $4f_{5/2}$ peaks, are presented in Table 5. 7. For the Pt/SAS-*x* catalysts, no clear trend exists between catalyst activity and Pt^{2+}/Pt^{0} ratio. Contrastingly, the Pt^{2+}/Pt^{0} ratio correlates with both initial propene yield and propene productivity following the trend: Pt/FSP-4 > Pt/FSP-1 > Pt/FSP-10.

As illustrated by Fig 7. 31 (see Appendix), which presents the Pt 4f XPS spectra of the Pt/FSP-4 post-reaction catalyst, only two Pt $4f_{7/2}$ peaks are observed after the 16-hour PDH

reaction. Due to BE values of 71.3 and 74.7 eV these species are identified as Pt $4f_{7/2}{}^{0}$, Pt $4f_{7/2}{}^{2+}$, respectively. Interestingly, the Pt^{2+}/Pt^{0} ratios are consistent for all tested catalysts post reaction. This observation provides further insights into the possible thermally and chemically induced change in Pt speciation produced by operating under reaction conditions.

In-situ characterization is required, under reaction conditions, to fully understand how the Pt species evolve with reaction temperatures and conditions which is beyond the scope of this project. However, these results indicate the reproducibility afforded by the Pt deposition technique on the ASA supports. Consistent particle sizes, size distribution and Pt^{2+}/Pt^{0} ratios in spent catalysts also suggest stabilization achieved under reaction conditions, potentially once steady state conditions are achieved.

5.8.2 Particle Size Effect on PDH Activity:

To clarify these observations, TEM and NMR studies were carried out. Increasing catalyst activity by enhancing dispersion is only effective to a certain extent. Size dependence of the PDH reaction are encountered with smaller, isolated Pt species favoured for high catalyst activity as reported in literature.[5,6] To shed light on the reasons for different activity during the reaction, the catalysts after reaction were analysed by HRTEM. The HRTEM images (*See Appendix* Figs 7. 22-25*)* portray highly dispersed Pt particles and accompanying particle size and distribution histograms of the spent catalysts. Negligible changes in the Pt particle size were found after the 16-hour PDH reaction for the Pt/FSP-X catalysts (Table 5. 7). The Pt nanoparticles appear to be relatively stable under reaction conditions maintaining atomic-level dispersion. The assignment of the promoted catalytic performance to different morphologies of the supported FSP catalysts is strengthened by the observation that the Pt/FSP-X catalysts maintain their size and size distribution under reaction conditions. This indicates the enhanced metal-support interactions between the Pt particles and FSP-synthesized ASA supports which resulted in greater stabilization of Pt nanoparticles on this set of Pt-based catalysts.

On the contrary, the HRTEM images of the Pt/SAS-X catalysts present larger Pt aggregates for the Pt/SAS-1 catalyst (4.6 ± 3.8 nm) with slightly less uniformity in Pt species over the support surface. As the Si/Al is increased another combinational effect between surface acidity and nanoparticle size is evident in the Pt/SAS-4 (2.2 ± 0.8 nm) and Pt/SAS-10 (1.4 ± 0.4 nm) catalysts. This suggests that there are commonalities in catalyst design between Pt/FSP and Pt/SAS catalysts exist which likely relate to the interaction of the active metal and the support. This is in view of atomic-level structural similarities between FSP, and SAS synthesized supports (Chapter 4). In the case of the Pt/SG-X catalysts larger Pt particles exist characterized by isometric or irregular shape and distribution over the support surface.

5.8.3 Surface acidity effect on PDH

Irrespective of ASA synthesis technique the ^{27}Al 1D MAS NMR (Chapter 3, Fig 3. 21) alluded to the Al speciation in ASAs which exhibit 3 broad, characteristic asymmetric peaks with chemical shifts of 4, 30 and 55 ppm which can be attributed to octahedral (Al^{VI}), pentahedral (Al^{V}) and tetrahedral (Al^{IV}) aluminium species, respectively. Due to the complex surface structure the spectra show heterogeneity in Al environments, with the relative proportion of signals associated with both Al^{V} and Al^{VI} species decreasing monotonically with Si/Al.

The surface structure is complex however it is understood that co-existent Brønsted type acid sites are observed (BAS-Al^{IV} and BAS-Al^{V}) which enhance the Brønsted acidity of ASAs. Al^{V} are known to be surface enriched species, providing anchoring sites for nanoparticles, and enhanced thermal stabilization. All the signals show a large distribution in isotropic chemical shifts and therefore they are not well resolved. This reflects the topological distribution of aluminium atoms in the disordered ASA materials. In crystalline materials, like zeolites, the bond angles are well defined, leading to a smaller distribution in NMR parameters. The ^{27}Al 2D MQMAS NMR spectra features three main off-diagonal correlations for Pt/FSP-1, Pt/SAS-1 and Pt/SG-1 catalysts (See Appendix, Fig 7.31). The results indicated that for the Pt catalyst supported on supports containing the highest

aluminium content (Si/Al=1), there are at least three different Al species in differing (Si-O-Al) bond angles. The two most intense (labelled **I and III** in Appendix, Fig 7.31) are associated with to Al^{IV} and Al^{VI} species, respectively. The remaining feature (labelled **II** in Appendix, Fig 7.31) results from Al^{V} species. The Al^{V} species are known to be surface enriched species existing in high concentrations at high Al content, with partial hydrolysis of Al^{V}, resulting in Al^{VI} in the hydrated state. The relative proportion of Al^{V} species, and consequently Al^{VI} species is known to decrease with Si/Al in the order: 1> 4> 10.

Irrespective of ASA synthesis procedure the spectra show heterogeneity in Al environments, with the relative proportion of signals associated with both Al^{V} and Al^{VI} species decreasing monotonically with Si/Al. The opposite trend is observed however for the signal associated with Al^{IV} polyhedral (centred at *ca.* 55 ppm). In the MQMAS spectra, the relative population of Al^{VI} and Al^{V} features are less prominent than anticipated. Consequently, it is fair to assume that Al^{V} and Al^{VI} in ASAs are largely NMR invisible under our measuring conditions. Second order quadrupolar interactions of Al nuclei with local electric field gradients are known to broaden the ^{27}Al MAS NMR signals of Al with distorted coordination symmetries, characteristic of ASAs, beyond detection. However, both that Al^{V} and Al^{VI} sites in ASAs are surface enriched and provide the amphoteric hydroxyls necessary to anchor the Pt nanoparticles. The nature of the line broadening in the 2D MQMAS allows further structural deductions whereby two types of line broadening can be differentiated. Horizontal broadening of lineshapes in the 2D spectrum is caused by quadrupolar coupling to local electric field gradients, the result of nearby cationic species or coordination-symmetry distortion. This is illustrated by the Al^{VI} lineshapes (labelled **I**) of all SAS (Appendix, Fig 7.31 **1**-**3**) and FSP-prepared ASAs (Appendix, Fig 7.31, **4**-**6**). On the other hand, chemical heterogeneity was reflected by elongation of lineshapes along the diagonal of the MQMAS spectrum.

The latter was evident for all observed lineshapes in the SAS and FSP-prepared ASAs. Interestingly, the MQMAS spectra yielded a characteristic fingerprint of the type of synthesis strategy used for the ASA based on the line-broadening and Al speciation features. In ZSM-5, all Al atoms are within the zeolite framework and appear NMR visible.

With catalyst design in mind, minimizing the formation of the alumina phase or Al^{VI} species during synthesis can maximise the dispersion of Al atoms and the generation of framework, Al^{IV}, and surface, Al^{V}, species for optimal surface acidity is highly desirable. Due to the highly defective structure of silica−alumina, the formation of reversible aluminium species is expected and has been reported to occur more readily than in zeolites.[30] Multidimensional MAS NMR analysis suggests the possibility of different types of hydroxyl groups are present on the surface of the SAS and FSP synthesized amorphous silica-aluminas. Although MQMAS is a highly informative NMR approach, it is not quantitative. NH_3-TPD has been used to quantify total acidity (Brønsted and Lewis acidity) and the acid site strength. The relation between the propene productivity, total acid site concentrations and densities are summarized in Figure 5. 17.

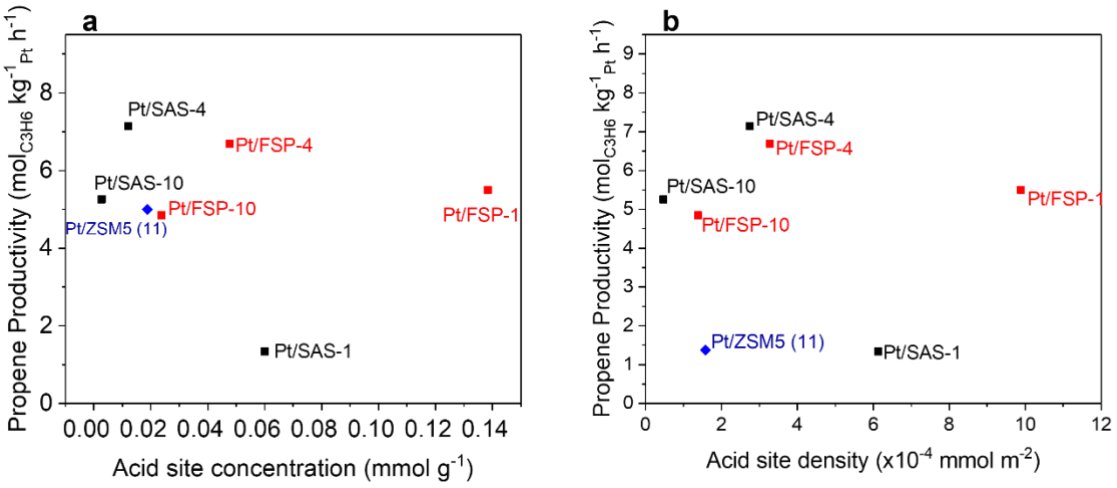

Figure 5.16: Propene productivity correlations with (a) acid site concentration; and (b) acid site density for the tested catalysts.

When considering the acid site concentration from ammonia TPD experiments, moderate acid site concentrations favour the highest propene productivities in both Pt/SAS-X and Pt/FSP-X catalysts. These correlations are consistent when the acid site density is considered, Fig 5. 17b. Deductions from the 2D MQMAS spectra show the presence of exclusively Al^{IV} in Pt/FSP-4 (Fig 5. 16, **5**) and Pt/SAS-4 (Fig 5. 16, **2**) result in the higher observed specific activities, respectively, their relative their counterparts with the lowest Si/Al. Thus, it is fair to assume the need for sufficient Al^{IV}-BAS, with the co-existent Al^{V}-BAS limited through modulation of Si/Al as well as in anchoring nanoparticles.

5.9 Conclusions

From this chapter, the reproducible preparation of Pt-based catalysts on SAS, FSP and SG-synthesised ASAs *via* the CEDI approach has been successfully carried out with characterisation revealing key microstructural parameters pertinent to catalytic performance. Of these parameters, the surface acidity has been shown to have a direct influence on catalytic performance when applied to the non-oxidative propane dehydrogenation reaction.

It is well understood that the synthesis method governs the extent to which such properties can be tuned. It has been demonstrated that the ASA materials display similar Al speciation, with a higher concentration of Al^{V} and Al^{VI} existing at low Si/Al ratios while 2D MQMAS provided additional 'fingerprint' information linking greater chemical heterogeneity, from line broadening analysis, in SAS and FSP based catalyst relative to the SG and zeolitic catalysts. 2D MQMAS NMR also suggest differences in the distribution of distorted Al sites, inherent to each support synthesis strategy. Tuning of synthetic parameters, such as Al content enabled changes to the surface composition and surface acidity. Consequently, direct impacts on the catalytic performance are observed with Pt/SAS-4 and Pt/FSP-4 catalysts showing the highest observed production rates of the required product.

On the contrary, the Pt/SG-*x* catalysts displayed a reciprocal correlation between surface acidity and catalytic performance, attributed to differences in the surface structure and thus surface acidity. The FSP based catalyst appear to be the most promising displaying enhanced activity, selectivity, and stability relative to the SAS and SG counterparts. It is assumed this is due to a possible higher concentration of surface enriched Al^{V} sites, able to sufficiently stabilize and disperse the active phase in the Pt-based catalysts. Other advantages of this include increasing metal surface area and improving catalytic performance through enhanced metal-support interactions otherwise verified by stabilised Pt nanoparticle sizes under reaction conditions. This appears to be enhanced at moderate Si/Al, Si/Al=4, insinuating the need for moderate surface acidity to improve catalytic performance. These attributes are essential in understanding the relation between the

synthesis method, physicochemical properties and catalyst performance otherwise referred to as *synthesis-structure-activity relationships*.

The results suggest that Pt particle size and size distribution largely depend on the support composition with the lowest observed particle sizes observed on catalyst with supports constituted by moderate Si/Al. Characterization has alluded to the difference in performance being down to a number of factors including and not limited to the type and strength of the acid sites, the platinum dispersion and morphologies in the different catalysts.

In the case of the Pt/SAS-X catalysts a correlation between increasing Si/Al and initial propane conversion was evident. Increasing Si/Al in the Pt/SAS-X catalysts resulted in a decrease in the activity with more pronounced deactivation observed with increasing Si/Al. This directly correlated with different rates of deactivation induced by the nature, strength, and concentration of surface acid sites such that more rapid deactivation occurred at low Si/Al. An illustrative example of this is in the comparison of the drop in propane conversion in the Pt/SAS-*x* catalysts whereby more pronounced deactivation exists in the Pt/SAS-10 catalyst relative to its counterparts with lower Si/Al.

5.10 References

1 Z.-J. Zhao, C. Chiu and J. Gong, Molecular understandings on the activation of light hydrocarbons over heterogeneous catalysts, *Chem. Sci.*, 2015, **6**, 4403–4425.

2 A. Farjoo, F. Khorasheh, S. Niknaddaf and M. Soltani, Kinetic modeling of side reactions in propane dehydrogenation over Pt - Sn/γ - Al2O3 catalyst, *Scientia Iranica*, 2011, **18**, 458–464.

3 Q. Li, Z. Sui, X. Zhou, Y. Zhu, J. Zhou and D. Chen, Coke Formation on Pt–Sn/Al2O3 Catalyst in Propane Dehydrogenation: Coke Characterization and Kinetic Study, *Top Catal*, 2011, **54**, 888.

4 R. M. Rioux, H. Song, J. D. Hoefelmeyer, P. Yang and G. A. Somorjai, High-Surface-Area Catalyst Design: Synthesis, Characterization, and Reaction Studies of Platinum Nanoparticles in Mesoporous SBA-15 Silica, *J. Phys. Chem. B*, 2005, **109**, 2192–2202.

5 M. Santhosh Kumar, D. Chen, J. C. Walmsley and A. Holmen, Dehydrogenation of propane over Pt-SBA-15: Effect of Pt particle size, *Catalysis Communications*, 2008, **9**, 747–750.

6 Y.-X. Tuo, L.-J. Shi, H.-Y. Cheng, Y.-A. Zhu, M.-L. Yang, J. Xu, Y.-F. Han, P. Li and W.-K. Yuan, Insight into the support effect on the particle size effect of Pt/C catalysts in dehydrogenation, *Journal of Catalysis*, 2018, **360**, 175–186.
7 J. Raskó, CO-induced surface structural changes of Pt on oxide-supported Pt catalysts studied by DRIFTS, *Journal of Catalysis*, 2003, **217**, 478–486.
8 A. Garnier, S. Sall, F. Garin, M. J. Chetcuti and C. Petit, Site effects in the adsorption of carbon monoxide on real 1.8nm Pt nanoparticles: An Infrared investigation in time and temperature, *Journal of Molecular Catalysis A: Chemical*, 2013, **373**, 127–134.
9 B. A. Riguetto, S. Damyanova, G. Gouliev, C. M. P. Marques, L. Petrov and J. M. C. Bueno, Surface Behavior of Alumina-Supported Pt Catalysts Modified with Cerium as Revealed by X-ray Diffraction, X-ray Photoelectron Spectroscopy, and Fourier Transform Infrared Spectroscopy of CO Adsorption, *J. Phys. Chem. B*, 2004, **108**, 5349–5358.
10 J. Reedijk and K. Poeppelmeier, in *V1 Main-Group Elem., Incl. Noble Gases V2 Transition Elem., Lanthanides and Actinides V3 Bioinorganic Fundam. and Appl.*, Elsevier Ltd., 2013, vol. 1, pp. 1–7196.
11 J. Callison, N. D. Subramanian, S. M. Rogers, A. Chutia, D. Gianolio, C. R. A. Catlow, P. P. Wells and N. Dimitratos, Directed aqueous-phase reforming of glycerol through tailored platinum nanoparticles, *Applied Catalysis B: Environmental*, 2018, **238**, 618–628.
12 N. Dimitratos, C. Messi, F. Porta, L. Prati and A. Villa, Investigation on the behaviour of Pt(0)/carbon and Pt(0),Au(0)/carbon catalysts employed in the oxidation of glycerol with molecular oxygen in water, *Journal of Molecular Catalysis A: Chemical*, 2006, **256**, 21–28.
13 L. Wen, J.-K. Fu, P.-Y. Gu, B.-X. Yao, Z.-H. Lin and J.-Z. Zhou, Monodispersed gold nanoparticles supported on γ-Al2O3 for enhancement of low-temperature catalytic oxidation of CO, *Applied Catalysis B: Environmental*, 2008, **79**, 402–409.
14 J. A. Lopez-Sanchez, N. Dimitratos, C. Hammond, G. L. Brett, L. Kesavan, S. White, P. Miedziak, R. Tiruvalam, R. L. Jenkins, A. F. Carley, D. Knight, C. J. Kiely and G. J. Hutchings, Facile removal of stabilizer-ligands from supported gold nanoparticles, *Nature Chem*, 2011, **3**, 551–556.
15 C. Cao, G. Yang, L. Dubau, F. Maillard, S. D. Lambert, J.-P. Pirard and N. Job, Highly dispersed Pt/C catalysts prepared by the Charge Enhanced Dry Impregnation method, *Applied Catalysis B: Environmental*, 2014, **150–151**, 101–106.
16 X. Zhu, H. Cho, M. Pasupong and J. R. Regalbuto, Charge-Enhanced Dry Impregnation: A Simple Way to Improve the Preparation of Supported Metal Catalysts, *ACS Catal.*, 2013, **3**, 625–630.
17 Q. Liu, J. Samad, J. E. Copple, S. Eskandari, C. Satterwhite and J. R. Regalbuto, A pinch of salt to control supported Pt nanoparticle size, *Catalysis Today*, 2017, **280**, 246–252.
18 S. Eskandari, A. Dong, L. T. De Castro, F. B. AB Rahman, J. Lipp, D. A. Blom and J. R. Regalbuto, Pushing the limits of electrostatic adsorption: charge enhanced dry impregnation of SBA-15, *Catalysis Today*, 2019, **338**, 60–71.
19 J. E. Samad, S. Hoenig and J. R. Regalbuto, Synthesis of Platinum Catalysts over Thick Slurries of Oxide Supports by Strong Electrostatic Adsorption, *ChemCatChem*, 2015, **7**, 3460–3463.
20 F. Regali, L. F. Liotta, A. M. Venezia, M. Boutonnet and S. Järås, Hydroconversion of n-hexadecane on Pt/silica-alumina catalysts: Effect of metal loading and support acidity

on bifunctional and hydrogenolytic activity, *Applied Catalysis A: General*, 2014, **469**, 328–339.

21 O. Y. Gutiérrez, Y. Yu, R. Kolvenbach, G. L. Haller and J. A. Lercher, Hydrogenation of tetralin over Pt catalysts supported on sulfated zirconia and amorphous silica alumina, *Catal. Sci. Technol.*, 2013, **3**, 2365–2372.

22 J. E. Samad, J. Blanchard, C. Sayag, C. Louis and J. R. Regalbuto, The controlled synthesis of metal-acid bifunctional catalysts: Selective Pt deposition and nanoparticle synthesis on amorphous aluminosilicates, *Journal of Catalysis*, 2016, **342**, 213–225.

23 J. E. Samad, Rational Design and Synthesis of Pt/Silica-Alumina Metal-Acid Bifunctional Catalysts, 172.

24 S. B. Simonsen, I. Chorkendorff, S. Dahl, M. Skoglundh, J. Sehested and S. Helveg, Direct Observations of Oxygen-induced Platinum Nanoparticle Ripening Studied by In Situ TEM, *J. Am. Chem. Soc.*, 2010, **132**, 7968–7975.

25 L. Deng, H. Miura, T. Shishido, Z. Wang, S. Hosokawa, K. Teramura and T. Tanaka, Elucidating strong metal-support interactions in Pt–Sn/SiO2 catalyst and its consequences for dehydrogenation of lower alkanes, *Journal of Catalysis*, 2018, **365**, 277–291.

26 Catalytic Dehydrogenation of Light Alkanes on Metals and Metal Oxides, *Chemical Reviews*, 2014, **114**, 10613–10653.

27 L. Xiao, F. Ma, Y.-A. Zhu, Z.-J. Sui, J.-H. Zhou, X.-G. Zhou, D. Chen and W.-K. Yuan, Improved selectivity and coke resistance of core-shell alloy catalysts for propane dehydrogenation from first principles and microkinetic analysis, *Chemical Engineering Journal*, 2019, **377**, 120049.

28 B. Xu, C. Sievers, J. A. Lercher, J. A. R. van Veen, P. Giltay, R. Prins and J. A. van Bokhoven, Strong Brønsted Acidity in Amorphous Silica−Aluminas, *J. Phys. Chem. C*, 2007, **111**, 12075–12079.

29 NIST XPS Database, Selected Element Search Result, https://srdata.nist.gov/xps/EngElmSrchQuery.aspx?EType=PE&CSOpt=Retri_ex_dat&Elm=Pt, (accessed 4 January 2022).

30 A. Omegna, J. A. van Bokhoven and R. Prins, Flexible Aluminum Coordination in Alumino−Silicates. Structure of Zeolite H−USY and Amorphous Silica−Alumina, *J. Phys. Chem. B*, 2003, **107**, 8854–8860.

6 Conclusions and future work

6.1 Conclusions

The title and objective of this thesis places emphasis on novel preparation methods targeted towards increasingly homogeneous amorphous silica-alumina (ASA) materials, with high concentrations of homotopic active sites ideal for establishing structure-performance relations.

With the antisolvent precipitation in mind, substantial efforts have been devoted to designing a systematic approach in the preparation detail capable of meeting the stringent microstructural property specification of the required product. In contrast, Baiker *et al.* demonstrated use of the flame spray pyrolysis (FSP) method offering scalable production of novel, thermally stable ASAs with the ability to address the demands imposed by numerous catalytic processes.[1–4] The novelty of this study is that it addresses a new synthetic route to ASAs, analogous to FSP-synthesized ASAs, *via* a systematic study of experimental and post-synthesis variables and their effect on the resultant catalytic materials. This work addresses the effect of solvent composition, process temperature, process pressure, calcination conditions, silicon and aluminium metal precursors but also advanced characterization and an investigation of the catalytic dehydration of methanol to dimethyl ether. The synthesis strategy has not been previously reported in literature and despite promising initial results, a further factorial design of experiments (DOE) study and quantifiable characterization are required for subsequent optimization.

Supported platinum-based propane dehydrogenation catalysts are among the most utilized in commercial process. Of these, supports with weak and moderate surface acidity (alkaline doped Al_2O_3, Mg(Al)O, ZrO_2, SAPO-34) coupled with promoting elements (Sn and Ga) result in improved Pt utilisation, which is desirable for industrial application. In a comprehensive review Carter, Bere and co-workers outline current efforts on the design of

future of catalysts, with research centred around similar concepts to the above-mentioned industrial catalysts.

One of the aims of this thesis is to correlation structure-activity relationships for the propane dehydrogenation reaction on a series of (ASA) supported monometallic (Pt) catalysts. In order to determine the effect of surface acidity on activity, a parallel study with pristine ASAs was applied to the catalytic dehydration of methanol to dimethyl ether. An interesting finding is that catalyst activity decreased with increasing Si/Al while catalyst productivity was maximized, in FSP-4, with moderate acidity and a balance of surficial acid sites (B:L). This insight directly translated to observed trends in desired product productivity and yield for the propane dehydrogenation reaction whereby under iso-conversion Pt/FSP-4 and Pt/SAS-4 displayed superior performance. Thus, it is imperative to investigate the effect of the support on catalyst performance employing further evaluation using the methanol-to-DME reaction as well as MQMAS, C_3H_8-TPD, C_3H_6-TPD, NH_3-TPD and Pyridine-DRIFTS characterization.

While investigations of the reproducible deposition of platinum nanoparticles on ASAs have been reported in a number of publications, the effect of a number of exchange methods (sol-immobilization, IWI, CVI, CEDI) have been addressed in this thesis. In addition, the application of dehydrogenation catalysts prepared by the CEDI method, has not been reported before. This study adopts an electron microscopy study to enhance understanding of the effect on metal size, size distribution, and dispersion of various calcination, and consecutive reduction, processes for systematically varied (Si/Al) supports prepared *via* different methods (SAS, FSP, and Sol-gel). Application of the CEDI exchange method allows the deposition of nano- and sub-nanometre platinum particles with high dispersion and low size distribution.

Additional characterization was performed to determine the effect of the support on the structural and electronic properties of the Pt catalyst on dehydrogenation performance. Interestingly, after a 16-hour reaction, the degree of platinum particle size and size distribution stabilization decreased in accordance with support preparation strategy in the

order of: FSP > SAS > SG. In the case of Pt/FSP-*x* catalysts where the CEDI method was utilized to deposit platinum HRTEM revealed no statistical significance in particle size and size distribution. Both FSP- and SAS-based supports possess a predominantly aggregated nanospheres morphology as well as another “cloud” like, non-spherical morphology with similar aluminium sites, acid site nature and concentration. Morphology and aluminium sites play a key role in localizing and anchoring platinum particles while surface acidity influence catalyst activity and selectivity. This study shows the superior propene yields and productivities of the Pt/SAS-*x* catalysts. In order to draw more definitive conclusions, it would be advantageous to normalize Pt loading to support surface area such that the moles of platinum per m^2 remain constant. An additional study into the reduction conditions is also necessary to further investigate the effect on metal support-interactions, and structural and electronic properties.

Catalyst deactivation is a ubiquitous problem which causes loss of catalyst activity and/or selectivity and is a current concern for the series of monometallic catalyst employed in this study. Among the tested catalysts results suggest the superior performance of the Pt/SAS-4 and Pt/FSP-4 catalysts, but potential application for industrial catalysts under real working conditions require the reduction of deep dehydrogenation reactions that lead to coking. Product distribution analysis suggests that the contribution of coke deposits is minimal. The results suggest the decreased tendency of the side reactions induced by specific sites, such as Brønsted acid site for cracking reactions and metal size; commonly large Pt ensembles display activity for hydrogenolysis, cracking and isomerization reactions.

At this stage it is increasingly difficult to compare catalyst performance obtained for the catalysts studied in this thesis due to differences in the experimental reaction conditions used and the lack of literature focusing on monometallic Pt catalysts supported on ASAs. However, similar catalyst with different support nature, morphology, and surface acid site properties are presented in literature. As a basis for comparison, propene productivity values for the most active catalysts seem to be comparable and, in some cases, superior to the closest analogues in literature. [our review] Therefore, to assess the novelty and impact

of this work additional reactions under identical conditions to literature benchmarked studies are essential accompanied by a regeneration-cycling study.

6.2 Final Conclusions

In summary, this work has addressed the challenge of novel approach to amorphous silica-alumina materials *via* the supercritical antisolvent precipitation method using a systematic approach of experimental and process variables. For comparison, results have shown microstructural similarities to the benchmark FSP-synthesized analogues. A systematic characterization approach has eluded to the achieved low Si/Al, homogeneity of Si and Al on a nanometer scale, high concentration of homotopic acid sites. The rationale design of a bifunctional catalyst has been achieved and a combined characterization and catalytic approach has enhanced understanding of the relevant structure-activity correlations pertinent to acid-catalyzed reactions. Though improved understanding of the catalyst design and activity have been realized, a significant amount of further work remains before scaled and commercial applications can be realized. These additional investigations include a relevant factorial DOE study for material optimization, quantifiable characterization (C_3H_8-/C_3H_6-TPD, MQMAS NMR, CO-DRIFTS) and catalyst performance (MTD and PDH) studies.

6.3 References

1 Z. Wang, Y. Jiang, O. Lafon, J. Trébosc, K. Duk Kim, C. Stampfl, A. Baiker, J.-P. Amoureux and J. Huang, Brønsted acid sites based on penta-coordinated aluminum species, *Nat. Commun.*, 2016, **7**, 13820.

2 J. Huang, N. van Vegten, Y. Jiang, M. Hunger and A. Baiker, Increasing the Brønsted Acidity of Flame-Derived Silica/Alumina up to Zeolitic Strength, *Angew. Chem. Int. Ed.*, 2010, **49**, 7776–7781.

3 L. Mädler, W. J. Stark and S. E. Pratsinis, Flame-made Ceria Nanoparticles, *J. Mater. Res.*, 2002, **17**, 1356–1362.

4 J. Grothe, K. Wegner, M. Medicus, E. Schade and S. Kaskel, Tailoring Catalytic Properties of Copper Manganese Oxide Nanoparticles (Hopcalites-2G) via Flame Spray Pyrolysis, *ChemCatChem*, , DOI:10.1002/cctc.201800639.

7 Appendix

7.1 Additional characterization for chapter 4

7.1.1 SEM/EDX analysis

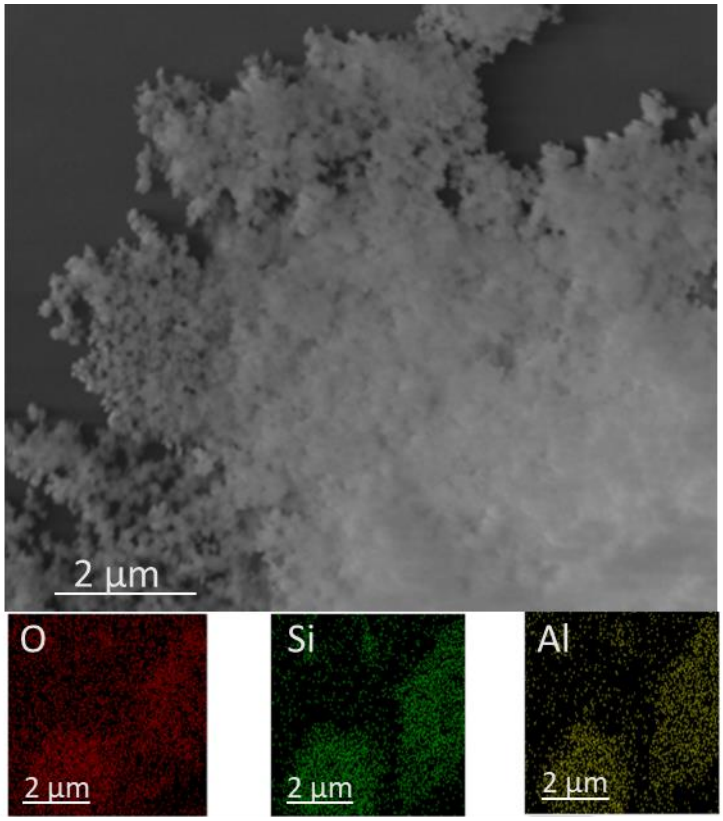

Figure 7. 1: SEM image showing aggregated nanosphere morphology and EDX elemental mapping of SAS-1, indicating homogeneous distribution of Al, Si and O on the material surface on a micrometre scale.

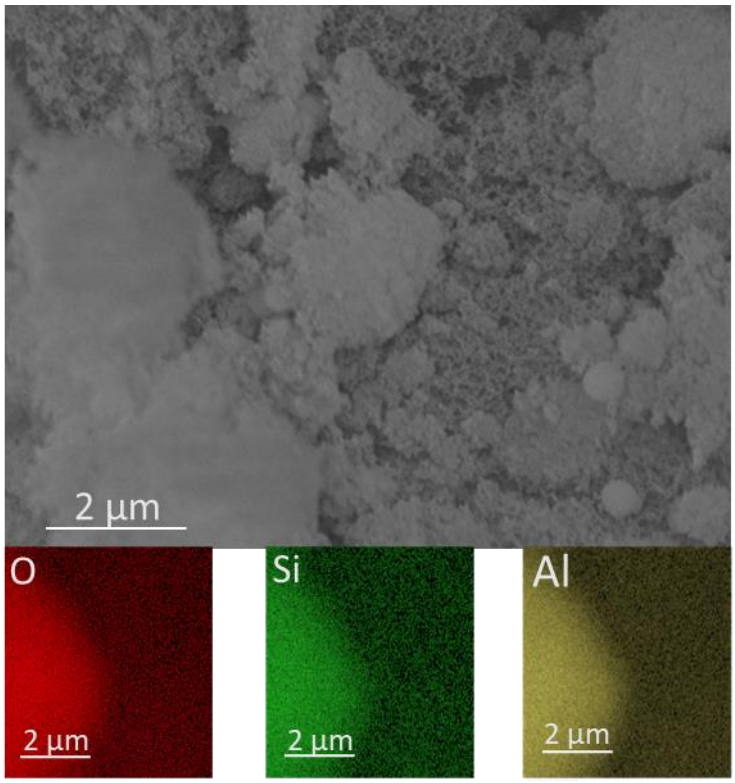

Figure 7. 2: SEM image showing aggregated nanosphere morphology and EDX elemental mapping of SAS-1, indicating homogeneous distribution of Al, Si and O on the material surface on a micrometre scale.

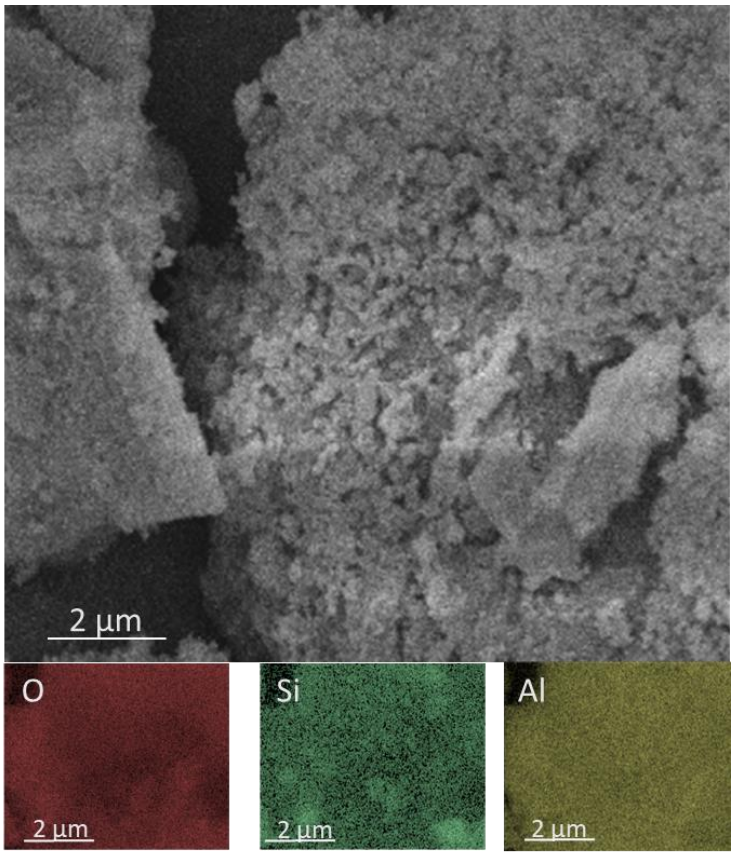

Figure 7. 3: SEM image showing aggregated nanosphere morphology and EDX elemental mapping of SG-1, indicating homogeneous distribution of Al, Si and O on the material surface on a micrometre scale.

7.2 Additional catalytic data for chapter 4

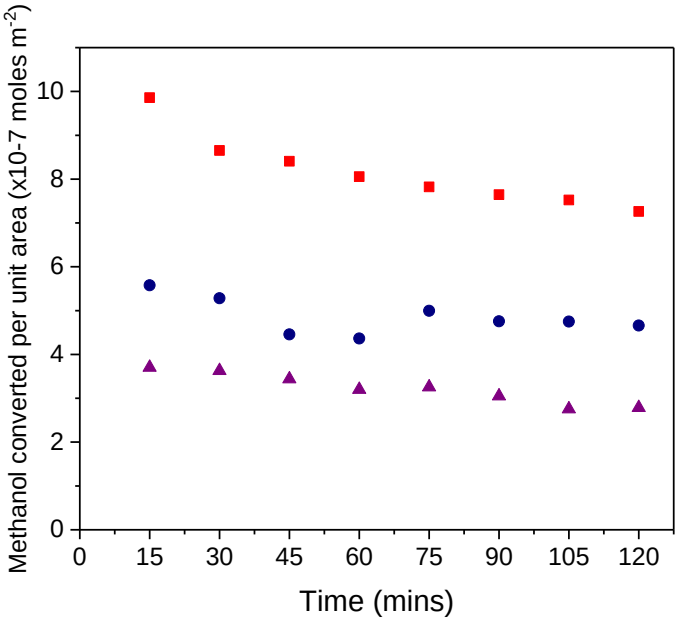

Figure 7. 4: Surface area normalised methanol conversion for FSP-1 (■), FSP-4 (●), and FSP-10 (▲) in the MTD reaction.

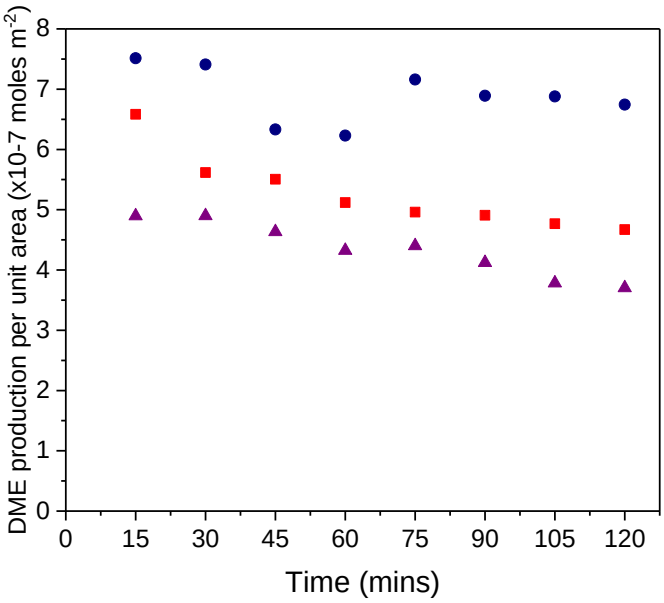

Figure 7. 5: Surface area normalised DME productivity for FSP-1 (■), FSP-4 (●), and FSP-10 (▲) in the MTD reaction.

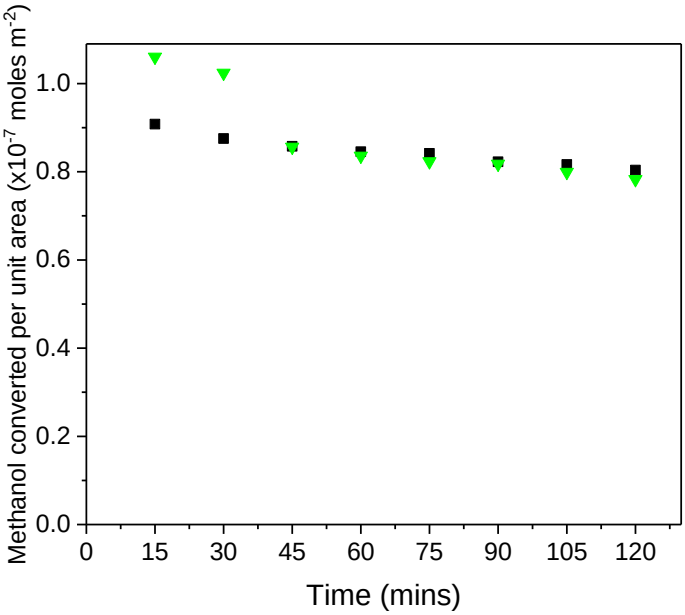

Figure 7. 6: Surface area normalised methanol conversion for SAS-1 (■), and SAS-4 (▼) in the MTD reaction.

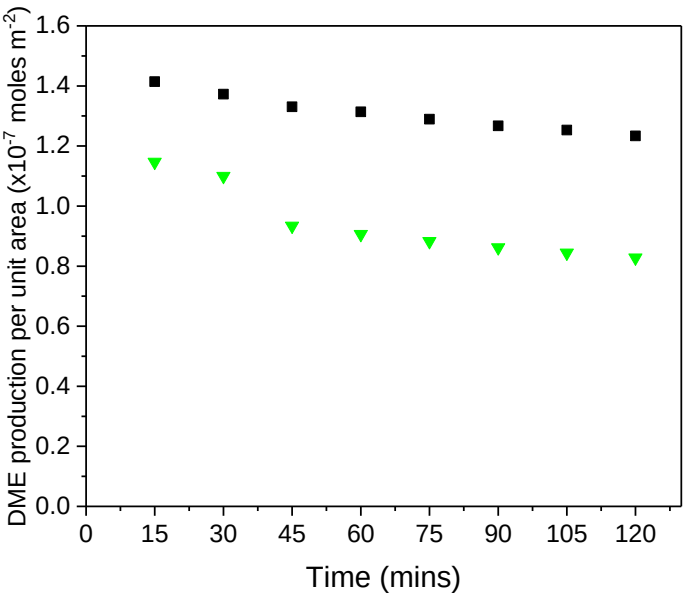

Figure 7. 7: Surface area normalised DME productivity for SAS-1 (■), and SAS-4 (▼) in the MTD reaction.

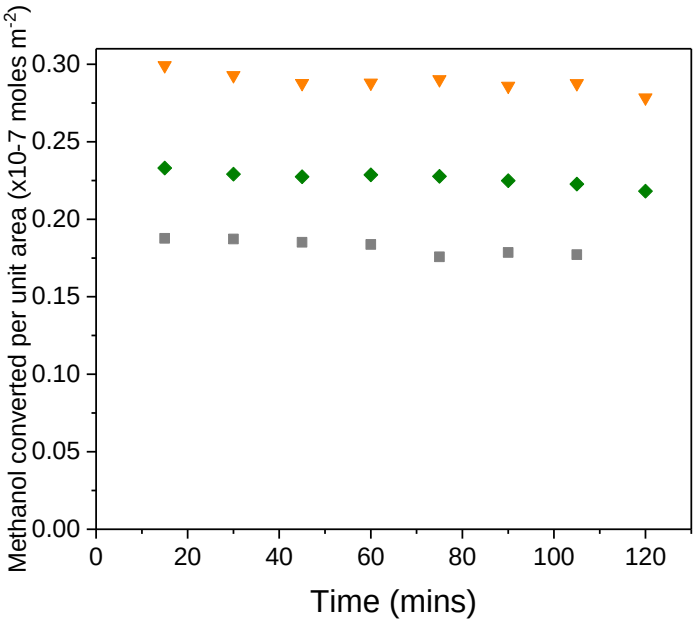

Figure 7. 8: Surface area normalised methanol conversion for SG-1 (■), SG-4 (▼) and SG-10 (◆) in the MTD reaction.

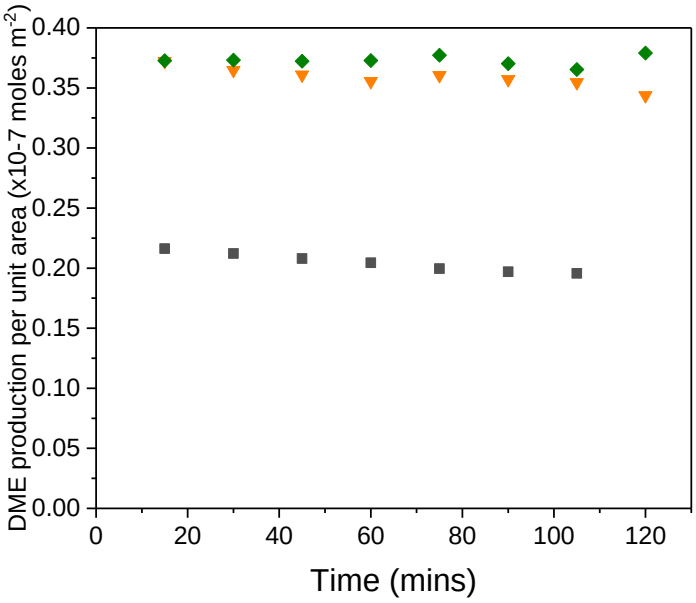

Figure 7. 9: Surface area normalised DME productivity for for SG-1 (■), SG-4 (▼) and SG-10 (◆) in the MTD reaction.

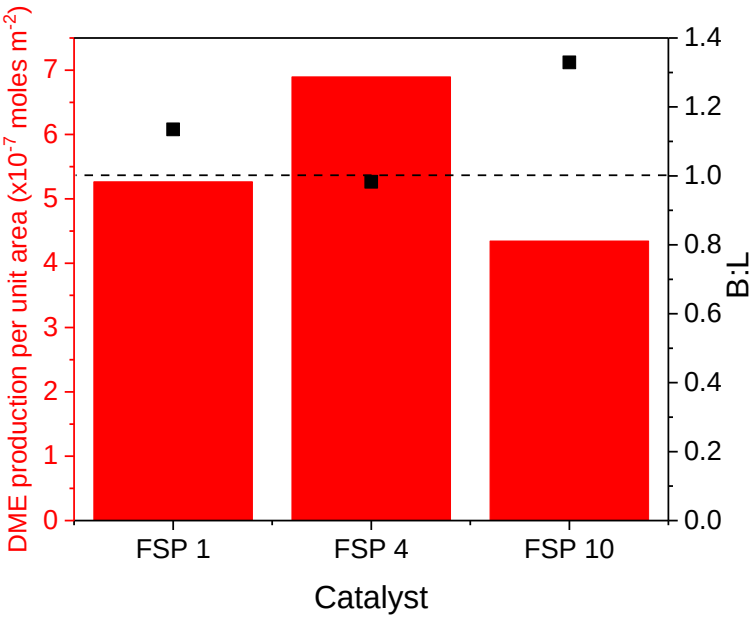

Figure 7. 10: DME productivity correlations with ratio of Brønsted to Lewis acid sites (B:L) for the tested FSP-based ASA catalysts.

7.3 Additional characterization for Chapter 5

7.3.1 HRTEM analysis: Sol-immobilisation catalysts

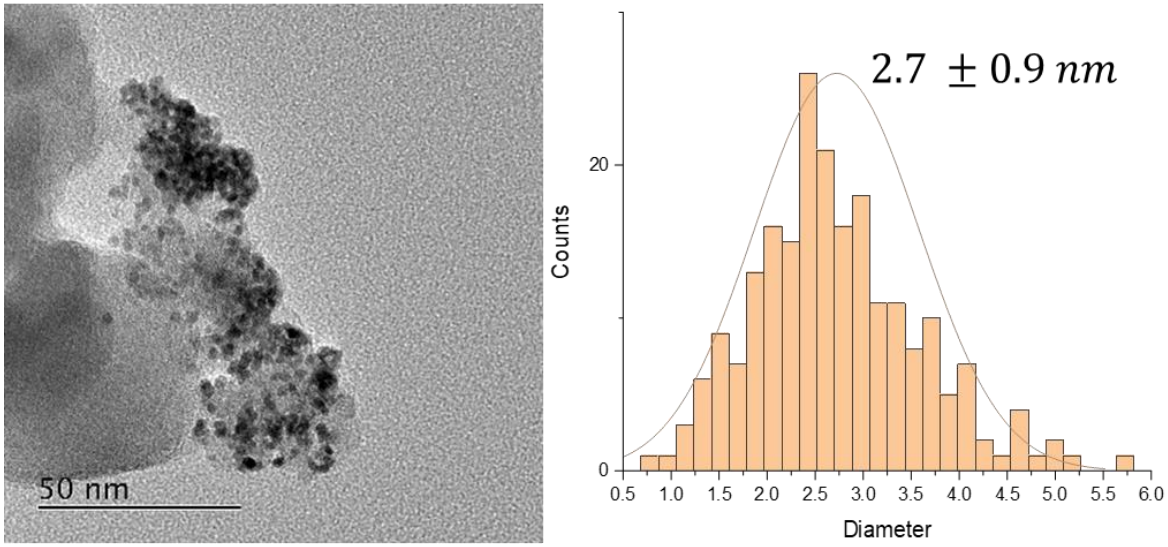

Figure 7. 11: HRTEM image and size distribution analysis of Pt deposited onto FSP-1 *via* sol immobilisation, dried at 110 °C for 16 h and reduced *in situ* at 350 °C for 1 h with 10 vol.% H_2/Ar (total flow rate = 50 ml min^{-1}).

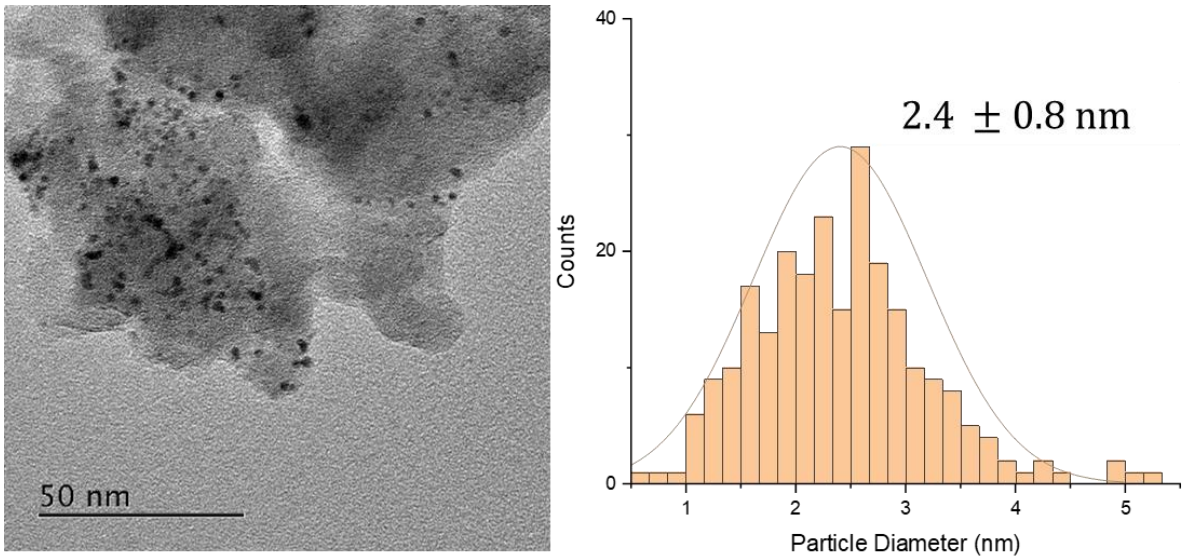

Figure 7. 12: HRTEM image and size distribution analysis of Pt deposited onto FSP-1 *via* sol immobilisation, with PVA removed utilising a 200 °C calcination and reduced *in situ* at 350 °C for 1 h with 10 vol.% H_2/Ar (total flow rate = 50 ml min^{-1}).

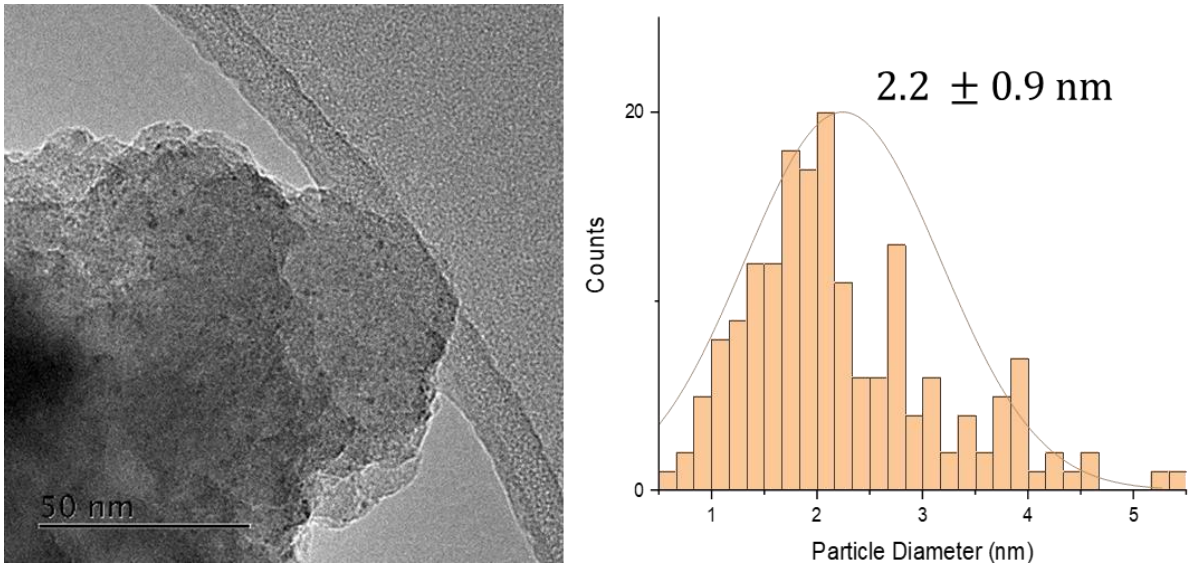

Figure 7. 13: HRTEM image and size distribution analysis of Pt deposited onto FSP-1 *via* sol immobilisation, with PVA removed utilising a 300 °C calcination and reduced *in situ* at 350 °C for 1 h with 10 vol.% H_2/Ar (total flow rate = 50 ml min^{-1}).

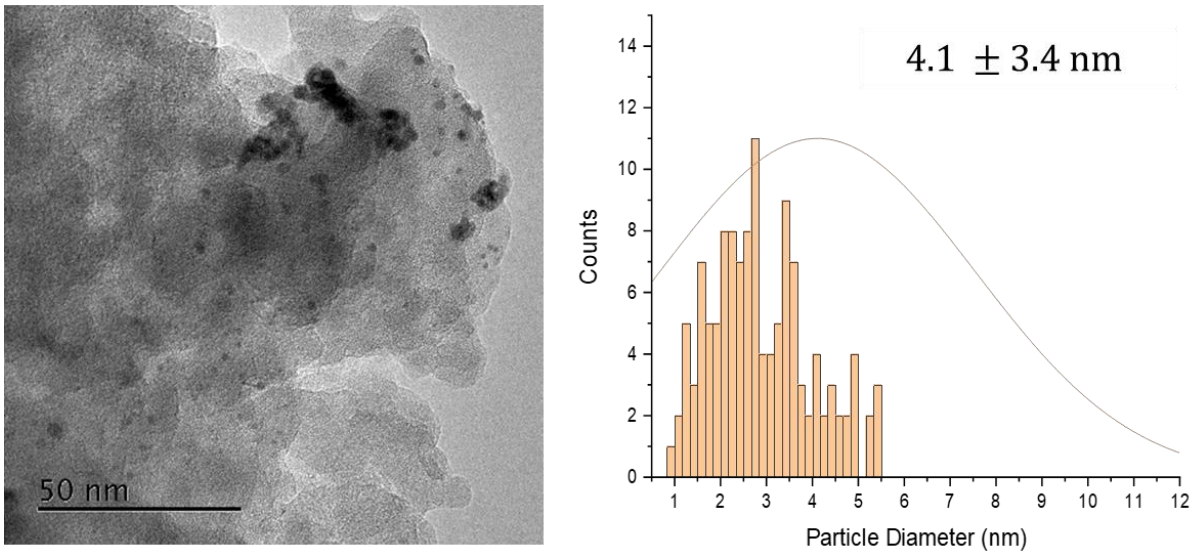

Figure 7. 14: HRTEM image and size distribution analysis of Pt deposited onto FSP-1 *via* sol immobilisation, with PVA removed utilising a 400 °C calcination and reduced *in situ* at 350 °C for 1 h with 10 vol.% H_2/Ar (total flow rate = 50 ml min^{-1}).

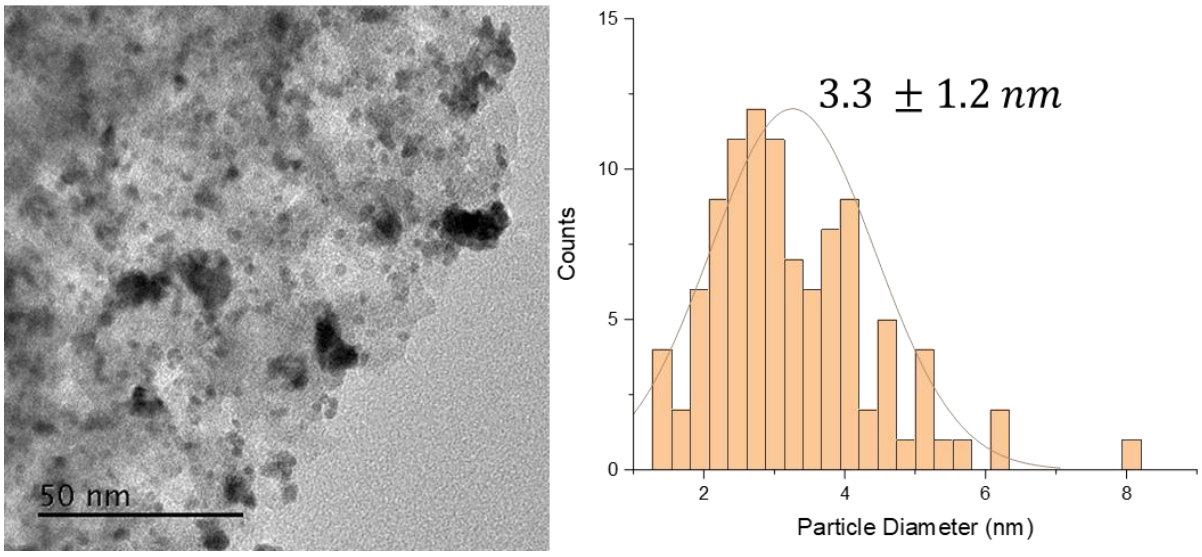

Figure 7. 15: HRTEM image and size distribution analysis of Pt deposited onto FSP-1 *via* sol immobilisation, with PVA removed utilising a 120 min reflux and reduced *in situ* at 350 °C for 1 h with 10 vol.% H_2/Ar (total flow rate = 50 ml min^{-1}).

7.3.2 HRTEM analysis: CEDI catalysts

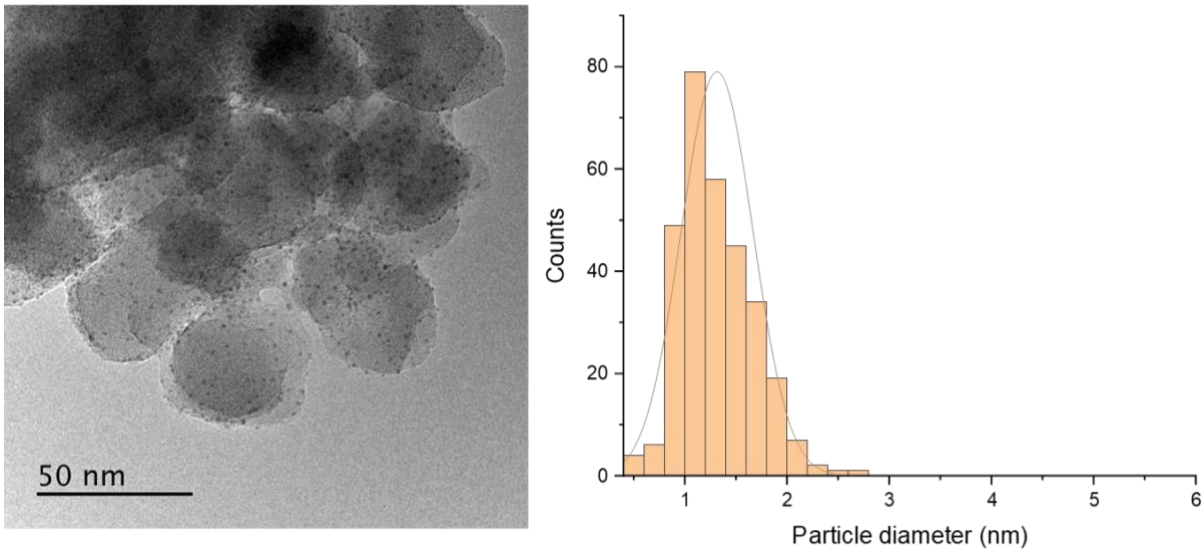

Figure 7. 16: HRTEM image and particle distribution analysis of CEDI prepared, Pt/SAS-4 catalyst after in-situ reduction at 350 °C for 1 h with 10 vol.% H_2/Ar (total flow rate = 50 ml min^{-1}).

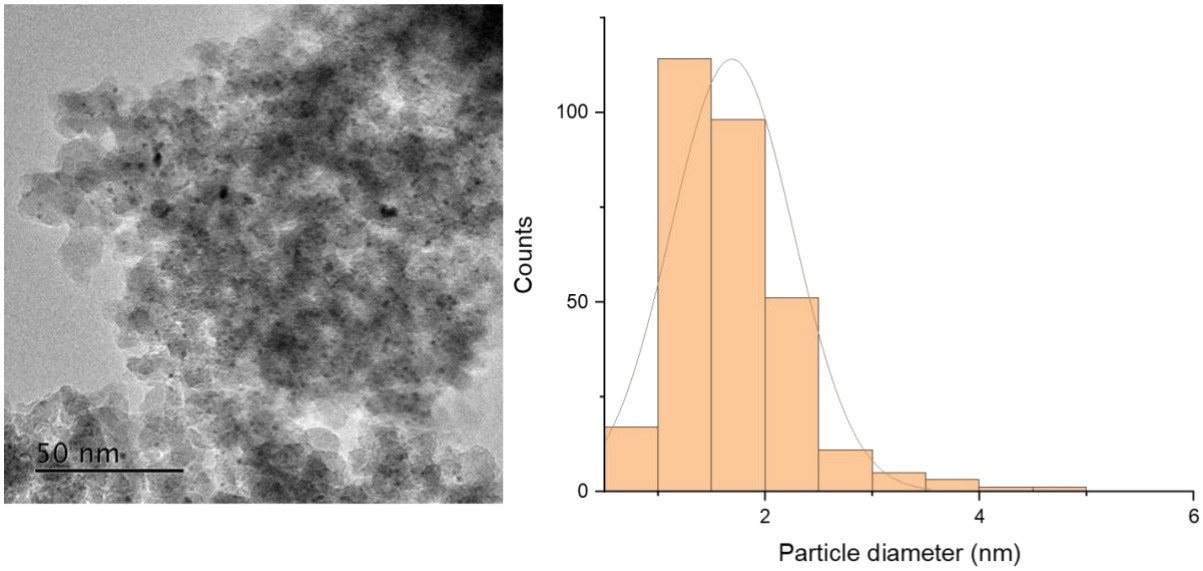

Figure 7. 17: HRTEM image and particle distribution analysis of CEDI prepared, Pt/FSP-4 catalyst after in-situ reduction at 350 °C for 1 h with 10 vol.% H_2/Ar (total flow rate = 50 ml min^{-1}).

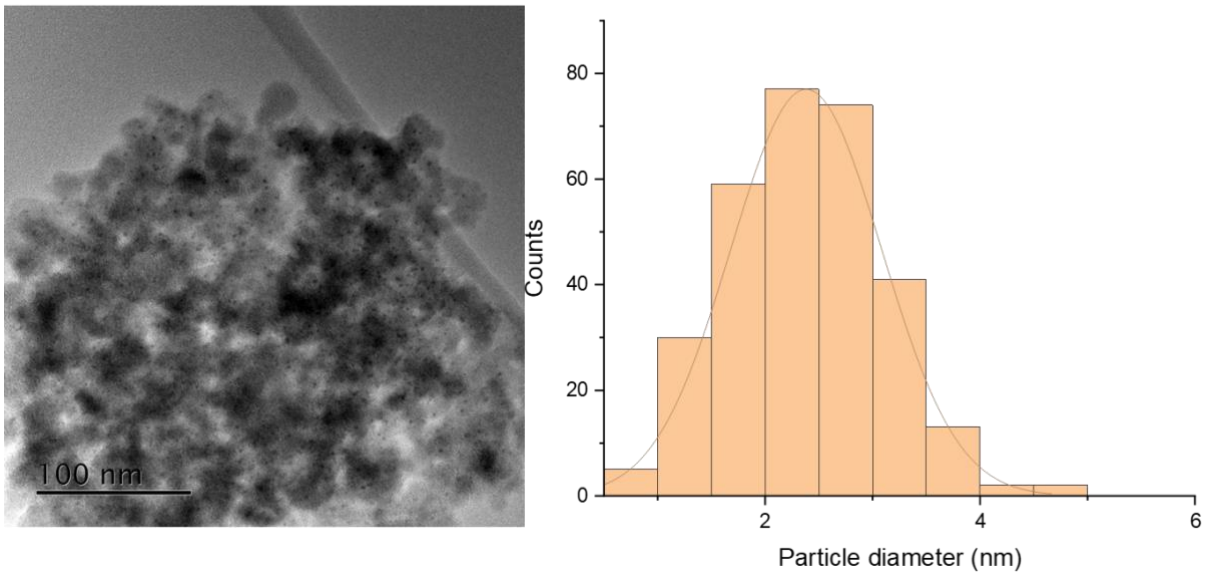

Figure 7. 18: HRTEM image and particle distribution analysis of CEDI prepared, Pt/FSP-10 catalyst after in-situ reduction at 350 °C for 1 h with 10 vol.% H_2/Ar (total flow rate = 50 ml min^{-1}).

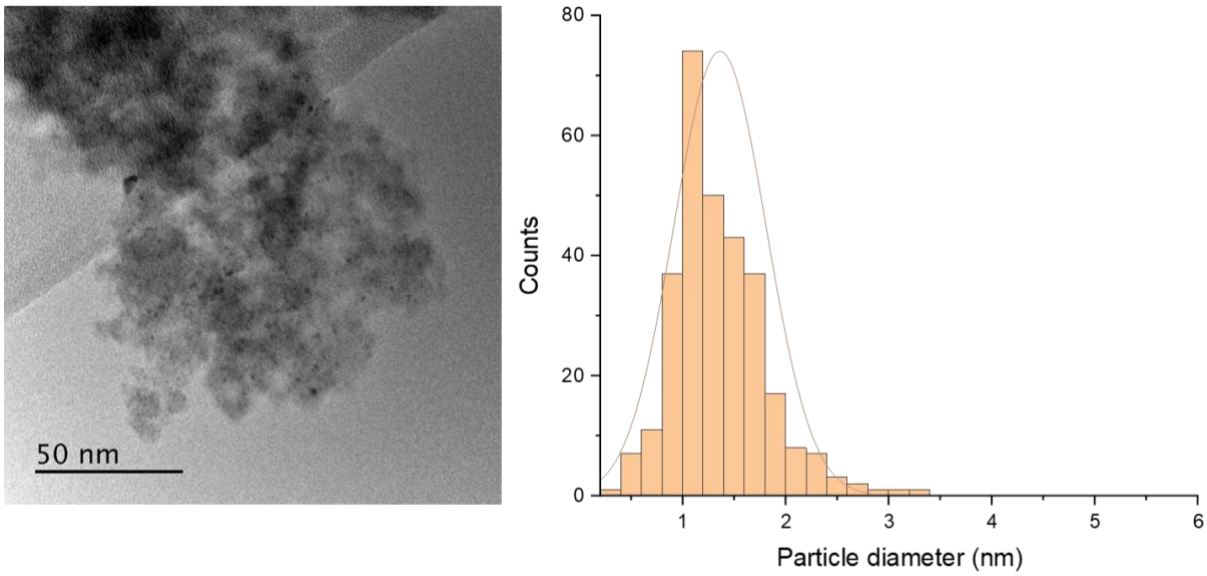

Figure 7. 19: HRTEM image and particle distribution analysis of CEDI prepared, Pt/SG-1 catalyst after in-situ reduction at 350 °C for 1 h with 10 vol.% H_2/Ar (total flow rate = 50 ml min^{-1}).

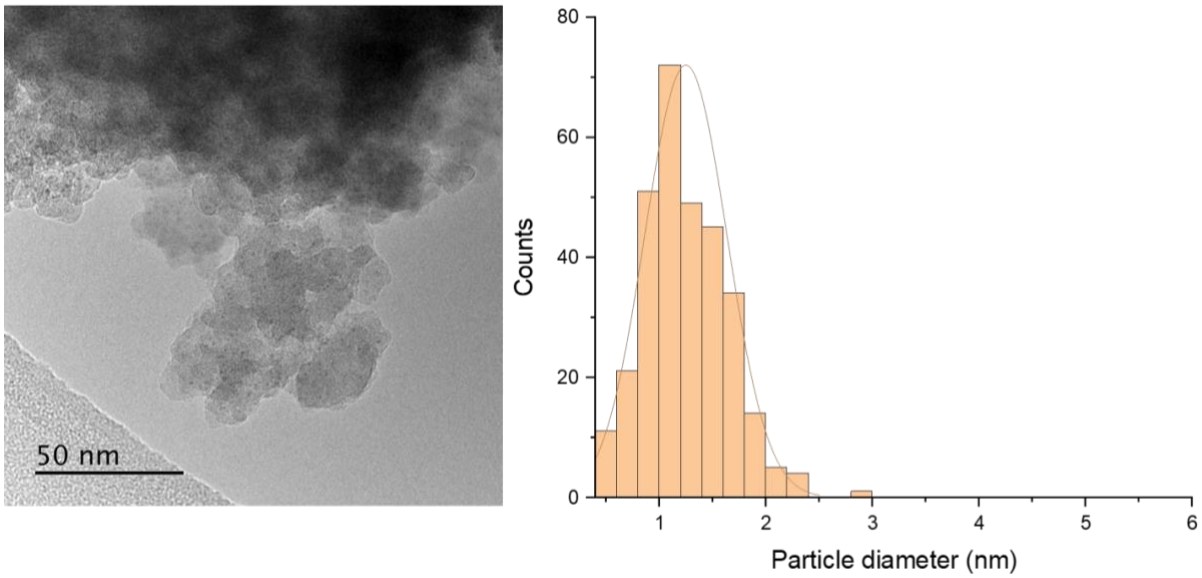

Figure 7. 20: HRTEM image and particle distribution analysis of CEDI prepared, Pt/SG-4 catalyst after in-situ reduction at 350 °C for 1 h with 10 vol.% H_2/Ar (total flow rate = 50 ml min^{-1}).

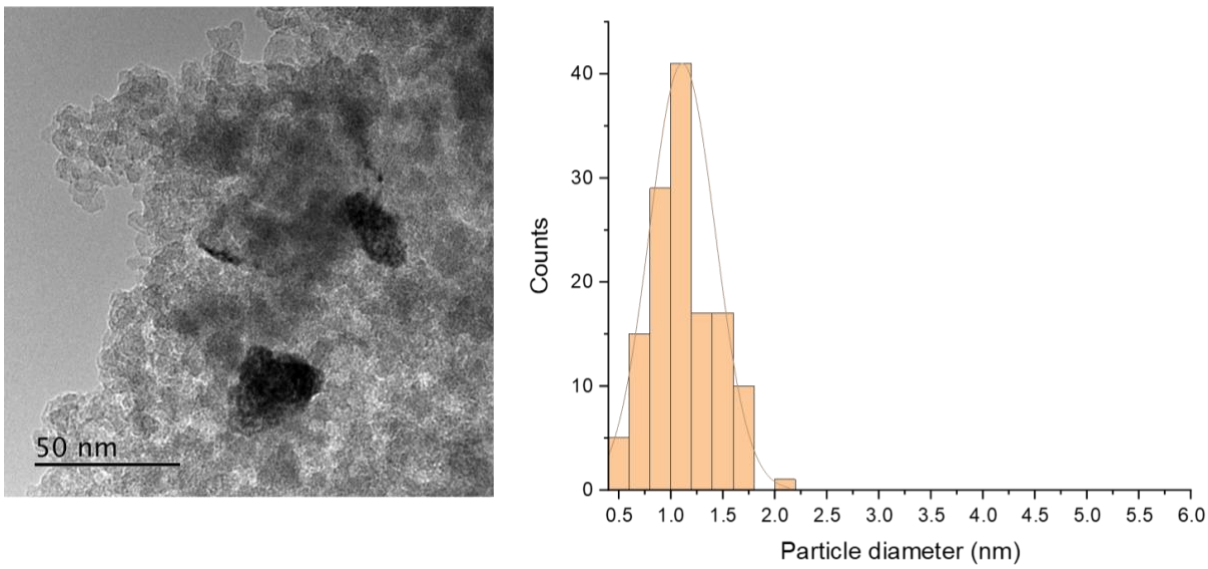

Figure 7. 21: HRTEM image and particle distribution analysis of CEDI prepared, Pt/SG-10 catalyst after in-situ reduction at 350 °C for 1 h with 10 vol.% H_2/Ar (total flow rate = 50 ml min^{-1}).

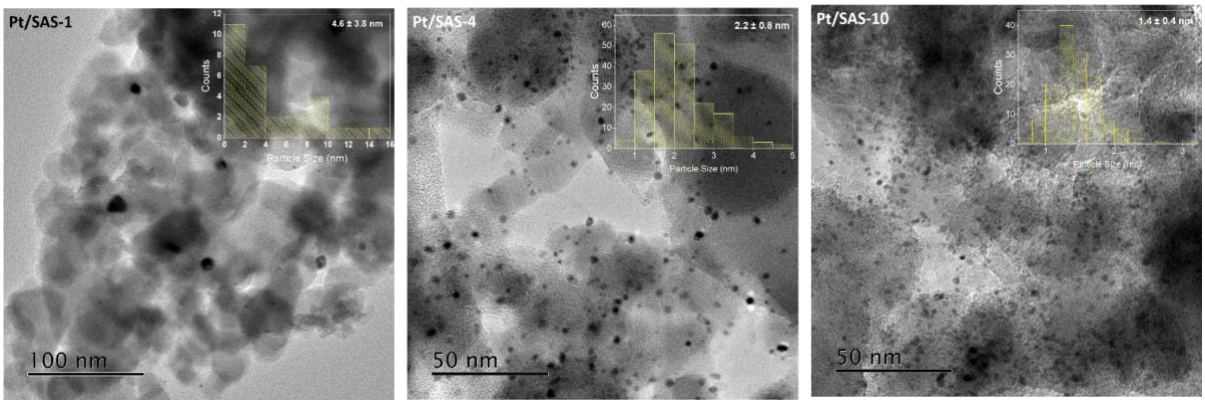

Figure 7. 22: HRTEM images and particle distribution analysis of recovered CEDI prepared, Pt/SAS-*x* catalysts after a 16 hour PDH reaction.

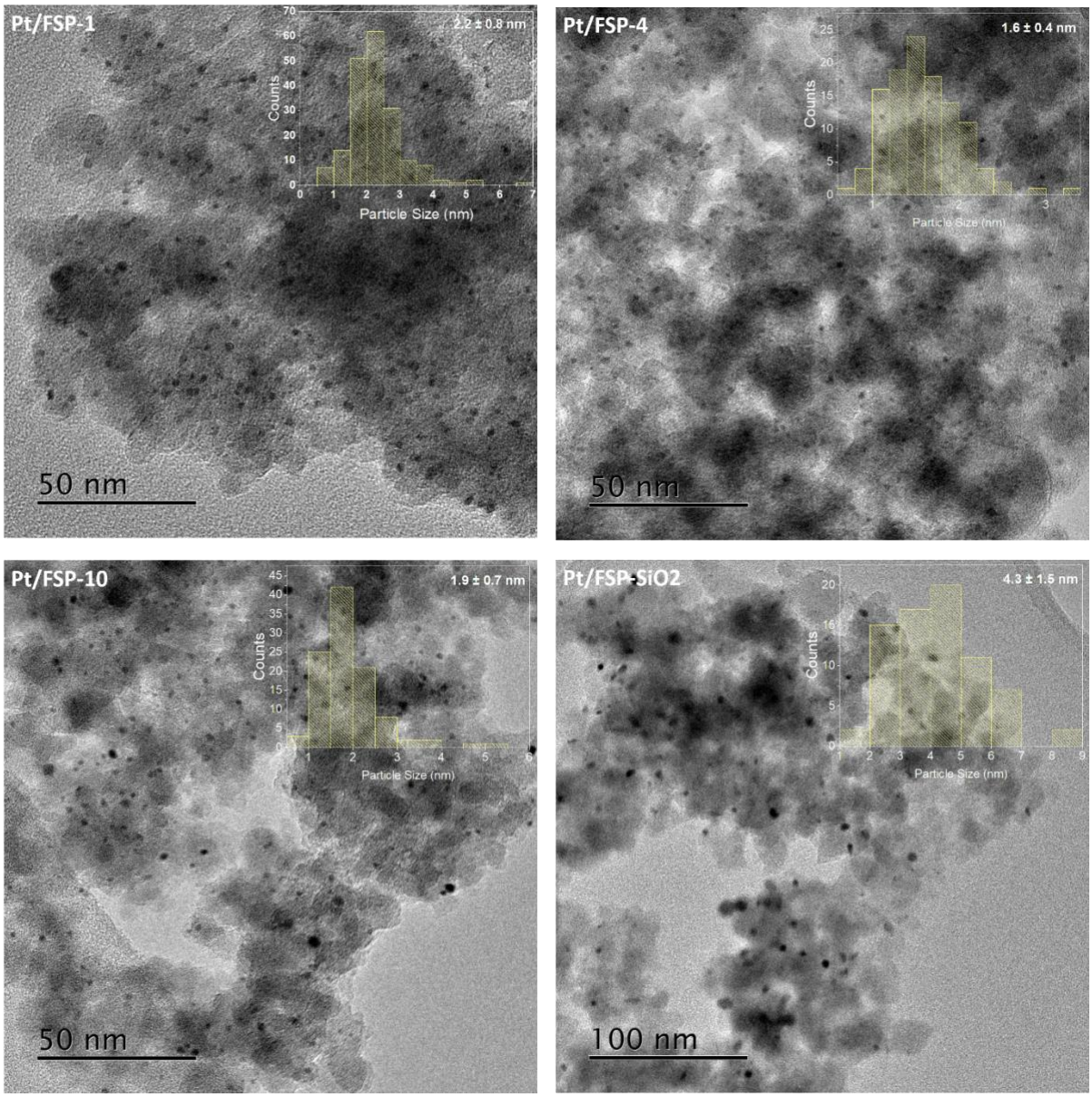

Figure 7. 23: HRTEM image and particle distribution analysis of recovered CEDI prepared, Pt/FSP-*x* catalysts after a 16 hour PDH reaction.

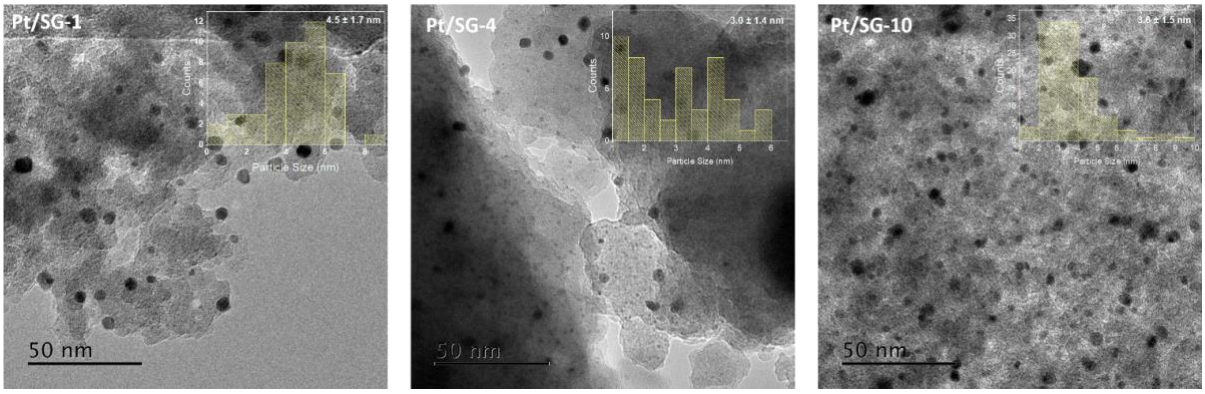

Figure 7. 24: HRTEM images and particle distribution analysis of recovered CEDI prepared, Pt/SG-*x* catalysts after a 16 hour PDH reaction.

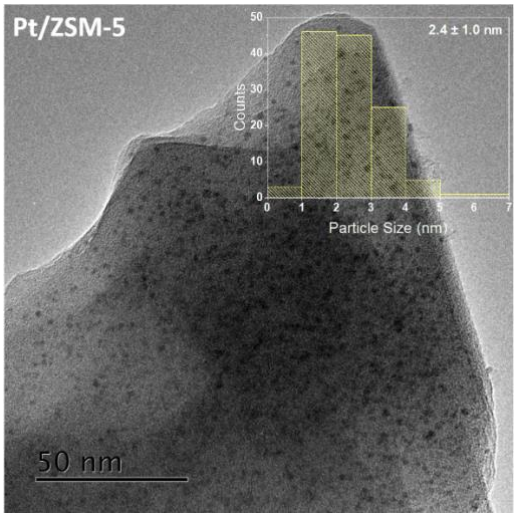

Figure 7. 25: HRTEM image and particle distribution analysis of recovered CEDI prepared, Pt/H-ZSM5 catalysts after a 16 hour PDH reaction.

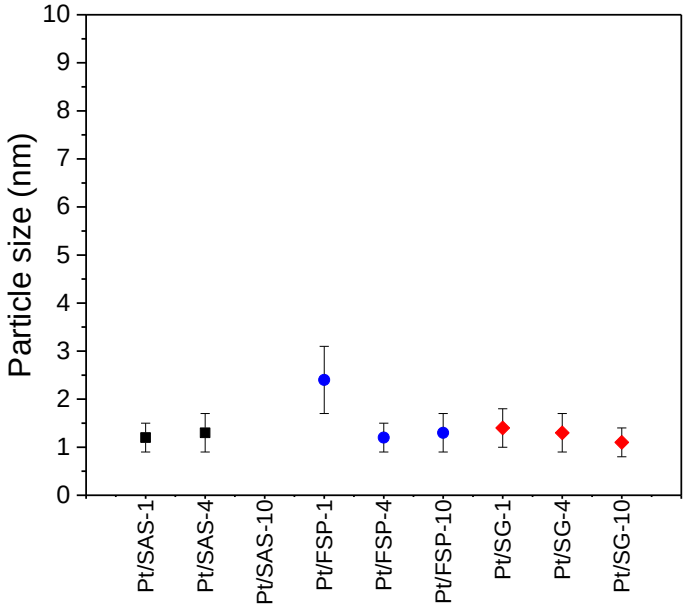

Figure 7. 26: Particle sizes and size distributions of reduced Pt-based, CEDI prepared and reduced catalysts with systematically varied supports.

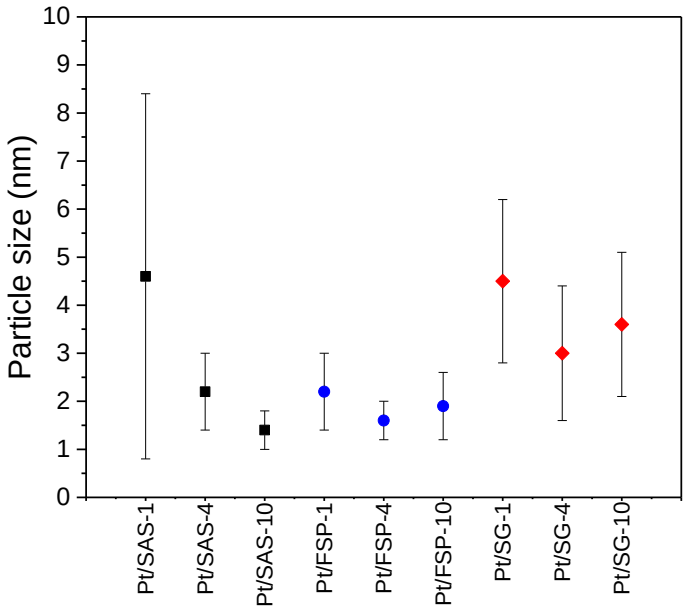

Figure 7. 27: Particle sizes and size distributions of post-reaction Pt-based, CEDI prepared and reduced catalysts with systematically varied supports.

7.3.3 XRD analysis

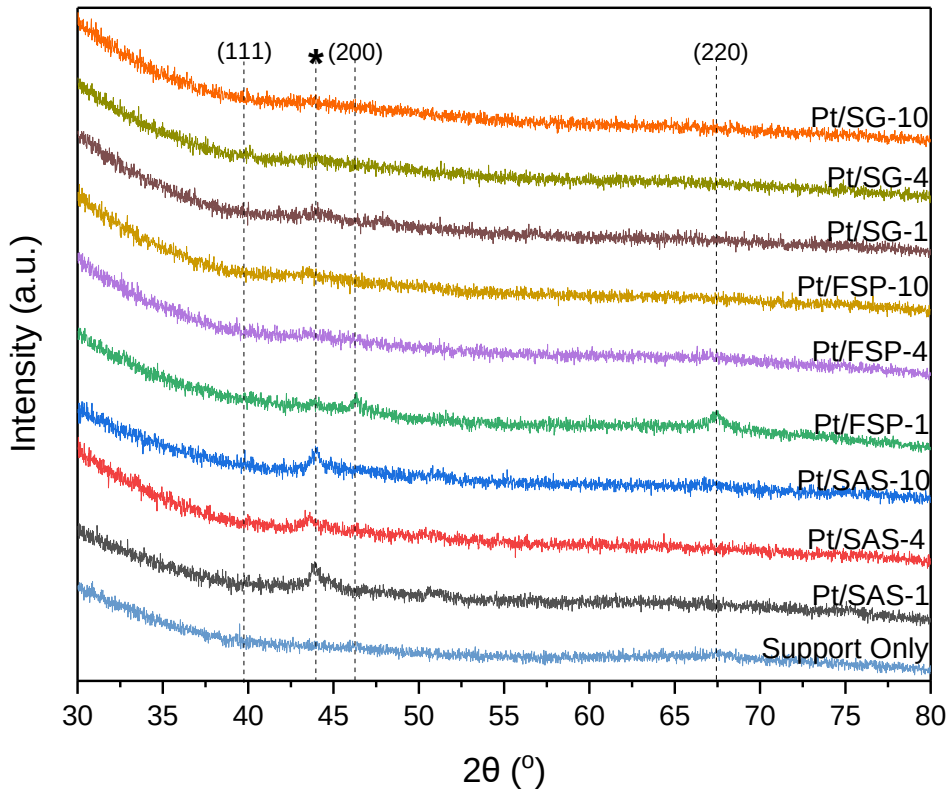

Figure 7. 28: XRD pattern for reduced CEDI-prepared Pt/SAS-*x*, Pt/FSP-*x*, Pt/SG-*x* catalysts and pristine ASA material.

7.3.4 NMR analysis

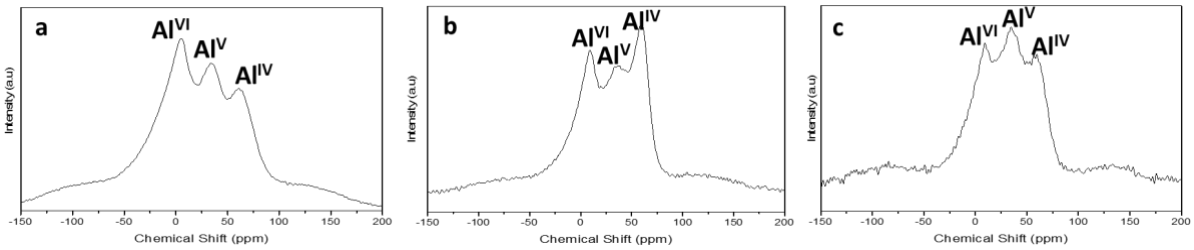

Figure 7. 29: 1D MAS ^{27}Al MAS NMR spectra of (a) SAS-1, (b) reduced CEDI prepared Pt/SAS-1, and (c) Post-reaction Pt/SAS-1 catalysts.

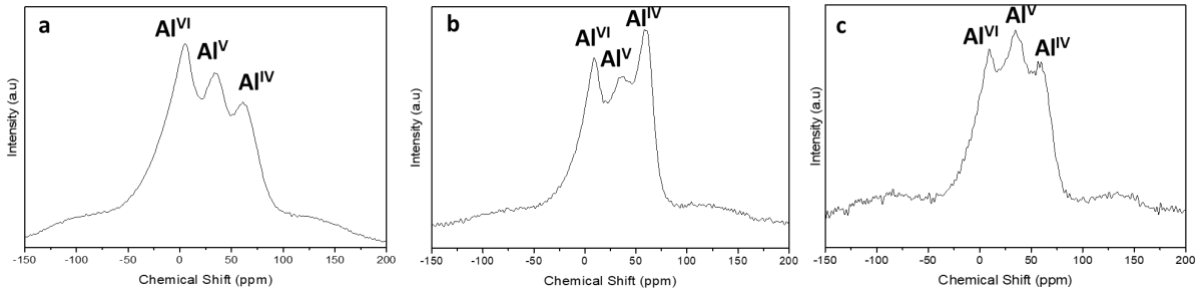

Figure 7. 30: 1D MAS ^{27}Al MAS NMR spectra of (a) FSP-1, (b) reduced CEDI prepared Pt/FSP-1, and (c) Post-reaction Pt/FSP-1 catalysts.

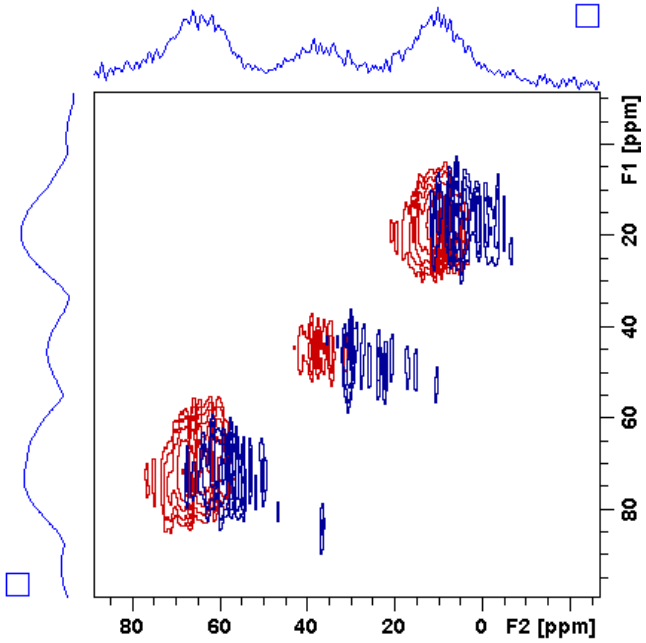

2D MQMAS ^{27}Al MAS NMR spectra of reduced CEDI prepared Pt/SAS-1 (red), and Post-reaction Pt/SAS-1 (blue) catalysts.

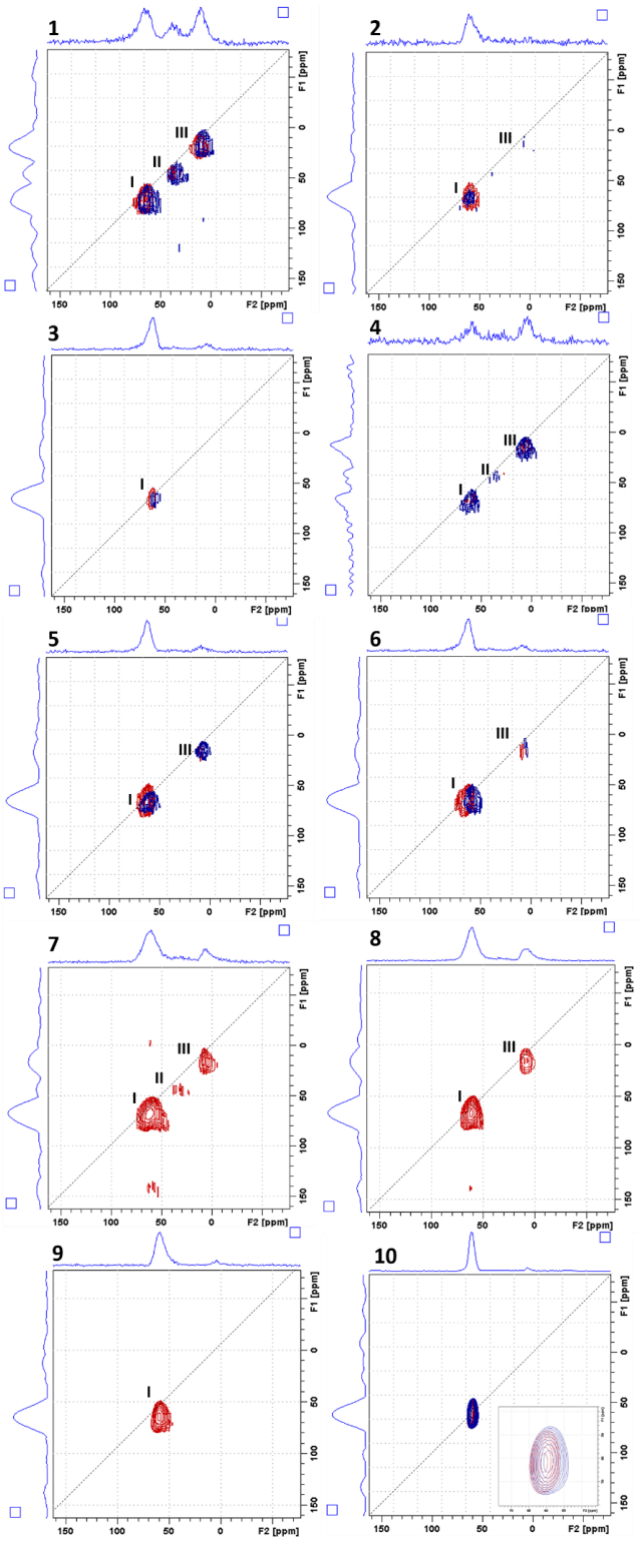

Figure 7. 31: 2D MQMAS ^{27}Al MAS NMR spectra of 10 **Pt-based catalysts**: (**1**) Pt/SAS-1, (**2**) Pt/SAS-4, (**3**) Pt/SAS-10, (**4**) Pt/FSP-1, (**5**) Pt/FSP-4, (**6**) Pt/FSP-10, (**7**) Pt/SG-1, (**8**) Pt/SG-4, (**9**) Pt/SG-10 and (**10**) Pt/ZSM5; and the corresponding **supports**. Projections on the vertical and horizontal frequency axes, F_1 and F_2, are indicated above and left of each spectrum.

7.3.5 XPS analysis

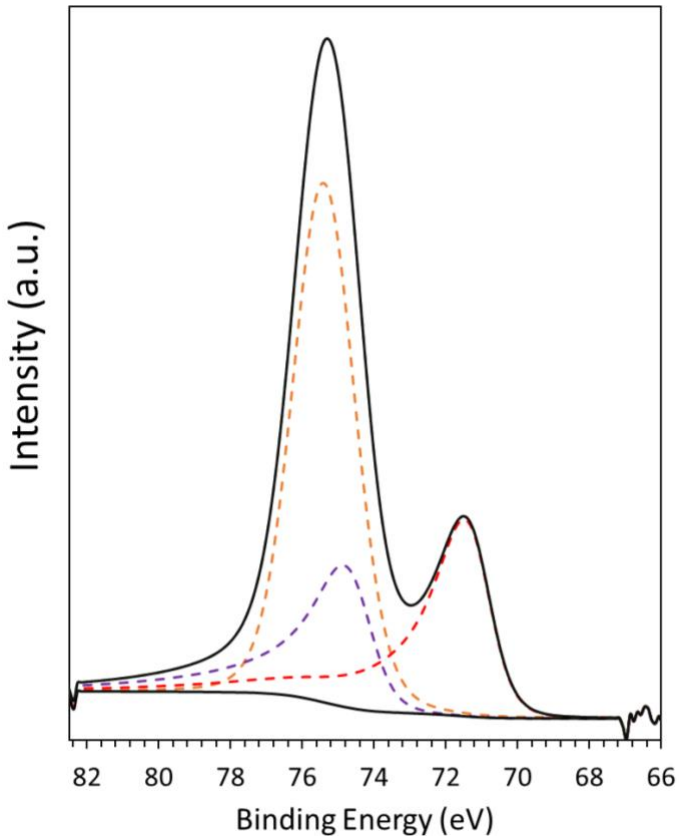

Figure 7. 32: XPS spectra of the Al2p (---) and Pt 4f (---Pt $4f_{7/2}{}^{0}$, ---Pt $4f_{7/2}{}^{2+}$) regions of post-reaction Pt/FSP-4 catalyst.

7.4 Additional catalytic data for chapter 5

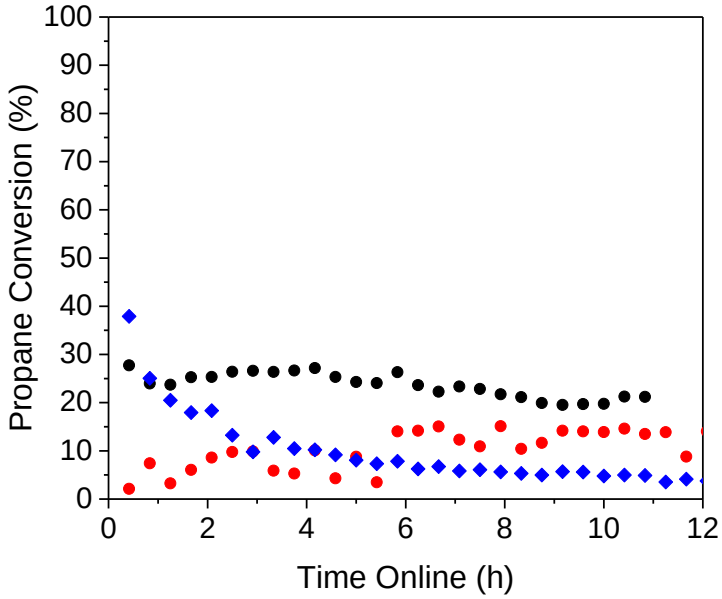

Figure 7. 33: Conversion of C_3H_8 for Pt/SAS-SiO_2 (●), Pt/FSP-SiO_2 (●), and Pt/H-ZSM5 (◆) catalysts.

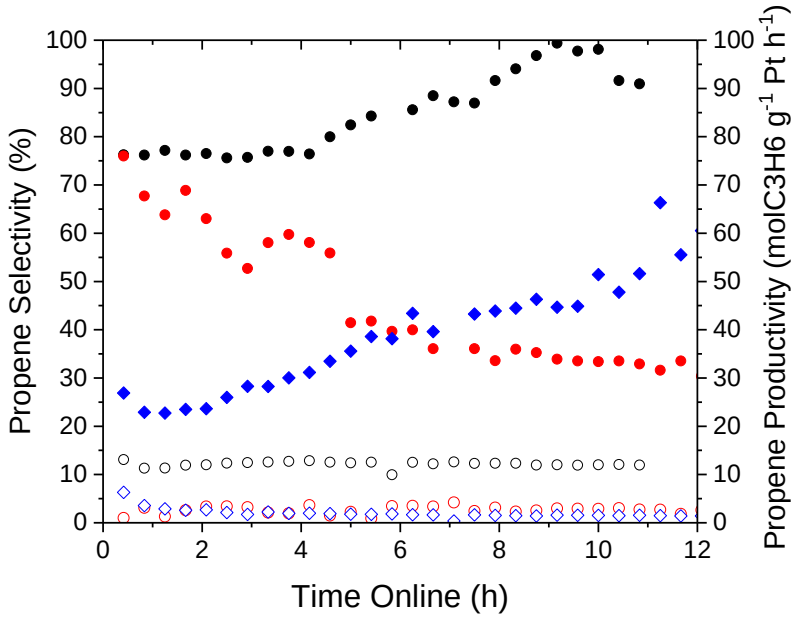

Figure 7. 34: Selectivity to C_3H_6 (full symbols) and C_3H_6 productivity (hollow symbols) for Pt/SAS-SiO_2 (●), Pt/FSP-SiO_2 (●), and Pt/H-ZSM5 (◆) catalysts.

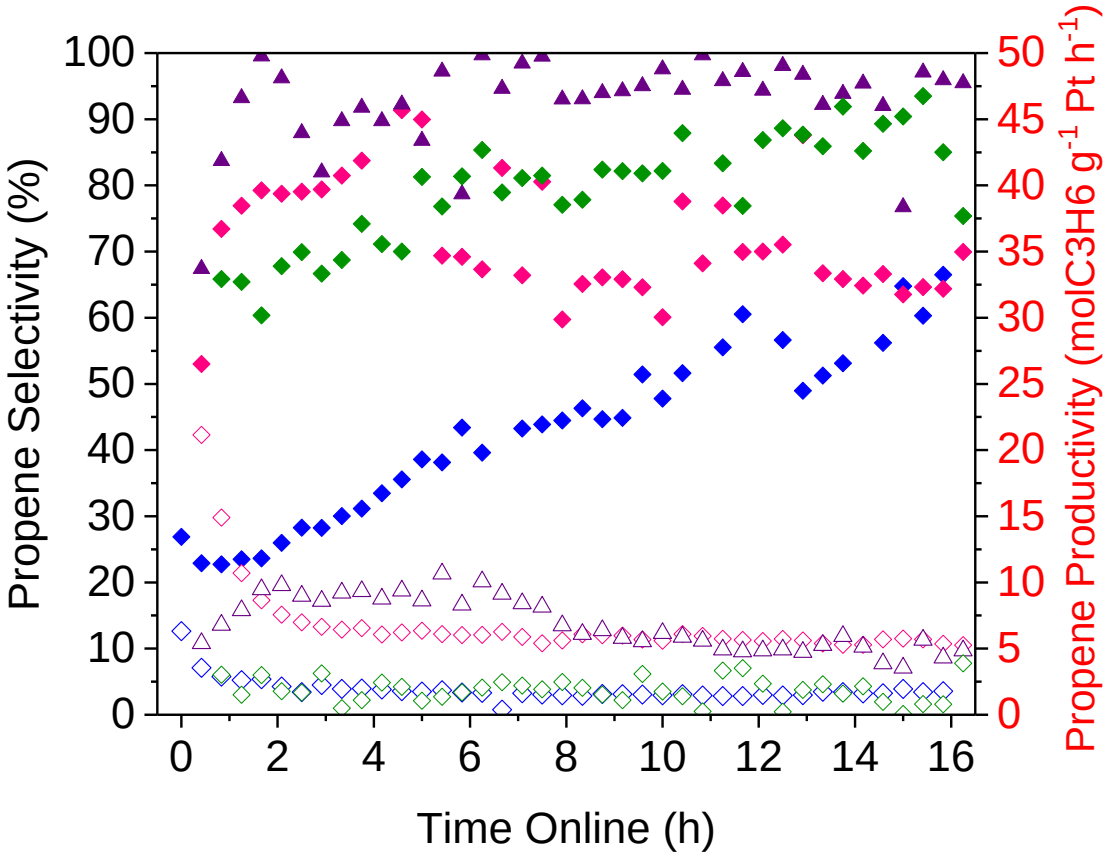

Figure 7.35: Selectivity to C_3H_6 (full symbols) and C_3H_6 productivity (hollow symbols) Pt/SAS-10 (◆); Pt/FSP-10 (▲); Pt/SG-10 (◆) and Pt/H-ZSM5 (◆) catalysts.

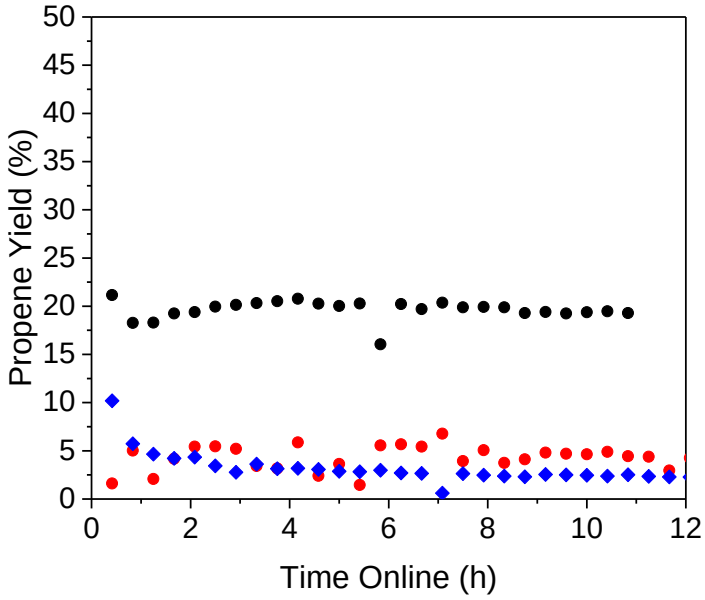

Figure 7. 36: Yield of C_3H_6 for Pt/SAS-SiO_2 (●), Pt/FSP-SiO_2 (●), and Pt/H-ZSM5 (◆) catalysts.

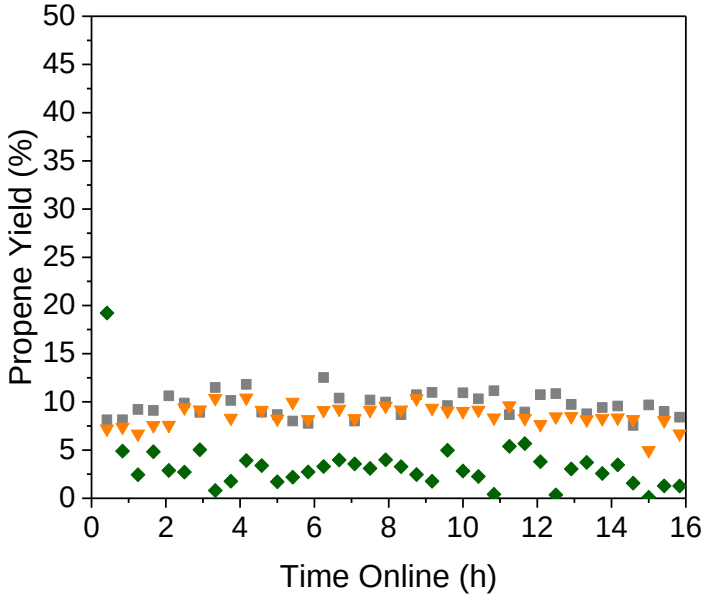

Figure 7. 37: Yield of C_3H_6 for Pt/SG-1 (■), Pt/SG-4 (▼) and Pt/SG-10 (◆) catalysts.

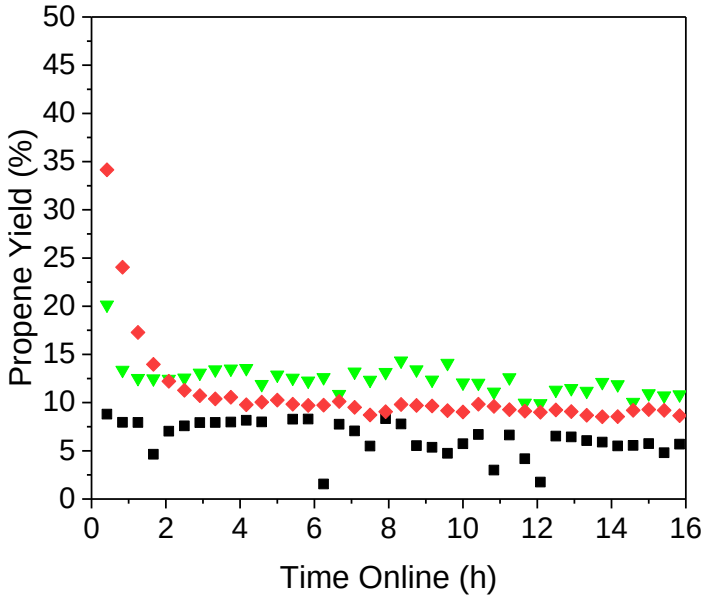

Figure 7. 38: Yield of C_3H_6 for Pt/SAS-1 (■), Pt/SAS-4 (▼), Pt/SAS-10 (◆) catalysts.

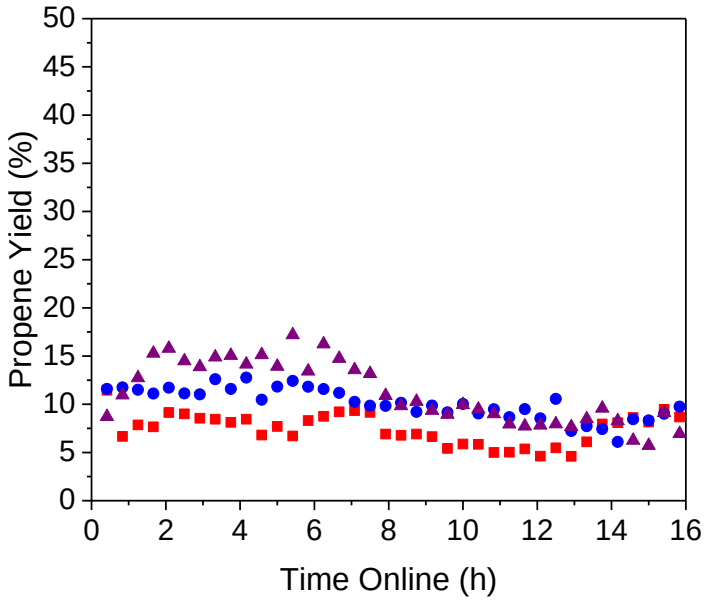

Figure 7. 39: Yield of C_3H_6 for Pt/FSP-1 (■), Pt/FSP-4 (●), Pt/FSP-10 (▲) catalysts.